Forschungszentrum Karlsruhe
Technik und Umwelt
Wissenschaftliche Berichte
FZKA 5665

Summary Report of NEPTUN Investigations into the Steady State Thermal Hydraulics of the Passive Decay Heat Removal

**K. Rust, D. Weinberg, H. Hoffmann,
H. H. Frey, W. Baumann, K. Hain,
W. Leiling, H. Hayafune, H. Ohira**

**Institut für Angewandte Thermo- und Fluiddynamik
Institut für Neutronenphysik und Reaktortechnik
Hauptabteilung Ingenieurtechnik
Projekt Nukleare Sicherheitsforschung**

Dezember 1995

FORSCHUNGSZENTRUM KARLSRUHE
Technik und Umwelt

Wissenschaftliche Berichte
FZKA 5665

SUMMARY REPORT OF NEPTUN INVESTIGATIONS INTO THE STEADY STATE THERMAL HYDRAULICS OF THE PASSIVE DECAY HEAT REMOVAL

K. Rust, D. Weinberg, H. Hoffmann, H.H. Frey,
W. Baumann, K. Hain, W. Leiling,
H. Hayafune *, and H. Ohira *

Institut für Angewandte Thermo- und Fluiddynamik
Institut für Neutronenphysik und Reaktortechnik
Hauptabteilung Ingenieurtechnik
Projekt Nukleare Sicherheitsforschung

* Power Reactor and Nuclear Fuel Development Corporation,
O-arai Engineering Center, O-arai, Ibaraki-ken 311-13, Japan

Forschungszentrum Karlsruhe GmbH, Karlsruhe
1995

Forschungszentrum Karlsruhe GmbH
Postfach 3640, 76021 Karlsruhe

ISSN 0947-8620

SUMMARY REPORT OF NEPTUN INVESTIGATIONS INTO THE STEADY STATE THERMAL HYDRAULICS OF THE PASSIVE DECAY HEAT REMOVAL

ABSTRACT

The reliable decay heat removal after shutdown of a reactor is an important safety criterion. For that reason, the design of the sodium-cooled European Fast Reactor provides a safety graded decay heat removal system in addition to the normal heat removal routes by way of steam/water circuits. This passive concept is based on several direct reactor cooling systems which operate independently from each other. Each of them consists of a sodium/sodium decay heat exchanger placed in the upper plenum of the primary vessel and connected via an intermediate sodium loop to a sodium/air heat exchanger arranged at the bottom end of a stack. The decay heat is removed by natural convection on the sodium side and natural draft on the air side.

To demonstrate the coolability of the pool-type primary system by buoyancy-driven natural circulation when forced convection is lost, many experiments are carried out under steady state and transient conditions in test facilities of different scale and detail. All these investigations serve to prove the inherent safe removal of the decay heat by totally passive measures, to study the physical processes taking place in the primary vessel and in the cooling circuits, and to provide a broad data basis for the development, improvement, and assessment of computer programs.

Following to the earlier RAMONA water experiments performed in a 1:20 scaled 3D setup equipped with all active components but a rather simple core design, the NEPTUN program was conducted utilizing a 1:5 scaled 3D apparatus. The very realistical core geometry designed for a maximum power of 1,600 kW allowed investigations into the thermal hydraulic interaction between the core including the interwrapper phenomena and the decay heat exchangers. Again, water was used as sodium simulant. Apart from measurements of the core power and core mass flow rate, the most part of the instrumentation served to measure coolant temperatures in the rod bundles and interwrapper spaces of the core, in the installed components, and in the different plena of the primary system. About 1,200 thermocouples were fixed in areas of interest. Furthermore, two movable measuring devices were available which enabled temperature measurements at nearly all positions within the upper plenum.

During the course of steady state NEPTUN investigations, the effects of different design and operating parameters were studied; in particular: the shell design

of the above core structure, the core power, the number of decay heat exchangers put in operation, the complete flow path blockage at the primary side of the intermediate heat exchangers, and the fluid level in the primary vessel.

The findings of the NEPTUN experiments indicate that the decay heat can be safely removed by natural convection. The interwrapper flow makes an essential contribution to that behavior. The decay heat exchangers installed in the upper plenum cause a thermal stratification associated with a pronounced gradient. The vertical extent of the stratification and the quantity of the gradient are depending on the fact whether a permeable or an impermeable shell covers the above core structure. An increase of the core power or a reduction of the number of decay heat exchangers being in operation leads to a higher temperature level in the primary system but does not alter the global temperature distribution. In the case that no coolant enters the inlet windows at the primary side of the intermediate and decay heat exchangers, the core remains coolable as far as the primary vessel is filled with fluid up to a minimum level. Cold water penetrates from the upper plenum into the core and removes the decay heat.

The thermal hydraulic computer code FLUTAN was applied for the three-dimensional numerical simulation of the majority of NEPTUN tests reported here. The comparison of computed against experimental data indicates a qualitatively and quantitatively satisfying agreement of the findings with respect to the field of isotherms as well as the temperature profiles in the upper plenum and within the core region of very complex geometry.

ZUSAMMENFASSENDER BERICHT ÜBER NEPTUN UNTERSUCHUNGEN ZUM STATIONÄREN THERMOHYDRAULISCHEN VERHALTEN DER PASSIVEN NACHWÄRMEABFUHR

KURZFASSUNG

Ein wichtiges Sicherheitskriterium für Kernreaktoren ist die zuverlässige Abfuhr der Nachwärme, die nach dem Abschalten der Anlage freigesetzt wird. Zur Nachwärmeabfuhr (NWA) steht daher im European Fast Reactor (EFR) das sicherheitstechnische NWA-System zusätzlich zum betrieblichen System mit Zwischen- und Wasser/Dampf-Kreisläufen zur Verfügung. Das sicherheitstechnische Kühlkonzept besteht aus mehreren unabhängig voneinander arbeitenden Kreisläufen mit jeweils einem Na/Na-Wärmetauscher, der im Oberplenum des Primärsystems angeordnet ist, einem Na-Zwischenkreislauf und einem Luftkühler, der in einem Kamin installiert ist. Die Nachwärmeabfuhr geschieht durch Naturkonvektion auf der Natriumseite und durch Naturzug auf der Luftseite.

Zum Nachweis der Kühlbarkeit des pool-förmigen Primärsystems durch Naturkonvektion, wenn das Betriebssystem ausfällt, werden zahlreiche Experimente durchgeführt. Für die Untersuchungen unter stationären und transienten Randbedingungen werden Versuchseinrichtungen verwendet, die sich im Maßstab und Detaillierungsgrad unterscheiden. Ziele dieser Experimente sind der Nachweis einer inhärent sicheren Nachwärmeabfuhr durch passive Maßnahmen, die Untersuchung der physikalischen Vorgänge im Primärsystem und in den Kühlkreisläufen sowie die Erstellung einer Datenbank zur Entwicklung, Verbesserung und Validierung von Rechenprogrammen.

Im Anschluß an Experimente in der RAMONA Testeinrichtung, einem Modell vom Maßstab 1:20, wurden Untersuchungen in der 1:5 skalierten NEPTUN-Anlage durchgeführt. In beiden Fällen handelt es sich um drei-dimensionale Anlagen, wobei das Kühlmittel Natrium durch Wasser ersetzt wird. Zur Simulation des Primärsystems wurde RAMONA zwar mit allen aktiven Komponenten, aber einer einfachen Nachbildung des Kerns ausgestattet. Die sehr detaillierte Simulation der Kerngeometrie, die eine Zwischenkastenströmung erlaubt, bietet die Möglichkeit, in der NEPTUN Anlage die thermohydraulische Wechselwirkung von warmem Wasser, das im Core mit einer maximalen Nennleistung bis zu 1.600 kW aufgeheizt wird, mit kaltem Fluid, das aus den Tauchkühlern austritt, zu studieren. Die Instrumentierung besteht, abgesehen von der Erfassung der Kernleistung und des Massendurchsatzes durch den Kern, hauptsächlich aus Thermoelementen, von denen ca. 1.200 Stück in den Heizstabbündeln und Zwischenkastenräumen des Kerns, in den Komponenten sowie den verschiedenen Plena des Primärsystems

zur Messung der Kühlmitteltemperaturen installiert sind. Zusätzlich sind zwei bewegliche Meßeinrichtungen eingebaut, mit deren Hilfe die Temperaturen an fast jedem Ort des Oberplenums gemessenen werden können.

Die Hauptparameter der stationären NEPTUN Untersuchungen, über die hier berichtet wird, sind die Geometrie des Instrumentierungsstopfens, die Kernleistung, die Anzahl der in Betrieb genommenen NWA-Wärmetauscher, die vollständige Blockade der Strömungspfade auf der Primärseite der Zwischenwärmetauscher sowie die Höhe des Fluidspiegels im Primärsystem.

Die Ergebnisse der NEPTUN Experimente zeigen, daß die Nachwärme sicher durch Naturumlauf abgeführt werden kann, wozu das in den Zwischenkastenräumen zirkulierende Fluid erheblich beiträgt. Die im Oberplenum angeordneten Tauchkühler verursachen im Gebiet zwischen ihren Austrittsfenstern und der Oberkante des Kerns eine horizontale thermische Stratifizierung mit einem ausgeprägten Temperaturgradienten. Die vertikale Ausdehnung der Schichtung sowie die Größe des Temperaturgradienten werden beinflußt durch die Gestaltung des Instrumentierungsstopfens mit durchströmbarer bzw. nicht durchströmbarer Ummantelung. Eine Erhöhung der Kernleistung oder eine Reduzierung der Anzahl der verfügbaren Tauchkühler führt zwar zu einer Anhebung des Temperaturniveaus im Primärsystem, nicht aber zu einer Änderung der globalen Temperaturfelder. Versuche mit versperrten Strömungspfaden auf der Primärseite der Zwischenwärmetauscher bzw. abgesenktem Fluidspiegel im Primärsystem zeigen, daß die Kühlbarkeit des Kerns auch dann noch sichergestellt ist, wenn der Flüssigkeitsstand im Tank soweit absinkt, daß zwar kein Kühlmittel in die Eintrittsöffnungen der Zwischenwärmetauscher und der Tauchkühler gelangen kann, der Kern aber mit Fluid bedeckt bleibt. Kaltes Wasser, das vom Oberplenum in den Kern eintritt, bewirkt dessen Kühlung.

Das thermohydraulische Rechenprogramm FLUTAN wird zur drei-dimensionalen Simulation der Mehrzahl der hier beschriebenen NEPTUN Versuche angewendet. Der Vergleich von numerisch bestimmten Daten mit Meßergebnissen führt zu qualitativ und quantitativ zufriedenstellenden Übereinstimmungen. Diese Feststellung gilt sowohl für die Isothermenfelder als auch für die Temperaturprofile im Oberplenum sowie für weite Bereiche der sehr komplexen Kerngeometrie.

CONTENTS Page

1. INTRODUCTION

The reliable removal of decay heat after the shutdown of a nuclear reactor is an important safety criterion. For this reason, passive measures are the guiding principle for the design of the European Fast Reactor (EFR) elaborated in a French/British/German cooperation [1], [2].

The EFR is a liquid-metal cooled plant with a total thermal power of about 3,600 MW_{th}. The compact primary system is based on a pool-type configuration as illustrated in Fig. 1. Sodium is circulated through the core by three primary pumps (PPs). The heat is transferred to the secondary sodium by six intermediate heat exchangers (IHXs). The decay heat removal (DHR) concept comprises two diverse systems:

1. Under nominal operating conditions including a scheduled reactor shutdown, the heat is removed by six parallel and independent main heat transfer systems. Figure 2 shows that each cooling circuit consists of one IHX (primary loop) located in the reactor vessel and one steam generator unit (SGU, secondary loop). The steam of the six SGUs is transferred to one water/steam plant with turbine, generator, condenser, and pumps. In this heat transfer system, the coolant is transported by the PPs in a forced convection mode. After a scram, the PPs are coasted down by controlling the electric power to values given as function of time. The coastdown characteristics determine the core mass flow rate and hence the core temperatures to meet the safety requirements. Normally the decay heat is removed by the aforementioned route except the heat is rejected and not used for power generation.

2. In unlikely cases of unavailability of the main heat transfer route via secondary system and water/steam plant or a complete loss-of-station service power (LOSSP), the decay heat will be removed by the safety graded system. This DHR system, shown in Fig. 3, is based on six direct reactor cooling (DRC) systems operating independently from each other. Each of them consists of a sodium/sodium decay heat exchanger (DHX) immersed in the upper plenum (UP) of the primary vessel and connected via an intermediate sodium loop to a heat sink formed by a sodium/air heat exchanger (AHX) arranged at the bottom end of a stack with air inlet and outlet dampers. Each of the six DRC loops is rated to a thermal power of 15 MW_{th} in nominal conditions (primary sodium of 530°C, ambient air of +35°C). There are two types of DRC systems [3], three passive DRC1 loops and three active DRC2 loops. The degree of diversity introduced into the DRC systems seems appropriate to exclude common mode failures from basis considerations:

- Significant differences exist in the design of the heat exchanging components between DRC1 and DRC2. This is also true for the components of the air side: the dampers, the damper drives, and their power supplies.

- The combinations of three passive (DRC1) with three active (DRC2) loops also leads to an operational diversity between the two systems.

Each DRC2 loop is equipped with an EM pump and with two fans in parallel on the air side. Therefore, that system is normally operated in forced flow. The active loop also has a passive DHR potential when the pump and the fans are off. It amounts to about 2/3 of that of the active flow mode. This report covers only the passive DRC1 loops, in the following simply called DRC loops. Using these DRC systems, the decay heat is removed by natural convection on both sodium sides and natural draft on the air side. [4], [5], [6]. To enforce the startup of the DRC circuits, the air dampers of the stacks must be opened initiated by an automatic signal of the reactor protection system or in case of a LOSSP mechanically by the operator staff. Except for this procedure, the DRC systems are entirely passive. During power operation of the plant, however, a certain mass flow in the passive DRC loops is maintained by an assured minimum level of heat loss from each loop. Sodium flow stagnation or reversal which could occur during transients on the primary side, e.g., during a reactor trip, is avoided by this continuous standby circulation. This issue is not subject of this document.

The objectives of the investigations into decay heat removal by natural convection are:

1. to demonstrate the capability of the passive DRC concept by means of natural convection without exceeding the maximum permissible load values specified for the respective structures,

2. to study the influence of different design geometries and operating parameters on the thermal hydraulic behavior in the primary vessel, the individual components, and the total DHR system,

3. to generate a broad data basis to analyse and identify physical processes which must/should be modeled in computer codes so as to ensure their quality to address a specific scenario and their relevance to apply experimental data obtained from scaled-down test facilities to full scale nuclear power plant conditions.

To address questions of an inherent safe operation of the DRC system, many experiments were carried out in test rigs of different scale and degree of detail using sodium or water as fluid [7]. The philosophy of the reactor typical tests was to start with a small geometry and a simple apparatus and to successively prog-

ress in both scale and complexity. Water instead of sodium was frequently preferred to make use of available measuring techniques and to allow the visualization of fluid motion and temperature fields.

The group of water test facilities includes the 1:20 scaled three-dimensional (3D) RAMONA test facilities [8]. To a large extent, the setups were made of plexiglass. The core with a maximum power up to 75 kW consisted of one heater rod and eight individually heatable rings forming eight concentric annular channels. The models were very flexible in design, measuring technique, and operation. About 250 thermocouples (TCs) served to record the fluid temperatures. Fluid velocities and mass flow rates were measured using laser-Doppler anemometry and magneto-inductive flowmeters, respectively. Flow paths were visualized by tracers. Numerous essentially laminar experiments were conducted under nominal and non-nominal conditions. The main parameters of steady state tests were in particular: the core power, the radial power profile of the core, the geometry of the above core structure (ACS), the design and number of the operated DHXs, the complete flow path blockage of the IHXs, the fluid level in the primary vessel, and the number of the DRC loops. The transient investigations concerned the transition range from forced to natural convection, i.e., the postscram influence of the aforementioned parameters on the thermal hydraulic of the primary system. In addition, the coastdown characteristics of the pumps at the primary and secondary sides, the startup time of the DHXs, and the number of DHXs put in operation were of interest.

In this report, the results of steady state NEPTUN investigations into decay heat removal by natural convection are summarized. Following to the earlier transient RAMONA tests, water experiments were conducted in the 1:5 scaled 3D NEPTUN apparatus. The aim was to examine the effects of different design and operating parameters such as the design of the ACS shell, the core power, the number of DHXs put in operation, the complete flow path blockage of the IHXs on their primary sides, and the fluid level in the primary vessel on the thermal hydraulics of the primary system, the components, and the total DHR system. For analyzing the combined fluid dynamics and heat transport, the FLUTAN computer code has been improved, validated, and applied for the 3D numerical simulation of the majority of NEPTUN tests documented here. The results of the computations are compared against the measurements.

The result of transient NEPTUN experiments on passive decay heat removal performed under nominal and non-nominal operating conditions are summarized in a separate report [9].

2. SCALING CONSIDERATIONS

The operation of the DRC systems causes two main flow paths in the primary vessel which are sketched in Fig. 4. The vertically upward flowing fluid is heated up in the core, enters the gap between the core and the ACS, and reaches the UP where the flow is bifurcated. One part circulates via the IHXs without heat removal to the core inlet side; the other one passes the DHXs, is cooled down, and flows into the lower part of the UP. These two natural circulation flow paths interact in the UP, mainly in the region between the core and the ACS. On the way between the outlet sides of the DHXs and of the core a stable stratification is developed. The homogenization of the coolant pool temperature by flow mixing, which is of 3D character, represents a crucial aspect for the reduction of thermal loads to the system components. Thus, the correct simulation of both the natural circulation flow paths and the mixing processes is an important issue for the down-scaling of prototype decay heat removal systems during the design phase.

Basing on these physical phenomena, some scaling relations are derived and reasons for their validity are given [10], [11], [12]. It is assumed that the pressure losses Δp along the flow paths can be described by:

$$\Delta p_{loss} = \frac{1}{2} \cdot \zeta \cdot \rho \cdot u^2 \tag{1}$$

where ζ is a coefficient accounting for all frictional and orifice losses, ρ the coolant density, and u the characteristic flow velocity. The friction coefficient is a function of the geometry and the velocity u itself. The pressure gain due to buoyancy effects is assessed by:

$$\Delta p_{gain} = \rho \cdot \beta \cdot g \cdot \Delta T \cdot L \tag{2}$$

where β is the coefficient of linear thermal expansion of the coolant and g the acceleration of gravity. ΔT denotes the temperature change within or along the heat source or sink relative to the UP bulk temperature. L is the relevant distance along which the buoyant up- or downdraft acts. The power Q of the heat source has to be removed by the heat sink according to the expression:

$$Q = \dot{m} \cdot c_p \cdot \Delta T \tag{3}$$

Substituting the mass flow rate $\dot{m}$ by $(u \cdot \rho \cdot A)$ gives:

$$Q = u \cdot \rho \cdot c_p \cdot A \cdot \Delta T \tag{4}$$

Here are $(\rho \cdot c_p)$ the heat capacity of the coolant and A the effective flow cross-section. For pure natural convection, the balance of the friction and buoyancy forces must satisfy the equation:

$$\Delta p_{loss} = \Delta p_{gain} \tag{5}$$

$$\frac{1}{2} \cdot \zeta \cdot \rho \cdot u^2 = \rho \cdot \beta \cdot g \cdot \Delta T \cdot L \tag{6}$$

Using the equations (4) and (6), the following characteristic correlations for the velocity and the temperature difference for the heat source (core) and the heat sink (DHX) can be deduced in an abbreviated way:

$$u = \left[\frac{1}{\rho \cdot c_p} \cdot \frac{Q}{A} \right]^{1/3} \cdot \left[\frac{2 \cdot \beta \cdot g \cdot L}{\zeta} \right]^{1/3} \tag{7}$$

$$\Delta T = \left[\frac{1}{\rho \cdot c_p} \cdot \frac{Q}{A} \right]^{2/3} \cdot \left[\frac{\zeta}{2 \cdot \beta \cdot g \cdot L} \right]^{1/3} \tag{8}$$

The coolant pool mixing occurs predominantly by penetration of the warm fluid coming from the core into the colder fluid stored in the UP. The warm fluid is guided by the lower contour of the ACS (see Fig. 5) and appears as a horizontally spreading quasi-free jet. The penetration depends strongly on the vertical temperature stratification in the UP (ΔT_{UP}) and on the horizontal flow velocity (u_o). A characteristic dimensionless group for the flow behavior is the Richardson (Ri) number. In this case, the Ri number is used to link the characteristic control parameters of the heat source and the heat sink:

$$Ri = \frac{g \cdot \beta \cdot \Delta T_{UP} \cdot L_{UP}}{u_o^2} \tag{9}$$

In order to preserve similarity of the overall steady state mixing process, it is obvious that the ratio $Ri^* = Ri_M / Ri_R$ must be one. M denotes the model and R the reactor. Inserting the above scales for the velocity (7) and the temperature difference (8), an expression is obtained which is only a function of the characteristic lengths, cross-sections, and pressure loss coefficients. For this relationship, i.e., to preserve similarity with respect to geometry and pressure loss coefficients, the Euler (Eu) number similarity is sufficient. The required pressure loss coefficients can be achieved by an adaption of flow resistances of the individual components.

So far, only the thermal aspects have been discussed. A crucial ingredient of a buoyancy induced mixing process, however, is the local fluiddynamic state which may be laminar or turbulent and, moreover, may vary across the pool. The magnitude of the Reynolds (Re) and the Péclet (Pe) number is commonly used as a criterion for the transition from laminar to turbulent flow. These dimensionless groups can be defined as:

$$Re = \frac{u \cdot L}{\nu} \qquad \text{and} \qquad Pe = \frac{u \cdot L}{a} \qquad (10), (11)$$

where ν and a denote the molecular kinematic and the thermal diffusivity, respectively. In geometrically similar small scale test facilities, the overall power and thus the velocity have to be reduced. Therefore, $Re^* = Re_M / Re_R$ may differ significantly from one and the flow conditions may change from turbulent in the prototype to laminar in the model.

For the design and the operation of scaled RAMONA and NEPTUN test facilities, the dimensionless groups have been defined as follows:

$$\text{Richardson number: } Ri = \frac{\text{buoyancy force}}{\text{inertia force}} = \frac{g \cdot \beta \cdot \Delta T_{UP} \cdot L_{UP}}{u_o^2} \qquad (12)$$

$$\text{Reynolds number: } Re = \frac{\text{inertia force}}{\text{friction force}} = \frac{u_o \cdot L_o}{\nu} \qquad (13)$$

$$\text{Péclet number: } Pe = \frac{\text{heat transfer by convection}}{\text{heat transfer by conduction}} = \frac{u_o \cdot L_o}{a} \qquad (14)$$

$$\text{Euler number: } Eu^+ = \frac{\left[\frac{\text{pressure force}}{\text{inertia force}}\right]_{DHX}}{\left[\frac{\text{pressure force}}{\text{inertia force}}\right]_{core}} = \frac{\Delta p_{DHX}}{\Delta p_c} \cdot \frac{u_c^2}{u_{DHX}^2} \qquad (15)$$

For the UP, the quantities and dimensions are summarized in Fig. 5. In equation (15), Eu^+ denotes the ratio of the pressure drops between the DHX and the core for the model and the reactor, respectively, and thus determines the main flow paths in the primary system. In Fig. 6, the ratios of dimensionless groups Ri*, Re*, Pe*, and Eu* are plotted versus the scale of the facilities:

$$Ri^* = \frac{Ri_M}{Ri_R}, \quad Re^* = \frac{Re_M}{Re_R}, \quad Pe^* = \frac{Pe_M}{Pe_R}, \quad Eu^* = \frac{Eu_M^+}{Eu_R^+} \qquad (16)$$

Using water as model fluid, the geometrically similar 1:20 scaled 3D RAMONA test facility gives identical Ri, Eu, and Pe numbers. For the Re number, however, there exists a deviation of up to 10^{-3}. This means that the RAMONA experiments were performed under laminar conditions. Therefore, the 1:5 scaled NEPTUN apparatus was built which diminishes the Re deviation by about one order of magnitude depending on the supplied heating power and consequently on the corresponding physical properties of the fluid. Thus, an extrapolation of NEPTUN results to the prototype conditions seems to be possible [13].

3. NEPTUN TEST FACILITY

The test facilities RAMONA I and II as well as NEPTUN were actually initiated during the former German SNR-2 project [14]. Cross-sections of the SNR-2 primary system are represented in Fig. 7. The design of that sodium-cooled reactor with a thermal power of 3.420 MW_{th} provided the installation of four PPs and eight IHXs in the pool-type primary vessel. For the heat transfer to the secondary system four independent circuits were planned each featuring two IHXs, one secondary pump located at a low elevation, one steam generator unit consisting of two apparates, and one sodium storage tank. Apart from the normal DHR system via secondary and steam/water circuits, a passive DRC concept was envisaged which comprised four independent loops. Each loop was designed to remove a decay heat rate of up to 30 MW_{th} from the primary vessel by a sodium/sodium DHX and to release it to the environment via an AHX located in a stack. Except for the air inlet and outlet dampers, the decay heat is removed by totally passive measures, i.e., by natural convection of the sodium on primary and secondary sides and by natural draft of the air in the stacks.

The design and structure of the NEPTUN test facility is very similar to the SNR-2 geometry. Despite this situation, the experiments cover all important physical effects with regard to the cooling modes in the primary and DRC systems of the EFR and provide useful test data for the development, improvement, and assessment of computer programs.

NEPTUN is a 1:5 scaled 3D water test facility [15]. A bird's eye view of the apparatus is shown in Fig. 8. Vertical and horizontal cross-sections of NEPTUN together with its main dimensions in millimeter are shown in Figs. 9 and 10, respectively. The vessel has an inner diameter of 3,950 mm and a height of 3,620 mm. The volume is about 30 m^3 filled with fully demineralized and degassed water. The open-topped vessel consists of three axially superimposed shells of cylindrical and semispherical shape, respectively, which are bolted together. The vessel contains the entire primary circuit, i.e., simulators of the reactor core, ACS, PPs, IHXs, and DHXs. These components will be described later on. In the lower part of the vessel, a core support structure is placed which consists mainly of two parallel perforated plates. Between the plates, shroud tubes are bolted which provide the location of the coolant supply for each rod subassembly (SA) of the core. Feedlines of the PPs penetrate the cylindrical shell at the periphery of the diagrid which represents the high pressure plenum (HPP). At the bottom end of the HPP, the reference or zero level is located in order to provide a common basis for the comparison of NEPTUN and RAMONA data as well as computations against measurements. Above the outer periphery of the HPP, a lateral neutron shield support plate serves for the arrangement of the shielding elements (see Chapter 3.1). There exists no flow path between the two grid structures. A construction unit of bi-toroidal shape forms the intermediate plenum (IP) which separates the hot

upper from the cold lower plenum (LP). The upper contour of the IP represents the so-called *"redan"*. The IP is fixed at its top end to the vessel and at its bottom end to periphery of the HPP. Vertical shrouds of two different diameters penetrate the IP and serve for the installation of the PPs and IHXs, respectively, as shown in Fig. 11. The lower part of the *"redan"* and the cylindrical structure of the core form the reactor typical cavity which represents the lower part of the UP. The bottom part of the cavity is built by an additional annular replacement body which is fitted between the core and the *"redan"*.

A lot of care was necessary to manufacture the components of the test facility and to assemble the NEPTUN apparatus in order to avoid any undesired geometry induced asymmetrical effect during the course of the studies. In particular, accurate dimensions were required with respect to the horizontal alignment over the circumference of the upper HPP plate and the core at their top ends as well as of the ACS at its bottom end. Furthermore, attention was focused to the installation of the four PPs and the eight IHXs, and especially of the four DHXs with regard to an axially uniform level of their inlet and outlet windows within the vessel.

3.1 Core

The core with an outer diameter of 1,620 mm is designed for a maximum electrical power of 1,600 kW and consists of 337 heatable fuel and storage SAs as well as 312 unpowered shielding and reflector elements. A 60° sector of the core is shown in Fig. 12. There are 16 different SA rows which include in radial direction: 253 fuel elements (rows 1 to 9), 60 reflector elements (row 10), 84 storage elements (row 11), 78 reflector elements (row 12), and 174 shielding elements (rows 13 to 16). The fuel rod SAs of the rows 1 to 9 and the storage elements of the row 11 are individually heatable in seven annular groups in order to generate a radial power profile.

Details of the bundle design are given in Fig. 13. Each of the 337 (253 + 84) heatable SAs consists of 19 rods having an outer diameter of 8.5 mm which are spaced on a triangular rod pitch of 9.52 mm. Two grid spacers with a height of 12 mm are installed at intervals of 10 mm (upstream) and 13 mm (downstream), respectively, of the heated bundle portion. The overall SA length above the top end of the HPP amounts to 860 mm and comprises the following axial sections:

- The lower unheated portion of 280 mm simulates the fertile section.
- The electrically heated portion of 220 mm represents the fuel section.
- The upper unheated portion of 360 mm simulates the fertile section, the reflector section, and the SA head.

In the bottom end of each heatable SA located within the heating groups 1 to 7, a mounting support system of the rod array, the power connections, and an orifice plate are arranged. By means of the selected orifice geometry, an adjustment of the coolant mass flow to the generated heat is possible in order to provide an identical temperature rise along all SAs during nominal operation conditions (forced convection mode). The unheated reflector and shielding elements are designed to simulate their hydraulic behavior only.

To reduce the manufacturing costs of the SA wrappers, the hexagonal geometry of the EFR was replaced by a circular design. The circular tubes having an outer diameter of 54 mm and a wall thickness of 2 mm are spaced on a triangular pitch of 58 mm. At the bottom ends, the wrapper tubes are bolted to the diagrid. About 220 mm below the upper edge of the core, a perforated plate is inserted to simulate the pad plane which supports the SAs at the prescribed wrapper-to-wrapper pitch. In order to establish the same hydraulic behavior in vertical direction, the interstitial mass flow is forced to penetrate a free flow area which is equal to that available between the wrapper tubes of hexagonal design. For that purpose, the plate contains an array of holes with a diameter of 5.2 mm. One hole is provided in the center of each interwrapper area formed by three neighboring circular shroud tubes. This measure causes a local reduction of the free flow area to 6.8%.

3.2 Above Core Structure

The cylindrical ACS with an outer diameter of 934 mm hangs from a platform and is centrically positioned to the core. The ACS comprises horizontal plates and vertical guide tubes which simulate the hydraulic behavior of the control rod drivelines and core monitoring systems. That arrangement is illustrated by Fig. 14. A horizontal plate having a permeability of 12.5% serves as lower guiding device of the tubes. The lower ends of the tubes protrude on a length of 197 mm from the bottom surface of that plate. This results in axial distance of 28 mm between the bottom end of the tubes and the top end of the core.

A perforated shell with a permeability of 15.2% covers the peripheral surface of the ACS jutting out the bottom edge of the plate by 25 mm. Therefore, the clearance between the bottom end of the ACS shell and the top end of the core amounts to 200 mm. On the left-hand side of Fig. 15, a schematic cross-section of the permeable ACS design is shown. At its periphery of the shell, several rows of holes are arranged which allow the fluid to pass through the ACS. In addition, there are two impermeable ACS versions under investigation. A solid sheet serving as a cover of the originally perforated ACS periphery excludes a flow through. The lower ends of the guide tubes, however, remain uncovered (see Fig. 15, middle). The second geometry of an impermeable ACS is similar to the just mentioned one. In that case, the guiding tube ends which protrude from the lower end

of the ACS are bordered by a skirt having a height of 172 mm and a diameter corresponding to the upper sheet covering. This leads to an axial distance of only 28 mm between the lower edge of the skirt and the top end of the core (see Fig. 15, right side).

3.3 Primary Pump

Each of the four PPs is hydraulically simulated by a cylindrical pump tube placed in a circular shroud. The suction side of the pump dummy communicates via the inlet slots with the LP of the test facility whilst the outlet side is connected via pipework to the HPP underneath the core. As shown in Fig. 10, the PPs are situated on a common pitch circle diameter of 3,240 mm at the periphery of the vessel with 90° intervals. This approach of the flow paths and pressure losses is only suitable to conduct natural convection experiments.

3.4 Intermediate Heat Exchanger

In accordance with the requirements of the natural circulation tests, the main feature of the eight IHXs is the simulation of the coolant flow at the primary side. In the UP, water enters at the inlet windows, flows downward through the dummy without tube bundle, and exits at the outlet windows in the LP. The arrangement of the IHX simulators is shown in Fig. 10. They are located at both sides of each PP on a common pitch circle diameter of 3,280 mm.

3.5 Decay Heat Exchanger

For the four DRC-loops, multi-row straight-tube heat exchangers operating on the counterflow principle are chosen. Figure 10 indicates the arrangement of two pairs of DHXs at adjacent sides of the NEPTUN vessel (pitch circle diameter of 3,520 mm, angular positions of 84°, 96°, 264°, and 276°). The immersion depth amounts to 1,015 mm from the water surface. This means that the top edge of the inlet windows at the primary side exceeds the regular water level by approximately 130 mm. Figure 16 shows a cross-section of the DHX used for the NEPTUN apparatus. Each unit is rated for a nominal power of 62.5 kW. The tube bundle having a height of 1,220 mm between the upper and lower plate consists of 184 straight tubes (7.0 mm o.d., 0.5 mm wall thickness) which are arranged on a triangular tube pitch of 11.65 mm between the DHX housing and a central supply tube (60.3 mm o.d., 2.6 mm wall thickness). The total height of the DHX windows amounts to 450 mm at the inlet side and to 100 mm at the outlet side. At the primary side, warm fluid enters the DHX via the inlet windows, flows downward along the tube bundle under heat removal, and exits immediately above the *"redan"*. On the secondary side, cold water enters the central supply tube, flows downwards to the bottom distributor from where it is fed to the 184 tubes. On an active length of about 940 mm, the upward flowing coolant is heated up before it reaches the

upper collector which surrounds the central supply tube. From here, the water exits to a secondary cooling circuit where specific measuring data are obtained for the performance of an analytical balance of the heat removed from the primary vessel. The main function of this circuit is to fulfill the necessary requirements to achieve uniform boundary conditions for all DHXs being in operation. This concerns in particular the mass flow rate and the inlet temperature at the secondary side of the DHXs.

4. INSTRUMENTATION

The measuring and control systems of the NEPTUN test facility can be subdivided into two parts, the real measuring system as well as the system for the adjustment, surveillance, and safe operation of the plant (see Chapter 5). Beside the primary system all secondary and tertiary circuits (see Fig. 27) are equipped with measuring devices to record temperatures and mass flow rates. In addition, pressure and fluid level detectors and power supply monitors are installed.

The most part of the instrumentation consists of NiCr-Ni thermocouples having a tip diameter of 0.5 mm. About 1,200 TCs are available which can be subdivided into two groups:

1. stationary measuring devices installed at various locations of interest within the core, the ACS, the PPs, the IHXs, the DHXs, the HPP, the IP, and the LP of the vessel,

2. measuring devices being installed on movable supporting systems which allow temperature measurements in the UP at nearly each position of the cylindrical coordinate system.

Please note: All axial dimensions reported here are related to the reference or zero level which is located at the bottom end of the HPP (see Fig. 9).

4.1 Stationary Measuring Devices

The instrumentation of the core comprises the measuring positions in the HPP, inside the SAs, and in the interwrapper spaces. The layouts of Figs. 17 to 19 illustrate the measuring positions. The temperatures of the coolant entering the SAs is recorded in the HPP along two diagonals (see lower part of Fig. 17). Each of these radial positions is equipped with one TC at the axial level of 158 mm. There are eight SAs (see upper part of Fig. 17, closed markers) which are instrumented at four axial levels (see Fig. 18). At the axial levels of 234 and 851 mm, six TCs are arranged to register the coolant temperatures upstream and downstream of the 19 heater rods. Three TCs are located at the axial level of 926 mm, i.e., in the region of an unheated seven rod bundle which simulates the neutron absorber pins. For the measurement of the coolant temperatures at the outlet side of the SAs, the

heads of the same SAs are provided with four TCs fixed at the axial level of 1,037 mm. In addition, there are 39 core element positions with one TC placed in the SA head (see upper part of Fig. 17, open markers). The instrumentation of the inter-wrapper spaces consists of two groups. The first group comprises ten measuring positions along a diagonal (see upper part of Fig. 19). Each radial position is equipped with five TCs located at different axial levels (see axial layout of Fig. 19a). A second group of measuring devices is at 60° intervals along the periphery of the core (see Fig. 19b). The TCs are located at four axial levels (see Fig. 19c).

The instrumentation of the ACS can be subdivided in three groups as shown in Fig. 20. The group (A) consists of 44 TCs which are situated all together at the axial level of 1,248 mm. The group (B) concerns five radial positions which are uniformly equipped with 14 TCs in axial direction. Between the axial levels of 1,129 and 1,285 mm, the TCs are installed at 12 mm intervals. The group (C) comprises two radial positions which have the same instrumentation in axial direction. The measuring traverses are located at the centerline and at a radial distance of 201 mm from it.

The PPs are instrumented at their lower ends of the inlet slots at an axial level of 1,421 mm. At the outside of each simulator, three TCs are located on pitch circle diameters of 248 mm at angular intervals of 120°. Details are shown in Fig. 21.

The inlet and outlet windows of two opposed IHXs (see Fig. 3: No. 2 at 69° and No. 6 at 249°) are equipped with TCs as shown in Fig. 22. The measuring devices are located inside the IHX housing on a common pitch circle diameter of 394 mm. Each axial position is provided with eight TCs at angular intervals of 45°. There are three axial TC positions at the inlet and outlet windows. The remaining six IHXs are less extensively instrumented with three TCs distributed over the periphery with an angular interval of 120°. The TCs are fixed at one axial level ($z = 1{,}832$ mm) at the inlet side and three levels at the outlet side.

The inlet and outlet windows of three DHXs (see Fig. 3: No. 1 at 84°, No. 3 at 264°, and No. 4 at 276°) are equipped with TCs as shown in Fig. 23. The temperatures are measured within the DHX housings on a common pitch circle diameter of 178 mm. Each of the six different axial levels includes eight TCs in circumferential direction. For control purposes, 25 TCs are installed at DHX No. 2 at 96°.

The IP which surrounds an area of stagnant water is instrumented at angular positions of 90° and 180°. The corresponding r- and z-coordinates are summarized in Fig. 24. That instrumentation serves for an estimation of the heat transmitted from the LP to the bottom end of the UP during natural convection.

The instrumentation of the LP is placed along vertical traverses as well as along the spherical profile of the vessel in the close neighborhood of the IHX outlet windows. The traverses are located at a distance of 1,290 mm from the vessel

centerline and at angular positions of 90°, 180°, and 270°. The periphery of the vessel is equipped with measuring devices at angular positions of 90°, 180°, 270° as well as 249°. Details are given in Fig. 25.

4.2 Movable Measuring Devices

In order to record the temperature profiles within the UP, two special appliances were developed which enable a controlled selection of the measuring points within the cylindrical coordinate system.

One support system is equipped with a single measuring lance (MEL). In general, that device is equipped with 15 TCs having an axial distance of 120 mm from each other. Figure 26a shows the actual TC positions along the MEL device. During the course of the investigations, however, it was necessary to add 10 TCs between the axial levels of 1,035 mm and 1,635 mm leading to an equidistant interval of 40 mm. The 3D freedom of movement is $\Delta r = 1.508$ mm (467 mm $< r <$ 1,975 mm) in radial direction, $\Delta\phi \leq 180°$ in azimuthal direction, and $\Delta z = 993$ mm in vertical direction.

A second support is equipped with a measuring rake (MER) consisting of a parallel arrangement of three vertical lances. These lances are different with respect to their length and to the axial intervals between the individual TCs. The lances are fixed with radial distances of 602 mm, 867 mm, and 1,227 mm from the NEPTUN centerline. The movement of MER allows temperature measurements within a sector of $\Delta\phi \leq 180°$ for each azimuthal position of the UP. Figure 26b shows a summarization of the radial and axial TC positions of the MER system.

4.3 Uncertainties of the Measurements

Before the start of the tests, all measuring devices were calibrated. Analyses of experimental uncertainties of the measurements gave the following results:

- The water temperatures are governed by the power supplied to the core. Within the test facility, the temperatures do not exceed $20°C < T < 70°C$ during the performance of steady state tests. The associated measuring uncertainty is $\Delta T \leq \pm 0.2$ K. This determination is based on a calibration of the temperature measurement system including TC, ice bath reference, digital voltmeter, and emf-temperature converting formula, against a PT100 precision thermometer.

- The mass flow rates of the core are measured by turbine-type flowmeters installed in the suction lines of the PPs. They were calibrated in the range of mass flow rates between 10 and 800 g/s providing an accuracy of 5%.

- Electromagnetic induction flowmeters are used to register the mass flow rates at the secondary side of the DHXs (see Fig. 27). Within the range of 50 and 500 g/s, the error amounts to less than 3%.

5. DATA ACQUISITION AND TEST CONTROL

Data acquisition takes place within an S-Net serial data transfer system using Isolated Measurement Pods (IMPs) and a VAX computer of the type MicroVAX 3400. A schematic of the data acquisition and test control system is shown in Fig. 28. It acquires and stores all temperature, mass flow rate, and power measurements. In addition, 20 digital input/output signals are recorded and stored for controlling external units and for counting of events.

The data are handled by a multi-user operating system in conjunction with graphics and specifically written software. The advantages of the utilized data acquisition system are a decentralized configuration of the acquisition units (IMPs) and the transfer by a simple shielded twisted wire ring circuit of a maximum length of 1,000 m (S-Net). As a result, the system can be operated at its maximum data transfer rate of 163 kbits/s at any time. Q-bus interface cards serve as link between the IMP and the computer. Each Q-bus can transfer a maximum of 50 IMPs = 1,000 data channels to the central VAX computer. All measured values are taken within a time interval of < 800 ms, even if the effective transfer rate would be reduced by a software overhead.

Due to the required accuracy of ≤ 0.2 K for the temperature measurements, a comparative reference temperature for the TC measurements is required. Originally, only thermistors are used for that purpose. Therefore, the terminal temperature (terminal block) is determined utilizing a 1/10-DIN PT100 measuring gauge mounted in the center of the isothermal screw connections of the TCs. The resistance of the PT100 is determined by a comparative at the 100 Ω precision resistor. By a common power source of about 1 mA and a reference resistor of 100 Ω, errors of the voltage measurements are compensated. The total error of the measuring section is < 0.177 K at an ambient temperature of 20 to 40°C. To obtain a more homogeneous temperature distribution in the connection field, a copper sheet is installed there. Conversion of the TC voltages is carried out by a user specified program.

Following the start by the central computer, the state of the experiment can be recorded, printed, or plotted (transfer rate of up to 38,400 bits/s) in real time or background mode, in tables or charts via three screens using the graphic software. For the measured values and the user software, a main memory of 20 MB and two Winchester disk drives with a gross capacity of 778 MB are available in the system. The current experimental data are stored and filed on a magnetic tape drive TK50 (50 MB). Via an Ethernet link and the LAN, the current measuring data

calculated by the user program are transferred to the central computer (IBM 9021-640) of the Research Center Karlsruhe for evaluation and documentation of the experiments. Together with the experimental RAMONA and computed FLUTAN data, the central computer allows the analysis, the comparison, and graphical representation of all findings gained during the course of this project.

6. PARAMETERS OF THE INVESTIGATION

The main test parameters which were varied during the course of this investigation include:

- the design of the ACS shell:
  - permeable shell design without skirt → axial gap height of 200 mm between the top end of the core and the bottom end of the ACS shell,
  - impermeable shell design without skirt → axial gap height of 200 mm between the top end of the core and the bottom end of the ACS shell,
  - impermeable shell design with skirt → axial gap height of 28 mm between the top end of the core and the bottom end of the ACS shell;

- the level of the core power in the range of 133 kW $< Q_M <$ 221 kW which corresponds to a decay heat power of the reactor in the range of 25 MW $< Q_R <$ 100 MW on the basis of similarity considerations; six differently heated groups of SAs consisting of a total of 253 fuel elements;

- the number of operable DHX circuits:
  - four operable DHX circuits → nominal cooling condition,
  - complete failure of two neighboring DHX circuits → non-nominal cooling conditions;

- the flow paths via the primary side of the IHXs:

  a) six differently heated groups of SAs including a total of 253 heated fuel elements, 84 unheated storage elements,
  blocked flow paths via the 138 reflector and 84 storage elements:
  - unblocked IHX flow paths → fluid flow from UP via IHXs, pump feedlines, and HPP to the inlet side of the core elements,
  - blocked IHX flow paths → core cooling from the UP only;

  b) seven differently heated groups of SAs including a total of 253 fuel and 84 storage elements,
  unblocked flow paths via the 138 reflector and 84 storage elements:
  - unblocked IHX flow paths → fluid flow from UP via IHXs, pump feedlines, and HPP to the inlet side of the core elements,
  - blocked IHX flow paths → core cooling from the UP only;

Table 1. Parameters under consideration.

Test No. / Parameter	Design of ACS shell	Total core power, kW	Number of heated SA groups	Number of operated DHXs	Fluid level in the upper plenum	Flow path via reflector and storage elements	Flow path via IHX primary loops	FLUTAN code simulation
T01	permeable without skirt	221	6	4	normal	blocked	unblocked	yes
T02	impermeable without skirt	221	6	4	normal	blocked	unblocked	yes
T03	impermeable with skirt	221	6	4	normal	blocked	unblocked	yes
T04	permeable without skirt	133	6	4	normal	blocked	unblocked	yes
T05	permeable without skirt	170	6	4	normal	blocked	unblocked	yes
T06	impermeable without skirt	133	6	4	normal	blocked	unblocked	yes
T07	impermeable without skirt	170	6	4	normal	blocked	unblocked	yes
T08	impermeable without skirt	133	6	2	normal	blocked	unblocked	no
T09	permeable without skirt	133	6	4	lowered	blocked	unblocked	yes
T10	permeable without skirt	133	6	4	normal	blocked	blocked	yes
T11 [1)]	impermeable without skirt	133	6	4	normal	blocked	blocked	yes [2)]
T12	permeable without skirt	150	7	4	normal	unblocked	unblocked	no
T13 [1)]	permeable without skirt	150	7	4	normal	unblocked	blocked	no
T14 [1)]	impermeable without skirt	150	7	4	normal	unblocked	unblocked	no
T15 [1)]	impermeable without skirt	150	7	4	normal	unblocked	blocked	no

[1)] Data of transient tests after reaching steady state conditions of natural convection.
[2)] Simulation performed under steady state conditions of natural convection.

- the fluid level in the primary system related to the reference level at the bottom end of the HPP:
  - normal fluid level of 2,359 mm,
  - lowered fluid level of 1,809 mm simulating a leakage of the primary tank.

Table 1 gives an overview on the individual parameters of the test runs T01 to T15. At the secondary side of each operated DHX, the mass flow rate of 2.1 kg/s per unit and the inlet temperature of 15°C are kept constant.

7. OPERATIONAL PROCEDURE

The investigation of separate effects during steady state decay heat removal by natural convection requires well defined initial conditions. The most important one is a uniform temperature in the whole test facility. The fulfillment of that prerequisite for the initiation of the data run guarantees the absence of extraneous buoyancy-related motions in the apparatus. In the following, the operational procedure is briefly outlined, particularly as the attainment of temperature uniformity is a process of experience gained in prior runs performed in the NEPTUN test facility [16].

For some hours prior to the initiation of the data run, the core is heated up using the test specific power. The water temperature in the UP is sensed by 15 TCs deployed along a vertical traverse ranging from the free water surface down to the bottom end of the cavity (MEL device). A second group of TCs serves to monitor the temperature rise in the core supporting structure and in the LP where the measuring devices are arranged in the neighborhood of an IHX outlet window. Experience has shown that it is very time consuming to heat up the water inventory of 30 m^3 to a uniform temperature. This concerns especially the cavity region of the UP as well as the LP. To accelerate this procedure, an external auxiliary water circuit is used in order to stir the water during the heating up phase. This simple circuit essentially consists of pipework and a pump with a maximum feed performance of 9 m^3/h and serves to carry water from the bottom end of the LP into the UP.

Figure 29 shows the temperature history registered in the UP during baseline test T02 (see Table 1). The graph represents 15 TC signals simultaneously recorded along MEL which is positioned at a radial distance of r = 1,030 mm from the centerline and at an angle of $\phi = 270°$ The TCs are installed with one at the axial of 555 mm in the cavity and others at 120 mm intervals throughout the measuring lance (see Fig. 26a). The character of the temperature transients allows the identification of different time phases consisting of a heating up phase followed by an isothermal conditioning phase, an evolution phase of the thermal equilibrium, and finally a phase of quasi-steady state conditions. As soon as the core power is

supplied, all monitored temperatures begin to rise starting from about 26°C. Within the first four hours, the temperatures increase nearly linear to 48°C with a gradient of approximately 5.5 K/h. During this heating up phase, water is pumped from the LP to the UP whilst the DHXs are out of order. The initial phase is followed by the isothermal conditioning phase in order to attain the required temperature uniformity within the whole primary system. During this period of three and a half hours, the power is turned off, but the external water circuit is still in operation. In the present test, a uniform temperature of 45.5°C is achieved. About eight and a half hours after start of the operational procedure, the external water circulation is stopped, the core power of 221 kW is turned on, and all DHXs are put in operation. At the secondary side of each DHX, a mass flow rate of 2.1 kg/s and an inlet temperature of 15°C is provided. These boundary conditions are kept constant during the experiment. The DHXs begin to deliver cold water into the cavity of the UP. The TCs located below the top end of the core (1,155 mm $\leq$ z $\leq$ 555 mm) display relatively steep temperature drops within a short time gap followed by a gradual transition to steady state conditions. On the same level as the area between the core and the ACS, the TC (z = 1,275 mm) registers a fluctuating signal. The nature of these test values can be attributed to the mixing effect of warm flow leaving the core and of cold flow coming from the DHXs. Details will be discussed later on. The measuring devices situated above the bottom end of the impermeable ACS shell (2,235 $\leq$ z $\leq$ 1,395 mm) indicate slight temperature rises before they start dropping to steady state. The temperature transients reflect that thermal equilibrium is achieved 16.5 hours after initiation of the test. At that time, the deviation of the thermal equilibrium of the core power and of the removed heat amounts to $\Delta Q \leq 5\%$. The data collected during the subsequent steady state period provide the basis for the test evaluation. After more than 30 hours had elapsed, the test was terminated.

For the evaluation of the local time averaged values, all samples are taken into account which were monitored during the time space of 17.0 h $<$ t $<$ 18.0 h. This time space is only valid for test T02. The signals were recorded with a frequency of 1/60 Hz.

8. NUMERICAL SIMULATION OF THE EXPERIMENTS

For the numerical simulation of the NEPTUN experiments, the fully vectorized thermal hydraulic computer program FLUTAN [17] is utilized. The code is a tool to analyze the combined fluid dynamics and heat transport for 3D, laminar and turbulent, steady state and transient problems. The selection of either rectangular Cartesian or cylindrical coordinates is provided. The program includes physical models for volume porosity, surface permeability, surface heat flux, volumetric heat source, thermal interaction between the immersed structure and surrounding fluid, and turbulence. Two temperature dependent fluid property packages are presently implemented, i.e., for water and sodium. Apart of the vectorization [18],

an essential feature of FLUTAN is the self optimizing algorithm CRESOR [19] for solving the Poisson equations for energy, pressure, and turbulence using a finite difference numerical technique. CRESOR is a red/black successive overrelaxation (SOR) method combined with the method of conjugate residuals supported by coarse-mesh rebalancing. The first-order upwind differencing method (donor cell method) is available for treating the convective terms of the momentum and enthalpy equations. This differencing scheme, however, may lead to dissipation and dispersion errors [20]. This combined effect, called numerical diffusion, becomes significant in multi-dimensional and steep gradient fields of velocity and temperature, especially when the flow direction is highly inclined to the grid lines. Several options (QUICK and LECUSSO technique) of a second-order differencing scheme are currently under assessment [21], [22] with the goal to reduce the numerical diffusion. A two-equation standard turbulence model (k,ε-model for turbulent kinetic energy and for the dissipation rate of turbulent kinetic energy) with an additional term for buoyancy forces is available to describe the turbulent flow. So far, the computer program was validated for laminar and turbulent forced convection flows under steady state and transient conditions. The same is true for the laminar natural convection flow under both steady state and transient conditions.

For the simulation of the experiments, a 90° sector of NEPTUN is modeled by using a three-dimensional noding scheme with about 20,000 volume cells. Figure 30 illustrates the nodalization of the test facility with r-ϕ and r-z cross-sections. The number of the chosen mesh cells depends on the degree of detail required to resolve the fluid field, the phenomena to be modeled, and practical restrictions such as computing time and computer storage limitations. To capture the dominant physical phenomena, the following approach is chosen:

- For the multi-dimensional simulation of the core, an unequal mesh spacing is selected according to different requirements. In vertical direction, a different node length has to be provided to fit the axial regions of the heated rod bundles, the pad plane, and the horizontal plate installed close to the upper end of the core. In addition, the axial noding scheme has to coincide with selected measurement locations. In angular direction, the positions of PPs, IHXs, and DHXs govern the nodalization. In radial direction, the arrangement of the fuel, reflector, storage, and shielding elements (see Fig. 12) together with the power profile determine the modeling. The flow area between the wrapper tubes is characterized by the radial length increment of the mesh. The chosen network, however, doesn't allow the simulation of the interstitial flow in angular direction. The volume cells of the SAs are described by porosities and permeabilities and by taking into account the space dependent heat capacities of the SAs in conformity with the actual radial power profile. Heat transport between the SA regions and the interwrapper spaces is taken into consideration by so-called *"slab-type thermal structures"*. Heat transfer between the interwrapper space and the pressure plenum is modeled. Furthermore, the

modeling includes local pressure losses due to the design of the SAs inlet and outlet sections, orifice plates, grid spacers, pad elements, and other obstructions along the flow route as well as such caused by friction forces. These values are specified for the data input by making use of pretest measurements with the original components of NEPTUN [23].

- In the case of a permeable ACS, the perforated shell of the ACS is approximated by solid walls and holes to meet the required permeability of 15.2%. The same procedure is applied to simulate bottom plate of the ACS having a permeability of 12.5%. The impermeable ACS version requires a modification of the data input to fit the fluid cell boundaries to the actual design of the ACS surfaces without and with skirt, respectively.

- The data input for the PPs and IHXs concentrates essentially on informations about the free flow areas which are the same as in NEPTUN and about the pressure losses in vertical flow direction caused by the presence of internal installations and friction forces. Additional specifications are not required since rather simple shrouds serve to simulate the hydraulic behavior of these components during the natural convection tests performed under steady state conditions.

- Identical free flow and heat transfer areas are attributed to the DHXs in the computer simulations as in the test facility. The conditions at the secondary sides of the components are calculated by a subroutine simulating a heat exchanger model [24] with inlet mass flow and inlet temperature and by taking into account the heat capacities of the solid material and the fluid which correspond to the reality of the experimental units. The thermal hydraulic characteristics of the DHXs are specified for the data input by making use of pretest measurements carried out with the original components [25].

- The actual contour of the *"redan"* is approximated by a graded net.

Except the core, adiabatic and slip boundary conditions are supposed at the solid surfaces. Friction losses and drag coefficients are modeled for all components and plena. Free slip is taken into consideration for the free water surface. All computations are based on essentially laminar conditions. Locally turbulent flows are taken into account. Initially uniform pressure, velocity, and temperature values are specified for all fluid cells at the beginning of a computer run. The initial values are specified following the measurements of the individual experiments. The chosen uniform temperature in the entire flow domain refers to the temperature recorded in the top part of the UP. The computation is treated by a transient procedure and is continued until a steady state solution is reached, i.e., when the energy generated in the core corresponds to the energy transferred to the DHXs as well as the values of the variables stop varying with the time and prescribed

convergence criterion parameters ($\varepsilon \leq 1 \cdot 10^{-5}$) are met for pressure, velocity, and enthalpy.

9. TYPICAL COMPUTED VELOCITY AND TEMPERATURE FIELDS

Figure 31 shows computed velocity fields of baseline test T02. The test parameters are listed in Table 1. The reference vector represents a velocity of 5 cm/s. The plots illustrate the flow paths with examples of four vertical sectional planes. The cuttings are indicated in Fig. 30.

The cross-section O-A is a cutting across the SAs of the core and the center of a DHX. It can be readily seen that there is a clockwise flow path in the UP. The vertically upward flowing water is heated up in the core and enters the 200 mm high gap between the core and the impermeable ACS without skirt. In this region, the warm fluid is deflected at the bottom end of the ACS and additionally altered by the lateral cold stream coming from the DHXs. Water of mixing temperature ascends in the UP along the impermeable surface of the ACS and circulates at the water surface to the periphery of the vessel where the flow is bifurcated. One part of the fluid enters the inlet windows of the DHXs and flows downward under removal of heat, the other part enters the IHXs (see cross-section O-B). The cold fluid leaving the DHX at its outlet windows impinges upon the *"redan"* and is deflected toward the center of the vessel. On the way to the mixing region between the core and the ACS, a stratified flow is established. Cross-section O-B includes an interwrapper plane of the core and the center of an IHX which is installed next to the just considered DHX position. The diagram indicates that the other part of the flow circulates from the UP via IHX, PP, and PP feedlines into the HPP where the fluid enters the core again. Within the interwrapper space of the core, two vortex flows can be identified, one above and one below the horizontal pad plane indicated by a dashed line. Below the pad plane, the clockwise flow is initiated by the heated central part of the core whilst the outer peripheral core section containing reflector and storage elements is unheated in this test. Above the pad plane, cold water coming from the DHXs penetrates into the outermost portion of the interwrapper space and proceeds clockwise guided by the pad plane toward the core centerline. As soon as this interwrapper fluid reaches the upper portion of the core, it mixes with the upward flowing warm fluid leaving the SAs. The cross-sections O-C and O-D illustrate the vector fields about a PP and a feedline from the PP to the HPP, respectively.

The temperature fields of test T02 are represented by the plots given in Fig. 32. The isotherm lines have an interval of 1 K. The computations show a uniform temperature of about 41°C in the lower region of the UP, a small layer of closely spaced isotherms in the vertical area between the top end of the core and the bottom end of the DHXs, and above another region with a uniform temperature of about 46°C. The horizontal character of the isotherms reaching from the gap bet-

ween the core and the ACS up to the outlet windows of the DHXs indicates the formation of a thermal stratification within which the entire temperature rise of almost 5 K occurs. The highest fluid temperatures take place in the center of the gap formed by the core and the ACS. With increasing distance from the centerline, the temperatures drop in radial direction mainly due to an increasing mixing effect of cold water coming from the DHXs on the warm flow exiting from the core. Within the heated portion of the SAs (see cross-sections O-A, O-C, and O-D), the isotherms have an essentially horizontal shape. Above and beside the heated core section, the temperatures are more or less influenced by the effectiveness of the interstitial flow. Cross-section O-B shows the effects of the fluid circulating in the interwrapper spaces on the field of isotherms. Again, the driving forces are the heating of the fluid taking place in the core and the cold fluid penetrating into the interwrapper spaces at the upper core periphery. Above the pad plane, the entering cold flow is heated up as it proceeds in radial direction. Below the pad plane, the cold flow circulates vertically downwards in the unheated outermost portion to the bottom end of the core from where it is drawn in radial direction toward the center. At the grid plate and in the powered portion of the core, the fluid flow is heated up. Due to the vortex flows above and below the pad plane, the isotherm lines are extended in radial direction to the core periphery.

10. EXPERIMENTAL RESULTS OF BASELINE TEST T02

In the following, the measurements of baseline test T02 are outlined to provide background information for the subsequent discussion on experimental and analytical results. The main characteristics of test T02 are listed in Tab. 1. The time history of the experiment is shown in Fig. 29 and explained in Chapter 7. The TC locations are illustrated in Figs. 17 to 26 and described in Chapters 4.1 and 4.2. At the end of this report, there are consistent sets of data plots for test runs T01 to T15. The measuring positions agree in every way (r-, ϕ-, and z-direction) to those of the baseline test.

10.1 Radial Power Profile of the Core

The vertical bars of Fig. 33 illustrate the power supplied to the fuel rod simulators as a function of the core radius. There are six annular groups of heatable SAs. Across the five central heating groups, an essentially flat power profile can be identified with a linear rod power of about 2.4 W/cm. Heating group 6 simulates the radial blanket and is characterized by a considerably lower power supply which results in a linear rod power of nearly 0.9 W/cm. The storage elements of heating group 7 remain unheated. Details of the radial power distribution of test T02 are listed in Table 2.

Table 2. Radial power distribution of test T02.

Heating group	No. 1	No. 2	No. 3	No. 4	No. 5	No. 6	No. 7
Number of heatable SAs	35[1)]	35[2)]	36	42	48	54	83[3)]
Total power supply, kW	38.48	36.17	36.04	42.04	47.96	20.28	---
Power supply/SA, kW	1.099	1.033	1.001	1.001	0.999	0.376	---
Linear rod power, W/cm	2.630	2.472	2.395	2.395	2.390	0.899	---

[1)] Two of a total of 37 SAs are unpowered.
[2)] One of a total of 36 SAs is unpowered.
[3)] One of a total of 84 SAs is unpowered.

10.2 Temperatures Inside the Rod Subassemblies

Figure 34 shows radial temperature profiles measured in the HPP. The TCs are located along horizontal measuring traverses at an axial level of 158 mm which corresponds to the position of the SA inlet openings. The diagram indicates a nearly uniform water temperature of 45°C. The core outlet temperatures represented in Fig. 35 are taken from measuring devices which are fixed at an axial level of 1,037 mm in the head of the rod bundles. The plotted values indicate a maximum outlet temperature of about 60°C measured at the centerline of the core. With increasing radial distance, the temperatures start dropping gradually, but slightly. The reduction of the linear rod power in heating group 6 results in a steep temperature gradient. Outside the heated core zone, the temperatures amount to roughly 41°C. These values are lower than the data measured at the inlet side of the heated SAs since this zone is affected by water of about 40 °C delivered by the DHXs. A qualitative indication about the temperature rises of the coolant flowing inside the wrapper tubes is given by Fig. 36. The measurements address those SAs which are assigned to the heating groups No. 4 to 6 and the unheated group No. 7. The axial positions of the heated bundle section and of the pad plane are indicated by dashed horizontal lines. It can be supposed that the coolant temperatures rise accordingly to the dashed straight lines which connect the data measured inside the SAs. Within the heating groups No. 4 and 5, the total temperature rises resulting from measurements performed at the axial levels of 234 and 1,037 mm are nearly identical and correspond to the data plotted in Figs. 34 and 35, respectively. Downstream of the pad plane, the coolant temperatures are influenced by the interstitial flow which has a growing efficiency as the core radius increases. The temperature reduction amounts to about 3 K for the SAs of heating groups No. 4 and 5. The inlet temperature of the SA belonging to heating group No. 6 also amounts to 45°C recorded at the axial level of 158 mm. However, the effectiveness of the interstitial flow surrounding that SA causes a temperature drop of 5 K of the fluid flowing inside the shroud tube on the way from the inlet side to the lowest measuring position within the rod bundle. In the heating zone, the

temperature rise amounts to only 11 K. At the top end of the SA, the interstitial flow results in another temperature reduction of 5 K leading to an outlet temperature of 46°C. Compared to the SAs of heating groups No. 4 and 5, a 10 K lower coolant outlet temperature is registered. Inside the unheated storage element of heating group No. 7, an inverse axial temperature profile can be identified, i.e., the top end is colder than the bottom end. The reasons for that thermal behavior are following: The water inventory of that core element is essentially stagnant due the plug installed in the SA head. The top end of the SA is surrounded by the cold interstitial flow which enters into the core at the upper periphery and slopes downward to the heat source. The botton end of this element is hydraulically connected to the HPP. Hence an internal circulation of the fluid is possible. The occurrence of such an effect can be assumed as the temperature at the bottom end of this SA is higher in comparison with that one of heating group No. 6. Finally, the temperature of the SA bottom end is influenced by heat transfer from the core grid plate.

10.3 Temperatures of the Interstitial Flow

Figure 37 shows azimuthal temperature profiles of the interstitial flow registered at four axial positions having a radial distance of 736 mm from the core centerline. The plot indicates that the temperatures are almost uniform in axial and circumferential direction and amount to about 40°C which corresponds roughly to the temperature of the fluid delivered by the DHXs. Axial temperature profiles of the coolant flow between the wrapper tubes are plotted in Figs. 38 and 39 for two diametrical traverses. It can be seen that the temperatures of the interstitial flow increase as the radial distance from the core centerline decreases. This is true for the axial positions above and below the pad plane located at the axial level of 870 mm. The amount, however, is more significant above that plane than underneath it. Above the plane, the cold interstitial flow is heated up on the horizontal way from the periphery to the center of the core and the maximum temperatures are gradually shifted to higher axial levels. This behavior has to be attributed to the countercurrent flow effects of the cold water coming from the DHXs and the warm flow leaving the core. That leads not only to a mixing of both streams but also to a deflection of the flow toward the bottom end of the ACS. In addition, it is noticeable that the interstitial flow is warmer in the unheated region between the core top end and the pad than below that plane. This shows clearly the appreciable cooling effect of the interstitial flow on this part of the core. These observations are confirmed by the computations represented in Figs. 31 and 32 (see cross-section O-B). Close to the core grid plate, at the axial level of 259 mm, temperatures are measured which are about 1 K higher compared to those at the next TC plane at the 509 mm level. Along the heated section of the core, the axial temperatures rise slightly. This behavior can be well explained by the flow path. Cold water delivered from the DHXs flows in radial direction toward the core and penetrates partially into the spaces between the unheated core elements placed in the outermost an-

nular section of the core. This water proceeds vertically downward and is drawn on the way to the bottom end of the core to an increasing degree in radial direction toward the center of the core. During that clockwise circulation below the pad plane, the interstitial flow removes heat from the core grid plate and the powered portion of the core before being fed into the gap between the core and the ACS due to buoyancy effects produced by the heat source and downward acting forces of the cold fluid coming from the DHXs. Temperature profiles measured at five different axial elevations are plotted in Fig. 40 as function of the core radius. Dashed vertical lines allow an assignment to the individual heating groups No. 1 to 6. The diagram illustrates the axis symmetrical character of the findings and the temperature drops in radial direction toward the periphery of the core. At the centerline of the core, a temperature reduction of almost 2 K becomes clearly visible which takes place at an axial level of 904 mm, i.e., immediately above the pad plane. This minimum is attributed to the efficiency of colder fluid fed from the upstream position to that level.

10.4 Temperatures at the Above Core Structure

In Fig. 41, TC signals are plotted versus the radius of the ACS. The measuring devices are distributed over a horizontal cross-section at the axial level of 1,248 mm. The measurements show a temperature maximum at the centerline and a dropping profile with increasing radial distance. A comparison of the data with the findings plotted in Figs. 35 and 40 indicates that the temperature level of this profile is lower than the coolant temperatures recorded at the outlet side of the SAs and higher than the values of the interstitial flow measured at the top end of the core. This behavior reflects the result of the mixing process which takes place in the space formed by the axial gap between the core and the ACS. The result of measurements along vertical traverses is plotted in Fig. 42. Dashed horizontal lines represent the top end of the core at the axial level of 1,089 mm, the position of the spacing plate at 1,177 mm, and the lower end of the impermeable ACS cylinder at 1,289 mm. The temperature profiles can be subdivided into three axial regions; the dividing points are roughly at the axial elevation of 1,140, 1,240, and 1,289 mm. In the lower region, the temperatures drop about 1 K compared to the data measured at the bottom end of the guiding tubes. In the succeeding region, the data are approximately constant on an axial extent of 100 mm. The temperature profiles of the third portion are significantly changed which finally leads to a uniform temperature of roughly 51°C at higher elevations. The associated temperature gradients become more pronounced as the radial distance from the centerline increases. These observations can be explained as follows: The space between the upper end of the core and the bottom of the ACS is cooled by cold fluid flowing toward the centerline of the core. Elevations above the bottom end of the ACS are affected by a warm water stream which enters the central guiding tubes protruding from the ACS and fills the whole ACS space. The data reveal the gen-

eral trends observed in the numerical simulation (see Figs. 31 and 32). Figure 43 shows that the temperatures remain essentially constant at 52°C inside the ACS surrounded by an impermeable shell which results in a stagnation of the stored water inventory. The measurements include the data registered along two vertical traverses which are placed at the centerline and at a radial distance of 201 mm of it (see Fig. 20, TC group C).

10.5 Temperatures at the Primary Pumps and Heat Exchangers

Figures 44 to 48 shows temperature profiles plotted versus the circumference of the PPs, IHXs, and DHXs. The angular position of $\phi = 0°$ is located at the wall of the primary vessel (see Fig. 10). Figure 44 documents the temperature distribution around the inlet sides of the PPs. The data reflect a uniform behavior for all units. The temperature level is almost the same as at the inlet side of the SAs (see Fig. 34) and a few lower than the measurements in the top part of the UP (see Figs. 55 and 56). The temperature distribution at the inlet and outlet sides of eight IHXs are plotted in Figs. 45 and 46. The graphs reflect the uniformity of the temperatures measured at the dummies and indicate that the inlet values are roughly 1 K higher than the minimum temperatures recorded at the outlet sides. At the inlet sides, the data correspond again to the UP temperatures. The lower temperatures of the outlet sides can be attributed to the mixing process of warm water leaving the IHXs with cooler water accumulated in the LP. At the primary sides of the DHXs, the inlet temperatures are nearly identical in circumferential direction and amount to about 46°C as shown in Fig. 47. At the outlet sides (see Fig. 48), it is hard to relate the measurements to each other. The diagram shows that water exits with a mixing temperature of roughly 37°C at the upper part and about 30°C at the lower part of the outlet window. It is nearly impossible to define a reliable mean value because of the lack of local mass flow rates. The effect of the observed temperature fluctuations is caused by the beginning of a mixing process of cold water leaving the DHXs with warm water of the environment. Similar observations were made during the course of separate effect tests [25].

10.6 Temperatures of the Intermediate and Lower Pleneum

The horizontal temperature distributions measured at the top and bottom sides of the IP are shown in Figs. 49 and 50. In radial direction (90° and 180°), the measurements deliver nearly identical results for both sides. The temperatures within the IP are lower than those data measured at the top end of the LP (see Figs. 51 and 52) and higher than the values registered in the cavity of the UP (see Fig. 54). This means that heat is transported in upward direction. This is the reason for a temperature drop of 1 K between the inlet and outlet sides of the IHX (see Figs. 45 and 46). The readings of TCs fixed in the LP are summarized in Figs. 51 and 52. The reference level as well as the height of the IHX outlet windows are given by dashed horizontal lines. Along the vertical traverses (see Fig. 51) as well

as at the periphery of the vessel (see Fig. 52), the temperature profiles of the LP are identical to each other and nearly constant in vertical direction. At the elevation of the IHX outlet windows, the temperature distribution is a little bit influenced by warmer water which exits from the IHXs into the LP. In circumferential direction, the profiles are altered to a minor degree due to mixing.

10.7 Temperatures of the Upper Plenum

The UP temperatures result from measurements along the movable MER and MEL devices. The data are taken at two opposite sides of the vessel, the home positions of the devices as illustrated in Table 3.

Table 3. Home positions of the measuring devices MEL and MER.

Coordinates / Device	Radius r mm	Angle ϕ deg	Height z [1] mm
MEL	1,030	270°	555 - 2,235
MER-1	535	90°	1,127 - 2,184
MER-2	939	90°	566 - 1,666
MER-3	1,158	90°	871 - 2,271

[1] Height indication related to the reference level at the bottom end of the HPP.

Vertical temperature profiles of the UP are shown in Figs. 53 to 55. The data represent measurements recorded at ϕ = 90° using the MER system. In the plots, the top end of the core, the bottom end of the ACS, and the axial height of the IHX inlet windows are marked up by dashed horizontal lines. Figure 53 shows the temperature distribution measured along a vertical traverse (MER-1) which is located at a radial distance of 68 mm from the ACS shell. The profile is characterized by a steep temperature gradient of more than 7 K which occurs in a layer with a thickness of about 20 mm located just below the bottom end of the ACS. This gradient results from a thermal stratification which takes place in the UP due the interaction of warm water exiting the SAs at the top end of the core with cold fluid flowing in radial direction from the DHX outlet windows toward the core. Fluid of mixing temperature leaves the gap between the core and the ACS in opposite direction to the inflowing cold stream by flowing mainly along the bottom end of the ACS. At this axial level, the fluid temperature rises to a peak value followed by a slight drop immediately above this axial position. In the top part of the UP, an essentially steady temperature of 47°C is observed. Figures 54 and 55 indicate that the local temperature gradient decreases slightly as the radius from the core centerline increases. The measurements along MER-2 and MER-3 indicate that the pronounced peak temperature is replaced by a region with a flattened maximum. Figure 56 shows the temperature profile monitored for a MEL position at ϕ = 270°. These measurements cover the area from the cavity up to the uppermost

portion of the UP. The findings are in good agreement with the results represented in Figs. 54 and 55. Detailed measurements of the temperature distribution in the UP indicate that the data are nearly equal when the MER device is moved in a semicircle around the centerline of the test facility.

11. DISCUSSION OF EXPERIMENTAL AND ANALYTICAL RESULTS

The results of the natural circulation tests discussed here include a total of 15 experiments which are listed in Table 1. The central idea of the parameter selection is to examine the effects of permeable or impermeable structural or functional components arranged in the primary vessel on the formation of the flow paths between the heat source (core) and the heat sink (DHX) and between the upper and lower plenum as well as on the mixing of warm and cold fluid. To address such questions, the effects of permeable and impermeable designs of the ACS shell (tests T01 to T03), the level of the core power (tests T04, T05, T01, and T06, T07, T02), the complete failure of two neighboring DHX circuits (tests T06, T08), open and closed flow paths via the primary loops of the IHXs and/or via the reflector and storage (unheated and heated) elements of the core (tests T04, T06, T10 to T15), and the fluid level in the UP (tests T04, T09) are under consideration.

From the amount of available test data (see Chapter 10), plots of isotherm lines basing on detailed measurements in the Up and in the core are discussed. In addition, axial and radial temperature profiles measured in the UP, at the inlet and outlet side of the rod bundles, inside a heated SA, and at the bottom and top ends of the interwrapper spaces are interpreted. A comprehensive presentation of the most important readings of tests T01 to T15 is annexed to this report. The arrangement of diagrams corresponds to the systematical variation of the parameters and allows a direct comparison of the data. In case of decisive differences with respect to the findings, comments are given in this Chapter.

To demonstrate the capabilities and possible deficiencies of the FLUTAN computer program, the analytical predictions are compared against the experimental findings. This examination, however, remains incompletely in some cases (see Table 1: tests T08 and T12 to T15) due to the aforementioned restrictions (see Chapter 8).

11.1 Design of the ACS Shell

The computed velocity plots shown in Fig. 57 illustrate the influence of the ACS design on the thermal hydraulic behavior with examples of two sectional planes for tests T01, T02, and T03. The cross-sections are indicated in Fig. 30. The reference vector represents a velocity of 5 cm/s.

On the left-hand side, the cross-sections O-A are cuttings across the SAs of the core and the center of a DHX. On the right-hand side, the cross-sections O-B are cuttings across the interwrapper space of the core and the center of an IHX. Within the UP, a natural circulation path forms between the core and the DHX. A second flow path is established between the upper and the lower plenum via the IHXs. A permeable design of the ACS shell (test T01) allows a part of the cold fluid coming from the DHXs to enter the 200 mm high gap between the core and the ACS and to advance up to the centerline of the apparatus. One partial flow of mixing temperature is deflected through the ACS. A second part is forced to move along the perforated bottom plate of the ACS in opposite direction of the flowing-in cold water and ascends parallel to the ACS shell into the UP. Within the interwrapper space, two vortex flows can be identified, one above and one below the pad plane indicated by a dashed line. Above, cold water fed by the DHXs penetrates into the outermost portion of the interwrapper space and proceeds along the pad plane toward the center of the core. As soon as this interstitial flow reaches the heated area of the core, it mixes with the upward flowing warm water leaving the SAs. Below the pad plane, the clockwise flow is mainly initiated by the buoyancy producing central part of the core, whilst the outer peripheral region remains unheated during these tests.

In the gap of 200 mm height between the core and an impermeable ACS shell (test T02), the warm flow exiting the SAs is forced to flow against the direction of the cold stream coming from the DHXs (countercurrent flow). Water of mixing temperature reaches the UP by flowing along the solid ACS shell and circulates at the water surface to the inlet openings of the DHXs and IHXs, respectively.

The use of an impermeable ACS shell together with an additional skirt (test T03) reduces the gap between the core and the ACS to a height of only 28 mm. Warm water leaving the core flows via this small gap radially outward and prevents a direct penetration of cold fluid into this area. For the most part, warm and cold fluid are mixed in the UP in the vicinity of the skirt. On the other hand side, cold fluid is able to enter the interwrapper spaces and to contribute to the cooling of the core region (see cross-section O-B on the right).

The influence of the ACS design on the experimentally and numerically determined isotherm fields is illustrated by Fig. 58. The cross-section O-E-F-A (see Fig. 30) includes the interwrapper space of the core and a DHX. The isotherm lines have an interval of 1 K. The experiments (left-hand side) and computations (right-hand side) reflect an essentially horizontal character of the isotherms in the UP due to a thermal stratification. In case of a permeable design of the ACS shell (test T01), the stratification is present throughout the entire UP with a pronounced temperature gradient taking place in the region between the top end of the core and the bottom end of the outlet windows of the DHXs. As a consequence of the flow behavior, the highest temperatures occur at the centerline of the test facility.

In the core region, the temperature lines show that cold fluid penetrates into the interwrapper spaces at the top end of the core periphery and moves downward to the bottom end of the core. At the core grid plate and along the heated section of the SAs, the fluid is heated up. Comparing the numerical against experimental findings, it can be seen that the temperature field of the UP is generally reasonable predicted. Even for the interwrapper space of the core, the agreement is acceptable in view of the fact that the chosen nodalization doesn't simulate the interstitial flow in azimuthal direction. The left diagram of Fig. 59 (test T01) allows to discuss the capability of of the FLUTAN computer program in detail. The temperatures are plotted versus a vertical measuring traverse (MEL device))which is located at a radius of 1,033 mm and an angular position of 270° (see Table 3). The experimental data are marked by symbols connected by straight dashed lines, the computations are represented by solid lines. Dashed horizontal lines indicate the top end of the core, the bottom end of the ACS, and the height of the IHX inlet windows. The diagram indicates that the temperature is constant in the cavity. The thermal stratification results in a temperature difference of roughly 4 K in the neighborhood of the bottom end of the ACS. Above a level of 1,400 mm, the temperature rises with increasing height up to a measured maximum of about 47°C. In general, the analytical data show a reasonable agreement with the measurements except the uppermost positions of the plenum, where a discrepancy of about 1 K exists. The reason for this behavior may be the coarse nodalization of the ACS shell with several rows of holes allowing the fluid to pass through that component. It should be noted that the measurements suffer to some degree from the instrumentation of the MEL device which doesn't provide enough data about the temperature gradient across the stratified layer (see Chapter 4.2: The MEL device having a more sophisticated instrumentation was available as from test T10).

The installation of an impermeable ACS shell without skirt leads to the earlier described countercurrent flow in the vertical gap existing between the core and the ACS (see Fig. 58, test T02). This flow behavior causes the formation of a strong thermal stratification which is characterized by a steeper temperature gradient amounting to about 6 K (see Fig. 59, test T02) compared to test T01. A comparison of the computations against the measurements show a qualitatively and quantitatively satisfying agreement of the vertical temperature profiles. The temperature deviation of nearly 2 K in the cavity may result from a numerical diffusion effect in computing the temperature gradient across the stratified layer.

The attachment of an additional skirt below the impermeable shell of the ACS leads to a radial shifting of the so far observed mixing region between the core and the ACS to an area next to the skirt (see Fig. 58, test T03). A comparison of the corresponding data shown on the right-hand side of Fig. 59 reflects a good matching of the vertical temperature profiles with a temperature gradient of 6 K.

Figures A.1.1 to A.1.6 of the Appendix illustrate the influence of the ACS design on the thermal hydraulics in more detail: Due to the temperature stratification extended over the whole UP of test T01, about 1 K colder fluid exists close to the inlet windows of the IHXs (see Fig. 59). This finding is in contrast to the tests T02 and T03 with an impermeable design of the ACS shell. This is the reason for the temperature level of the measurements performed in the core, at the IHXs and PPs as well as in the IP and LP which is lower compared to the data recorded during the tests T02 and T03 (see Appendix: Figs. A.1.2 and A.1.3). The profiles of the corresponding temperatures, however, are very similar. The region above the core shows a decisive difference of the thermal hydraulic behavior. A comparison of horizontal temperature profiles is shown in Fig. 60. The measuring traverse is located below the ACS shell at an axial level of 1,248 mm. The plot shows a hyperbolic profile for test T01, a parabolic one for test T02, and a uniform one for test T03. The trace of the curves is governed by the penetration of cold fluid into the space between the core and the bottom end of the ACS surrounded by a shell of different design. A permeable shell design allows the cold water under mixing with warm water leaving the SA heads to proceed up to the centerline of the rig where it is deflected through the ACS. In the case of an impermeable ACS without skirt, the radial penetration depth of cold fluid is highly reduced due to the countercurrent flow of warm water which cannot pass through the ACS. The installation of an additional skirt at the bottom end of the ACS prevents at all a penetration of cold fluid into the remaining small gap. Inside the ACS, the temperatures measured along vertical traverses reach values which are equivalent to those measured along the horizontal traverse underneath the ACS. The data increase when the permeable shell is replaced by an impermeable design and reach maximum values when a skirt is mounted (see Appendix: Fig. A.1.4).

In Fig. 61, inlet and outlet temperatures of the heated SAs are plotted versus the core radius. The radius of the heated portion of the core is 493 mm. The comparison of calculated with measured data refers to the vertical heights of 158 mm and 1,037 mm, respectively. The experimental data of tests T01 to T03 show that the water temperature decreases by 1 to 2 K on the way from the IHX inlet windows (see Fig. 59) to the inlet side of the SAs (see Fig. 61). This different temperature can be identified from all data represented in Figs. 61 and 62 and is caused by heat losses from the LP via the *"redan"* to the UP. The essentially constant temperature profiles of the core inlet side are well predicted. The reduction of the core power in the outer heating zone to less than 40% of the inner core zone (see Table 3) results in a steep drop of the outlet temperatures which is also accurately simulated. For a core radius of -400 mm $< r <$ +400 mm, however, the computation predicts temperatures which are up to 5 K higher than the corresponding local measurements (see test T01). This deviation has to be attributed to the number of mesh cells chosen to resolve the complex phenomena taking place in the core and to the coarse modeling of the ACS as mentioned before. The thermal hydraulic

interaction between the core elements and the interstitial flow is mainly governed by the flow resistance and the heat transfer. By the code simulations can be demonstrated that a modification of these parameters strongly influences the portion of energy transported by the fluid flowing in the SAs and in the interwrapper spaces. The discrepancy between the computed and measured coolant outlet temperatures has to be attributed to a higher computed mass rate flowing in the SAs in spite of the fact that the same amount of energy is removed as in the experiment. This experience leads to the conclusion that the calculated pressure drop within the SAs is too low although drag coefficients are specified for the input data which are based on separate effect tests carried out utilizing original components [23]. The results of test T03 show in addition that a modeling of radially directed interwrapper spaces has a minor influence on the computed data since the efficiency of the interstitial flow advancing to the center of the core is diminished by the small gap existing between the core and the ACS in this case.

Qualitative and quantitative indications about the temperature rises of the coolant flowing inside a SA are given by Fig. 62. The measurements are taken from a rod bundle which is located at a radial distance of 362 mm from the core centerline and belongs to the heating group 4. In a first approximation, it can be supposed that the coolant temperature increase accordingly to the dash-lined straights connecting the available vertical measuring positions. Upstream and inside the heated bundle region, the calculated temperature rises follow substantially these straight lines. Downstream of the heated region, however, the temperature differences become larger with increasing height and the underprediction amounts to about 5 K in test T01. This behavior is not only caused by the relationship of mass flow and temperature rise in the SAs but also by the distribution of energy to the flows in the SAs and in the interwrapper spaces.

The influence of ACS design on the comparison of computed against measured radial temperature profiles of the interwrapper flow is illustrated by Fig. 63. The measuring positions are located at vertical heights of 259 mm and 1,029 mm. At the lower level, the agreement of the findings is nearly perfect, but less satisfying for the upper level. This behavior emphazises once more the necessity to specify an appropriate number of mesh cells for this region and to review the axial and radial friction factors required as input data.

A comparison of measured and computed core mass flow rates, temperature rises, and percentage of the core power removed by the interwrapper flow is given in Table 4 for the tests T01 to T03. The data demonstrate the significant cooling part of the interwrapper flow and emphasize the important advantage of the NEPTUN test facility. It can be gathered from the experimental data that roughly 50% of the produced power is removed by the interwrapper flow. The FLUTAN code overpredicts the effectiveness of the flow for the case of an impermeable ACS shell with an additional skirt (test T03).

Table 4. Influence of the ACS design on the comparison of measured and computed mass flow rates, temperature rises, and percentages of the core power removed by the interwrapper flow.

		NEPTUN experiment					FLUTAN code simulation				
Test No.	Total core power, kW	Total mass flow rate flowing through the heated SAs, kg/s	Mean temperature rise of the flow through the heated SAs, K	Power removal by the flow through the heated SAs, kW	Power removal by the interwrapper flow, kW	Percentage of power removal by the interwrapper flow, %	Total mass flow rate flowing through the heated SAs, kg/s	Mean temperature rise of the flow within the heated SAs, K	Power removal by the flow through the heated SAs, kW	Power removal by the interwrapper flow, kW	Percentage of power removal by the interwrapper flow, %
T01	221	2.15	12.2	109	112	51	2.75	10.0	115	106	48
T02	221	2.26	11.9	113	108	49	2.80	8.5	100	111	50
T03	221	2.41	12.0	120	101	46	2.64	7.7	85	136	62

Basically, a less satisfactory matching of test T03 is experienced with regard to the mass flow rates fed through the heated SAs which results in an underprediction of the mean temperature rises of the coolant flowing inside the SAs. The thermal hydraulic interaction of coolant flowing inside the core elements and in the interwrapper spaces is essentially governed by the resistance to the flow and the heat transfer which have a significant influence on the amount of decay heat removed by the partial mass flow rates. The computed overprediction of the core mass flow rates indicates that the used pressure loss equations resulting from pretests give too low pressure losses. The consequence of this hydraulic behavior is the prediction of backflow effects for test T03. Such effects occur in SAs which belong to the heating group 6. The result of the backflow, however, is neglected in Table 4. Under the assumption that the ratio of computed to measured mean mass flow rate through the core is the same in test T03 as in tests T01 and T02 and under neglection of heating group 6 in taking the mean value of the calculated temperature rise of test T03, the following results: A mean mass flow rate of 3.03 kg/s and a mean temperature rise of 9.7 K. This leads to the conclusion that 44% of the decay heat is removed by the interstitial flow, an amount which is in good agreement with the percentage of 46% gained on the basis of experimental data. Nevertheless, the occurrence of backflow has a strong influence on the thermal hydraulic behavior of the core cooling.

11.2 Level of the Core Power

The investigation into the influence of the core power on the data comparison includes two test series which differ only in the design of the ACS shell. The first series (tests T04, T05, and T01) refer to a permeable design of the ACS shell, the second one (tests T06, T07, and T02) to an impermeable design, both of them without skirt. The core power amounts to 133, 170, and 221 kW. The remaining parameters and boundary conditions of these experiments are identical and summarized in Table 1.

The measured and computed results of the first series are represented in Figs. 64 to 69, those of the second series in Figs. 70 to 75. The plotted fields of isotherms, shown in Figs. 65 and 71, indicate a similar distribution of the temperatures for the prevailing series. This leads to the conclusion that the core power influences the level and not the distribution of the temperatures in the whole primary system (see Appendix: Figs. A.2.1 to A.3.6). The comparison of the numerical simulations against the experimental findings leads basically to a satisfying agreement of the findings. The local discrepancies, however, are similar to those described earlier (see Chapter 11.1). The same has to be said about the data summarized in Table 5.

11.3 Failure of Two Neighboring DHX Circuits

Test T08 differs from test T06 only by the number of operable DHX circuits. That means the same amount of decay heat has to be removed by two units only, since all other test parameters as well as boundary conditions are kept constant. To remove a twice as high power per component, an increase of the driving temperature difference and of the mass flow rate is necessary at the primary side of each serviceable DHX placed at angular positions of 264° and 276° in the NEPTUN test facility (see Fig. 10).

In Figs. 76 to 81, data are represented which illustrate the different thermal behavior of an asymmetrical compared to a symmetrical cooling mode (see also Appendix: Figs. A.4.1 to A.4.6). From the isotherms plotted in Fig. 76, it can be seen that the operation of two DHXs causes a temperature level which is approximately 12 K higher than that measured during test T06. The profiles of the isotherms, however, remain by far as they are measured in the UP and in the interwrapper spaces under symmetrical cooling conditions. A numerical simulation of test T08 was not performed with respect to the number of mesh cells required for a proper modeling of a 180° sector of the NEPTUN apparatus. The thermal behavior of the UP is shown in Figs. 77 and 78. The data taken along the vertical traverses of the MEL and MER-3 devices reflect an unaltered temperature distribution in spite of the fact that two diametrically opposite measuring positions are

Table 5. Influence of the core power on the comparison of measured and computed mass flow rates, temperature rises, and percentages of the core power removed by the interwrapper flow.

		NEPTUN experiment					FLUTAN code simulation				
Test No.	Total core power, kW	Total mass flow rate flowing through the heated SAs, kg/s	Mean temperature rise of the flow through the heated SAs, K	Power removal by the flow through the heated SAs, kW	Power removal by the interwrapper flow, kW	Percentage of power removal by the interwrapper flow, %	Total mass flow rate flowing through the heated SAs, kg/s	Mean temperature rise of the flow within the heated SAs, K	Power removal by the flow through the heated SAs, kW	Power removal by the interwrapper flow, kW	Percentage of power removal by the interwrapper flow, %
Permeable design of the ACS shell without skirt											
T04	133	1.61	10.0	68	65	49	1.92	7.4	59	71	56
T05	170	1.85	11.4	88	82	48	2.29	9.0	86	84	49
T01	221	2.15	12.2	109	112	51	2.75	10.0	115	106	48
Impermeable design of the ACS shell without skirt											
T06	133	1.67	9.6	67	66	50	1.96	6.5	53	80	60
T07	170	1.92	10.7	86	84	49	2.34	7.0	69	101	59
T02	221	2.26	11.9	113	108	49	2.80	8.5	100	111	50

under consideration. Changed temperature levels and nearly identical temperature profiles can be identified from Figs. 79 to 81, i.e., at the inlet and outlet side of the SAs, inside the heated rod bundle, as well as at the top and bottom end of the interwrapper spaces.

11.4 Flow Path Blockage of the IHX Primary Sides

The objective of this test series is to simulate the thermal hydraulic behavior following a possible break of the hot leg piping system in a top-entry loop-type reactor [26], [27], [28]. For that purpose, the inlet windows at the IHX primary

sides are closed in order to block the flow paths between the UP, the LP, and the coolant inlet side of the core. This means that the core is coolable only from above.

The program of the experimental work consists of two steps (see Chapter 6):

a) The core power results from six differently heated groups of SAs including a total of 253 fuel elements. The 84 storage elements remain unheated. The flow paths via the 138 reflector and 84 storage elements are blocked by plugs installed at their top ends.

b) The core power results from seven differently heated groups of SAs including a total of 253 fuel and 84 storage elements. The flow paths via the 138 reflector and 84 storage elements are unblocked.

11.4.1 Unheated storage elements, blocked flow paths via reflector and storage elements

The plots of Fig. 82 show a comparison of velocity fields computed for both cases under consideration, test T04 (see upper graphs) performed with unblocked flow paths and test T10 (see lower graphs) having blocked flow paths via the primary loops of the IHXs. A comparison of the cross-sections O-A (left-hand side) indicates that because of the blocked IHX channels cold water delivered by the DHXs flows from the UP downward and penetrates into quite a number of heated SAs which are placed in the outer region of the core. This pronounced backflow is predicted to exist mainly in the cross-section which includes the DHXs. With increasing azimuthal distance from that position, the radial range affected by backflow is diminished. In contrast to the computer code simulations, the experimental data do not give any indication about the occurrence of backflow effects. This leads to the assumption that these core elements are cooled by thermosiphon effects, events which are governed by the balance of the drag and inertia forces caused by the upward moving warm main flow and the downward acting forces of the penetrating cold flow. The occurrence of thermosiphon effects is coupled with an increased resistance to the coolant flowing inside a SA and leads to a higher temperature rise which causes an enhanced heat transfer to the interstitial flow. The latter one can be identified from Fig. 82 (see test T10, cross-section O-B) indicating a somewhat more pronounced flow in the interwrapper space.

To demonstrate again the important cooling part of the interstitial flow, Fig. 83 illustrates the field of isotherms on the basis of measured (left side) and numerically determined (right side) values for both the unblocked (upper part) and the blocked (lower part) flow channels between the upper and lower plenum. The isotherm lines of the blocked case are closer together and indicate a higher temperature gradient for the interwrapper space compared to the unblocked case. From that can be concluded that the contribution of the interstitial flow to the de-

cay heat removal is enhanced. Apart from the fact that the maximum temperature is about 4 K higher at the top end of the core, the coolability of the core from above seems to be feasible without any difficulty. As a result of the permeable design of the ACS shell, the thermal stratification is present throughout the entire UP with a temperature gradient which is a little bit higher in test T10 compared to test T04. A comparison of the FLUTAN calculations against the measurements indicates a fairly reasonable agreement even for the interwrapper space.

A comparison of observed and computed UP temperatures is represented in Fig. 84. A similar agreement of the findings can be gathered from both diagrams. Except the uppermost positions of the plenum, the predictions of both test runs agree well with the observed trends along the vertical traverse of the MEL device.

The left diagram of Fig. 85 shows the known measured and computed temperature profiles of test T04. The code simulation results in a more intensified core cooling since the lower pressure drop allows an increased mass flow rate through the SAs and the outlet temperatures are correspondingly about 3 K lower compared to the measurements. The computation of test T10 (right diagram) comes to a similar output. The deviation of the calculated against measured inlet temperatures can be attributed to the backflow in the SAs which brings up a temperature increase of 3 K in the HPP. The right diagram of Fig. 86 indicates also a temperature discrepancy of 3 K for the bottom end of the interwrapper space. Again, that can be put down to the computed warm backflow into the HPP and the heat transfer via grid plate to the interstitial flow.

A comparison of the results plotted in Figs. 87 to 91 (impermeable design of the ACS shell) with the corresponding findings presented in Figs. 82 to 86 (permeable design of the ACS shell) leads to the conclusion that the design of the ACS shell is of secondary importance for the core cooling. Possible differences are to be attributed to the changed flow pattern in the region between the top end of the core and the bottom end of the impermeable ACS shell.

The measured data of tests T04 and T10 performed with a permeable ACS shell are shown in Figs. A.5.1 to A.5.6 of the Appendix. The findings of tests T06 and T11 utilizing an impermeable ACS shell are given Figs. A.6.1 to A.6.6. Appendix.

11.4.2 Heated storage elements, unblocked flow paths via reflector and storage elements

Out of the above reported two test series, the experiments T12 to T15 were performed with the purpose to study the influence of heat release by storage elements. In this case, seven SA groups are heated. The flow paths via the reflector and storage elements are unblocked. All specific data of these four test runs are

summarized in Table 1. The results presented in Figs. 92 to 95 refer to a permeable design of the ACS shell and those plotted in Figs. 96 to 99 make use of an impermeable design.

A comparison of the radial temperature profile measured at the SA outlet side of test T12 (see Fig. 94, left side) with that of test T04 (see Fig. 85, left side) indicates a temperature minimum for a core radius of about 500 mm and a temperature increase close to the periphery of the core. This behavior is caused by the unheated row of reflector elements and the additional power input of 17 kW via heating group No. 7 simulating one row of heated storage elements, respectively. That effect is nearly independent of the fact whether the flow paths via the IHX primary loops are unblocked or blocked.

The measured data are plotted in Figs. A.7.1 to A.7.6 (permeable ACS shell) as well as in Figs. A.8.1 to A.8.6 (impermeable ACS shell) of the Appendix.

11.5 Fluid Level in the Upper Plenum

To demonstrate the influence of the water level on the thermal hydraulic behavior of the primary vessel, the results of test T09 and of test T04 will be compared. The parameters of both tests are listed in Table 1. A lowering of the water level from 2,359 mm to 1,809 mm has the consequence that no water can either enter the inlet windows of the IHXs nor reach those of the DHXs. Therefore, no fluid can reach the core via the pump feedlines and the operation of the DHXs is of such a mode that lateral flowing fluid coming from the core is suctioned from the upper part of the DHX outlet windows and is fed back to the UP via the lower half of the same openings. This exiting flow serves to cool the core by penetrating into the interwrapper spaces and by entering into the SAs at their heads (thermosiphon effects). The lower part of Fig. 100 illustrates this behavior by means of two computed vector plots. Under such conditions, the temperature level of the primary system undergoes a temperature increase of approximately 20 K as demonstrated by the plots of Fig. 101. This is due to the fact that the DHXs are not fully immersed into the fluid and only a part of the heat exchanging surfaces is actively involved in the decay heat removal process. The isotherm fields of test T09 allow a comparison of the computation against the corresponding experimental observations. The agreement of the findings is remarkably good. The same can be said about the vertical temperature profiles of the UP between the cavity and the lowered water surface (see Fig. 102). The results presented in Figs. 103 and 104 indicate that the computation of test T10 leads to major divergences of the compared data especially at the bottom end of the core. Again, backflow is predicted to appear in the core which significantly influences the radial temperature profiles at the inlet side of the SAs as well as at the bottom end of the interwrapper spaces.

The observed increase of the temperature level in the primary system can be halfed just by removing the shrouds of the DHXs. In this way, the fluid of the UP can easier reach the cooling surfaces of the DHXs along the whole immersed length. This behavior was demonstrated by earlier RAMONA tests [8].

A data comparison of tests T04 and T09 is represented in Figs. A.9.1 to A.9.6 of the Appendix.

12. SUMMARY AND CONCLUDING REMARKS

Following to the earlier RAMONA water experiments performed in a 1:20 scaled 3D setup equipped with all active components but a rather simple core design, the NEPTUN program was conducted utilizing a 1:5 scaled 3D apparatus. The very realistical core geometry consisting of some hundreds of SAs and the corresponding interwrapper spaces allowed a thorough investigation of the thermal hydraulic interaction between the heat source and the heat sink in the water filled primary vessel [29]. During the course of steady state NEPTUN investigations, the effects of different design and operating parameters were studied; in particular: the shell design of the ACS, the core power, the number of DHXs put in operation, the complete flow path blockage at the primary side of the IHXs, and the fluid level in the primary vessel. In order to assess the capability of the thermal hydraulic computer program FLUTAN, the code was applied for the 3D numerical simulation of the majority of NEPTUN tests reported above. The code predictions were compared against the measurements. The obtained results allow the following summarization:

- Using water as fluid, a geometrically similar model with a scale of 1:20 gives identical Ri, Pe, and Eu numbers (see Fig. 6). The Reynolds number ratio Re*, however, is 10^{-3}, i.e., laminar flow conditions are obtained. This deviation is reduced by more than one order of magnitude in the 1:5 scaled model. In Fig. 105, the normalized characteristics Ri*, Re*, and Pe* are plotted versus the dimensionless model power $Q^* = Q_M / Q_R$. The symbols indicate findings obtained from experiments carried out in both test facilities. The result is encouraging for an extrapolation to prototypical conditions.

- The results of the experiments indicate that the decay heat can be safely removed by natural convection as far as the vessel is filled with fluid up to a minimum level. This level is assured by the second safety tank. If the DHXs are arranged in the UP, always flow paths develop which ensure an effective cooling of all regions. The interstitial flow makes a very important contribution to that behavior.

- A permeable design of the ACS shell results in a thermal stratification which extends over the total height of the UP. The characteristic temperature gra-

dient observed in the region between the core and the ACS is lower compared to the case of an impermeable shell design. The thermal stratification is limited to a small axial space of the UP. The attachment of an additional skirt below the impermeable shell prevents to a great degree the penetration of cold water coming from the DHXs into the small gap between the top end of the core and the bottom end of the ACS.

- A higher core power results in an overall increase of the system temperature and of the temperature differences. That observation does not depend on the design of the ACS shell.

- The complete failure of two neighboring DHX circuits causes an increase of the temperature level in the primary vessel, but doesn't alter the global overall temperature distribution.

- A flow path blockage of the IHX primary loops leads to the occurrence of thermosiphon or/and backflow effects in the elements placed at the periphery of the core and to an enhanced cooling effect of the interstitial flow. At the upper end of the core, the temperatures increase slightly, but the core coolability from above seems to be feasible without any difficulty.

- A reduced fluid level in the primary system due to leakage into the safety tank doesn't affect the core coolability even if no coolant can enter the inlet windows of the IHXs and DHXs. Under such conditions, the core is cooled from the UP.

- The comparison of FLUTAN code predictions against the measurements shows a qualitatively and quantitatively satisfying agreement of the findings with respect to the field of isotherms and the temperature profiles in the UP as well as within the core region.

- The cause for differences between computed and measured results, especially within the core region, is mainly attributed to the chosen nodalization of the very complex geometry and in particular to the modeling of the core consisting of heated SAs and interwrapper spaces. The noding scheme of the area between the wrapper tubes allows only an approximated description of the interstitial flow field in radial and axial direction, but doesn't account for an azimuthal flow.

- The thermal hydraulic interaction of coolant flowing inside the SAs and in the interwrapper spaces is essentially governed by the resistance to the flows and the heat transfer which have a significant influence on the amount of energy removed by the partial mass flow rates.

13. ACKNOWLEDGMENTS

The authors gratefully acknowlegde the fruitful cooperation of scientists of the Power Reactor and Nuclear Fuel Development Corporation (PNC), O-arai, Japan, with members of the research staff from the Institute of Applied Thermo- and Fluid-dynamics of the Research Center Karlsruhe.

We express gratitude for the support from the PNC management in providing the opportunity for the delegations of Messrs. Y. Ieda, H. Kamide, H. Ohshima, H. Ohira, and H. Hayafune to Karlsruhe. In 1987 to 1994, they made valuable contributions to the success of the Project on Passive Decay Heat Removal of Advanced Sodium-cooled Reactors (RAMONA program and NEPTUN program).

Furthermore, the untiring scientific, technical, and administrative assistance of Messrs. H. Borgwaldt, A. Class, M. Daubner, C. Günther, J. Harbauer, A. Hinz, F. Hofmann, H. Krause, K. Marten, D. Miatke, L. Pawlak, K. Sakai, G. Schnetgöke, K. Thomauske, and G. Willerding is highly appreciated.

14. NOMENCLATURE

a	thermal diffusivity, m^2/s
A	flow cross-section, m^2
Eu	Euler number (pressure/inertia), dimensionless
c	specific heat, kJ/(kg K)
g	acceleration of gravity, m/s^2
L	characteristic length, m
$\dot{m}$	mass flow rate, kg/m^3
p	pressure, N/m^2
Pe	Péclet number (conduction/convection), dimensionless
Q	core power, kW
r	radius, mm
Re	Reynolds number (inertia/friction), dimensionless
Ri	Richardson number (buoyancy/inertia), dimensionless
t	time, s
T	temperature, °C
u	characteristic velocity, m/s
z	length, mm
β	coefficient of thermal expansion, 1/K
Δp	pressure drop, N/m^2
Δr	radial difference, mm
ΔT	temperature difference, K
Δz	length difference, mm
$\Delta\phi$	angle difference, deg
ε	convergence criterion parameter, dimensionless
ζ	friction coefficient, dimensionless
ν	kinematic viscosity, m^2/s
ρ	density, kg/m^3
ϕ	angle, deg

Subscripts

c	core
DHX	decay heat exchanger
M	model
p	pressure
R	reactor
th	thermal
UP	upper plenum

Superscript

*	ratio of M/R

Abbreviations

ACS	above core structure
AHX	sodium/air heat exchanger
DHR	decay heat removal
DHX	decay heat exchanger
DRC	direct reactor cooling
EFR	European fast reactor
EM	electromagnetic
HPP	high pressure plenum (diagrid)
IHX	intermediate heat exchanger
IMP	isolated measurement pod
IP	intermediate plenum
LAN	local area network
LOSSP	loss-of-station service power
LP	lower or cold plenum
MEL	measuring lance
MER	measuring rake
o.d.	outer diameter
PP	primary pump
SA	subassembly
SOR	successive overrelaxation
SGU	steam generator unit
SNR-2	German design of a sodium-cooled fast reactor
TC	thermocouple
UP	upper or hot plenum
3D	three-dimensional

15. REFERENCES

[1] EFR Associates (eds.): European Fast Reactor, consistent design, concept design specification. EFR Associates, 10 rue Juliette Récamir, BP 3087, F-69398 Lyon, Cedex 03, France, EFR A000/0/0034B, September 1991.

[2] EFR Associates (eds.): European Fast Reactor, concept design specification and justification. EFR Associates, 10 rue Juliette Récamir, BP 3087, F-69398 Lyon, Cedex 03, France, EFR A000/0/0333A, June 1993.

[3] EFR Associates (eds.): European Fast Reactor, the approach to Europe's future need for electricity. EFR Associates, 10 rue Juliette Récamir, BP 3087, F-69398 Lyon, Cedex 03, France, December 1993.

[4] M. Düweke, H.J. Friedrich, F. Hofmann, B. Valentin, and R. Webster: The direct reactor cooling system of EFR, overview and R&D activities. Proc. of the 1990 Internat. Fast Reactor Safety Meeting, Snowbird, UT, USA, Vol. II, pp. 309-318, August 1990.

[5] M. Köhler and H.J. Friedrich: Das passive Nachwärmeabfuhrsystem des European Fast Reactors, (in German), Fachsitzung: Naturumlaufprobleme zur passiven Nachwärmeabfuhr bei fortschrittlichen Reaktoren. Jahrestagung Kerntechnik '91, Bonn, Germany, Kerntechnische Gesellschaft e.V., Deutsches Atomforum e.V., Bonn: INFORUM 1991, pp. 13-46, May 1991.

[6] C. Essig, M. Düweke, V. Ruland, V. Ertel, and M. Kiera: Consistent thermal hydraulic approach of EFR decay heat removal by natural convection. Proc. of the 5th Internat. Topical Meeting on Nuclear Reactor Thermal Hydraulics (NURETH-5), Salt Lake City, UT, USA, Vol. I, pp. 135-142, September 1992.

[7] H. Hoffmann, P. Sardin, and R. Webster: The European R&D program on natural convection decay heat removal of the EFR. Proc. of the Internat. Conference on Fast Reactors and Related Fuel Cycles, Kyoto, Japan, Vol. II, pp. 13.5/1-5/9, November 1991.

[8] H. Hoffmann, K. Marten, D. Weinberg, H.H. Frey, K. Rust, Y. Ieda, H. Kamide, H. Ohshima, and H. Ohira: Summary report of RAMONA investigations into passive decay heat removal. Wissenschaftliche Berichte, FZKA 5592, July 1995.

[9] D. Weinberg, H. Hoffmann, K. Rust, H.H. Frey, K. Hain, W. Leiling, and H. Hayafune: Summary report of NEPTUN investigations into the transient thermal hydraulics of the passive decay heat removal. Wissenschaftliche Berichte, FZKA 5666, December 1995.

[10] D. Weinberg, H. Hoffmann, H. Tschöke, and H.H. Frey: unpublished internal report, September 1985.

[11] D. Weinberg, H. Hoffmann, K. Hain, and M. Düweke: Experimental and theoretical program to study the natural convection decay heat removal system of the SNR-2. Proc. of the Internat. Conf. on Science and Technology of Fast Reactor Safety, St. Peter Port, Guernsey, GB, Vol. 1, pp. 289-294, May 1986.

[12] J.U. Knebel, D. Weinberg, and U. Müller: Scaling of natural circulation decay heat removal from coolant pools. Y.A. Hassan and R.M. Singer (eds.): Thermal hydraulics of advanced nuclear reactors. Papers Pres. at the Winter Annual Meeting of the American Society of Mechanical Engineers, Chicago, IL, USA, HTD-Vol. 294, pp. 31-38, November 1994.

[13] D. Weinberg, D. Suckow, U. Müller, and H. Hoffmann: The transferability to reactor conditions of thermal hydraulics model investigations of decay heat removal. Proc. of the 1990 Internat. Fast Reactor Safety Meeting, Snowbird, UT, USA, Vol. II, pp. 341-350, August 1990.

[14] SNR-2 - Abschlußbericht der SNR-2-Pool-Vorplanung (Phase 1c) (in German), Kraftwerk Union AG, Interatom, Bensberg, No. 41.07117, December 1983.

[15] K. Hain: unpublished internal report, Dezember 1991.

[16] G. Schnetgöke, K. Hain, A. Hinz, W. Leiling, H. Ohira, and K. Thomauske: unpublished internal report, April 1993.

[17] H. Borgwaldt, W. Baumann, and G. Willerding: FLUTAN input specifications. KfK 5010, Kernforschungszentrum Karlsruhe, May 1992.

[18] H. Borgwaldt and H.H. Frey: Vektorisierung und Einsatz eines 3D-Thermohydraulik Codes auf dem Siemens Vektorrechner VP50 (in German). Tagungsband anläßlich des Symposiums zur Vorstellung des Projektes ODIN und zur Inbetriebnahme des Höchstleistungsrechners Siemens VP400-EX, A. Schreiner, Ed., Technische Universität Karlsruhe, Germany, pp. 59-72, April 1989.

[19] H. Borgwaldt: CRESOR, - A robust vectorized Poisson solver implemented in the thermal hydraulic Code COMMIX-2(V). Proc. of the First Internat. Conference on Supercomputing in Nuclear Applications, Mito City, Japan, pp. 346-351, March 1990.

[20] J. C. Tannehill: Hyperbolic and hyperbolic-parabolic systems. 12, Handbook of Numerical Heat Transfer, W.J. Minkowycz, E.M. Sparrow, G.E. Schneider, and R.H. Pletcher, Eds., John Wiley & Sons Inc., New York, pp. 463-517, 1988.

[21] K. Sakai and D. Weinberg: Investigation on the LECUSSO (locally exact consistent upwind scheme of second order) scheme, - extension to nonuniform mesh size grids and numerical stability analysis, application for natural circulation test analyses using COMMIX-2(V). Proc. of the First Internat. Conference on Supercomputing in Nuclear Applications, Mito City, Japan, pp. 57-62, March 1990.

[22] C. Günther: Fortschrittliche Upwind-Differenzenverfahren zur numerischen Lösung der Konvektions-Diffusionsgleichung (in German). KfK 4697, Kernforschungszentrum Karlsruhe, May 1992.

[23] J. Krapp, W. Leiling, M. Prüßmann, and F. Schloß: unpublished internal report, October 1987.

[24] A. Class: unpublished internal report, January 1990.

[25] V. Brems, H. Tschöke, and H. Hoffmann: unpublished internal report, July 1988.

[26] K. Satoh, S. Kotake, Y. Tsukui, T. Inagaki, and M. Miura: Summary review of demonstration reactor safety. Proc. of the Specialists' Meeting on Passive and Active Safety Features of LMFBRs, O-arai, Japan, IWGFR/85, pp. 52-59, November 1991.

[27] Y. Eguchi, K. Yamamoto, T. Funada, T. Koga, H. Takeda, K. Sasaki, H. Kajiwara, M. Toda, and I. Maekawa: Experimental and computational study on prediction of natural circulation in top-entry loop-type FBR. Proc. of the Specialists' Meeting on Evaluation of Decay Heat Removal by Natural Convection, O-arai, Japan, IWGFR/88, pp. 86-96, February 1993.

[28] T. Koga, H. Takeda, S. Moriya, T. Funada, K. Yamamoto, Y. Eguchi, K. Sasaki, H. Kajiwara, O. Watanabe, and I. Maekawa: Natural circulation water tests for top-entry loop-type LMFBR. M. Courtaud and J.M. Delhaye (eds.): Proc. of the 6th Internat. Topical Meeting on Nuclear Reactor Thermal Hydraulics (NURETH-6), Grenoble, France, Vol. 2, pp. 1302-1308, October 1993.

[29] D. Weinberg, H. Hoffmann, and K. Rust: Overview report of RAMONA/NEPTUN program on passive decay heat removal. Wissenschaftliche Berichte, FZKA 5667, December 1995.

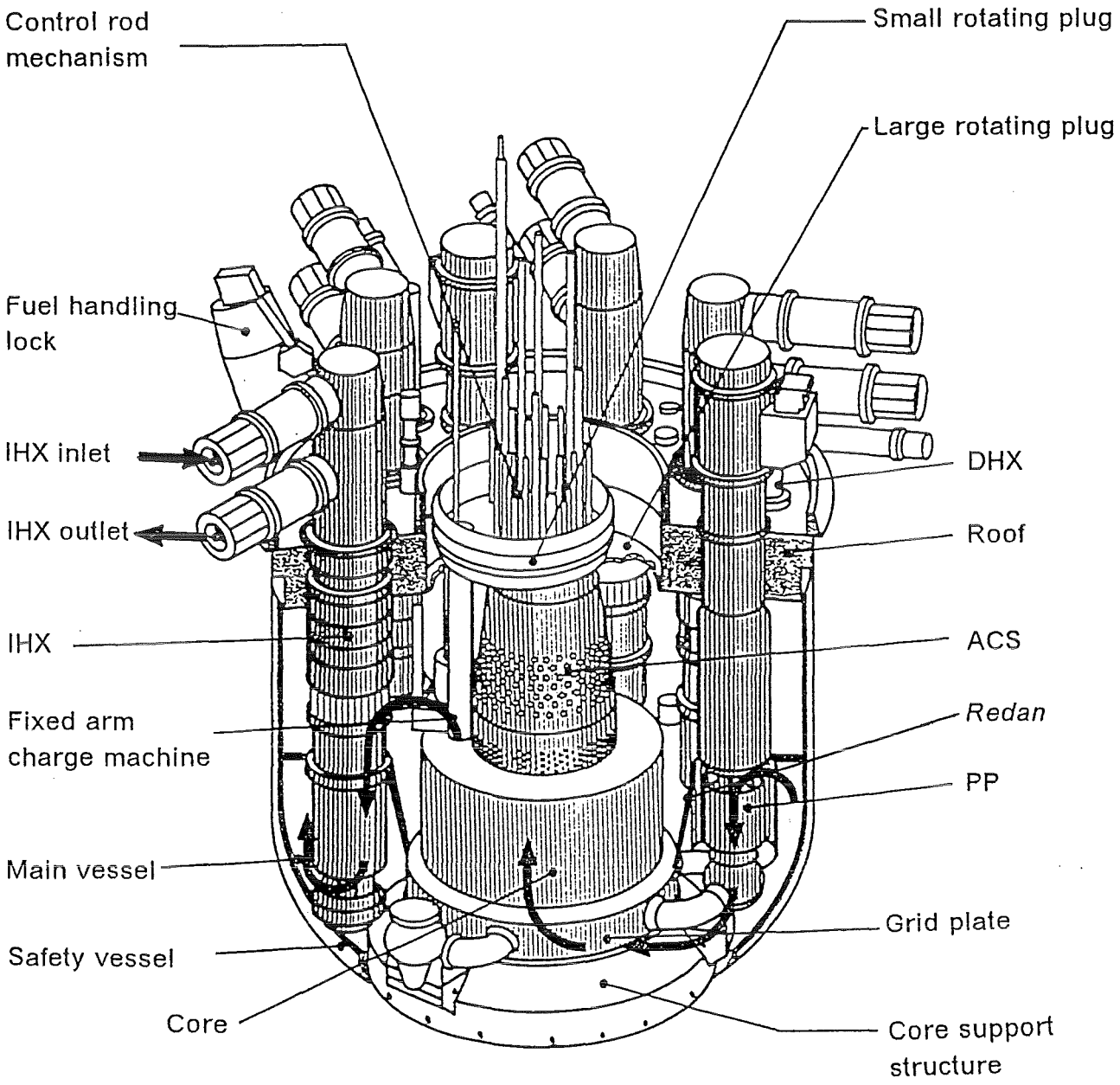

Fig. 1. Primary system of the EFR.

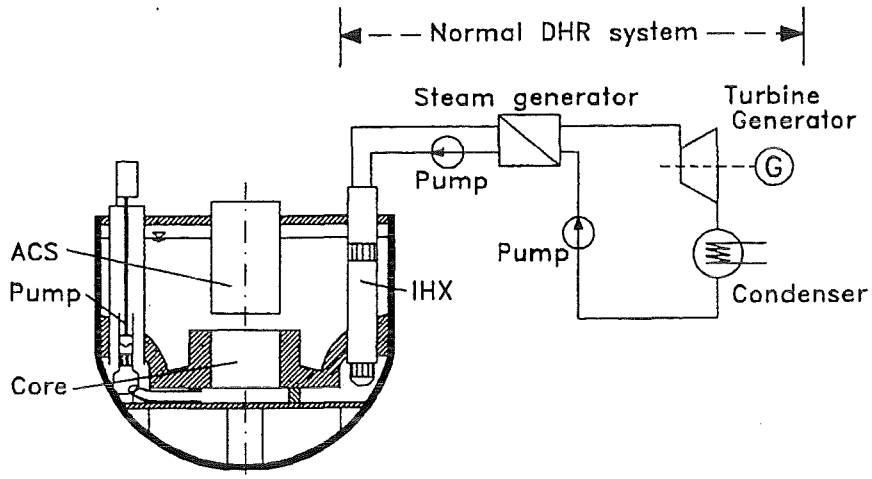

Fig. 2. Nominal decay heat removal system.

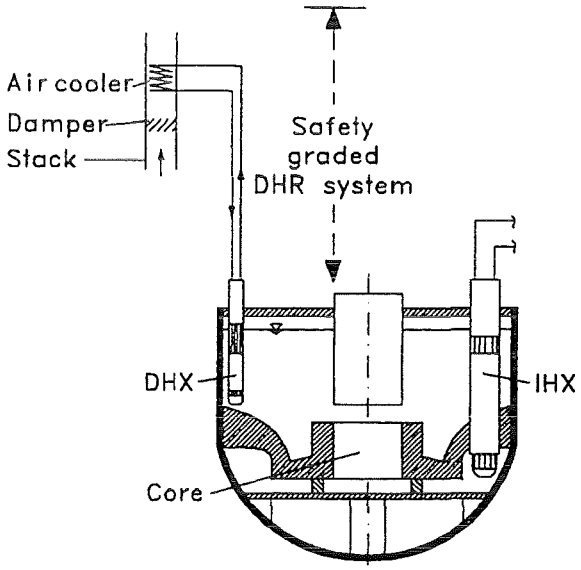

Fig. 3. Safety graded decay heat removal system.

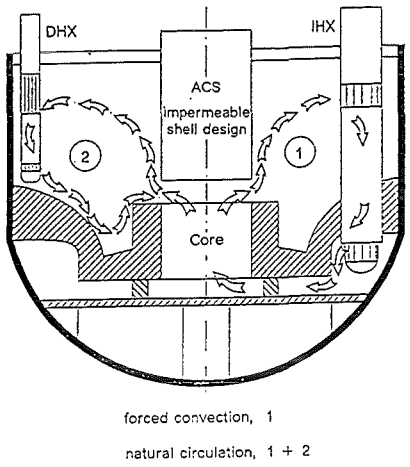

Fig. 4. Main flow paths before and after scram.

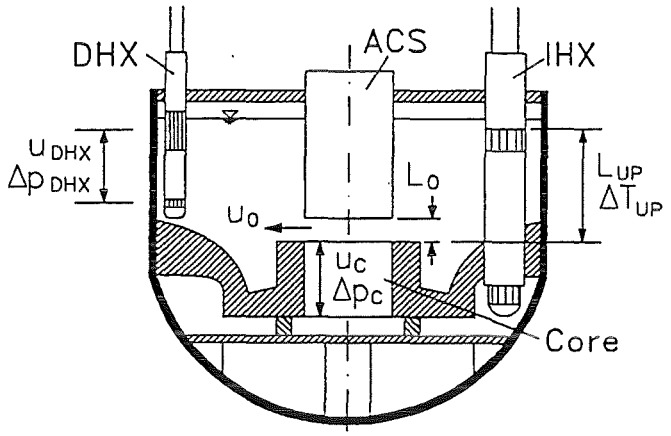

$$Ri = \frac{g \cdot \beta \cdot \Delta T_{UP} \cdot L_{UP}}{u_o^2}$$

$$Re = \frac{u_o \cdot L_o}{\nu}$$

$$Pe = \frac{u_o \cdot L_o}{a}$$

$$Eu^+ = \frac{\Delta p_{DHX}}{\Delta p_c} \cdot \frac{u_c^2}{u_{DHX}^2}$$

Fig. 5. Definition of the characteristic numbers.

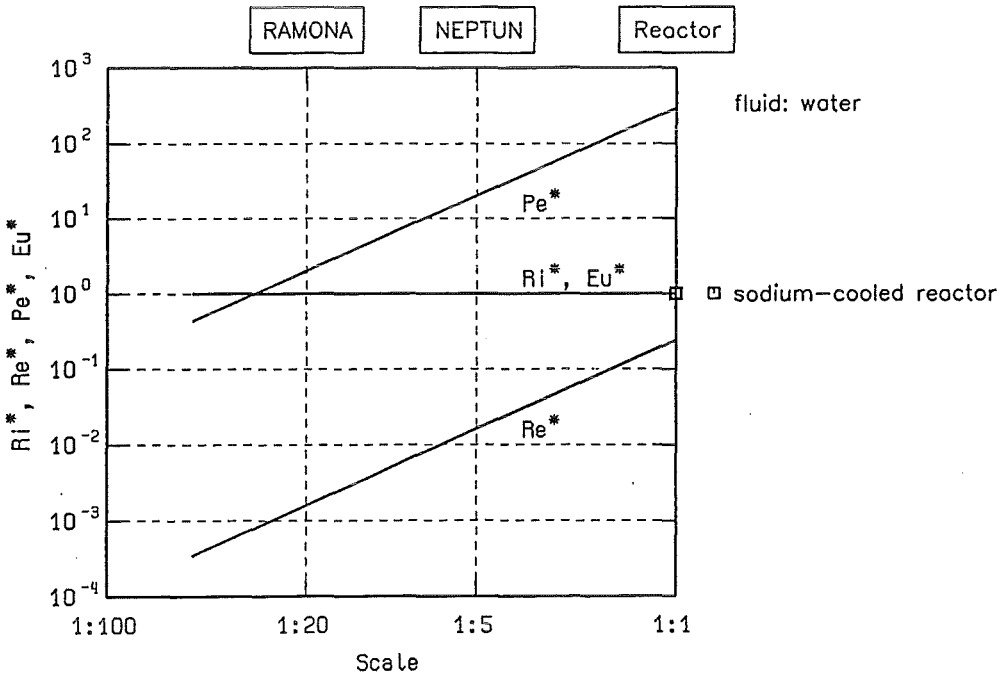

Fig. 6. Characteristic numbers as function of the model scale.

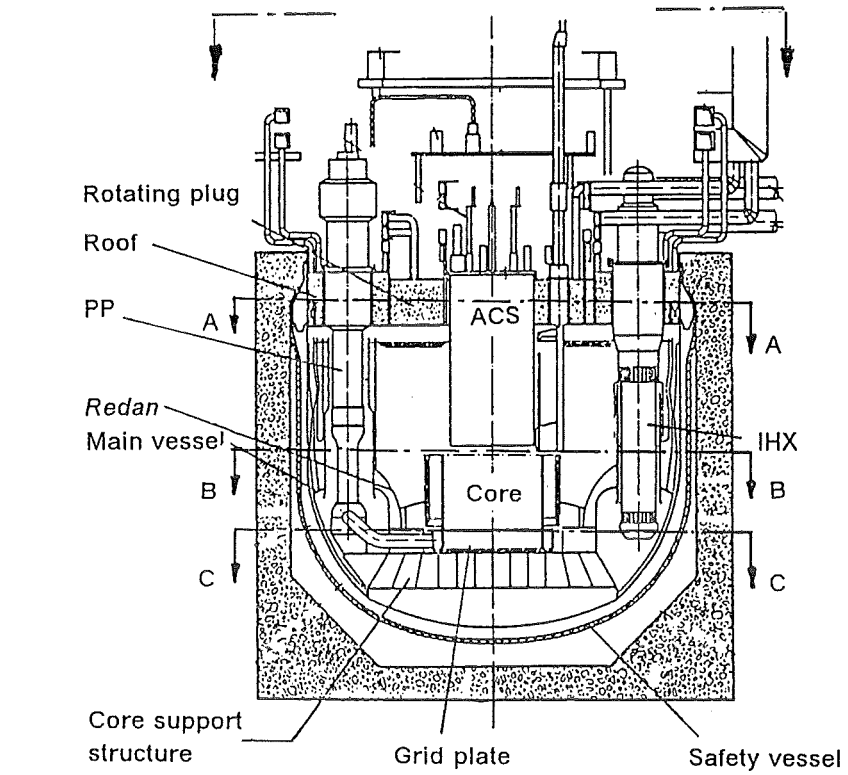

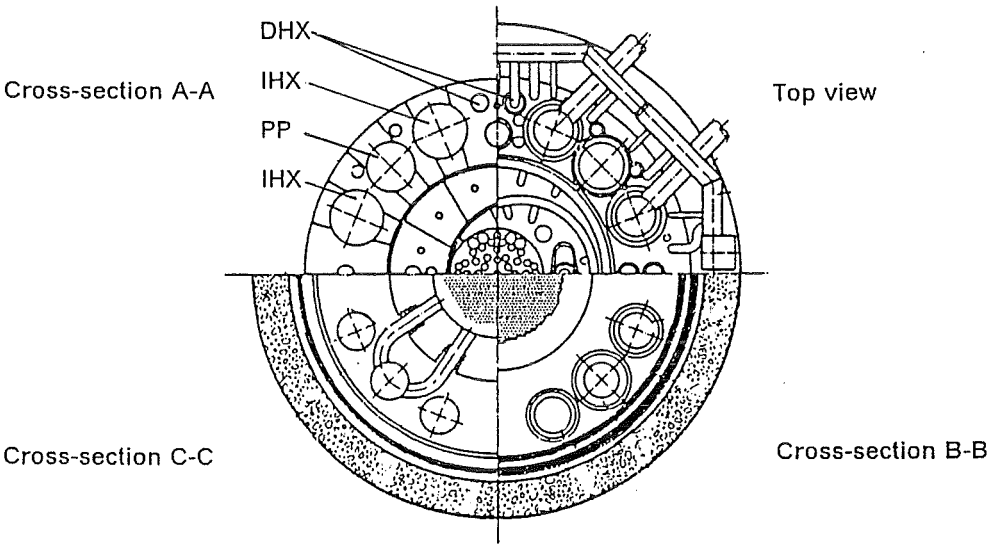

Fig. 7. Cross-sections of the SNR-2 primary system.

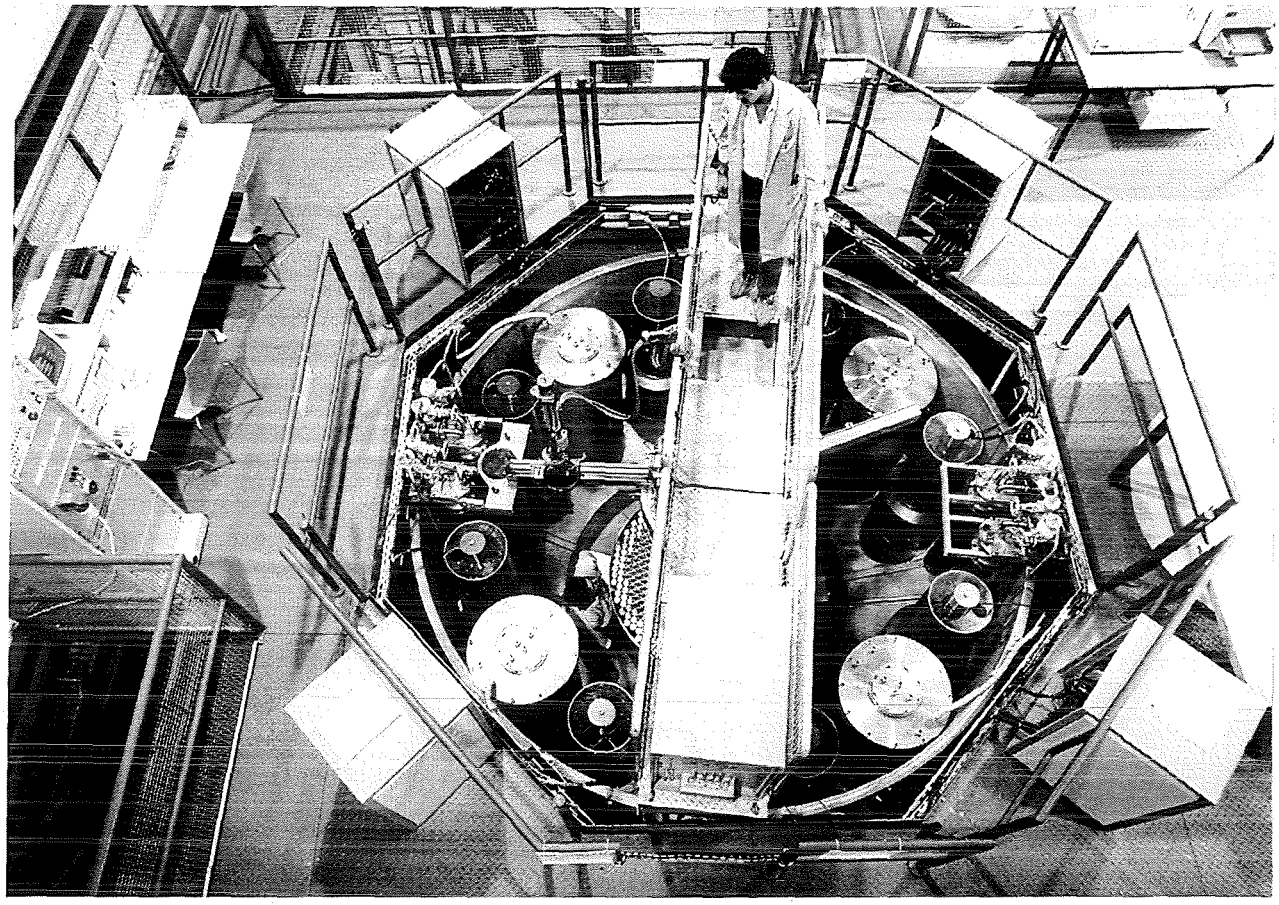

Fig. 8. Bird's eye view of the NEPTUN test facility.

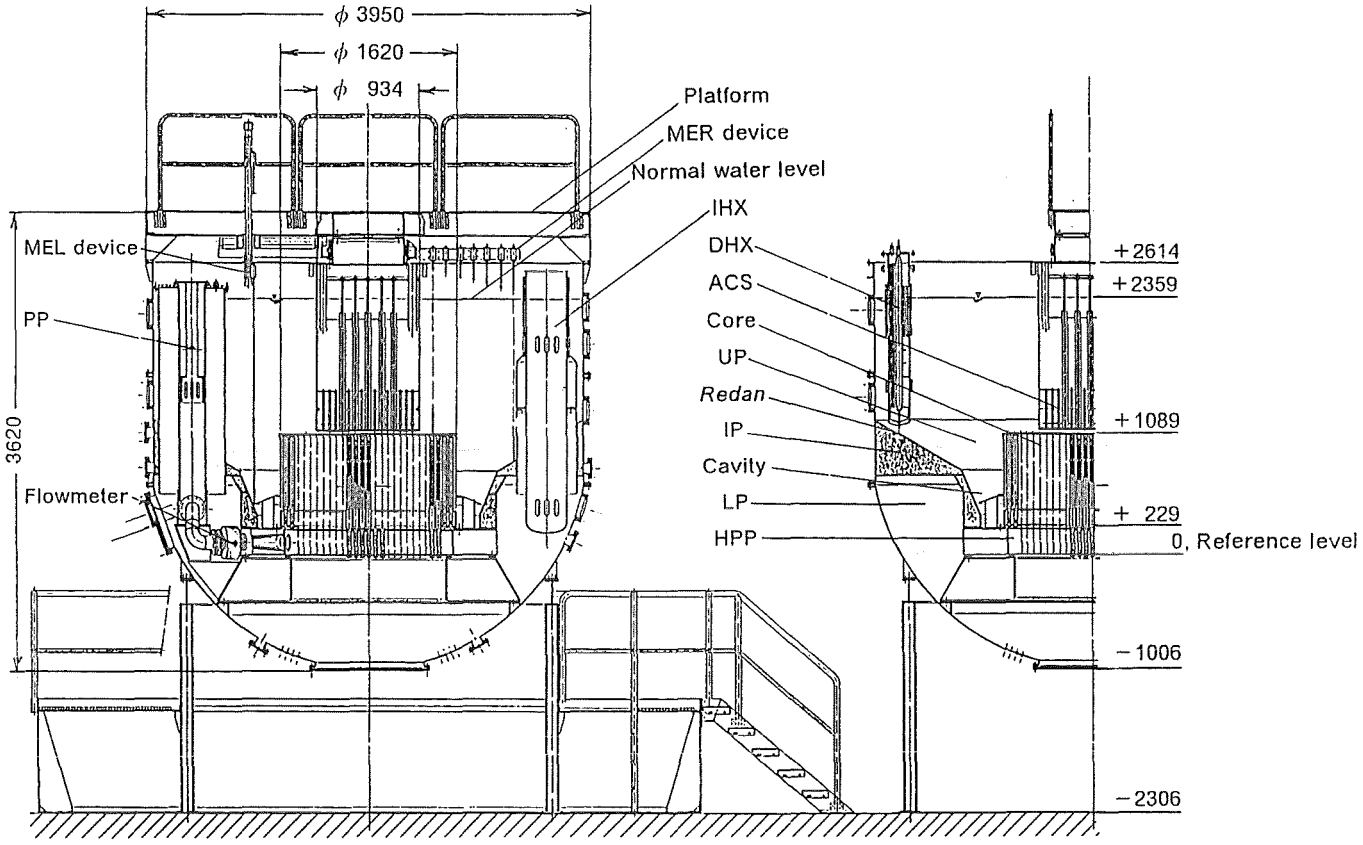

Fig. 9. Vertical cross-section of the NEPTUN test facility (dimensions in millimeter).

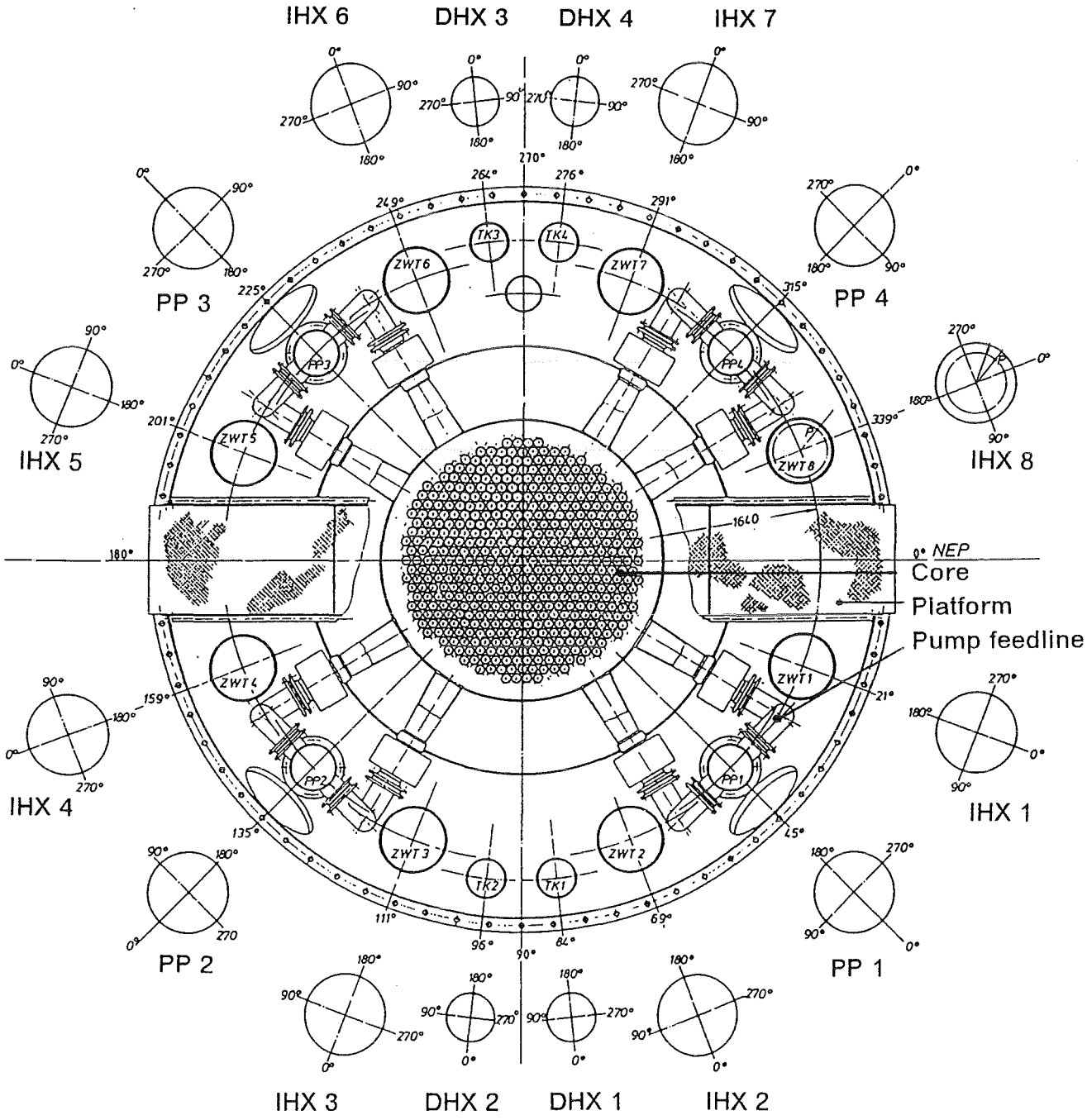

Fig. 10. Horizontal cross-section of the NEPTUN test facility.

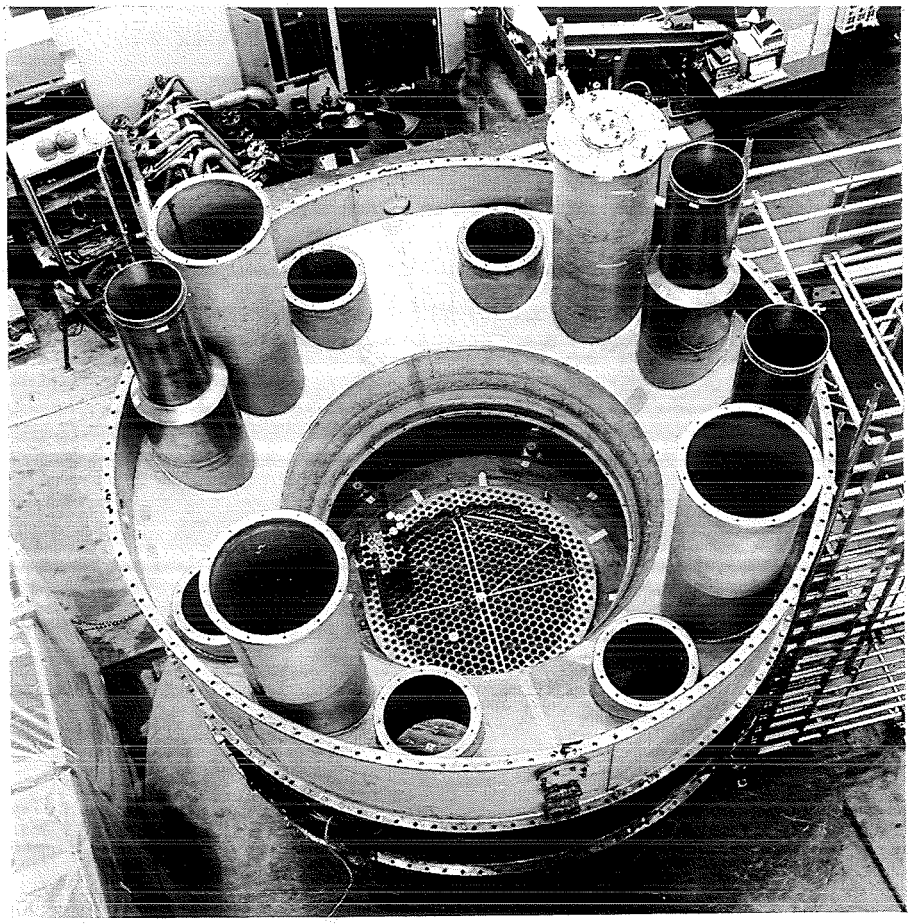

Fig. 11. Bird's eye view of the lower part of the NEPTUN test facility.

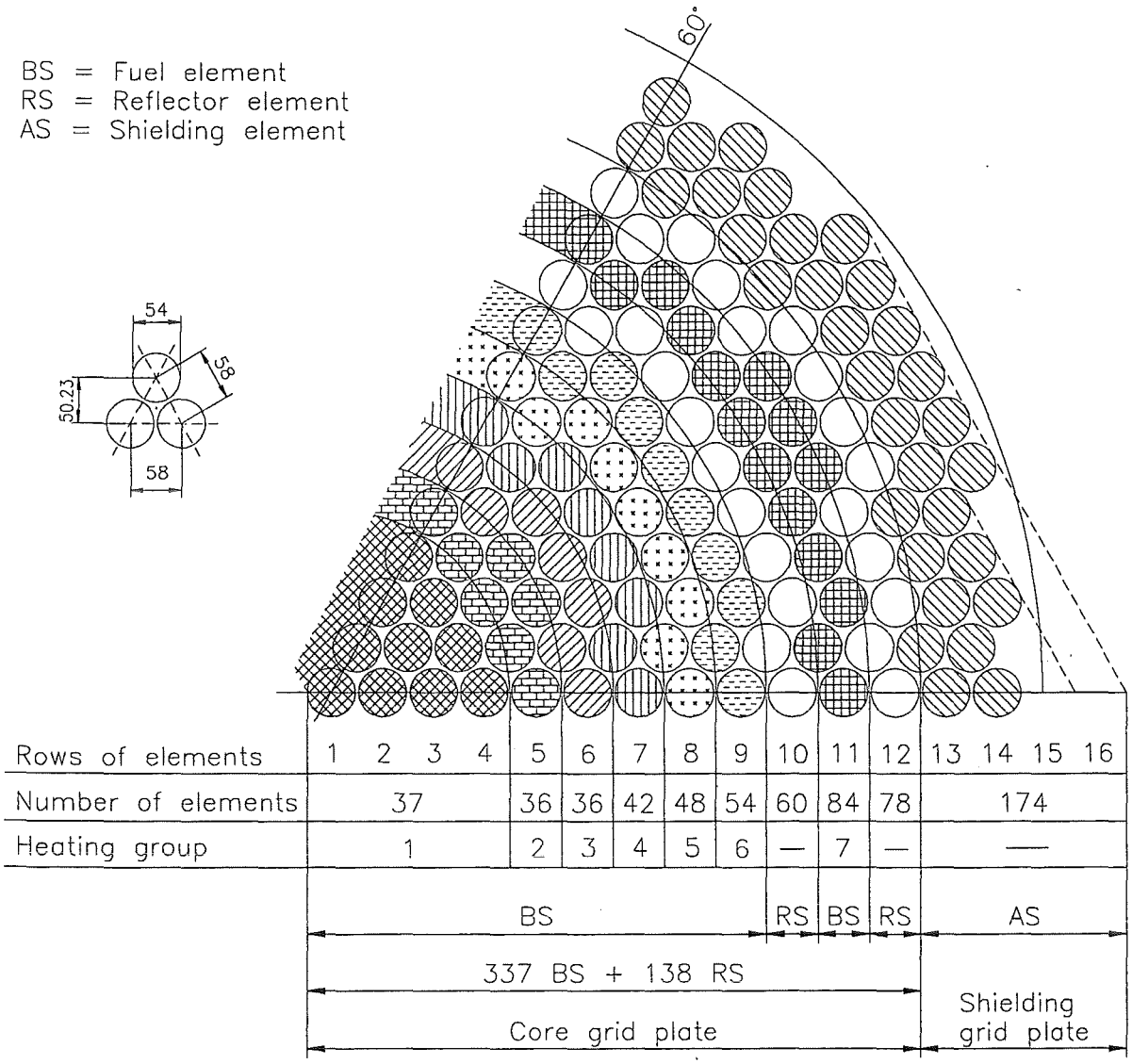

Fig. 12. 60° sector of the core.

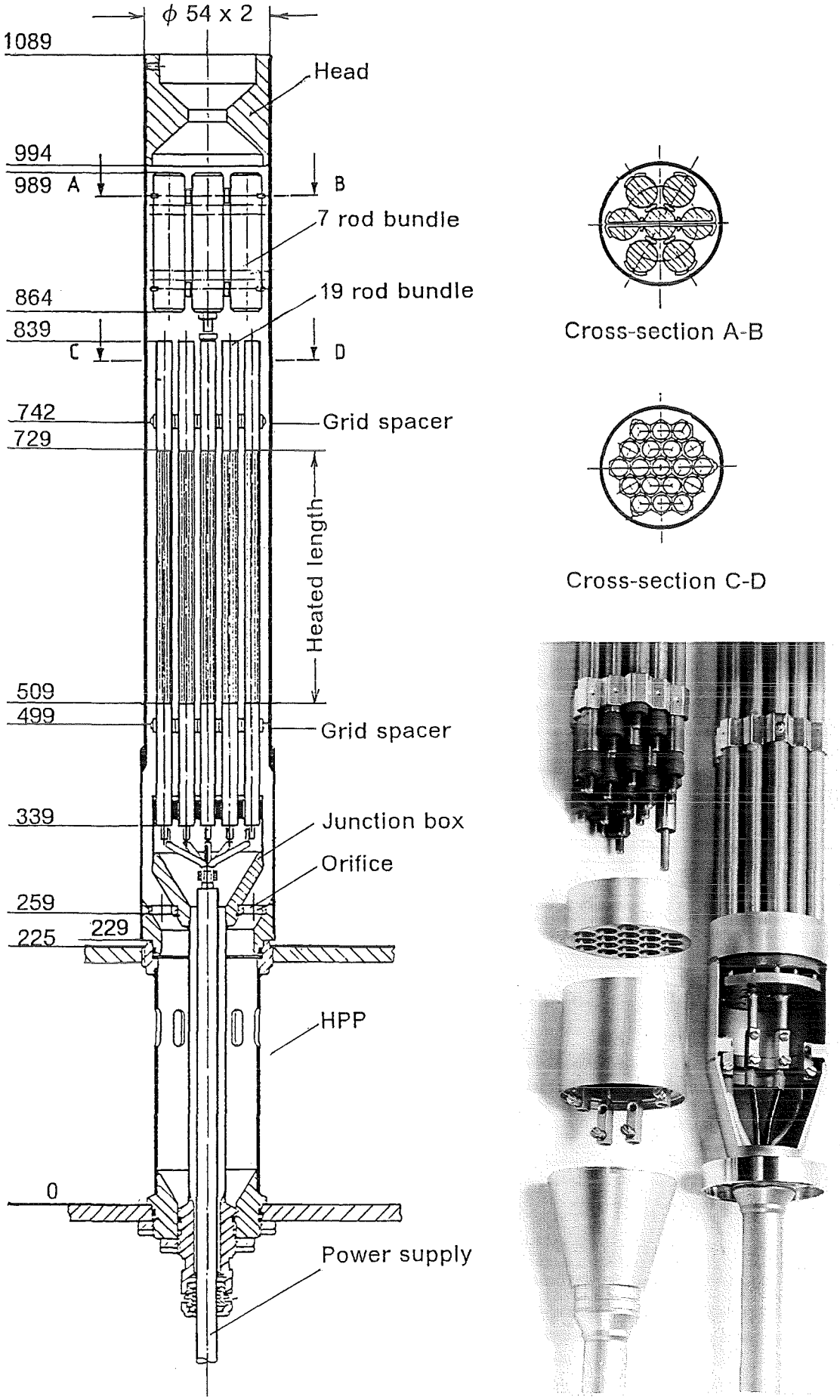

Fig. 13. Arrangement of 19 electrically heated rods in a bundle (dimensions in millimeter).

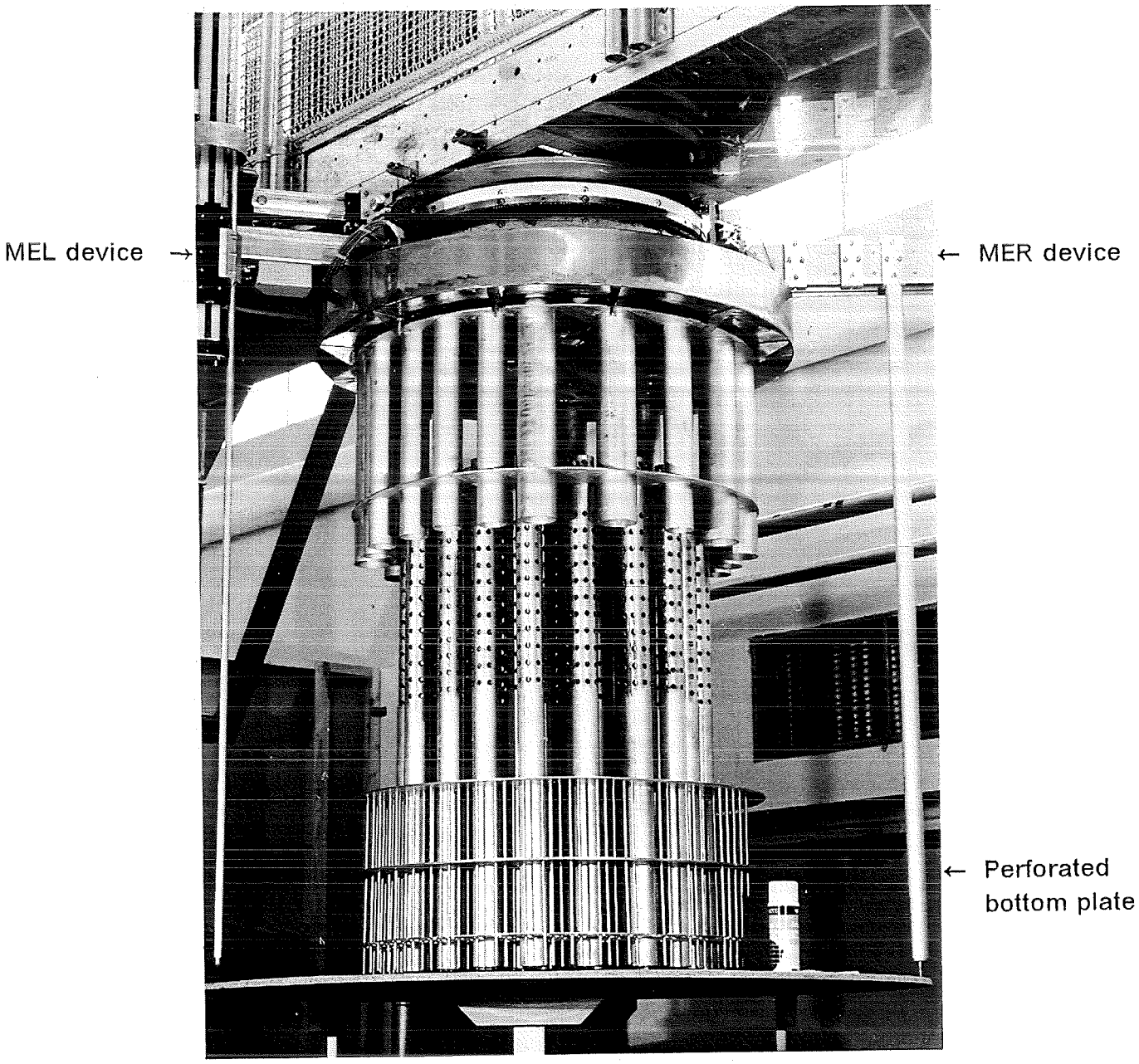

Fig. 14. Above core structure with vertical guiding tubes simulating control rod drivelines and core monitoring systems.

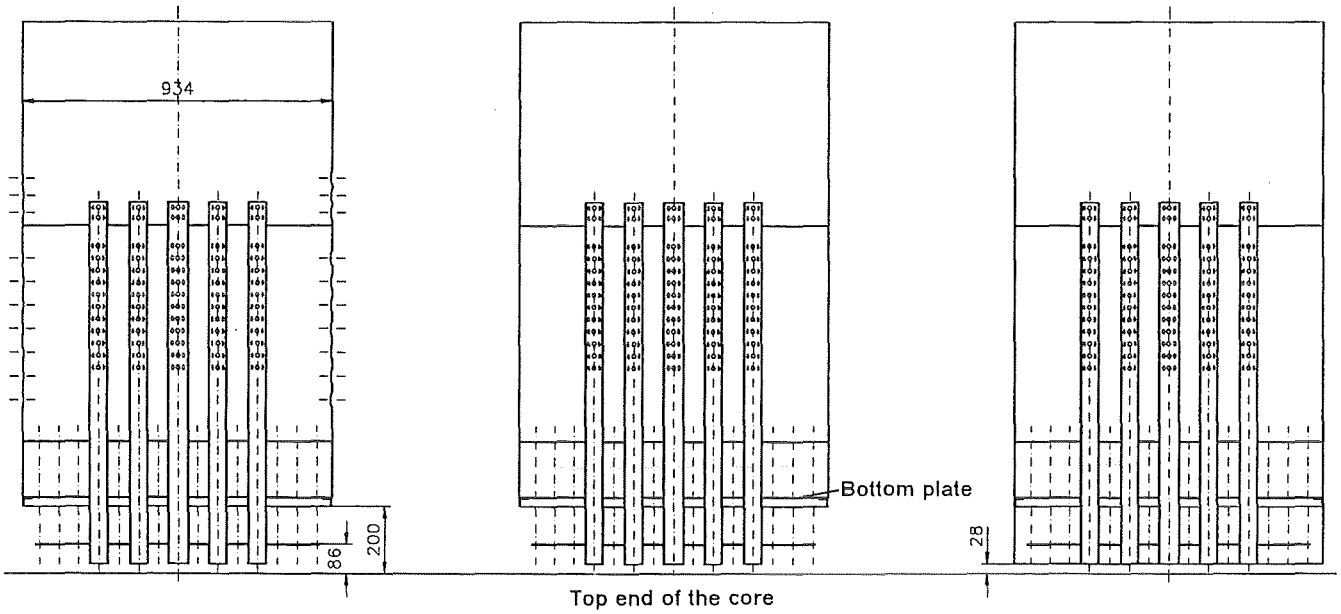

permeable shell (15.2%) without skirt,	impermeable shell without skirt	impermeable shell with skirt
permeable bottom plate (12.5%)	permeable bottom plate (12.5%)	permeable bottom plate (12.5%)

Fig. 15. Different designs of the above core structure.

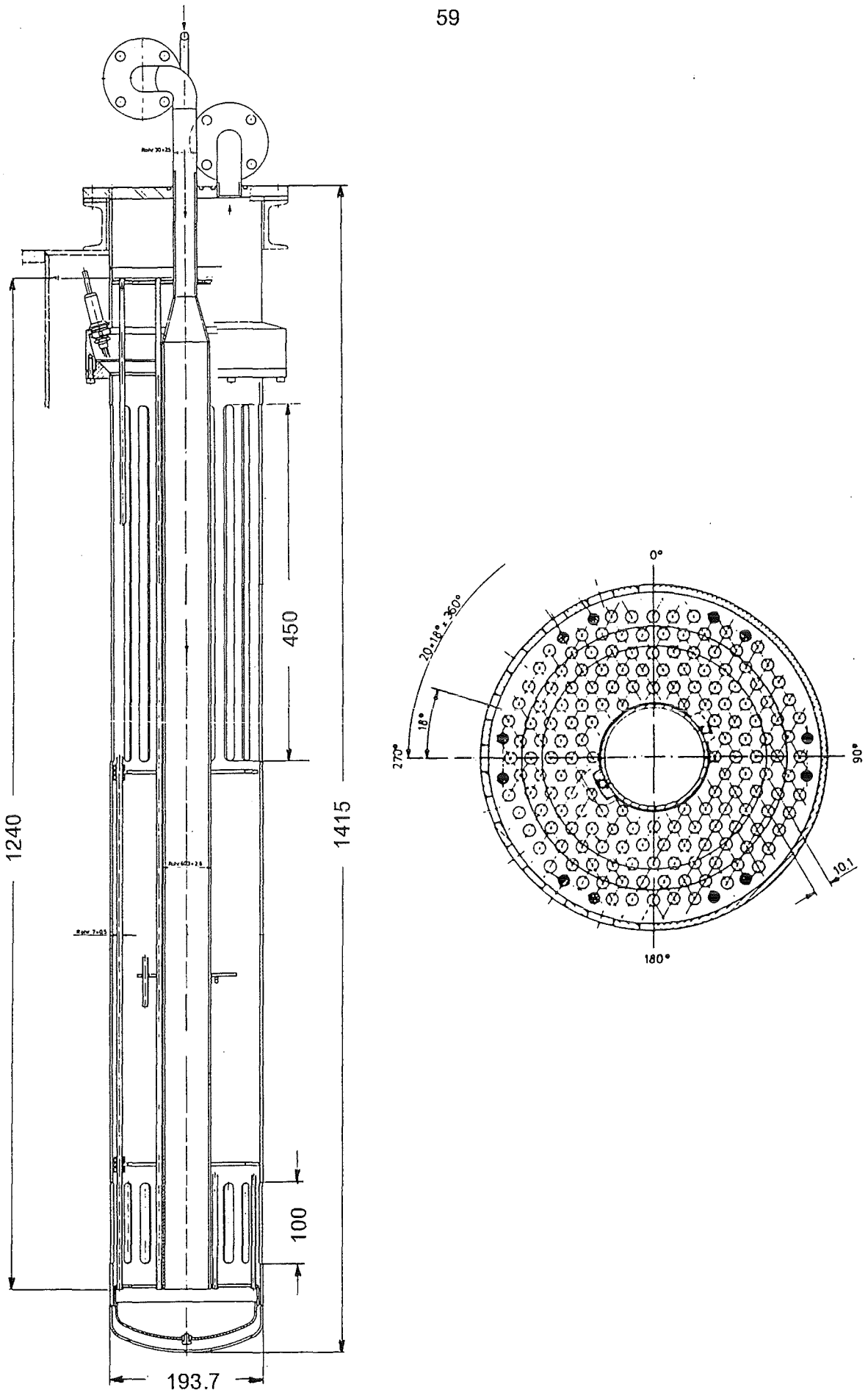

Fig. 16. Cross-section of the decay heat exchanger (dimensions in millimeter).

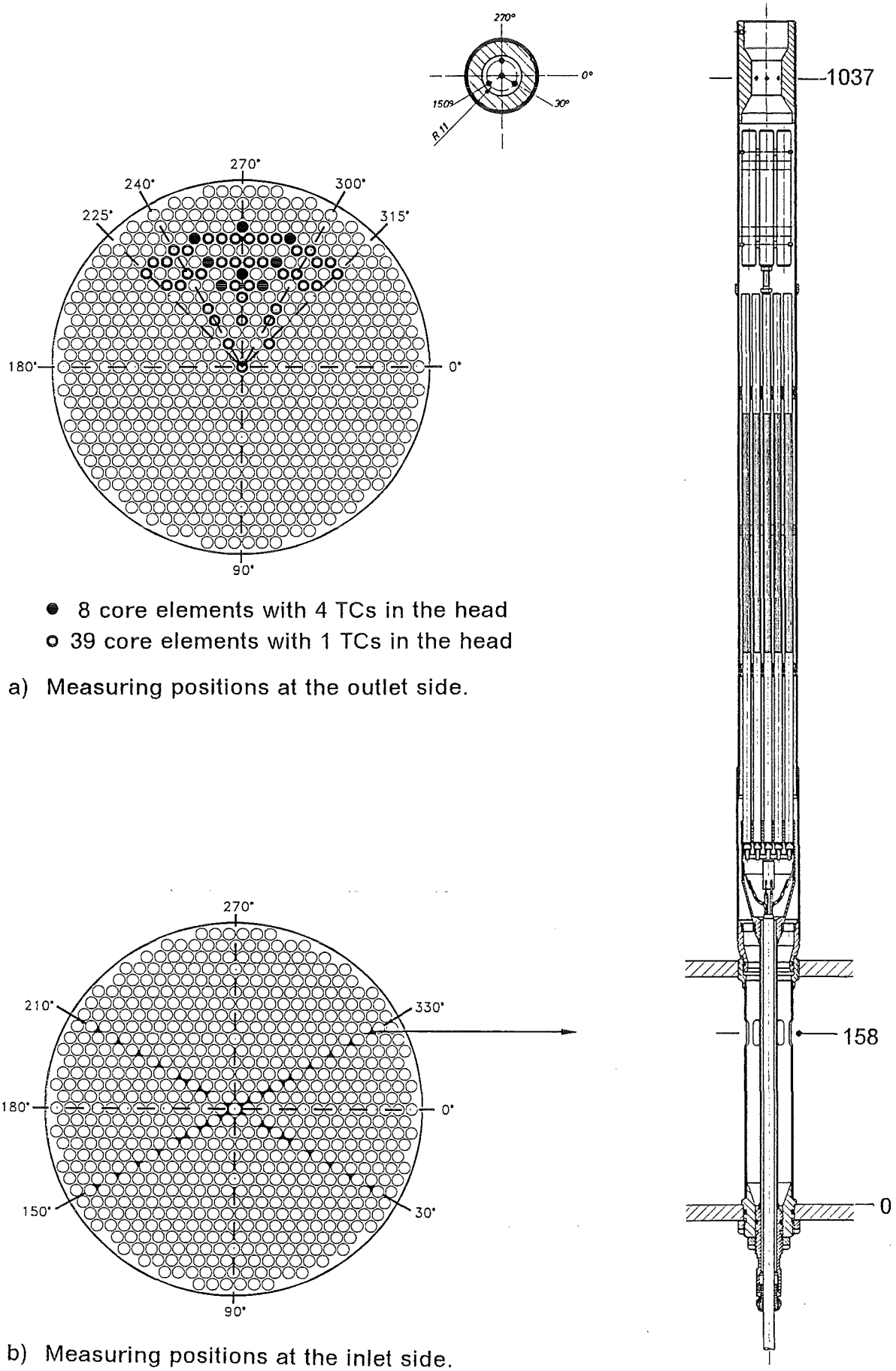

- 8 core elements with 4 TCs in the head
- 39 core elements with 1 TCs in the head

a) Measuring positions at the outlet side.

b) Measuring positions at the inlet side.

Fig. 17. Instrumentation of the core elements at the inlet and outlet side (dimensions in millimeter).

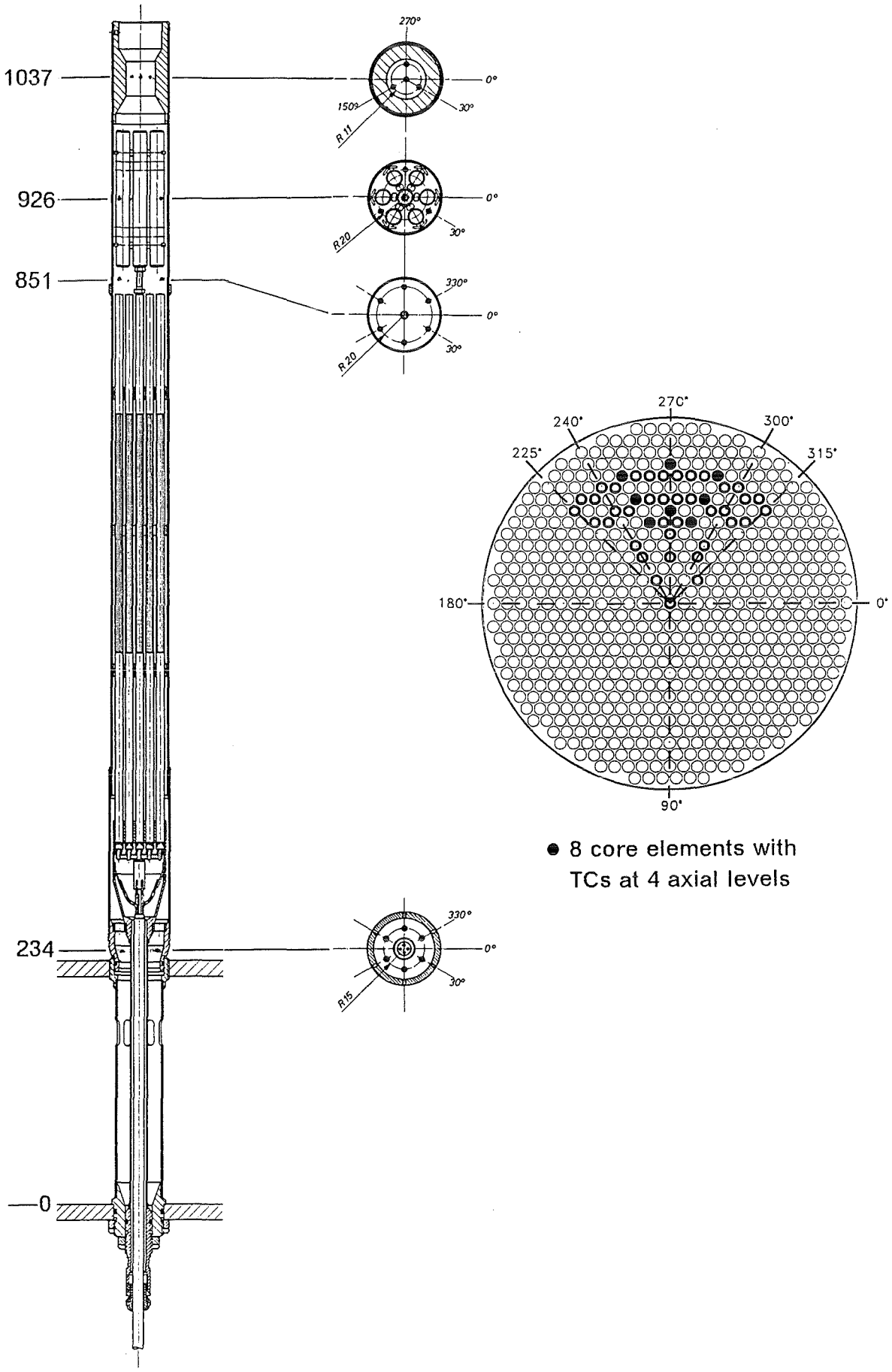

Fig. 18. Instrumentation inside the core element (dimensions in millimeter).

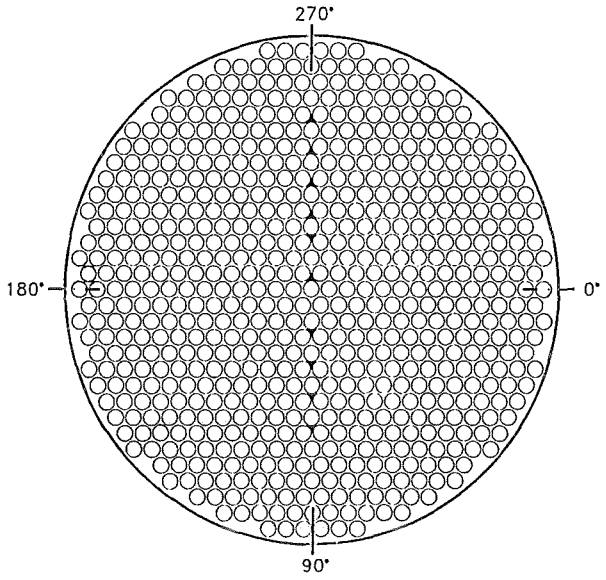

a) Radial positions

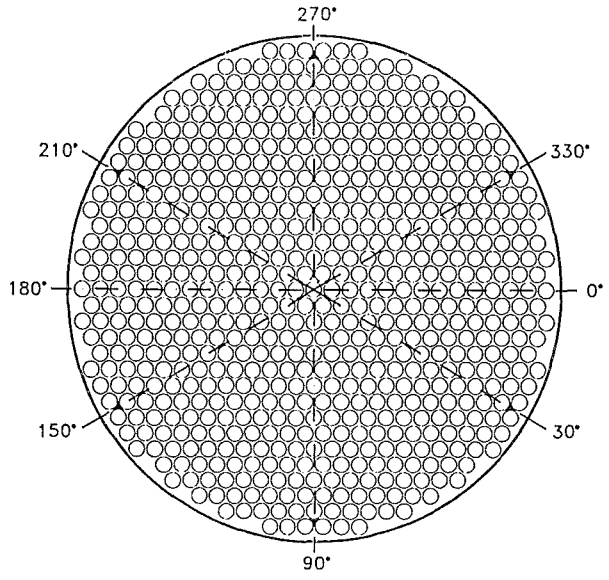

b) Peripheral positions

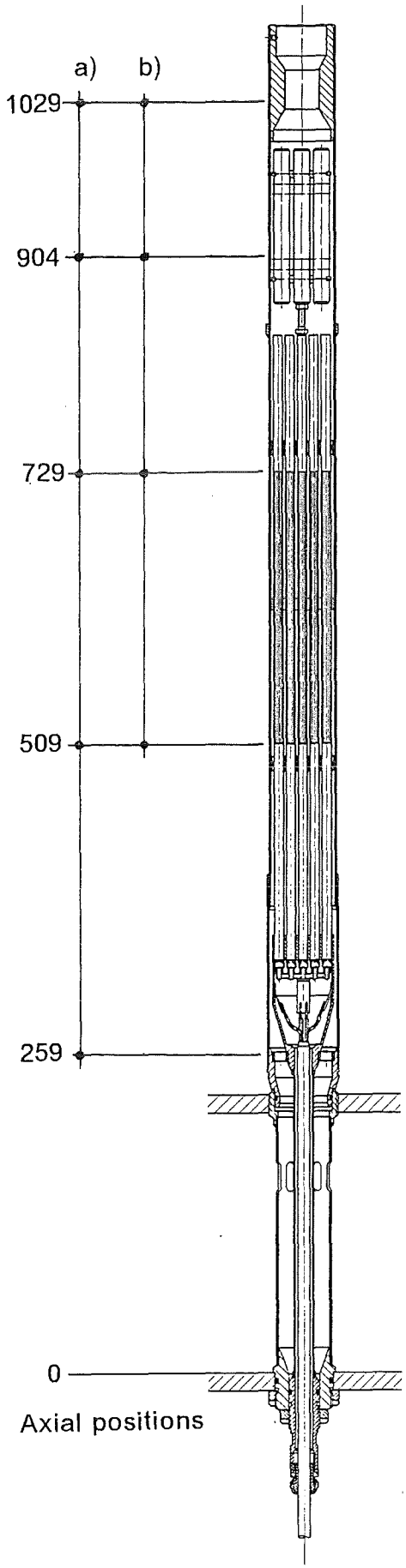

c) Axial positions

Fig. 19. Instrumentation of the interwrapper space (dimensions in millimeter).

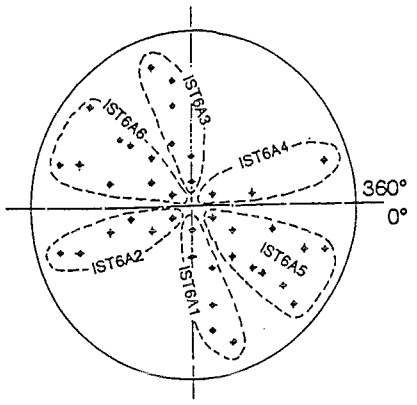

a) Horizontal position of TC group (A).

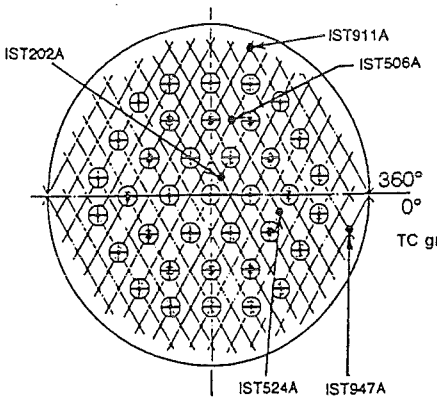

b) Axial position of TC group (B).

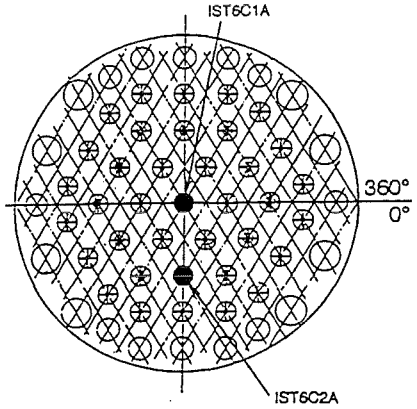

c) Axial position of TC group (C).

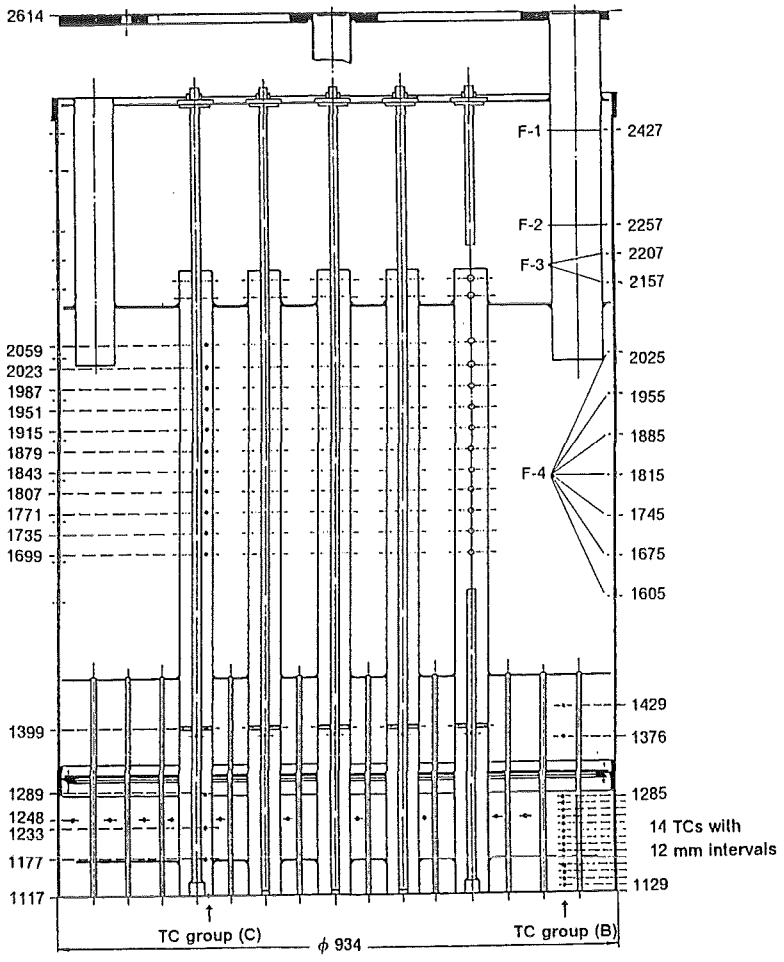

Permeable shell design (15.2%):

F-1: 1 row with 12 holes of ϕ 30 mm,
F-2: 1 row with 40 holes of ϕ 40 mm,
F-3: 2 rows with 40 holes of ϕ 40 mm,
F-4: 7 rows with 36 holes of ϕ 40 mm

at equal intervals throughout the periphery.

Fig. 20. Instrumentation of the above core structure (dimensions in millimeter).

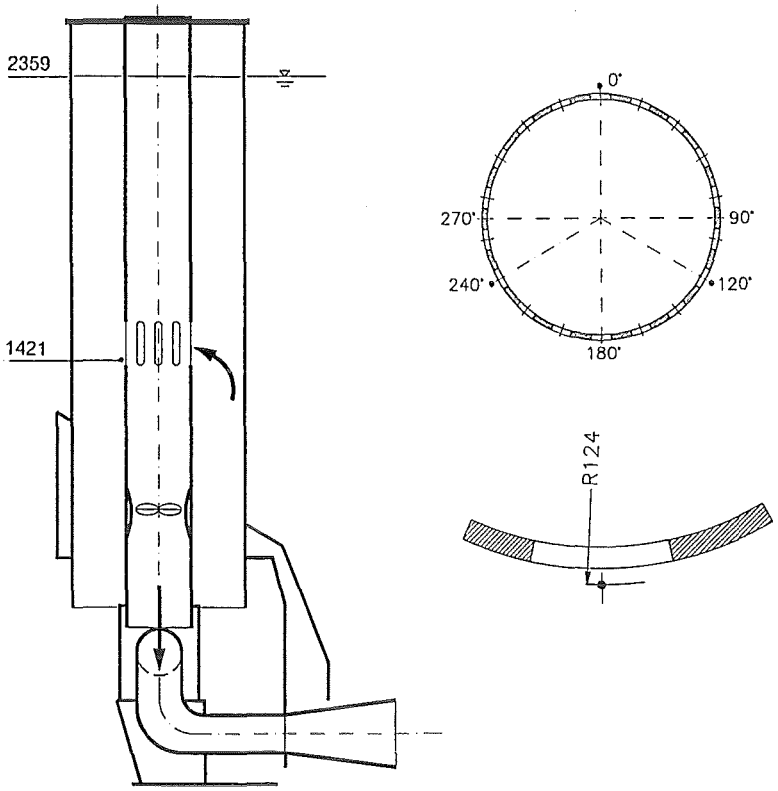

Fig. 21. Instrumentation of the primary pump (dimensions in millimeter).

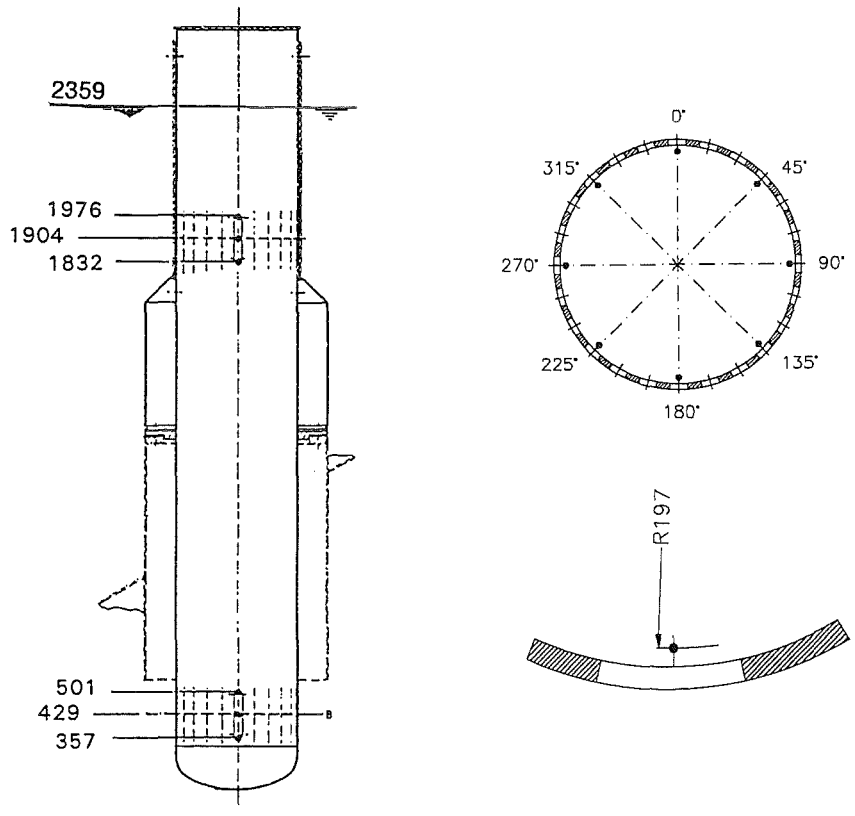

Fig. 22. Instrumentation of the intermediate heat exchanger (dimensions in millimeter).

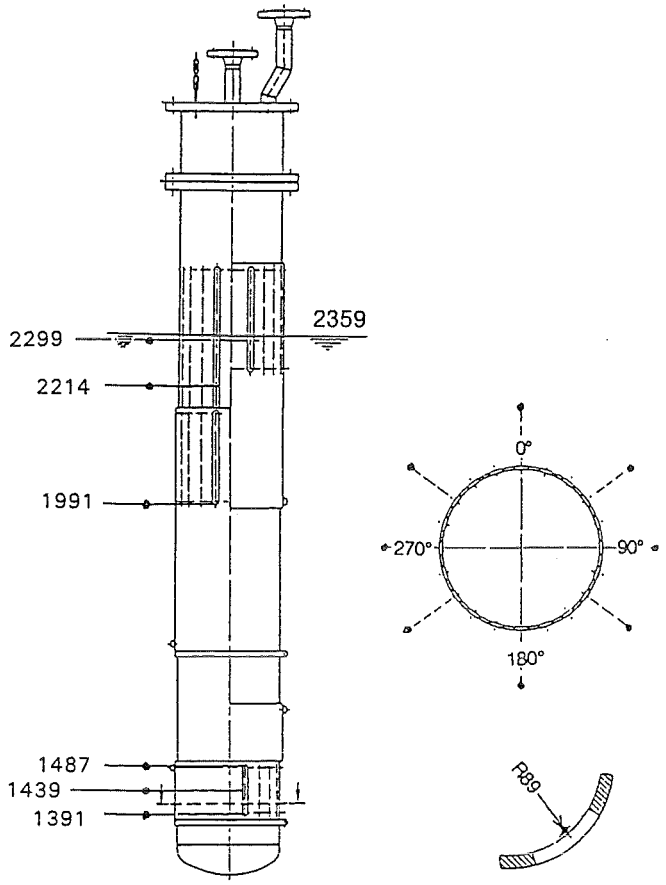

Fig. 23. Instrumentation of the decay heat exchanger (dimensions in millimeter).

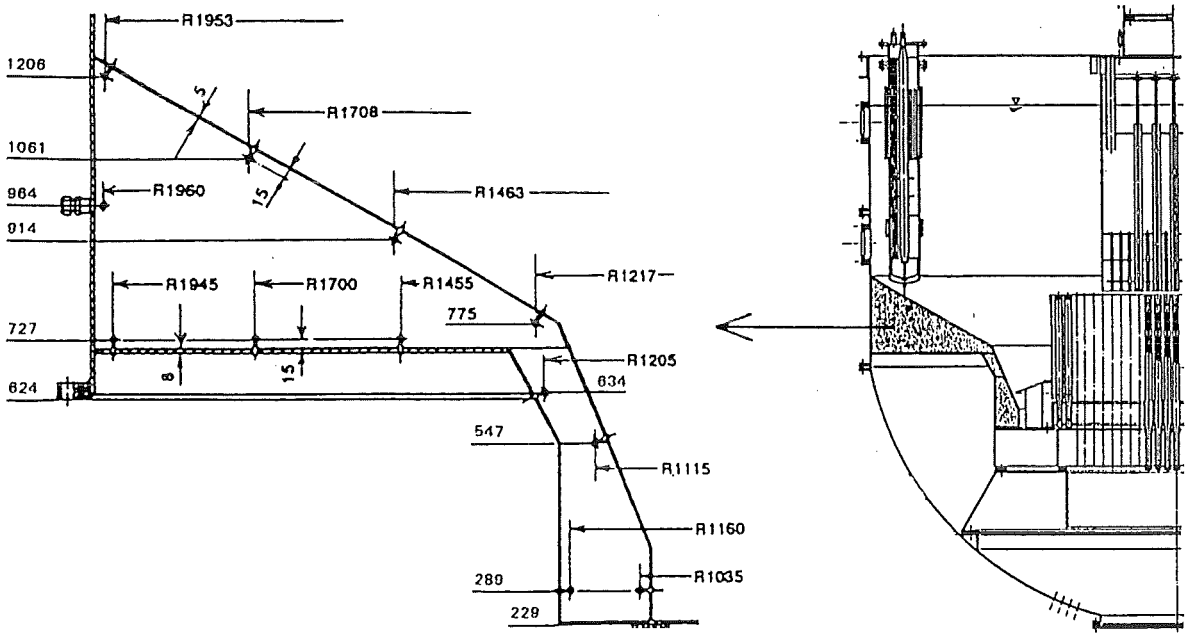

Fig. 24. Instrumentation of the intermediate plenum (dimensions in millimeter).

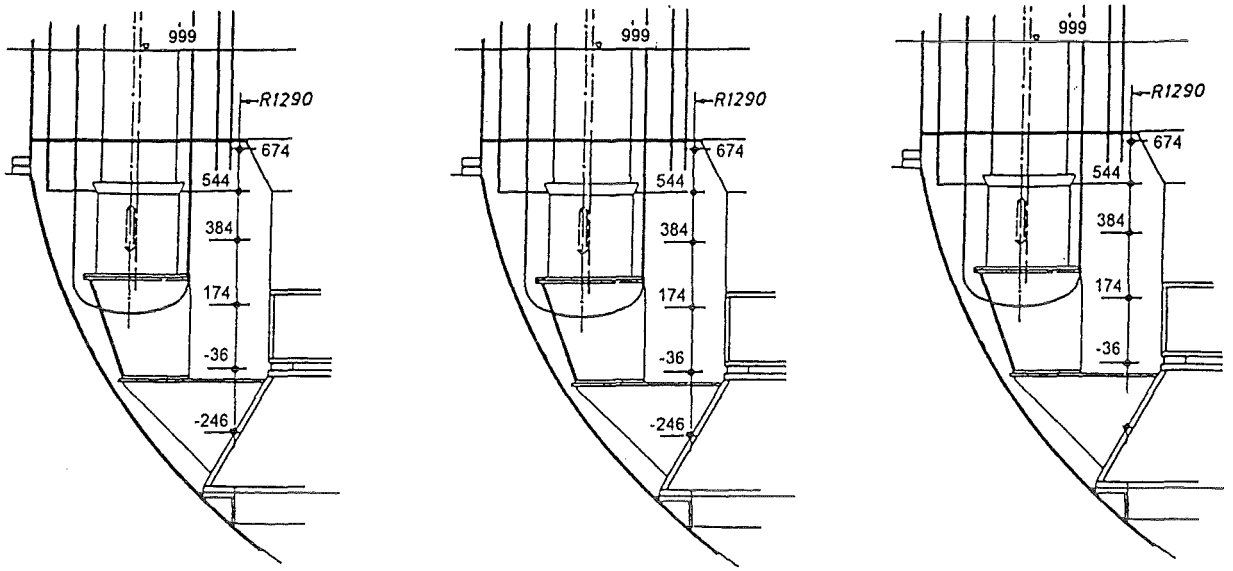

Angular position of 0° Angular position of 270° Angular position of 225°

a) Axial measuring traverse.

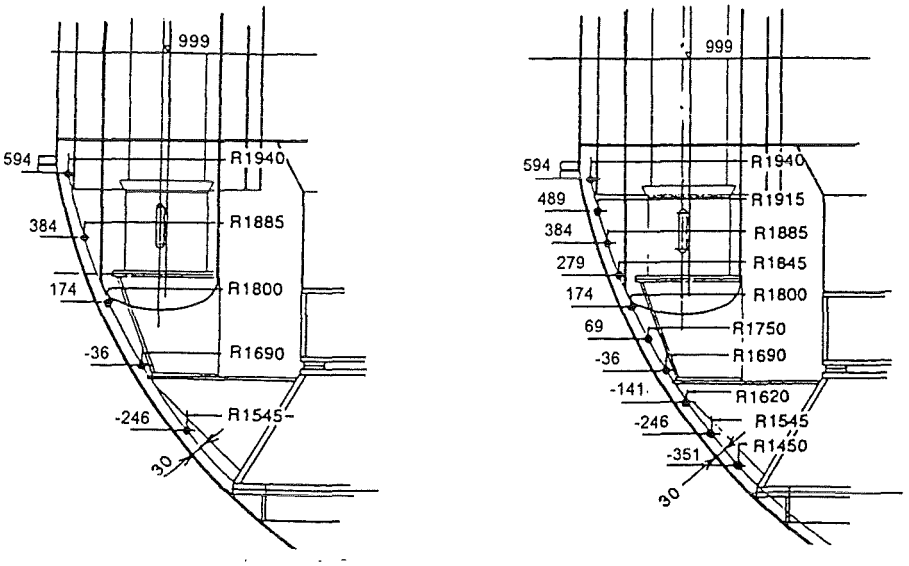

Angular position of 249° Angular positions of 90°, 180°, and 270°

b) Measuring positions along the wall of the vessel.

Fig. 25. Instrumentation of the lower plenum (dimensions in millimeter).

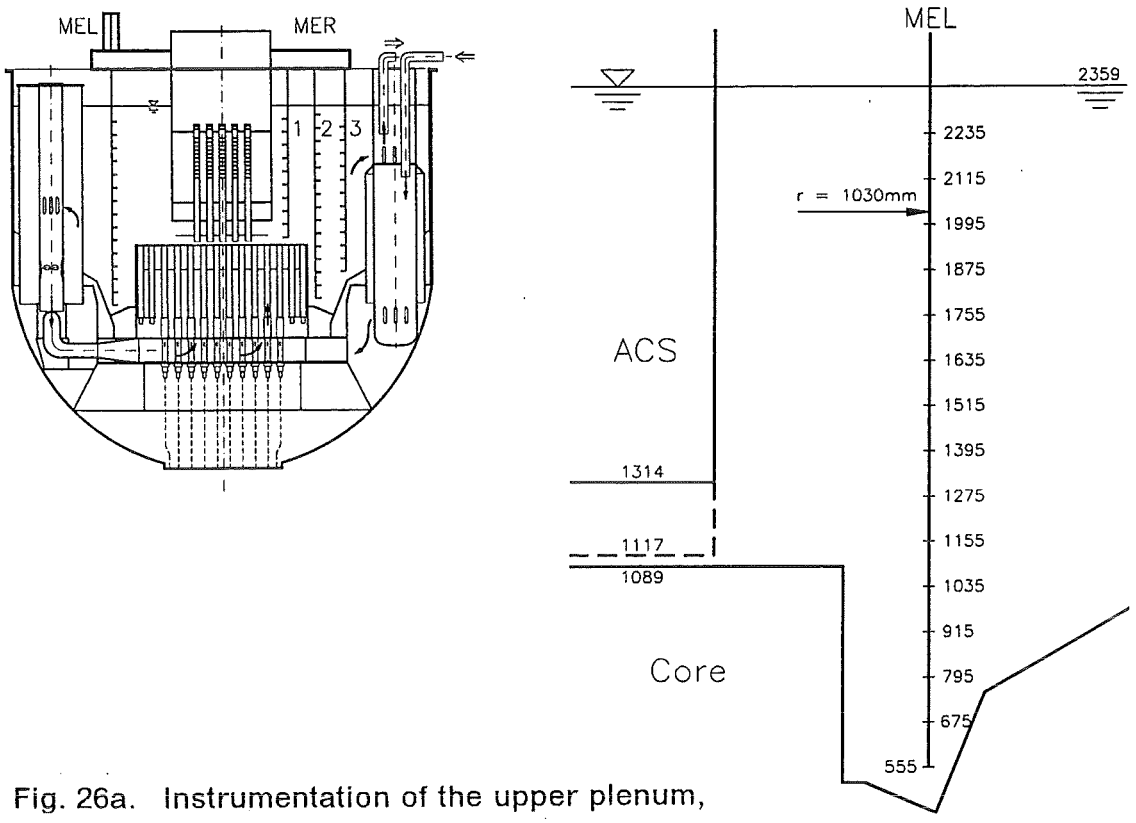

Fig. 26a. Instrumentation of the upper plenum, MEL device (dimensions in millimeter).

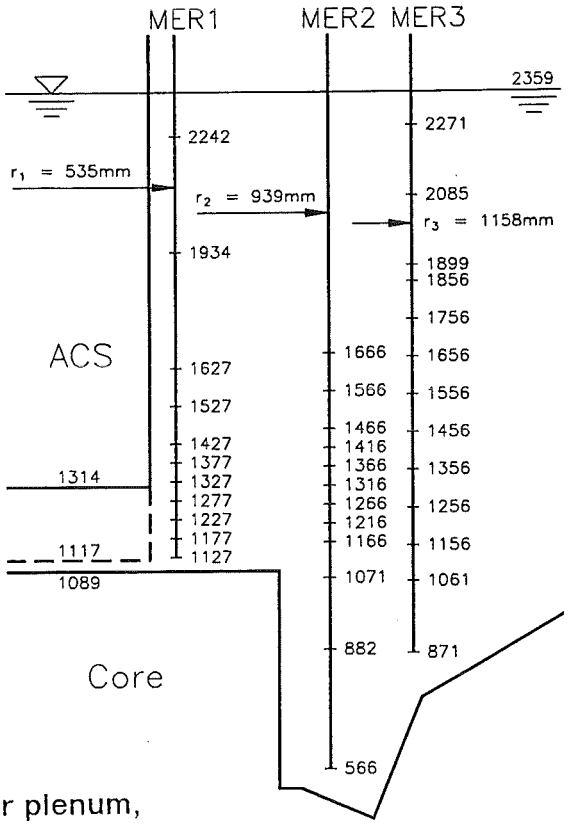

Fig. 26b. Instrumentation of the upper plenum, MER device (dimensions in millimeter).

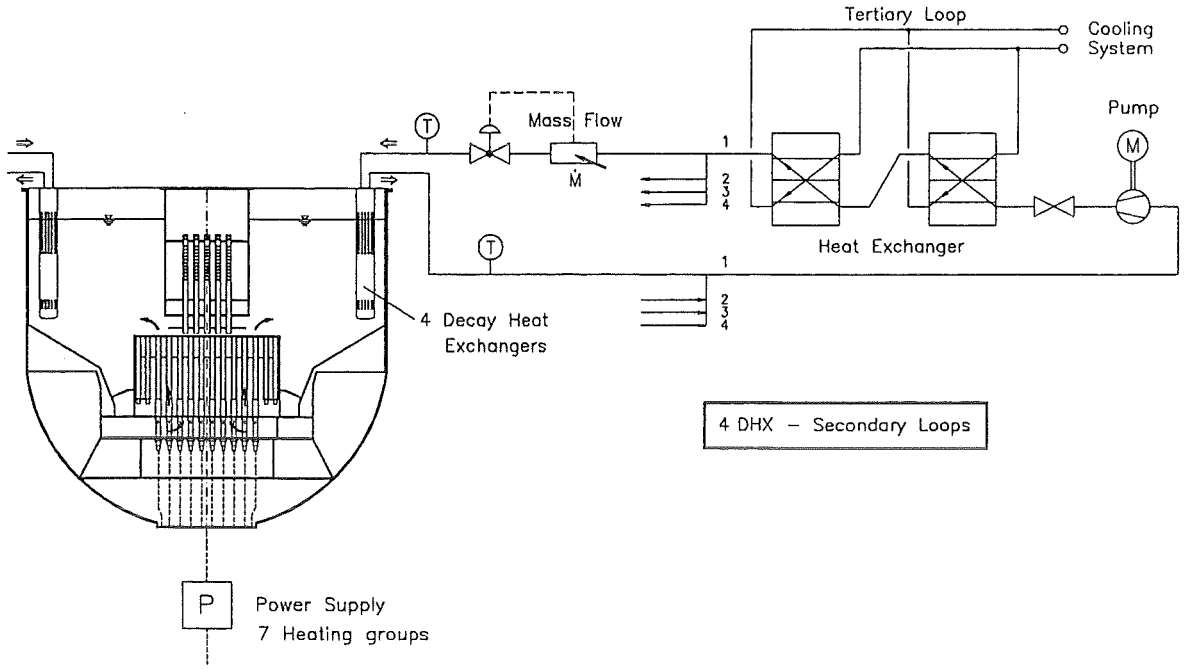

Fig. 27. Instrumentation of the DHX circuits at the secondary sides.

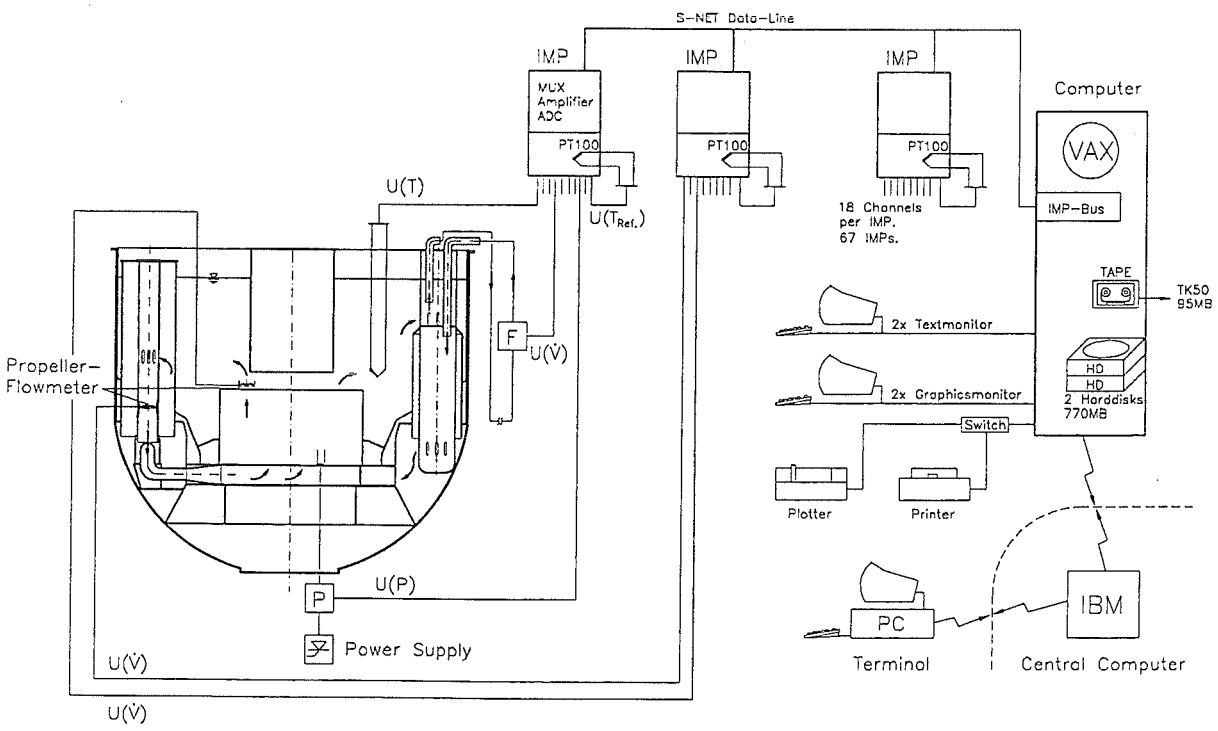

Fig. 28. Schematic of the data acquisition and test control system.

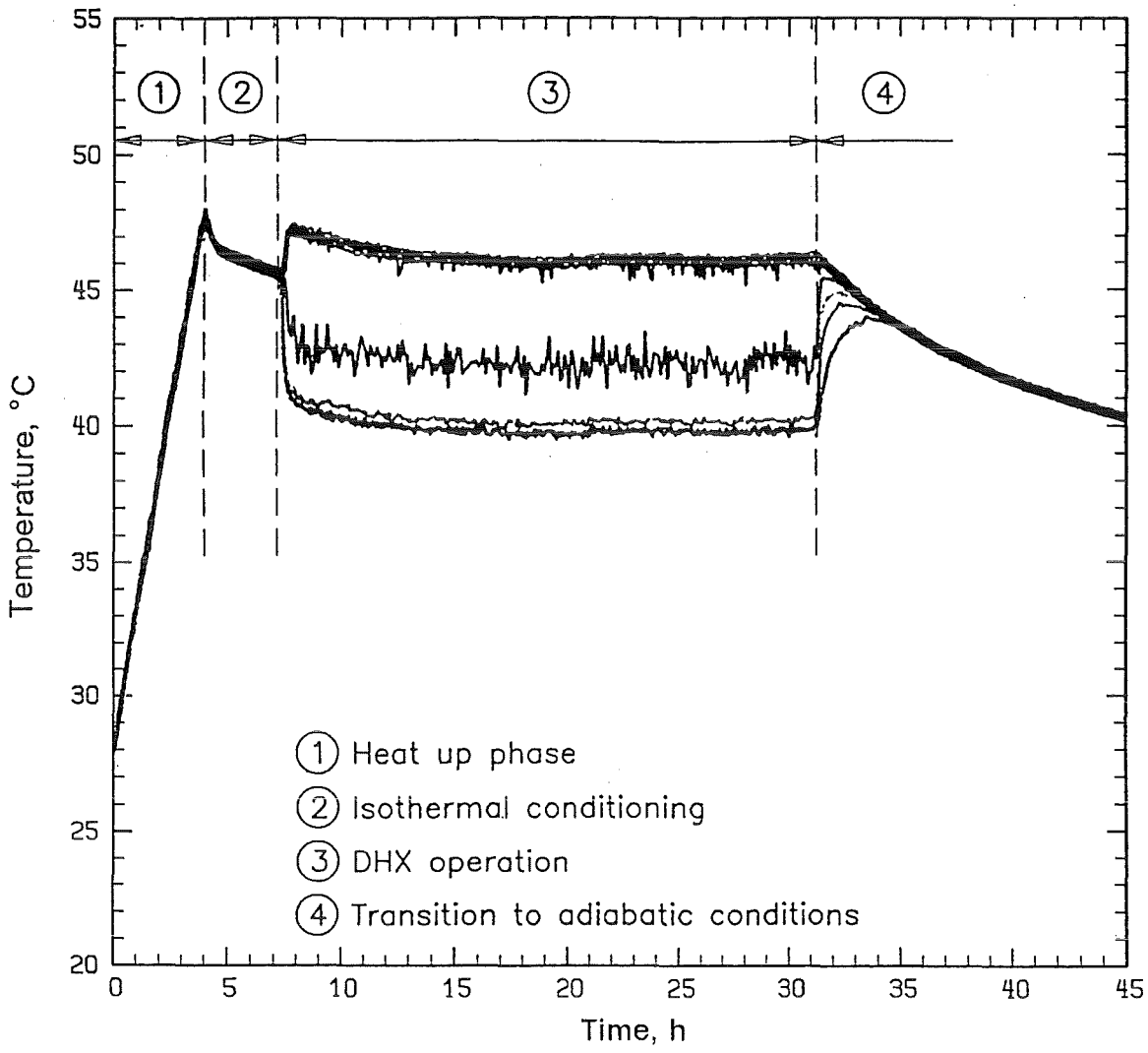

Fig. 29. Transient temperatures of test T02 measured in the UP along the MEL device (r = 1,030 mm and ϕ = 270°).

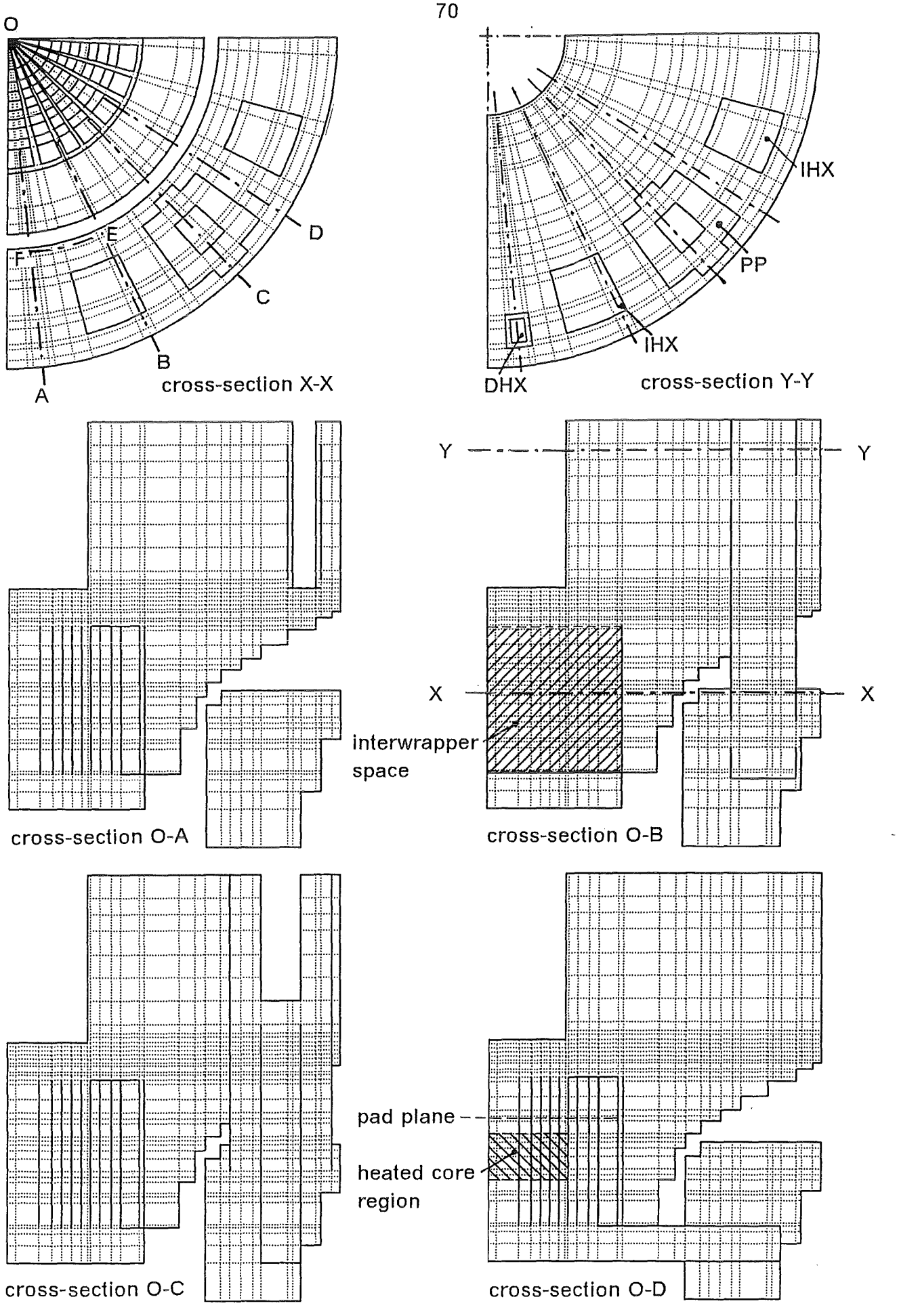

Fig. 30. Nodalization of the NEPTUN geometry.

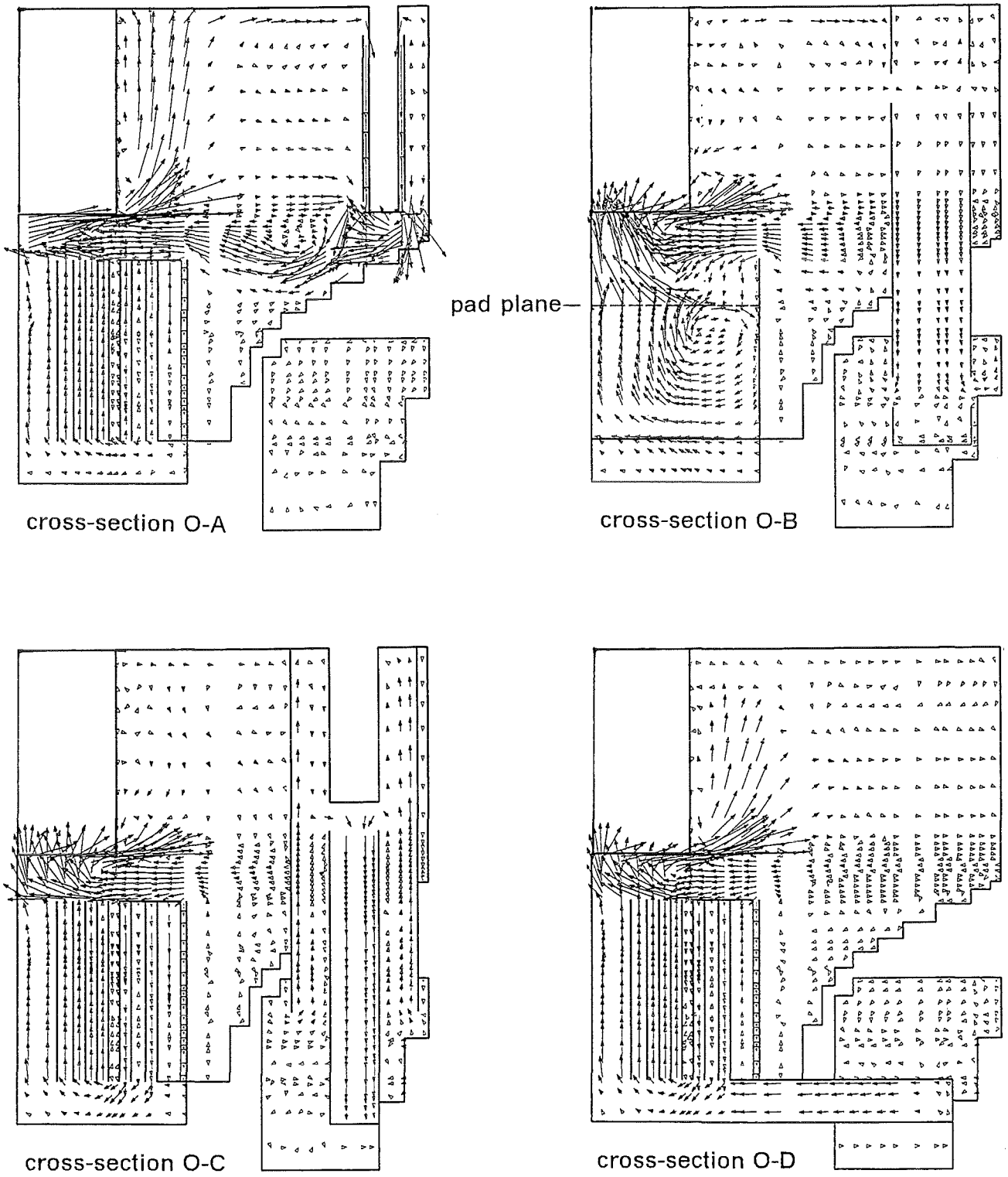

Fig. 31. Computed velocity fields of test T02.

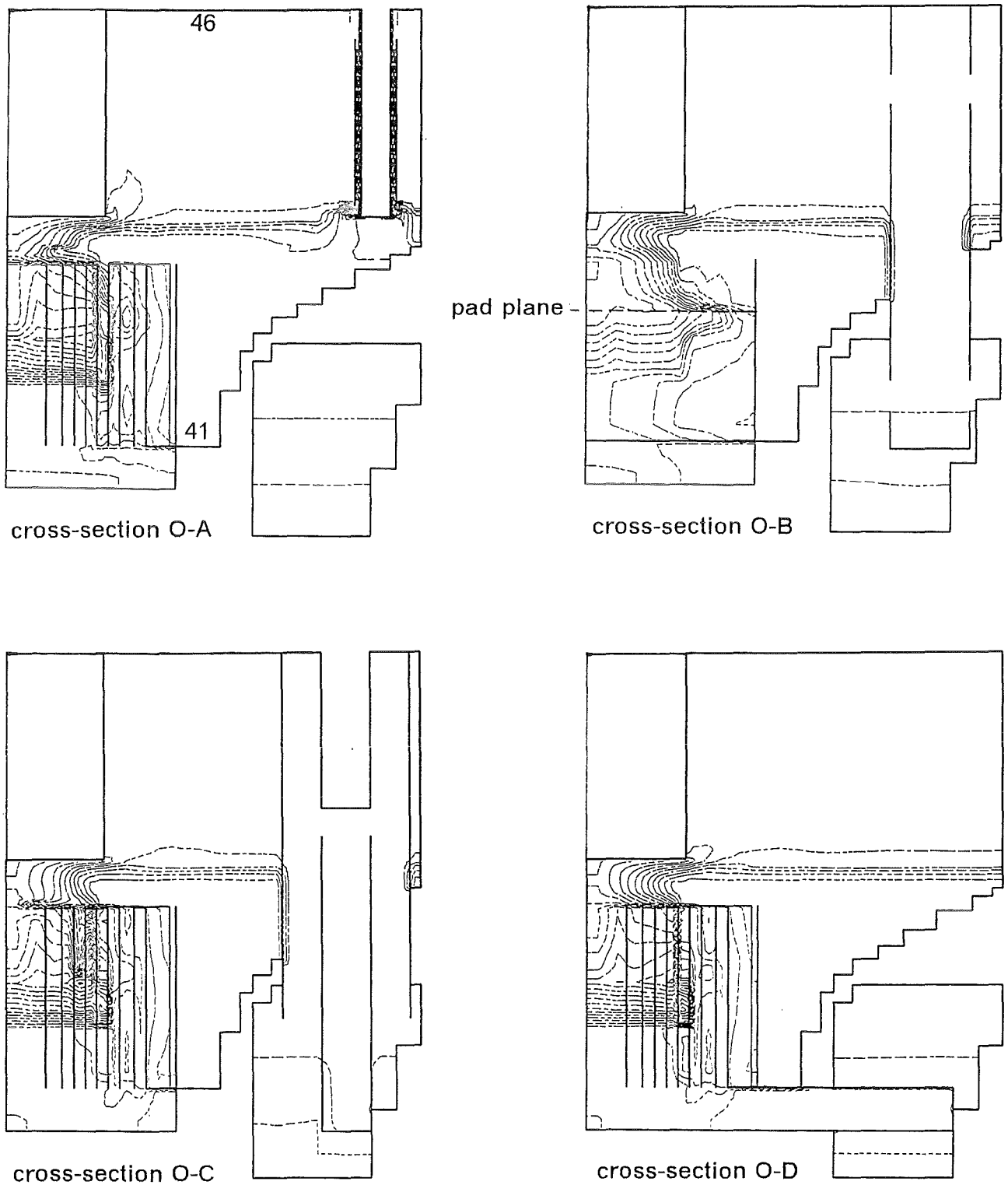

Fig. 32. Computed isotherm fields of test T02.

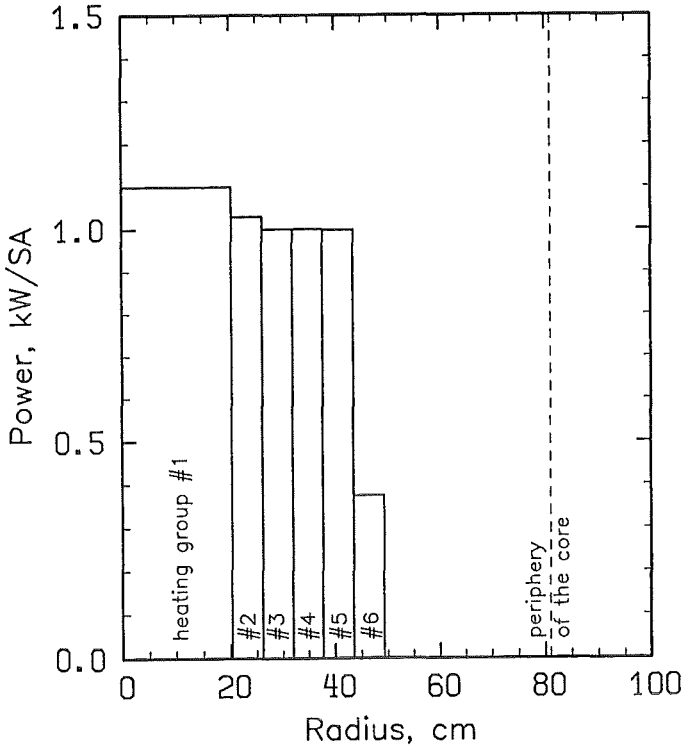

Fig. 33. Radial power profile, test T02.

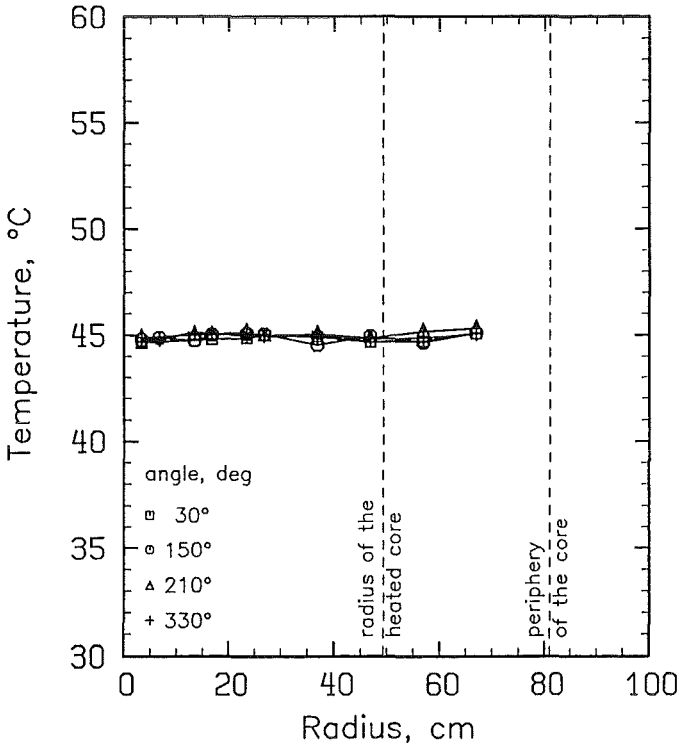

Fig. 34. Radial temperature profiles of the coolant measured at the SA inlet sides, test T02.

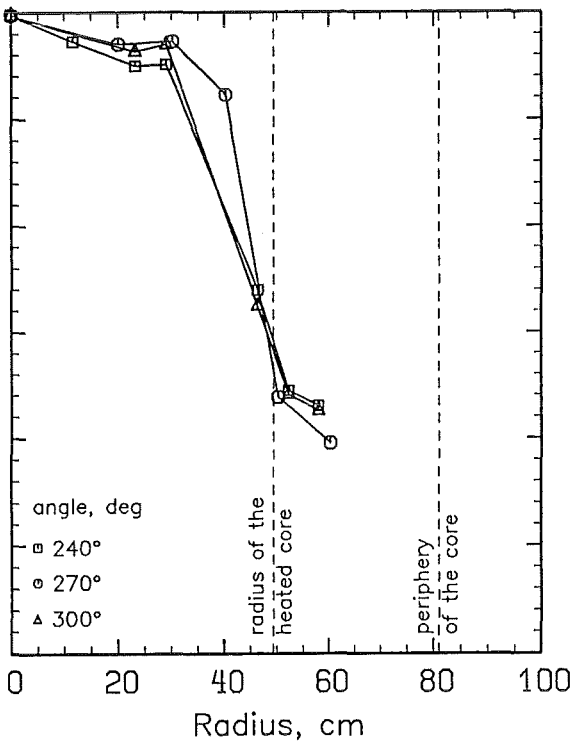

Fig. 35. Radial temperature profiles of the coolant measured at the SA outlet sides, test T02.

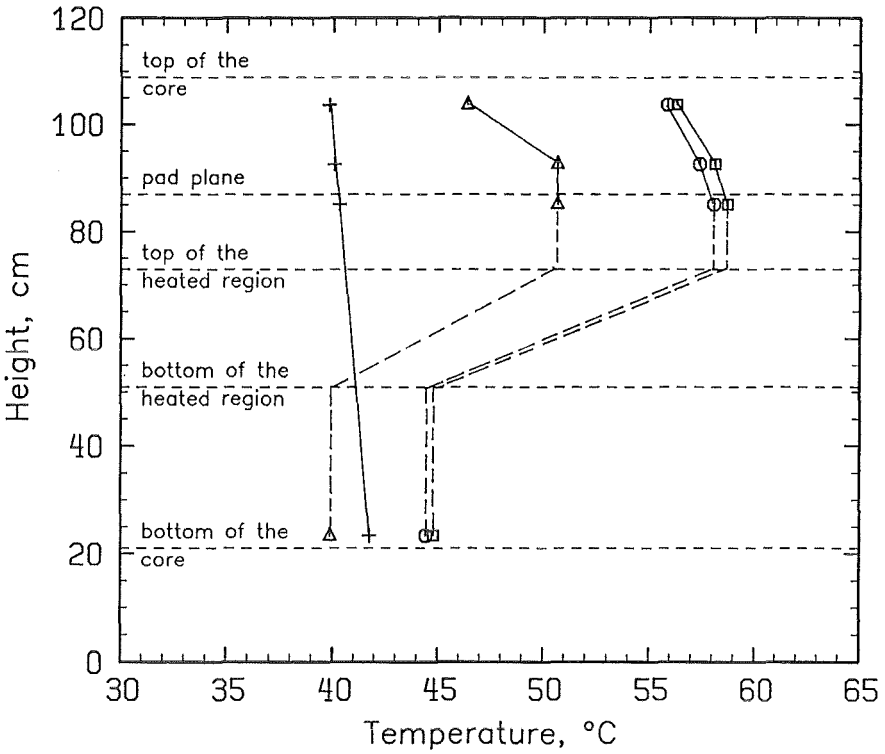

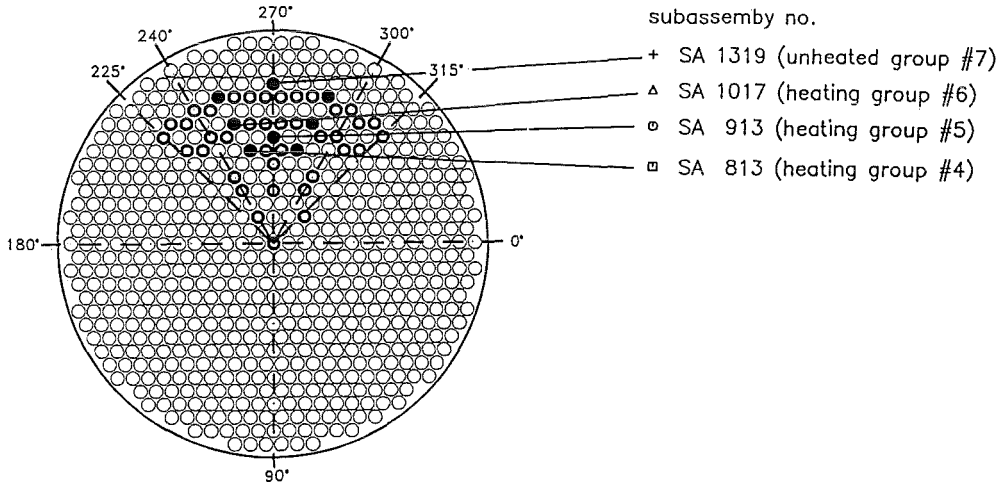

Fig. 36. Axial temperature profiles of the coolant measured inside SAs with different power suppply, test T02.

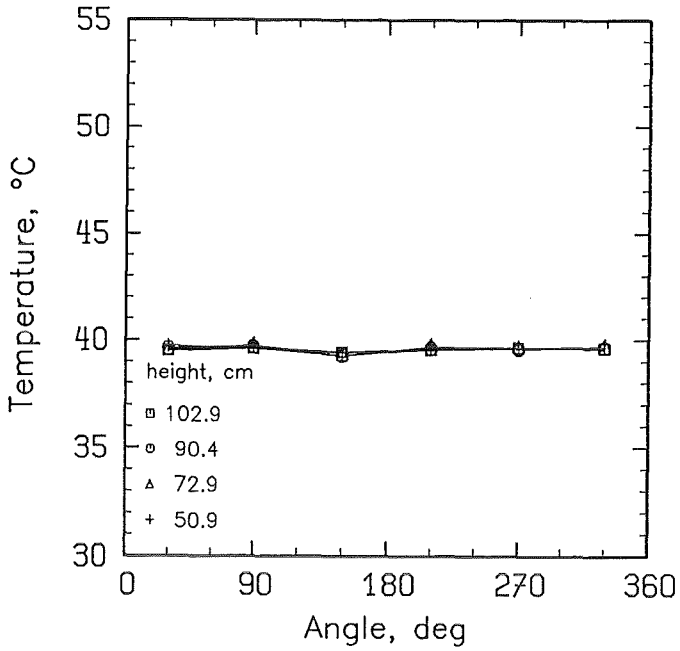

Fig. 37. Azimuthal temperature profiles of the interstitial flow measured at the periphery of the core, test T02.

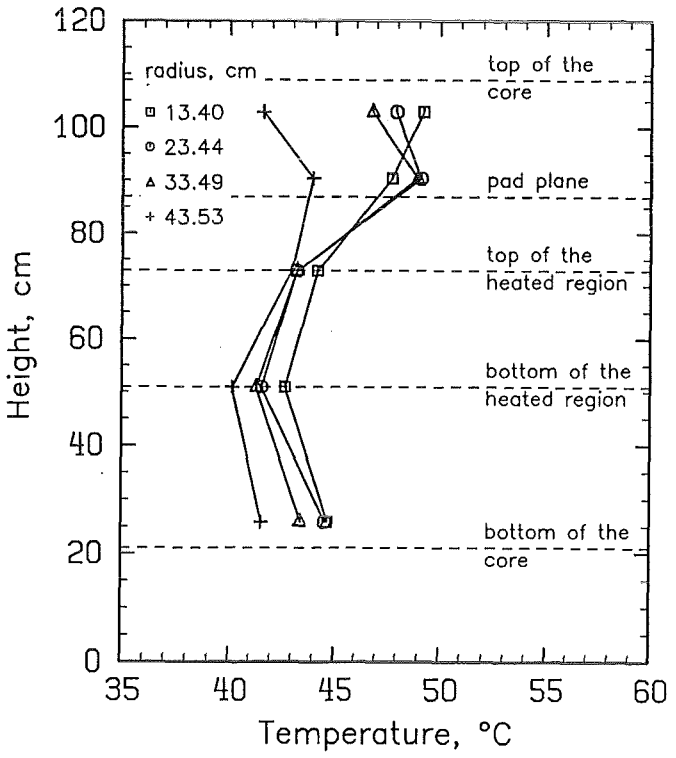

Fig. 38. Axial temperature profiles of the interstitial flow measured at different radial positions, core center → 90° point, test T02.

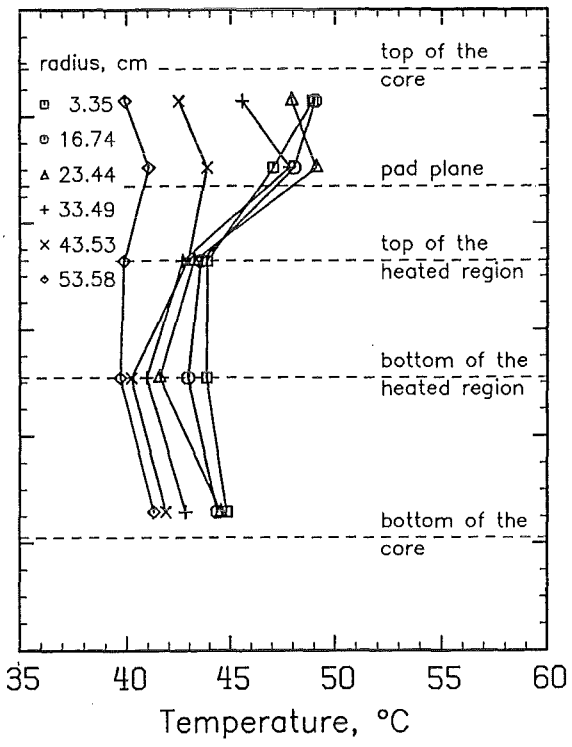

Fig. 39. Axial temperature profiles of the interstitial flow measured at different radial positions, core center → 270° point, test T02.

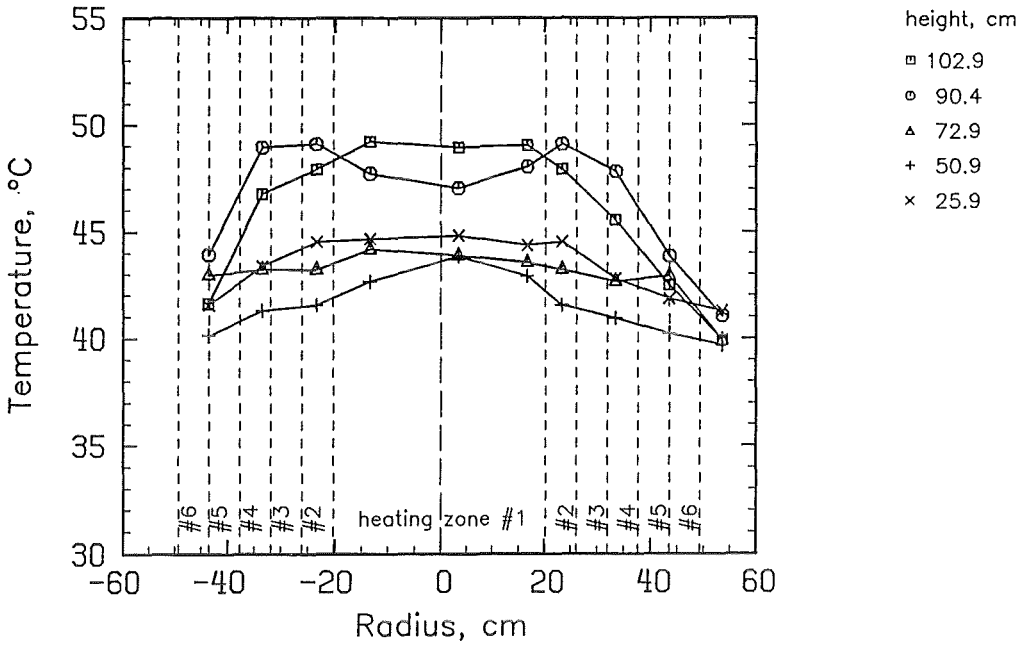

Fig. 40. Radial temperature profiles of the interstitial flow measured across the core, 90° point → 270° point, test T02.

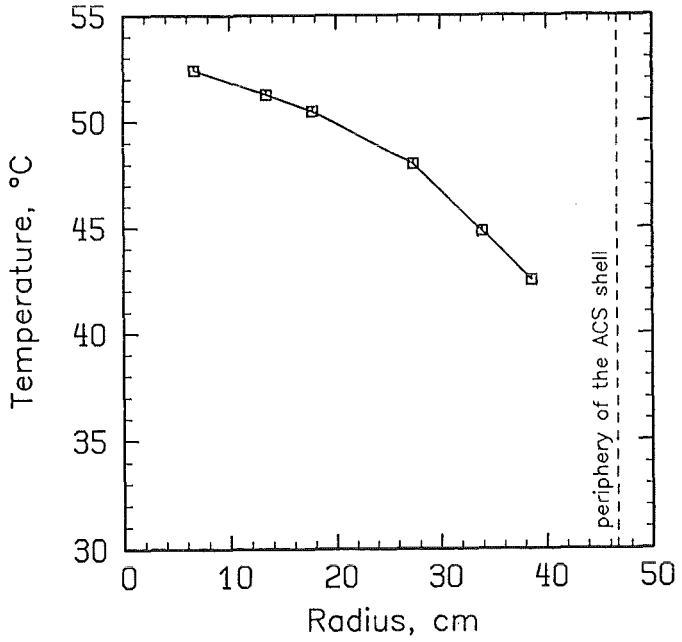

Fig. 41. Radial temperature profile measured at the bottom end of the ACS, test T02.

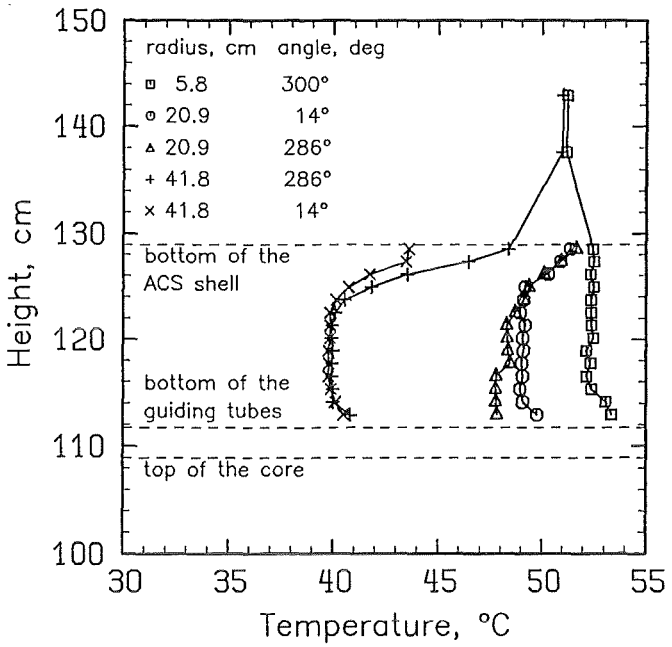

Fig. 42. Axial temperature profiles measured at the bottom end and inside the lower part of the ACS, test T02.

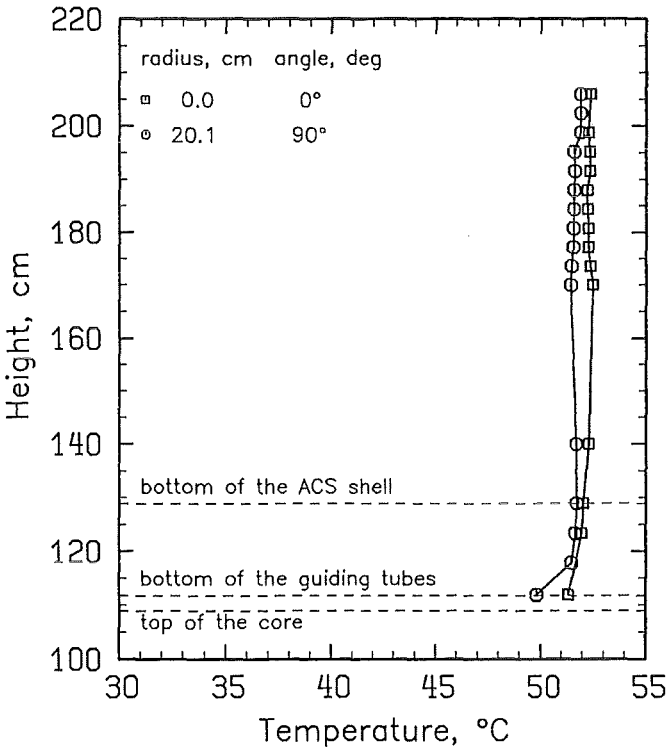

Fig. 43. Axial temperature profiles measured inside the ACS, test T02.

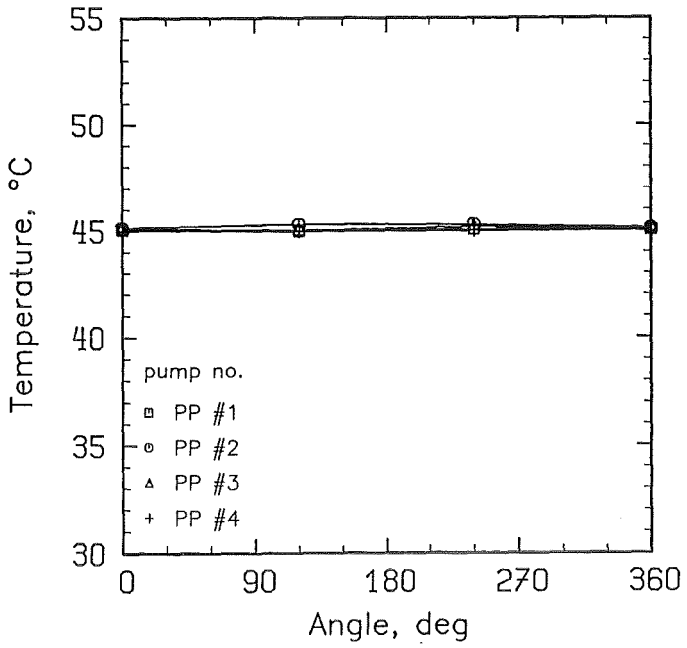

Fig. 44. Azimuthal temperature profiles measured at the inlet windows of the PPs (z = 1,421 mm), test T02.

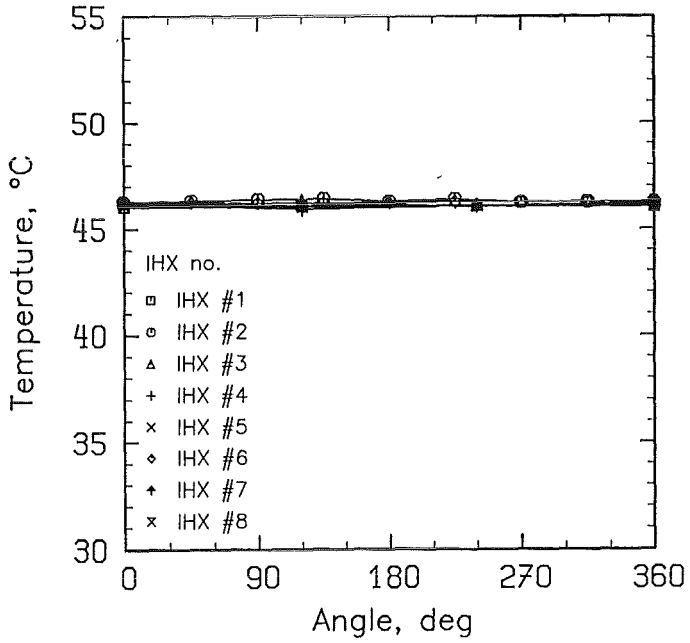

Fig. 45. Azimuthal temperature profiles measured at the inlet windows of the IHX primary loops (z = 1,904 mm), test T02.

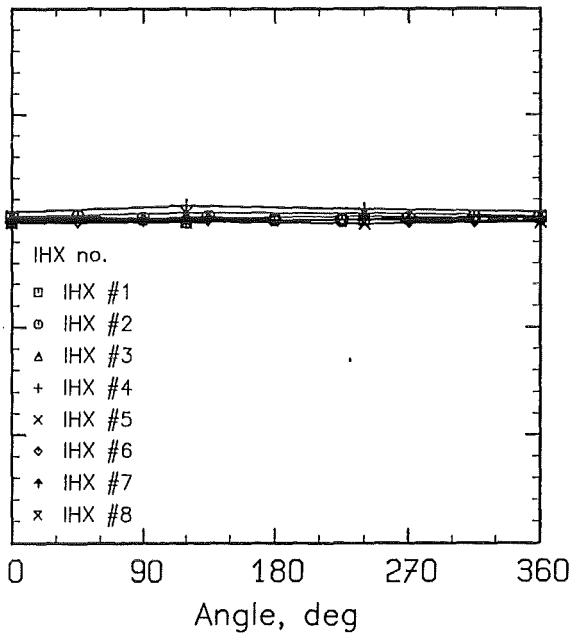

Fig. 46. Azimuthal temperature profiles measured at the outlet windows of the IHX primary loops (z = 429 mm), test T02.

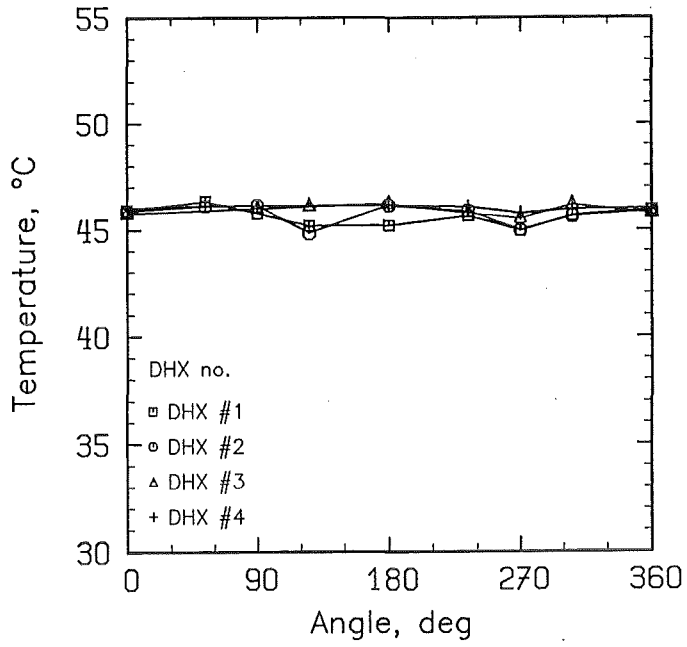

Fig. 47. Azimuthal temperature profiles measured at the inlet windows of the DHX primary loops (z = 2,300 mm), test T02.

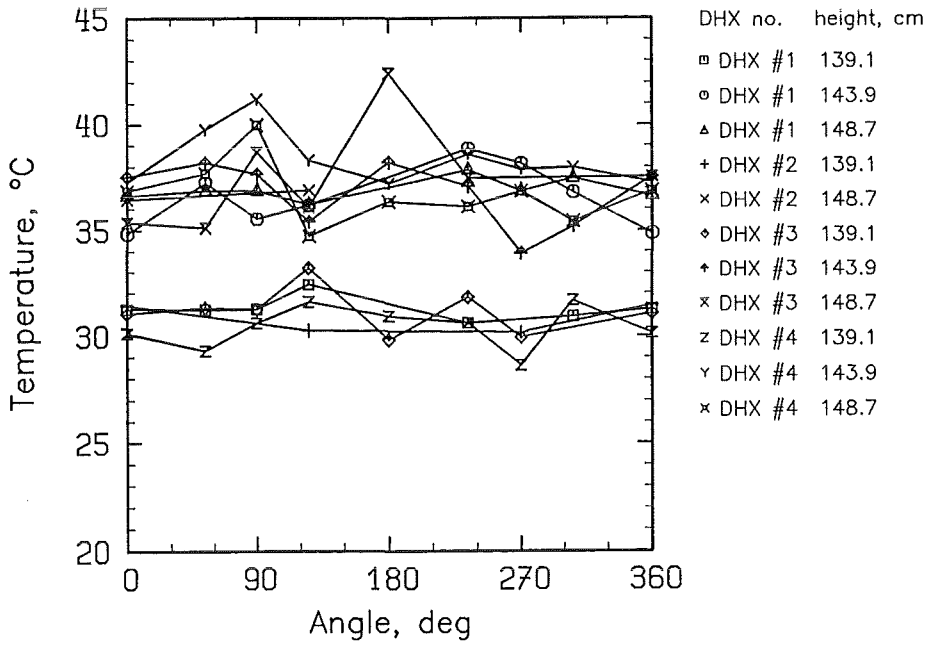

Fig. 48. Azimuthal temperature profiles measured at the outlet windows of the DHX primary loops, test T02.

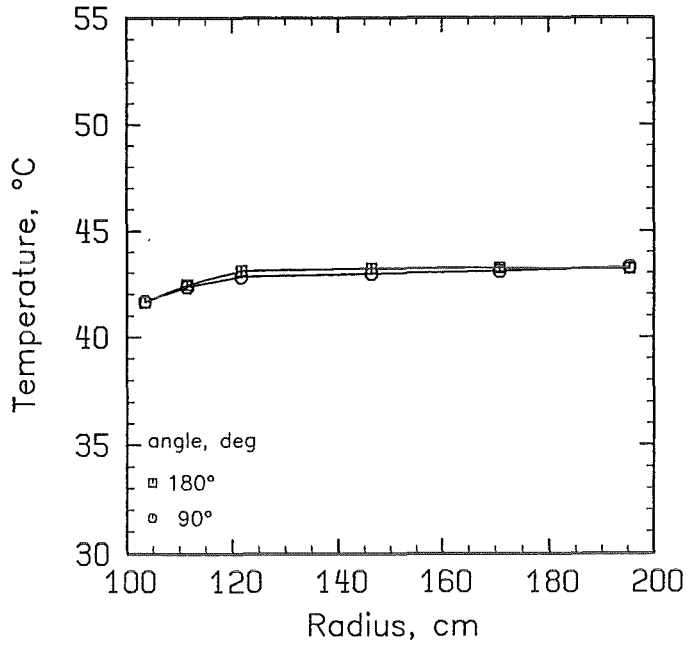

Fig. 49. Radial temperature profiles measured at the top end of the IP, test T02.

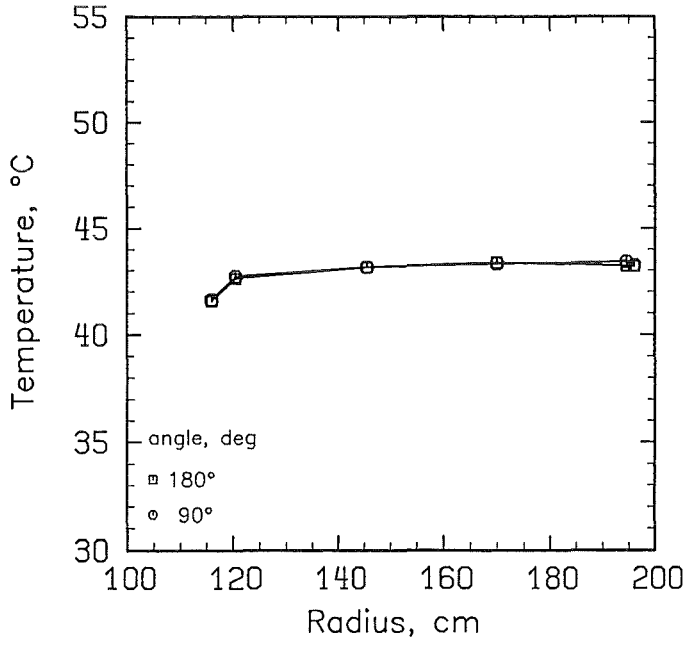

Fig. 50. Radial temperature profiles measured at the bottom end of the IP, test T02.

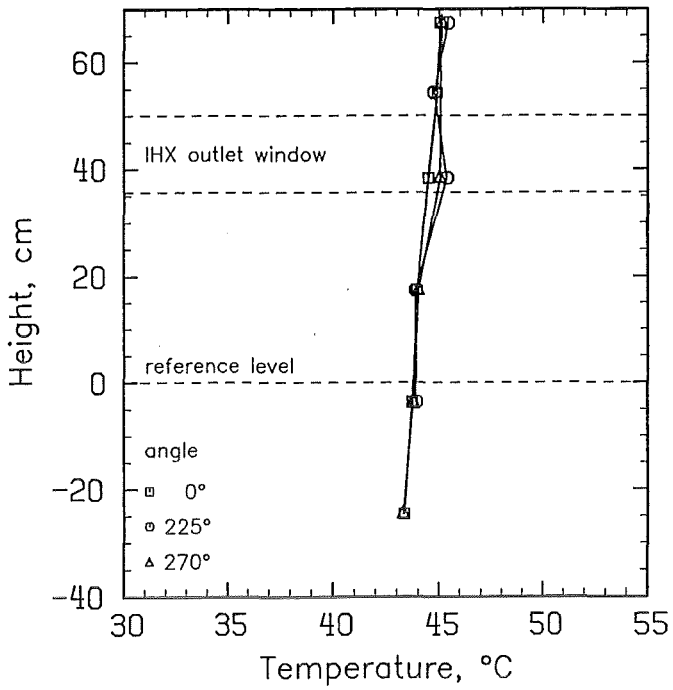

Fig. 51. Temperature profiles measured in the LP along a vertical traverse, test T02.

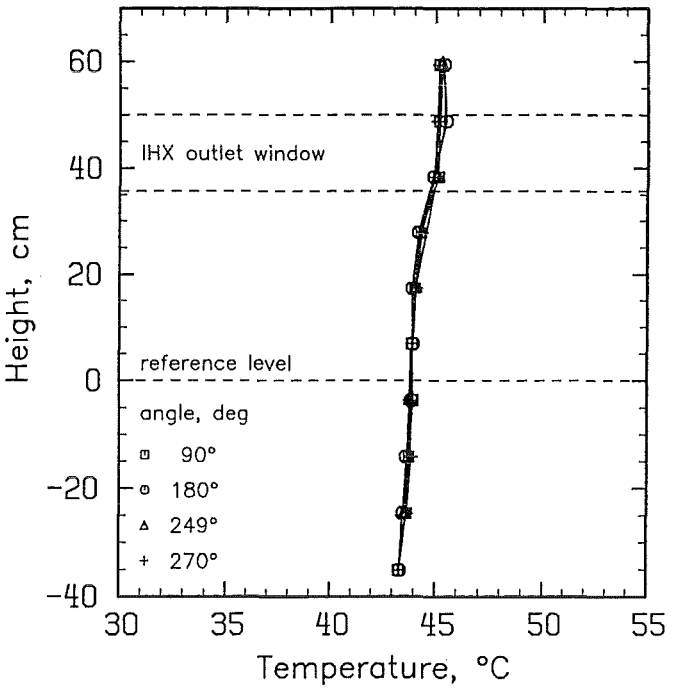

Fig. 52. Temperature profiles measured in the LP along the periphery of the tank, test T02.

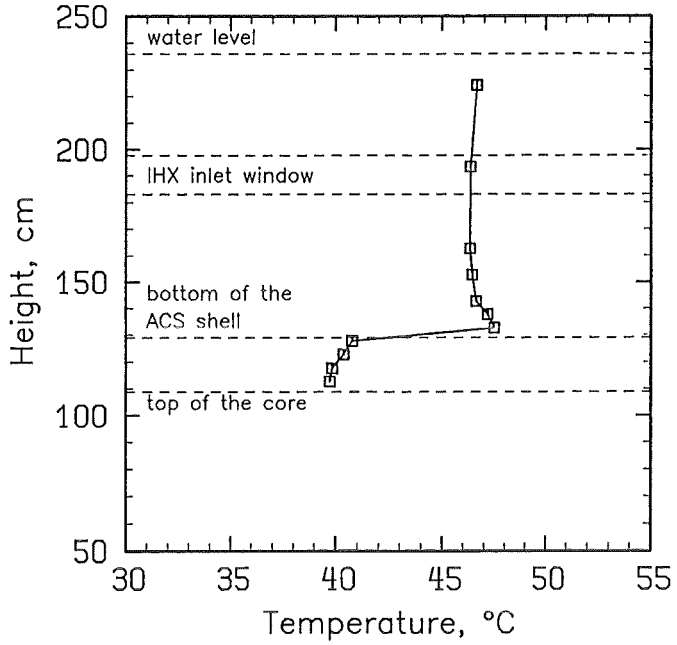

Fig. 53. Axial temperature profiles measured in the UP along MER-1, test T02.

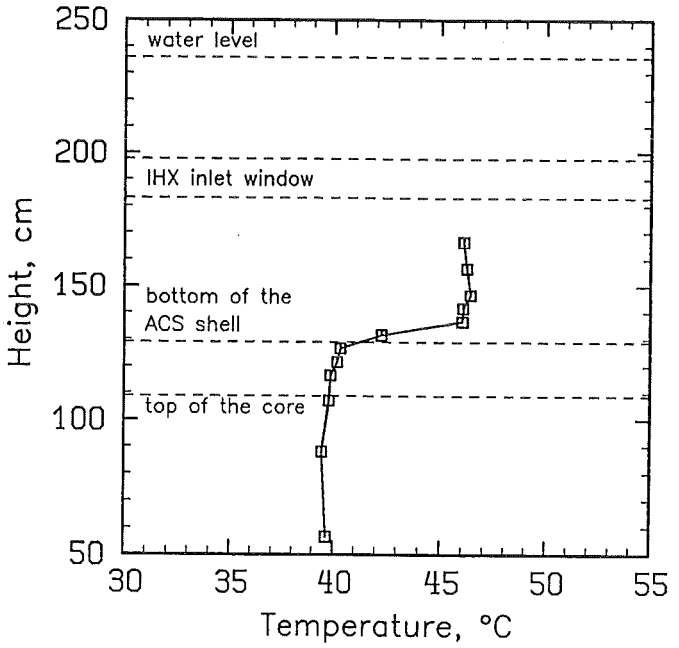

Fig. 54. Axial temperature profiles measured in the UP along MER-2, test T02.

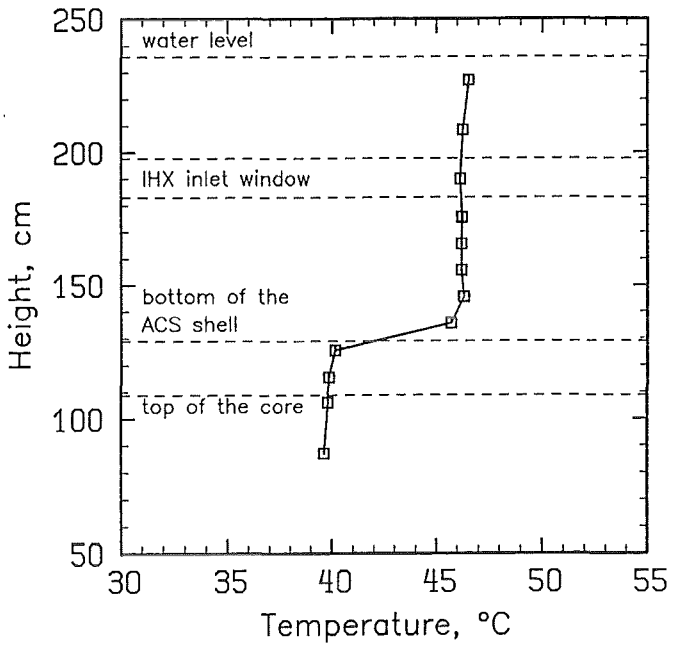

Fig. 55. Axial temperature profiles measured in the UP along MER-3, test T02.

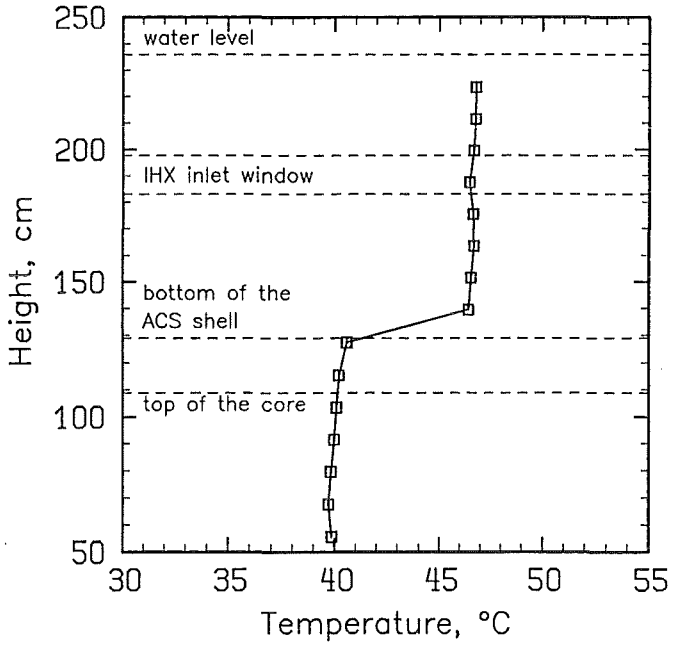

Fig. 56. Axial temperature profiles measured in the UP along MEL, test T02.

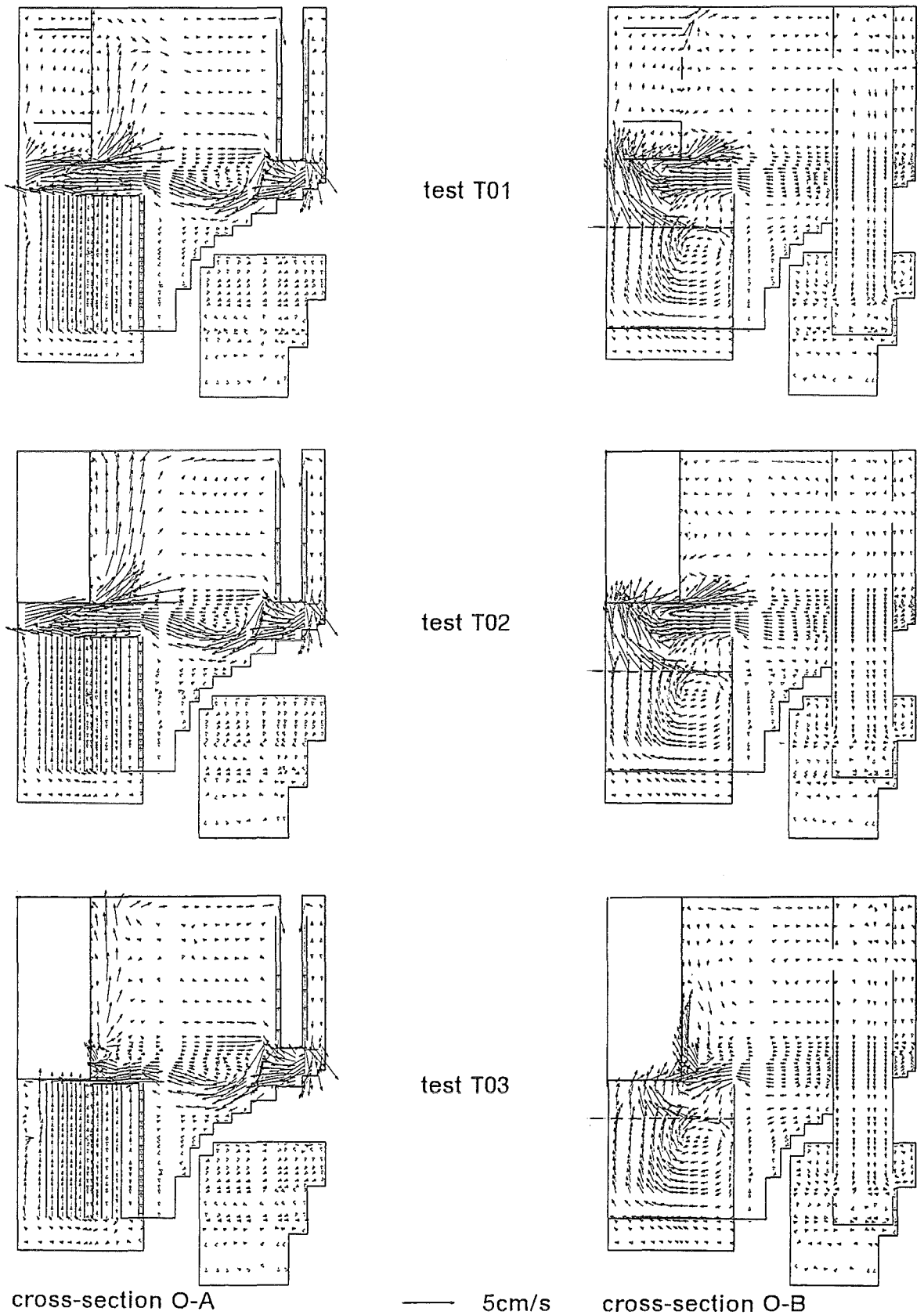

Fig. 57. Influence of the ACS design on the computed velocity fields, tests T01, T02, and T03.

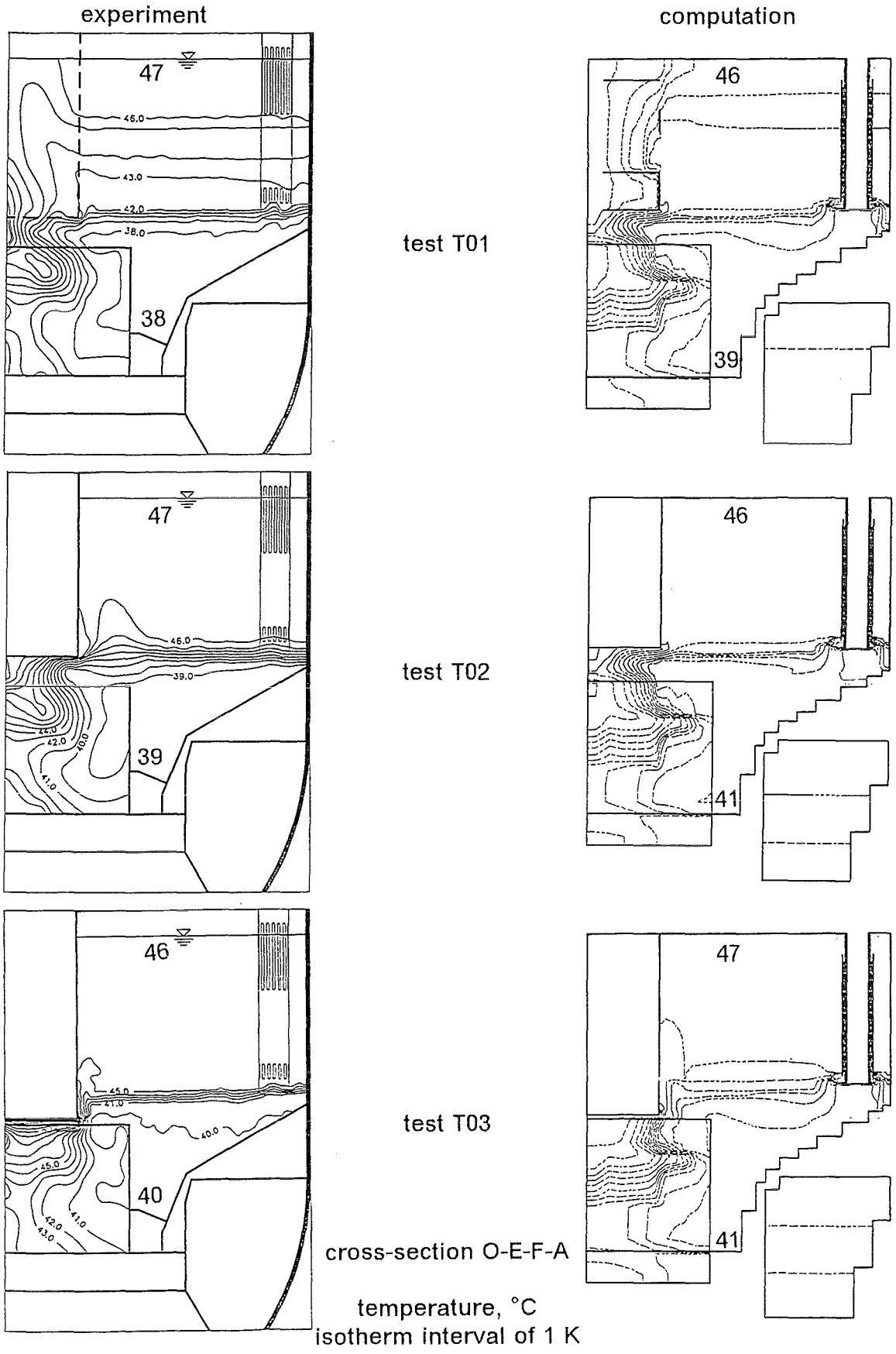

Fig. 58. Influence of the ACS design on the measured and computed isotherm fields, tests T01, T02, and T03.

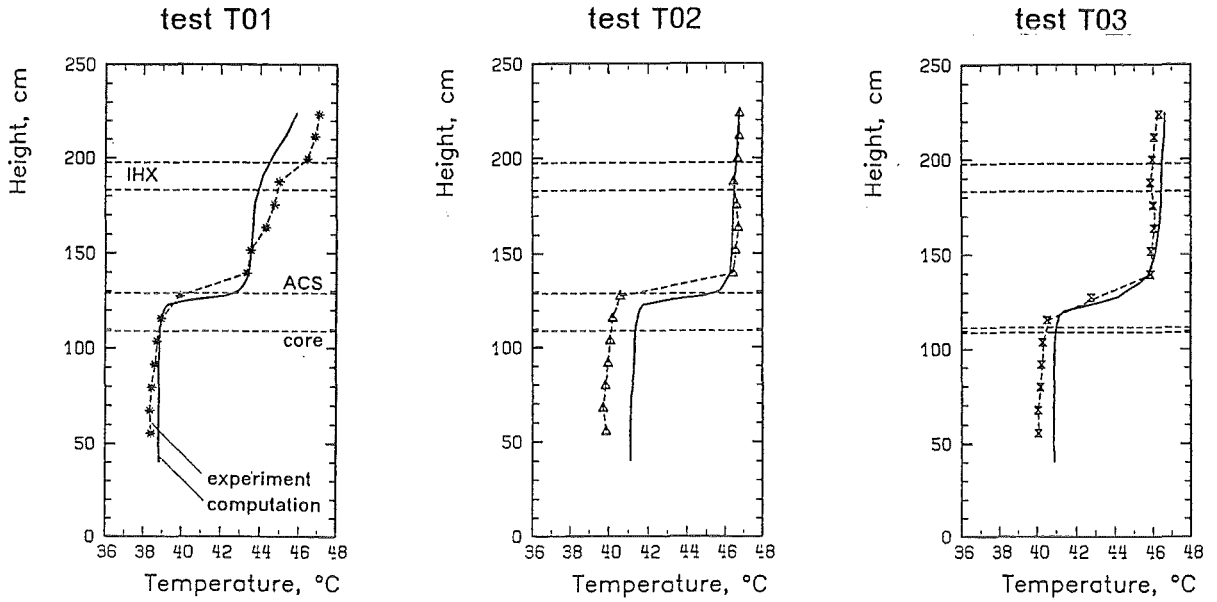

Fig. 59. Influence of the ACS design on the measured and computed axial temperature profiles in the UP, tests T01, T02, and T03.

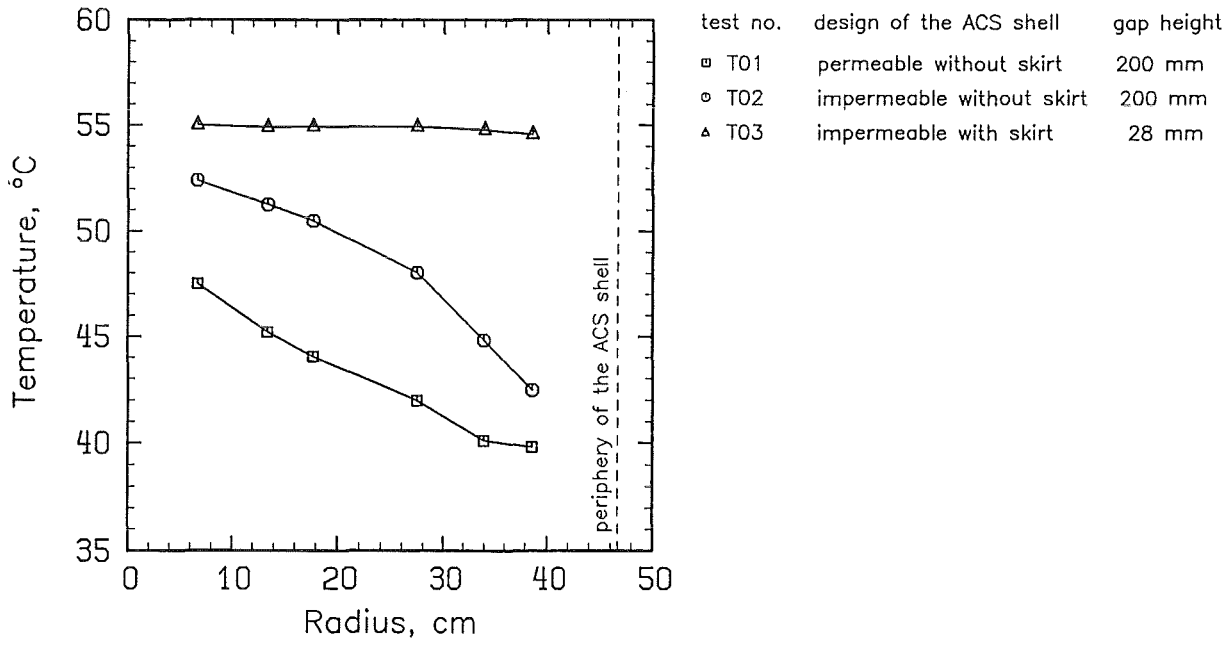

Fig. 60. Influence of the ACS design on the horizontal temperature profiles measured in the gap between the core top end and the ACS bottom end (z = 1,248 mm), tests T01, T02, and T03.

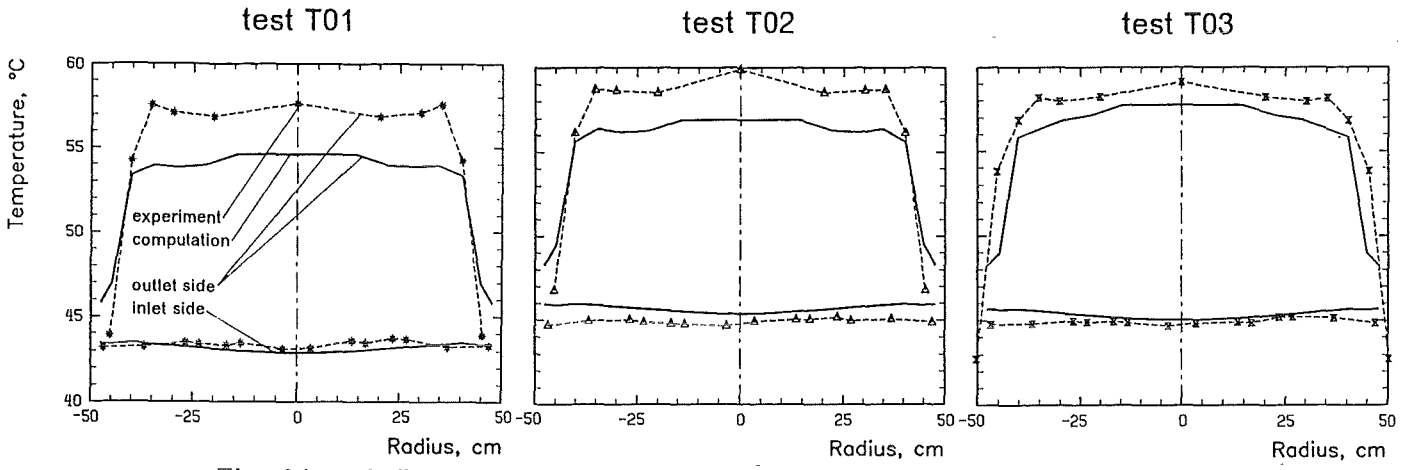

Fig. 61. Influence of the ACS design on the measured and computed radial temperature profiles at the inlet and outlet side of the heated SAs, tests T01, T02, and T03.

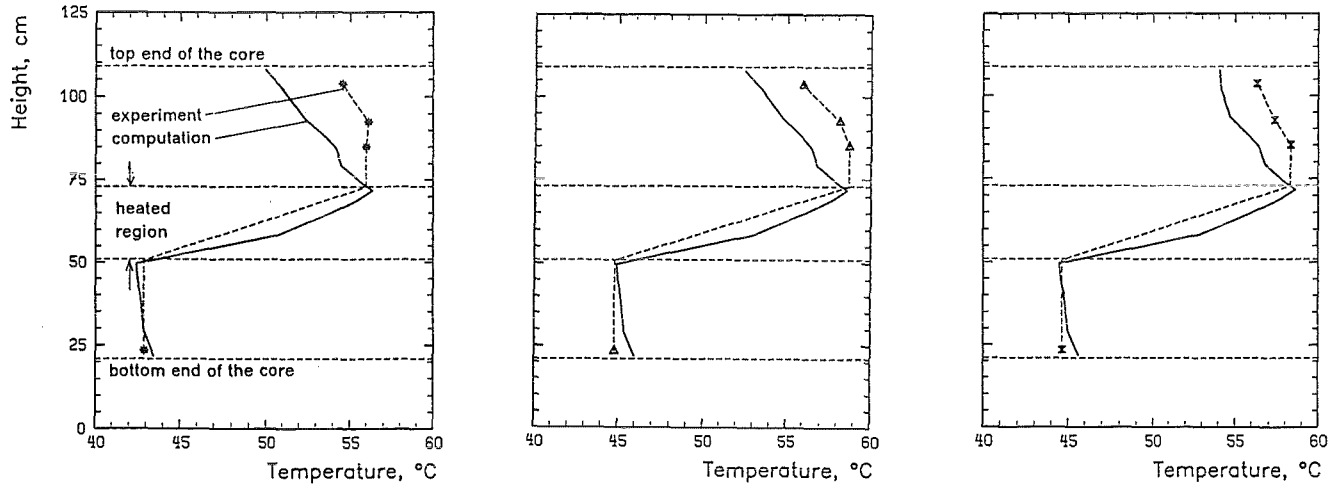

Fig. 62. Influence of the ACS design on the measured and computed axial temperature profiles inside a SA of heating group #4, tests T01, T02, and T03.

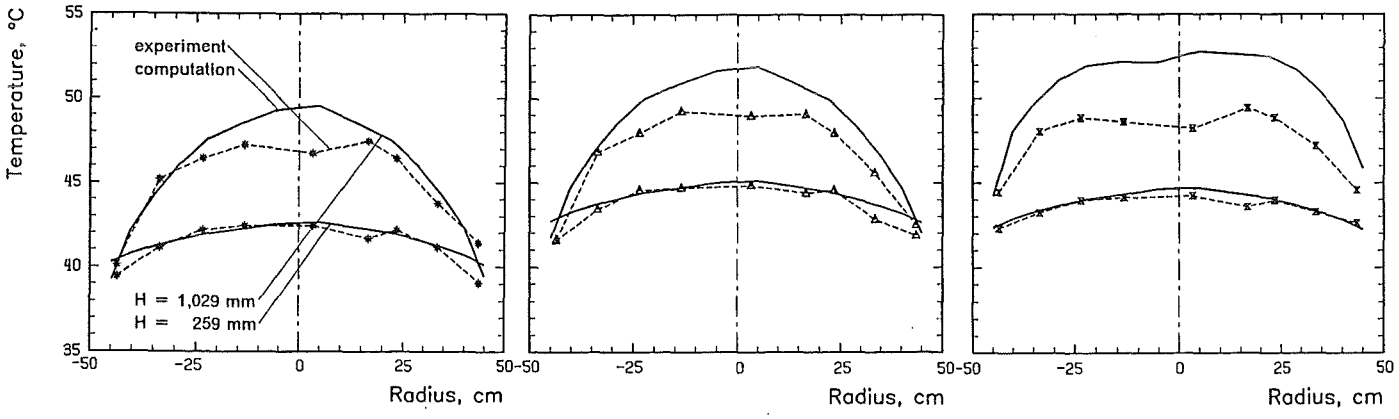

Fig. 63. Influence of the ACS design on the measured and computed radial temperature profiles at the top and bottom end of the interwrapper space, tests T01, T02, and T03.

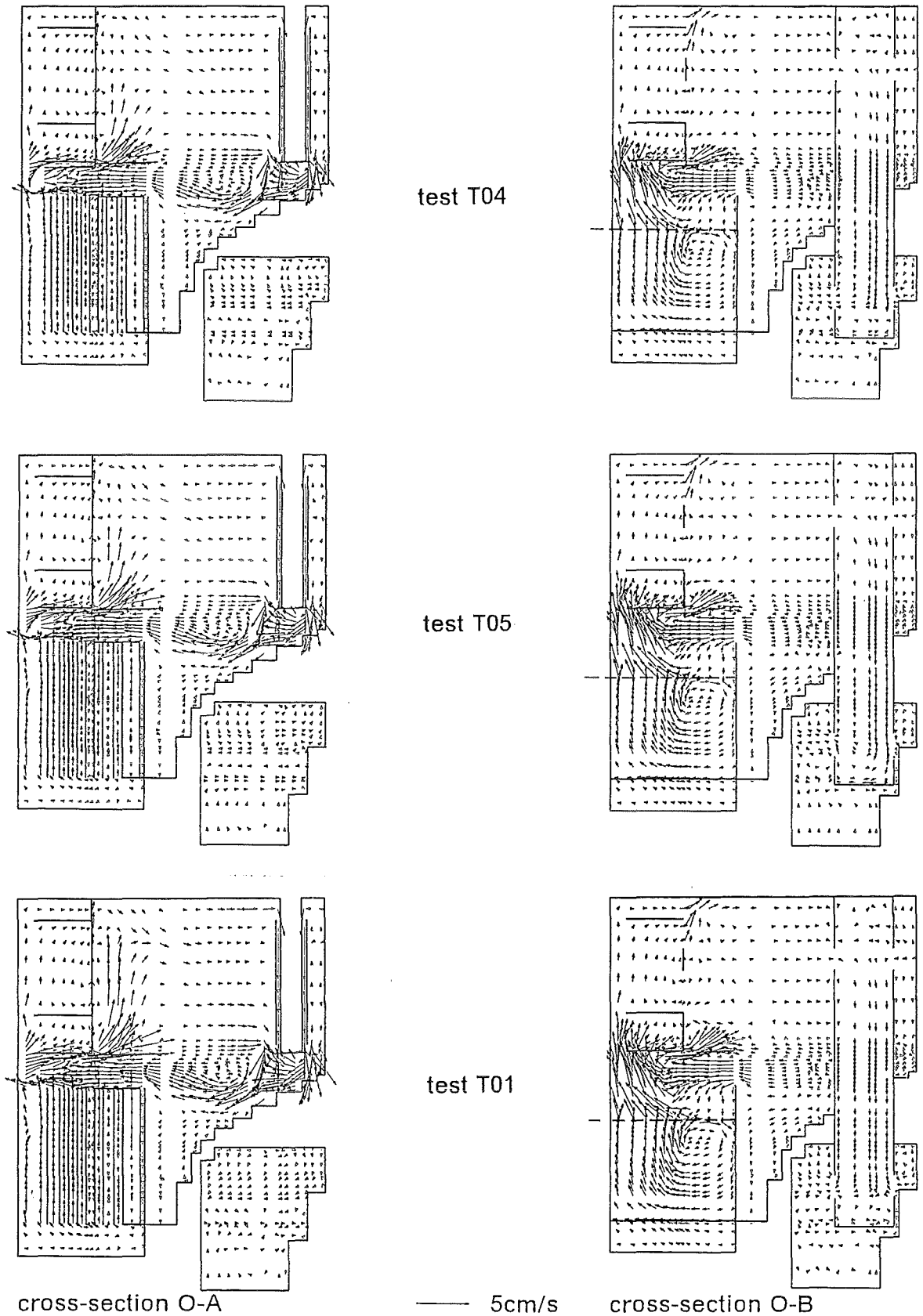

Fig. 64. Influence of the core power on the computed velocity fields, tests T04, T05, and T01.

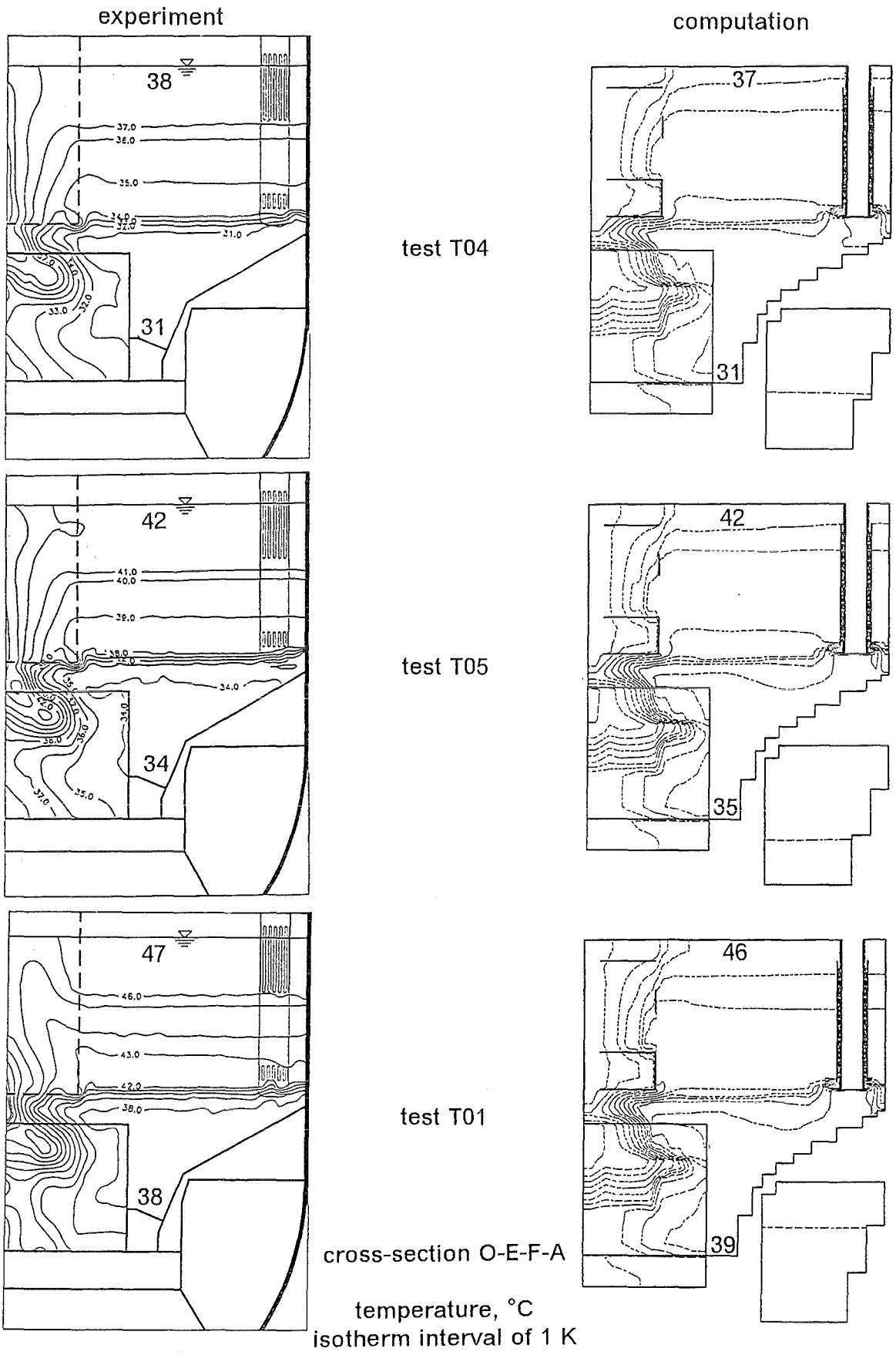

Fig. 65. Influence of the core power on the measured and computed isotherm fields, tests T04, T05, and T01.

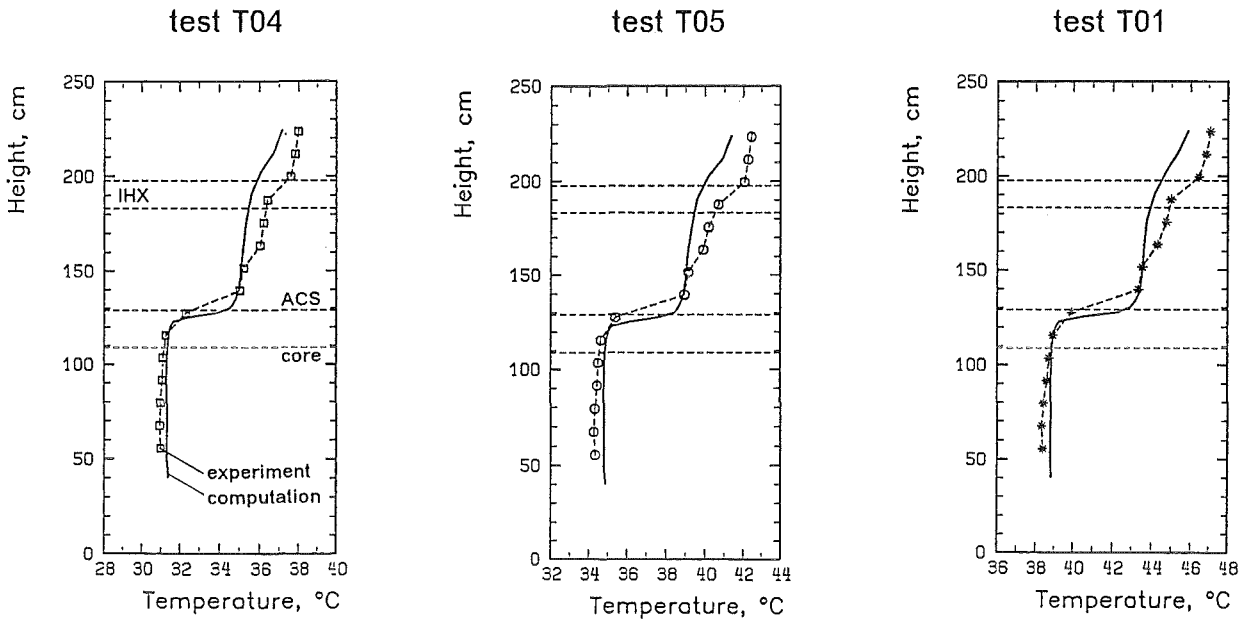

Fig. 66. Influence of the core power on the measured and computed axial temperature profiles in the UP, tests T04, T05, and T01.

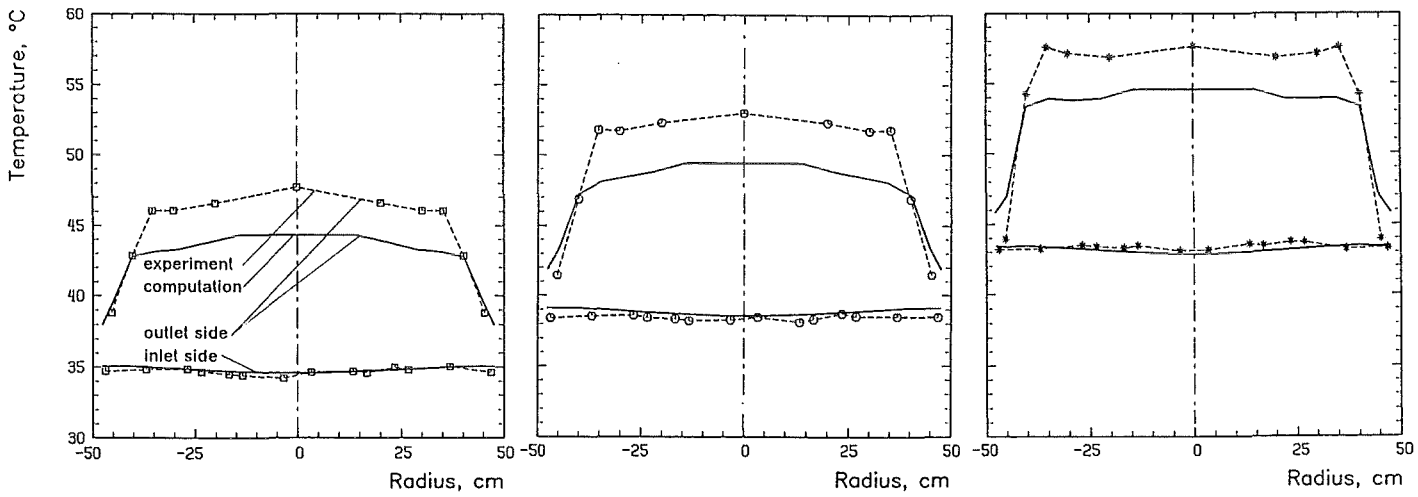

Fig. 67. Influence of the core power on the measured and computed radial temperature profiles at the inlet and outlet side of the heated SAs, tests T04, T05, and T01.

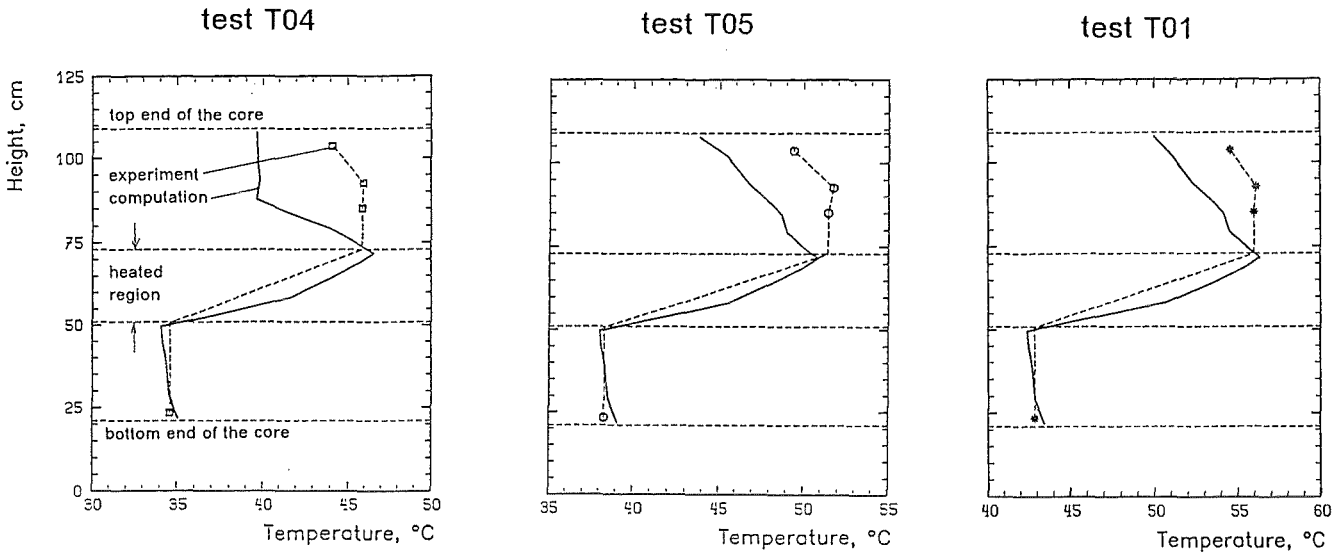

Fig. 68. Influence of the core power on the measured and computed axial temperature profiles inside a SA of heating group #4, tests T04, T05, and T01.

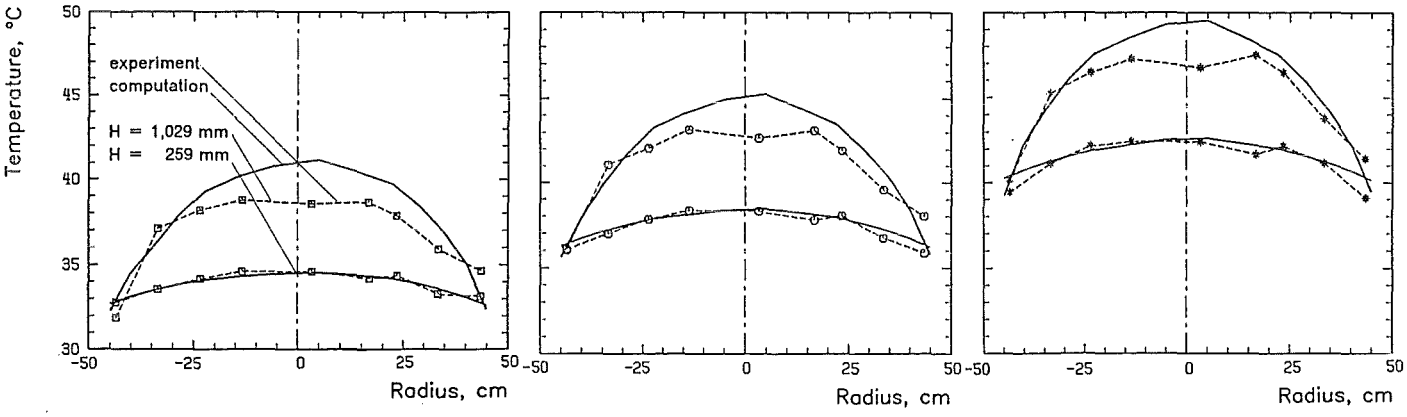

Fig. 69. Influence of the core power on the measured and computed radial temperature profiles at the top and bottom end of the interwrapper space, tests T04, T05, and T01.

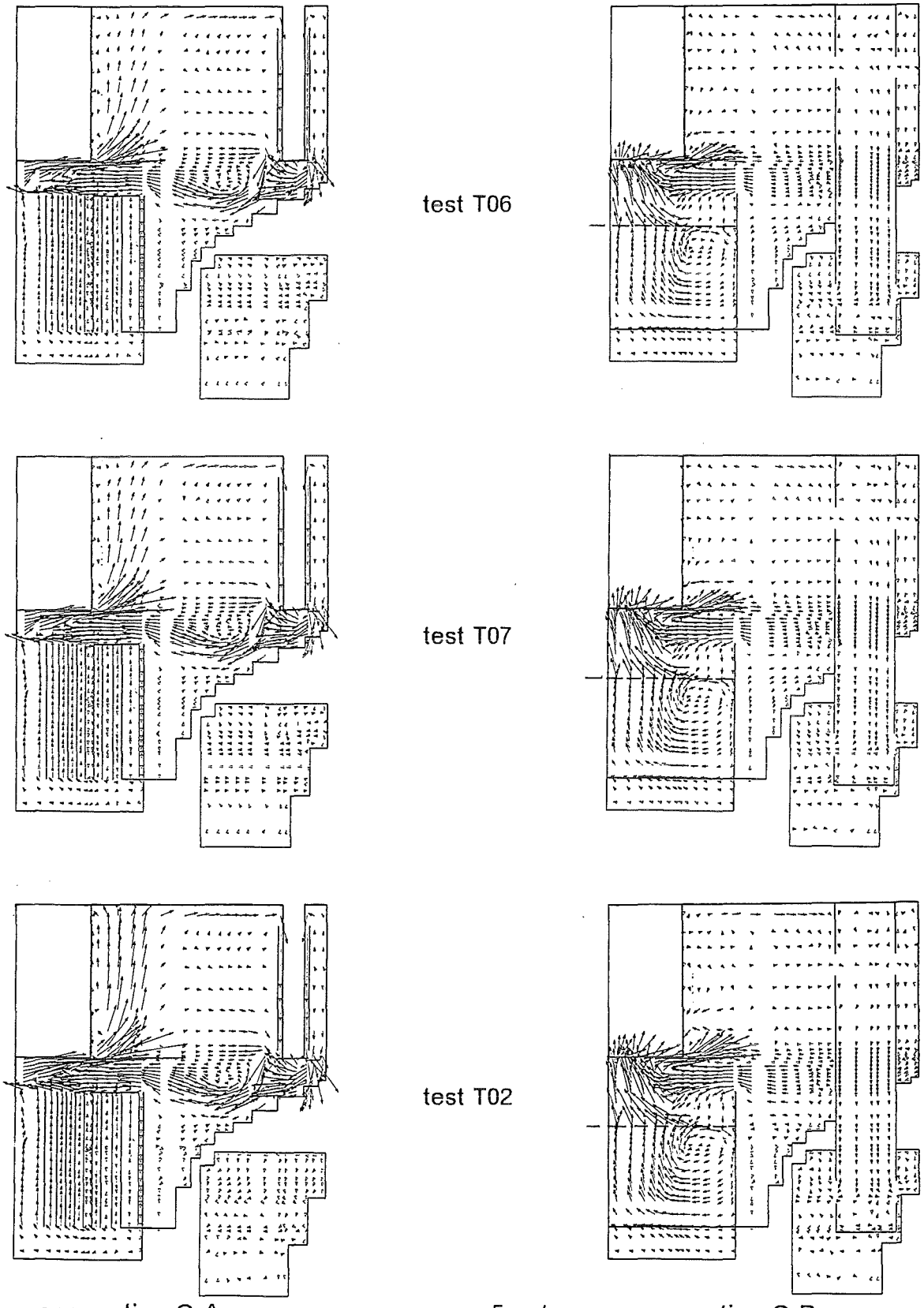

Fig. 70. Influence of the core power on the computed velocity fields, tests T06, T07, and T02.

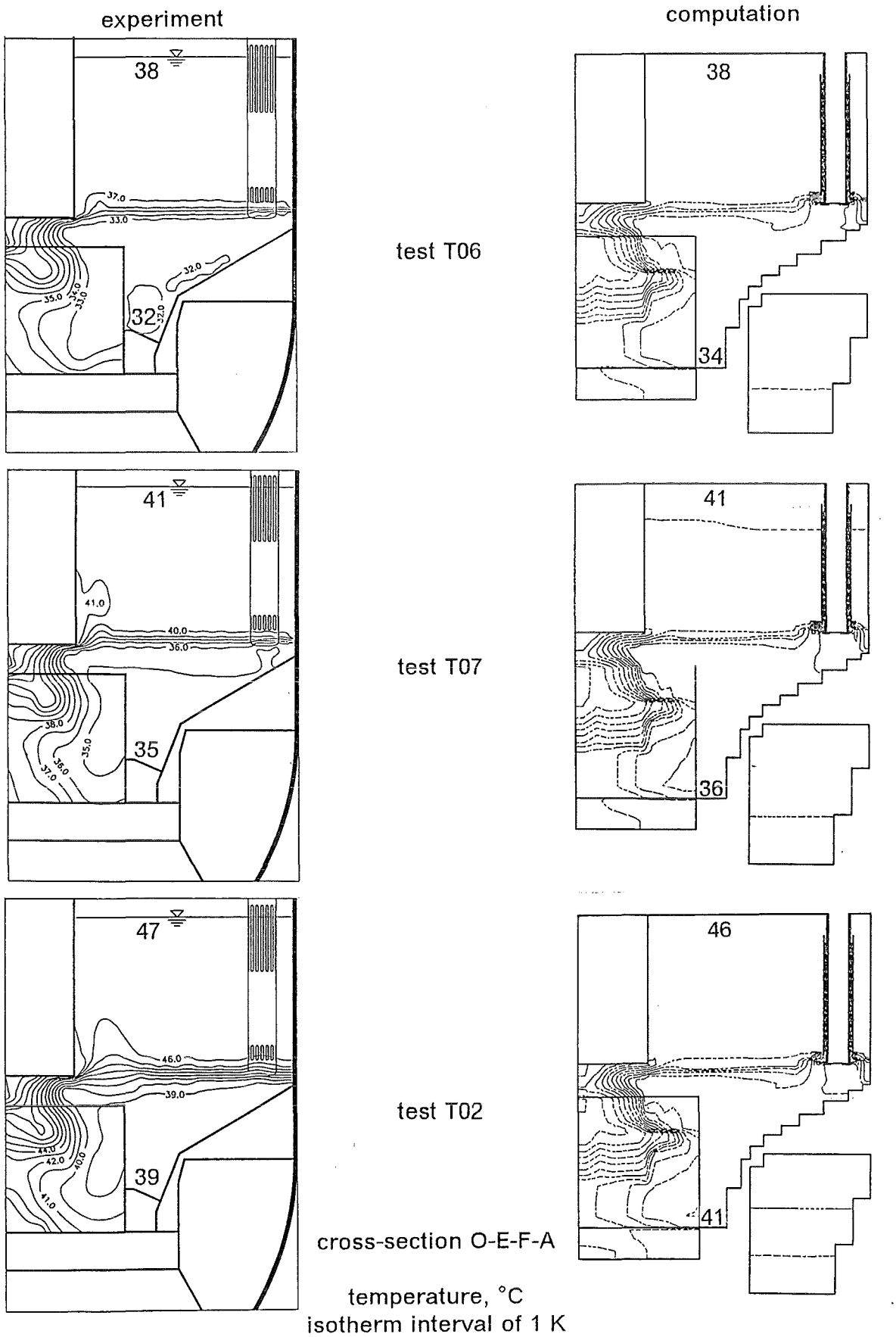

Fig. 71. Influence of the core power on the measured and computed isotherm fields, tests T06, T07, and T02.

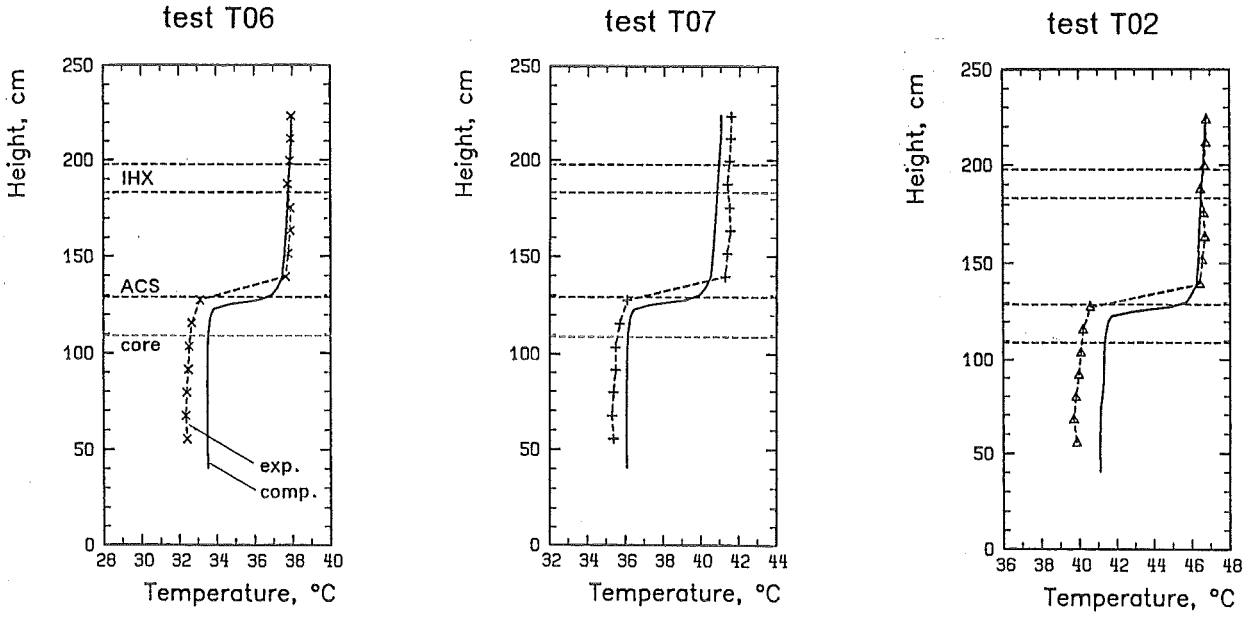

Fig. 72. Influence of the core power on the measured and computed axial temperature profiles in the UP, tests T06, T07, and T02.

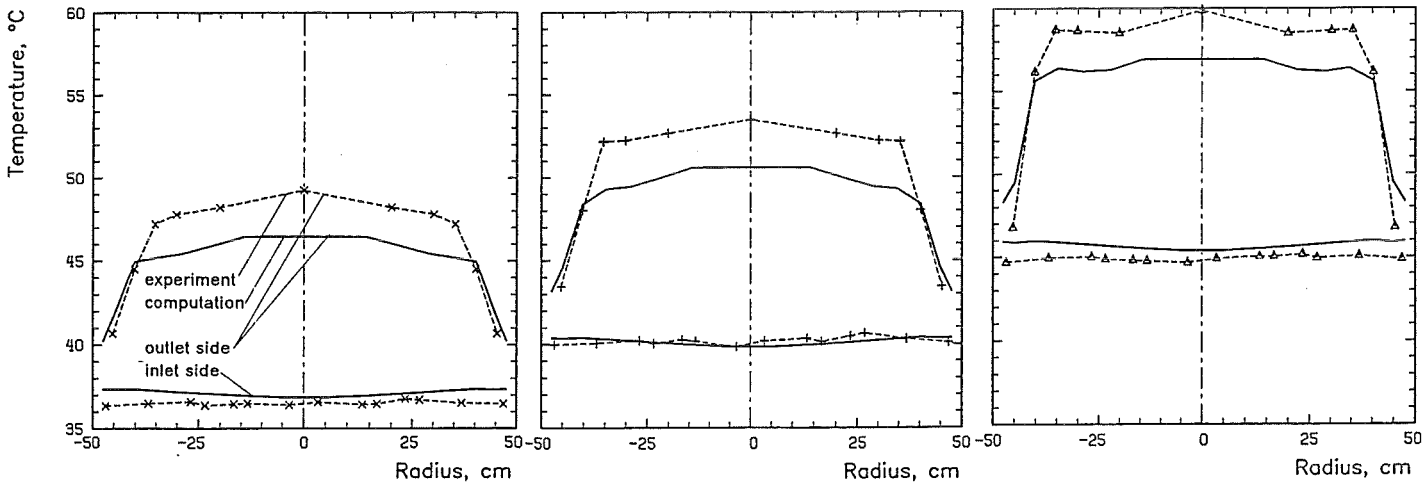

Fig. 73. Influence of the core power on the measured and computed radial temperature profiles at the inlet and outlet side of the heated SAs, tests T06, T07, and T02.

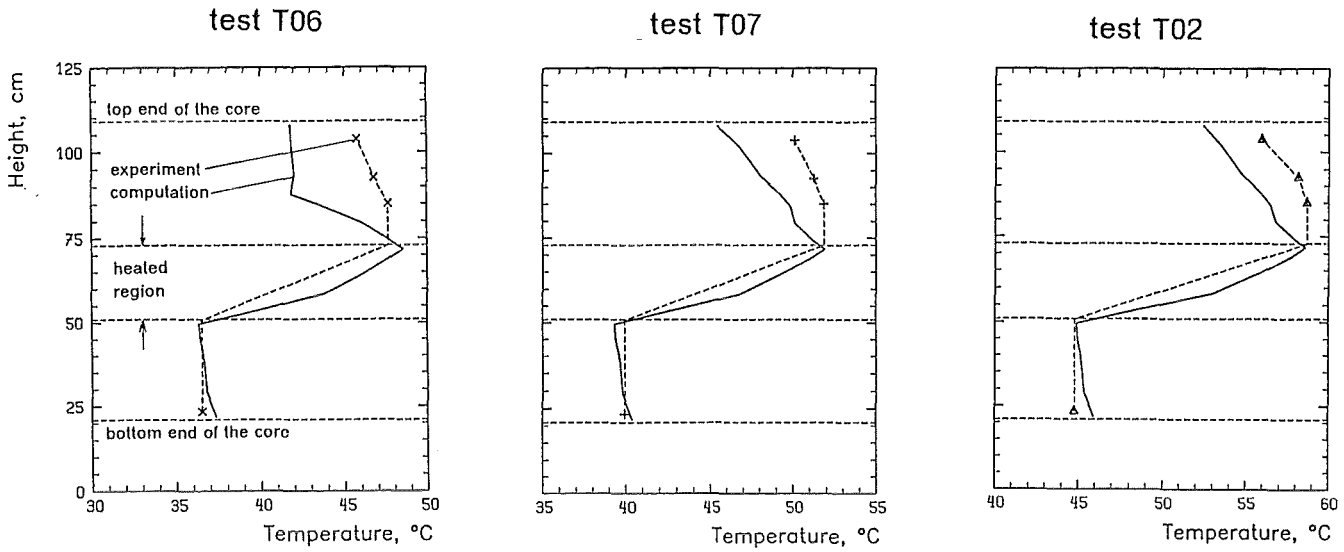

Fig. 74. Influence of the core power on the measured and computed axial temperature profiles inside a SA of heating group #4, tests T06, T07, and T02.

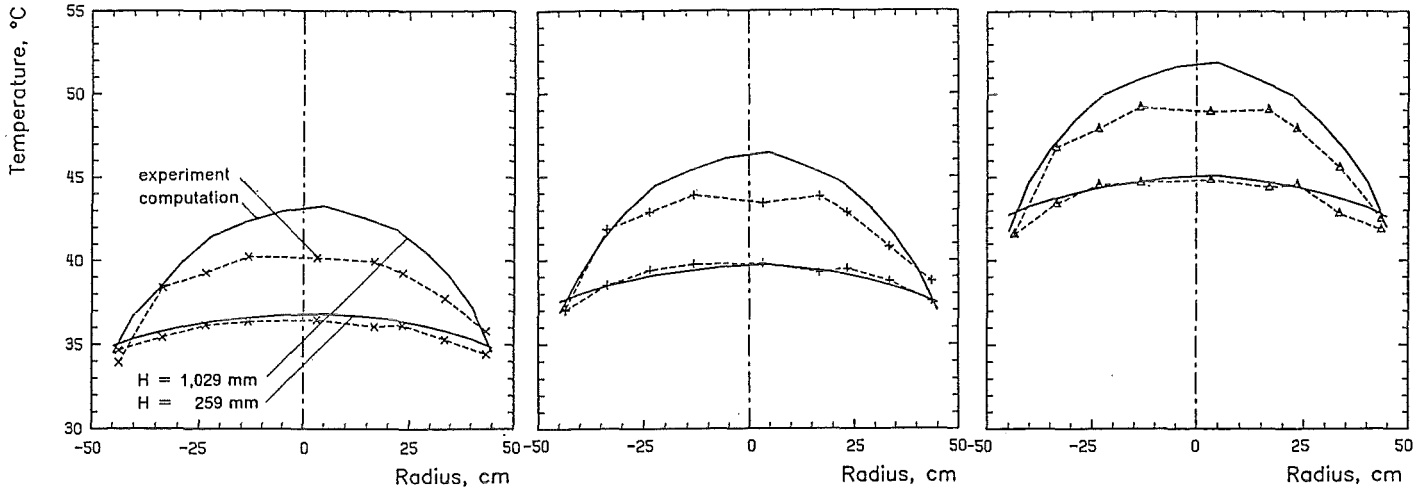

Fig. 75. Influence of the core power on the measured and computed radial temperature profiles at the top and bottom end of the interwrapper space, tests T06, T07, and T02.

experiment

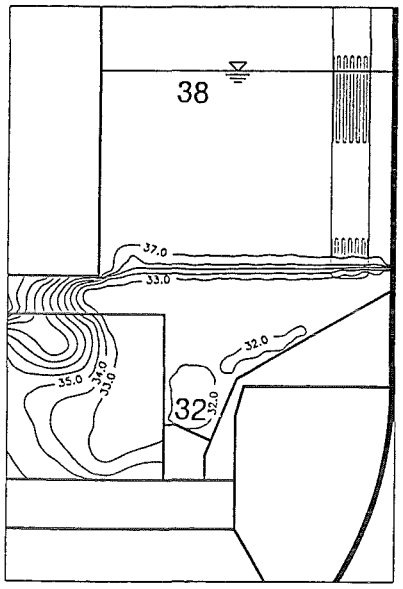

test T06

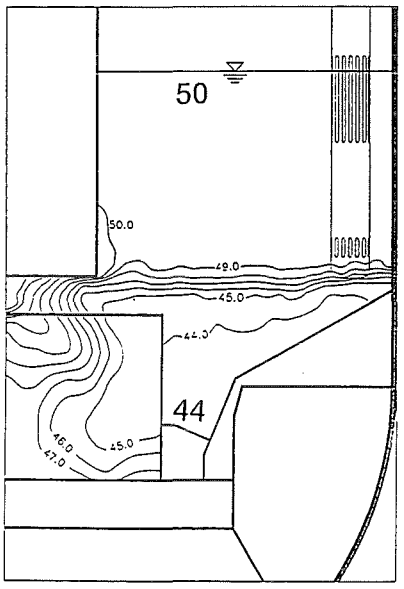

test T08

cross-section O-E-F-A

temperature, °C
isotherm interval of 1 K

Fig. 76. Influence of the number of operated DHX circuits on the measured isotherm fields, tests T06 and T08.

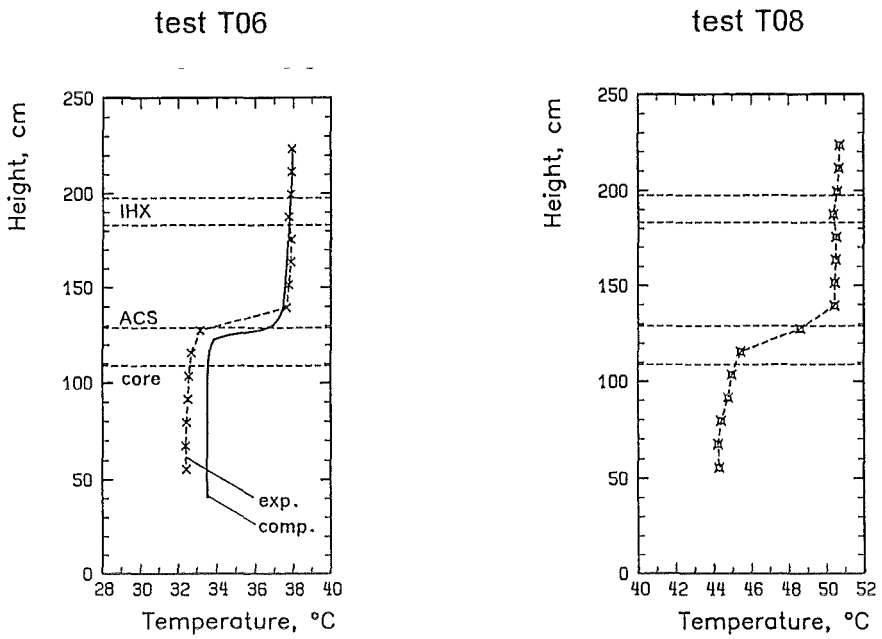

Fig. 77. Influence of the number of operated DHX circuits on the measured axial temperature profiles (MEL) in the UP, tests T06 and T08.

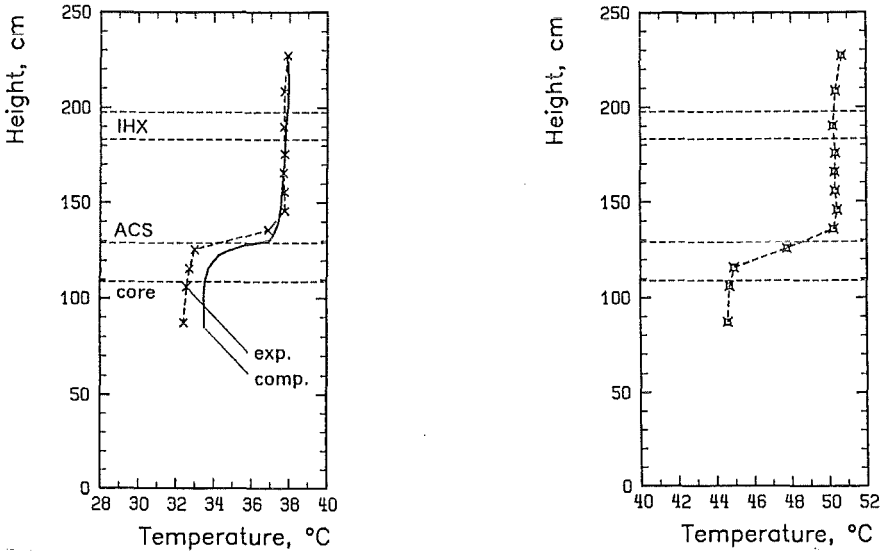

Fig. 78. Influence of the number of operated DHX circuits on the measured axial temperature profiles (MER-3) in the UP, tests T06 and T08.

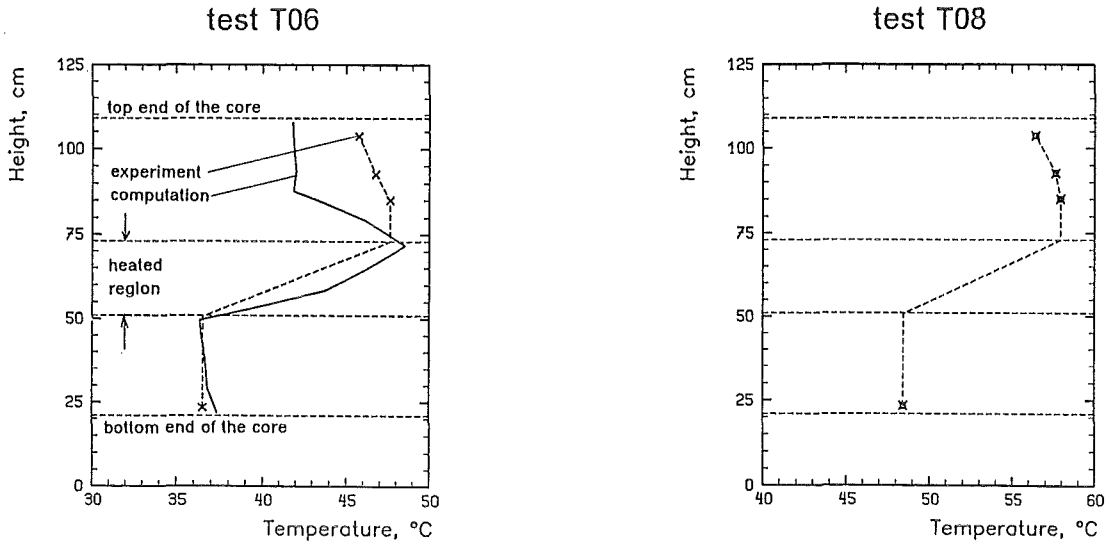

Fig. 79. Influence of the number of operated DHX circuits on the radial temperature profiles measured at the inlet and outlet side of heated SAs, tests T06 and T08.

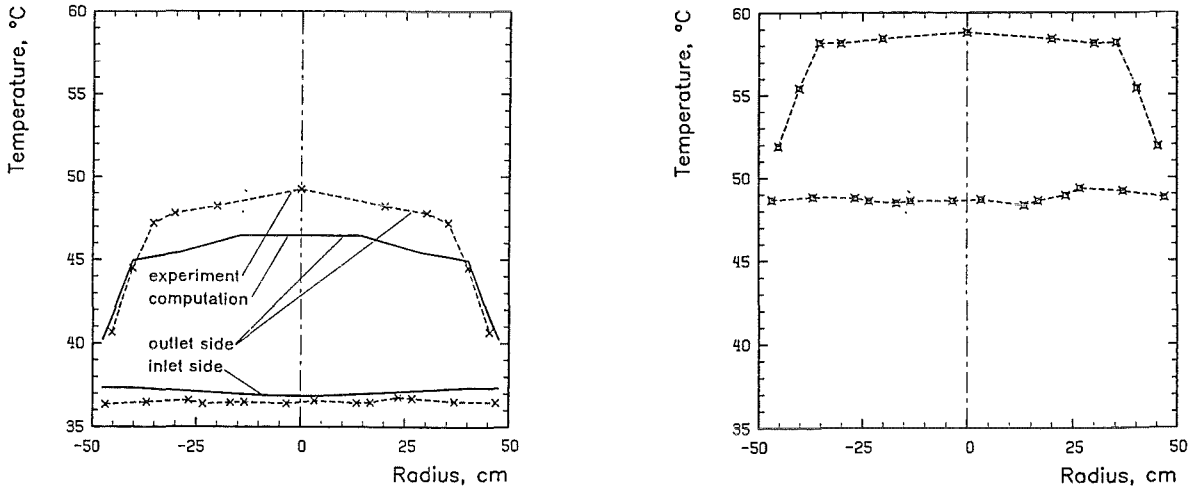

Fig. 80. Influence of the number of operated DHX circuits on the axial temperature profiles measured inside a SA of heating group #4, tests T06 and T08.

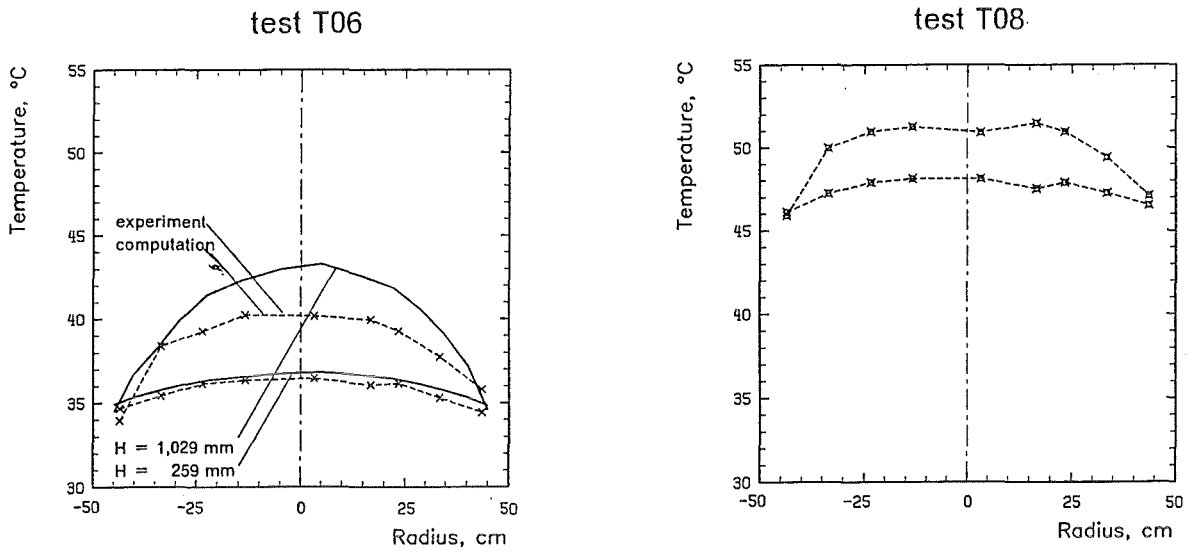

Fig. 81. Influence of the number of operated DHX circuits on the radial temperature profiles measured at the top and bottom end of the interwrapper space, tests T06 and T08.

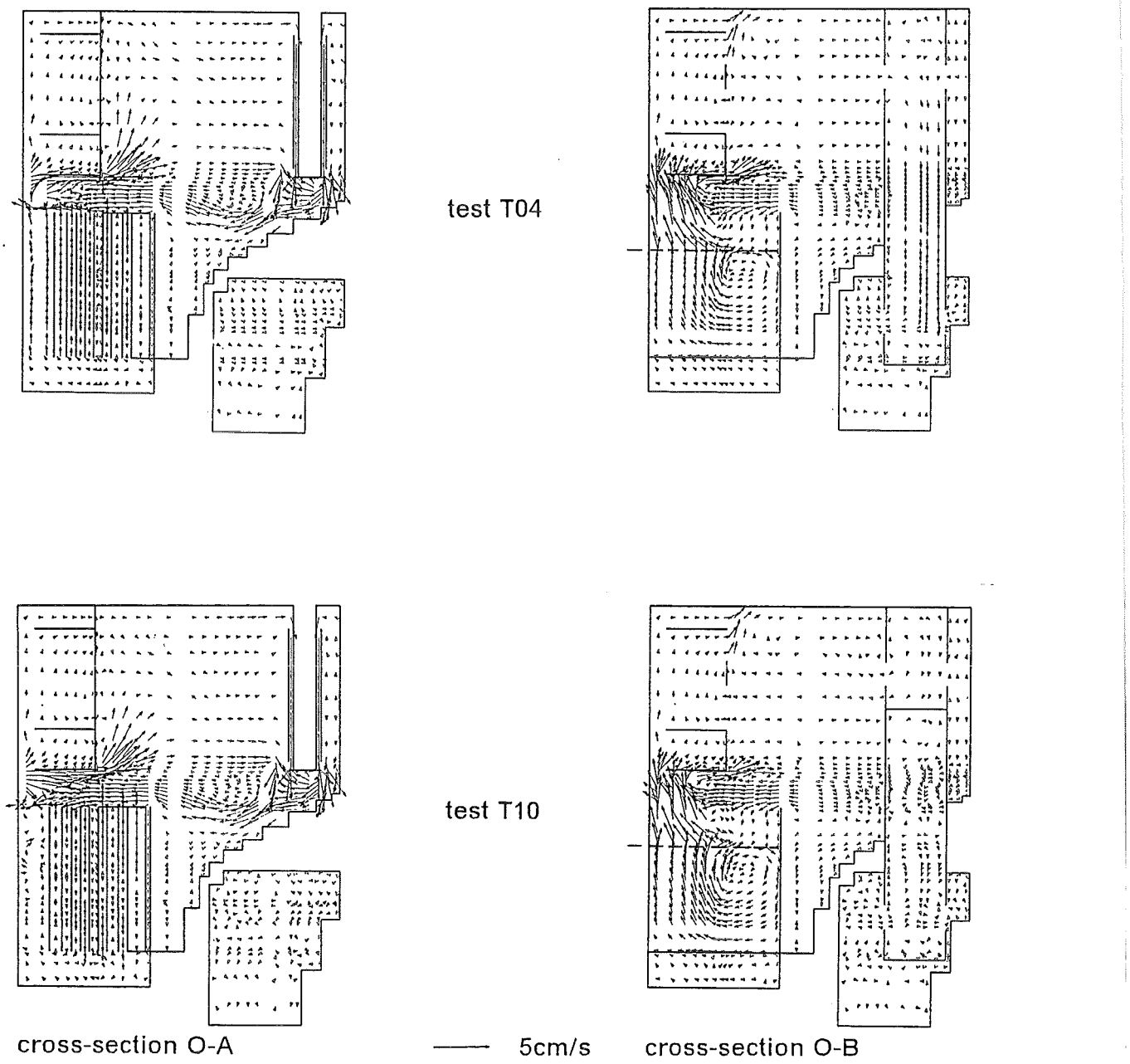

Fig. 82. Influence of the flow path blockages at the IHX primary sides on the computed velocity fields, tests T04 and T10.

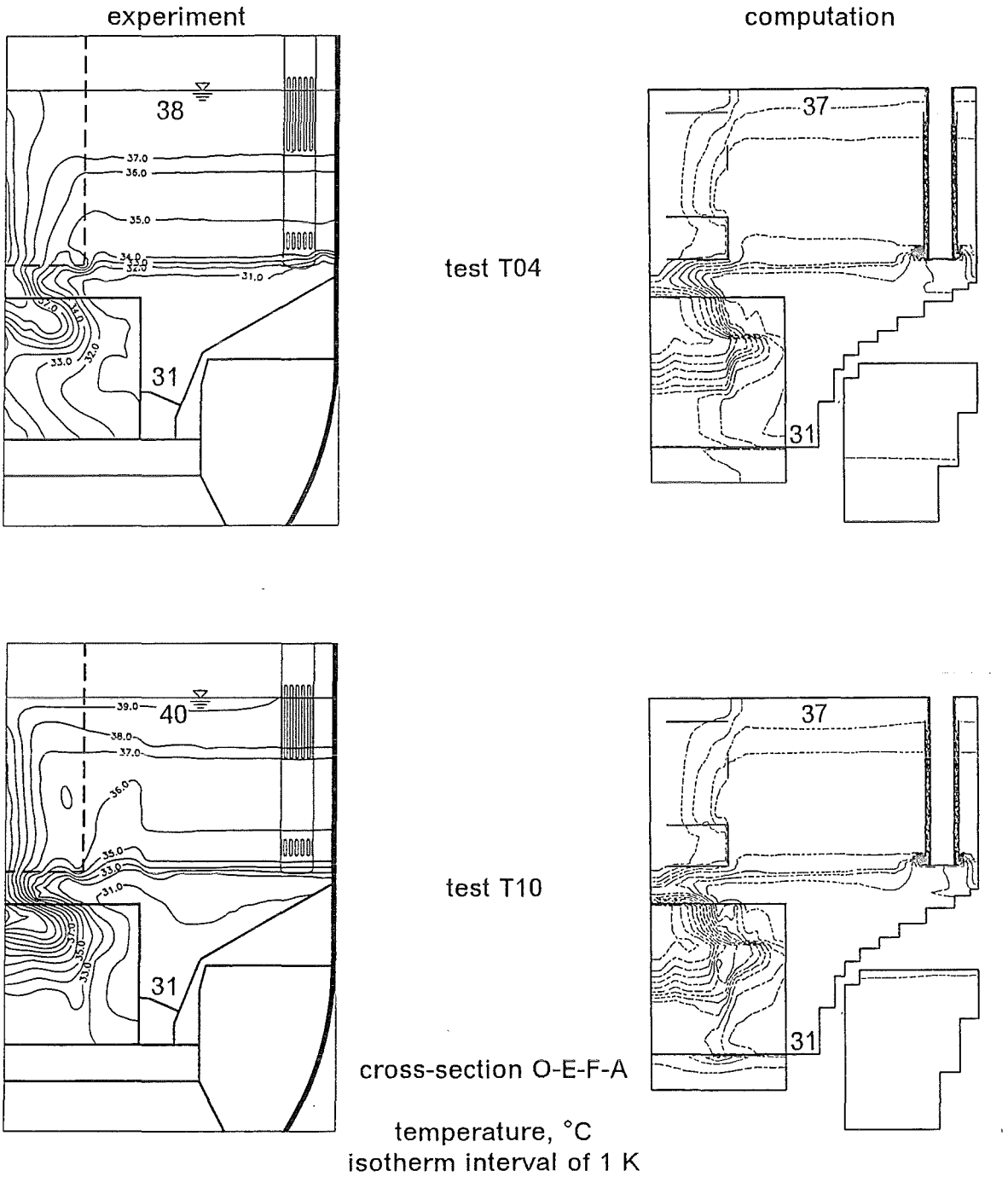

Fig. 83. Influence of the flow path blockages at the IHX primary sides on the measured and computed isotherm fields, tests T04 and T10.

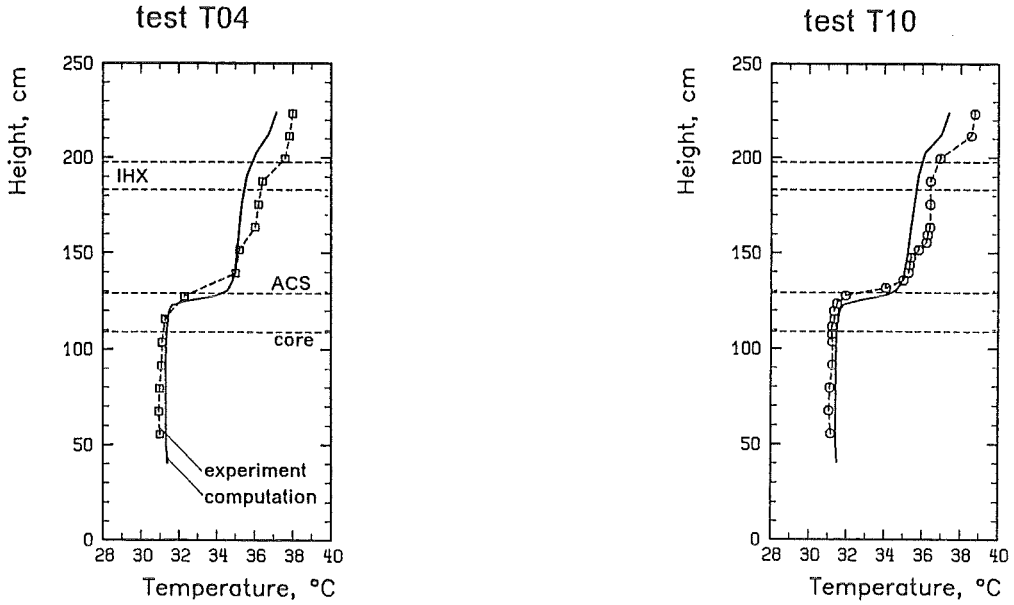

Fig. 84. Influence of the flow path blockages at the IHX primary sides on the measured and computed axial temperature profiles in the UP, tests T04 and T10.

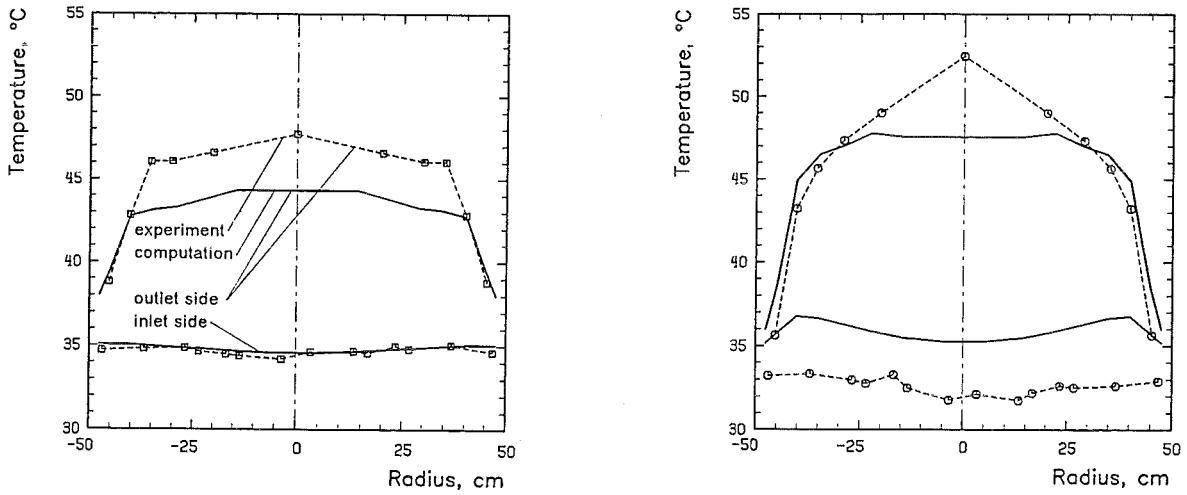

Fig. 85. Influence of the flow path blockages at the IHX primary sides on the measured and computed radial temperature profiles at the inlet and outlet side of heated SAs, tests T04 and T10.

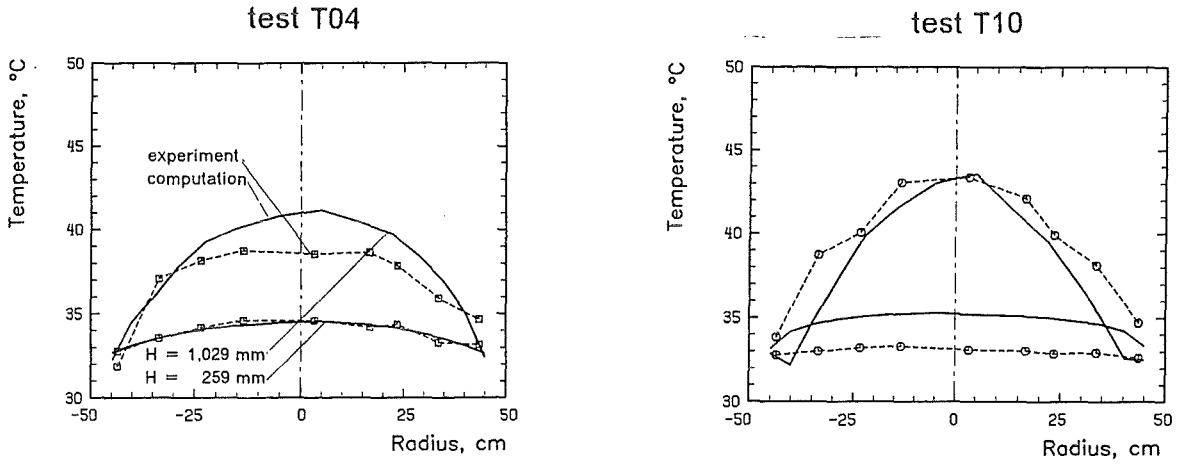

Fig. 86. Influence of the flow path blockages at the IHX primary sides on the measured and computed radial temperature profiles at the top and bottom end of the interwrapper space, tests T04 and T10.

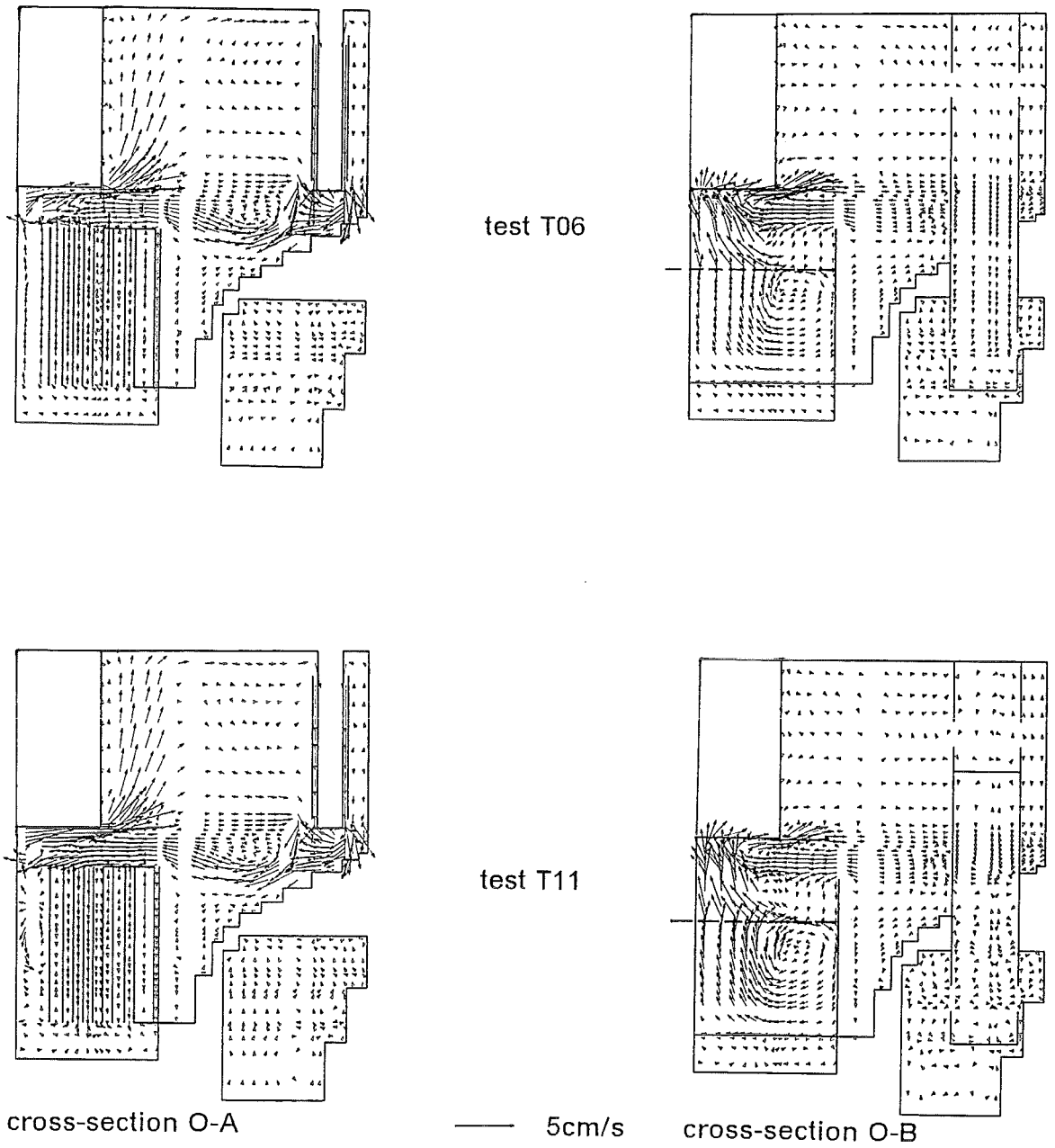

Fig. 87. Influence of the flow path blockages at the IHX primary sides on the computed velocity fields, tests T06 and T11.

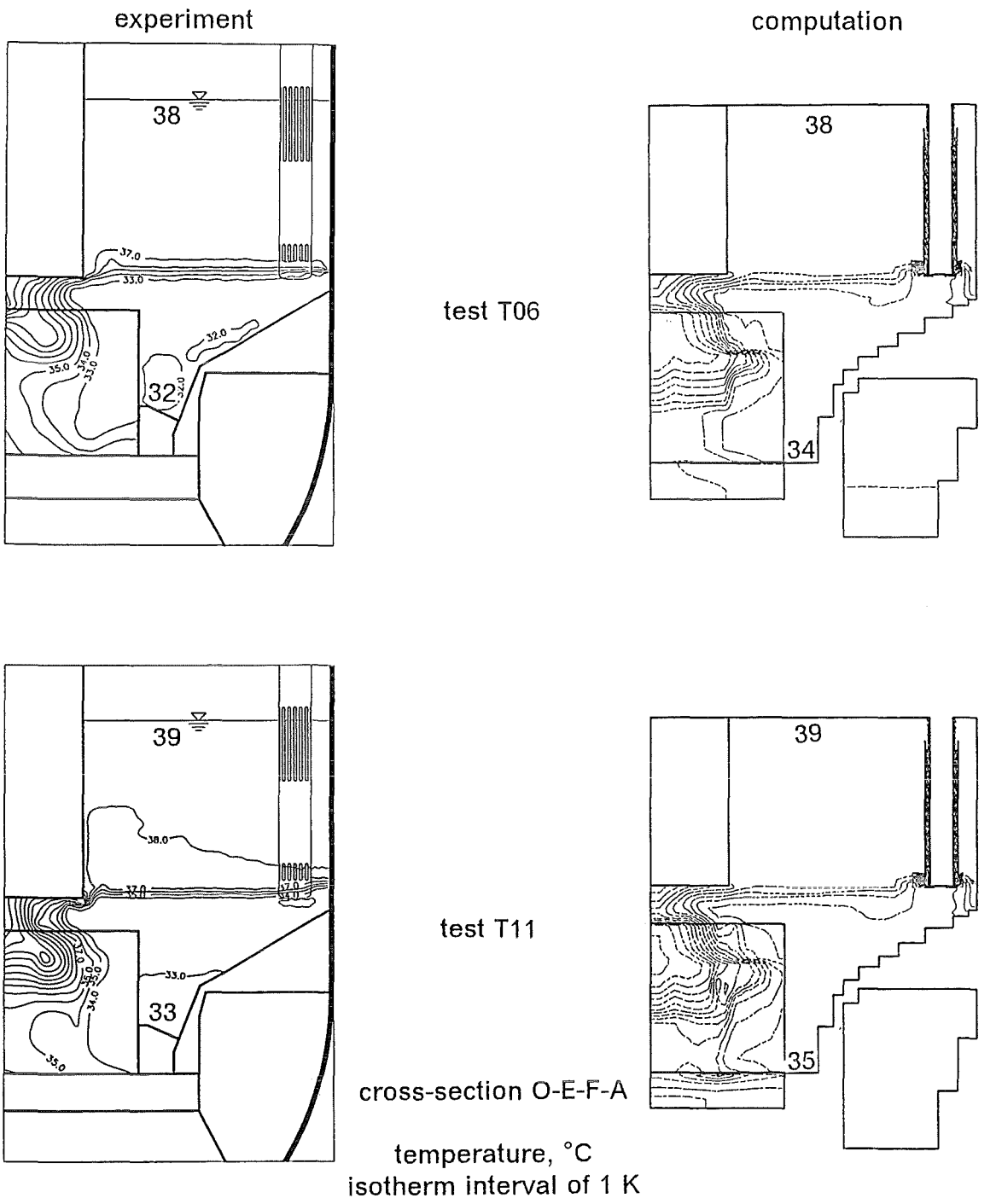

Fig. 88. Influence of the flow path blockages at the IHX primary sides on the measured and computed isotherm fields, tests T06 and T11.

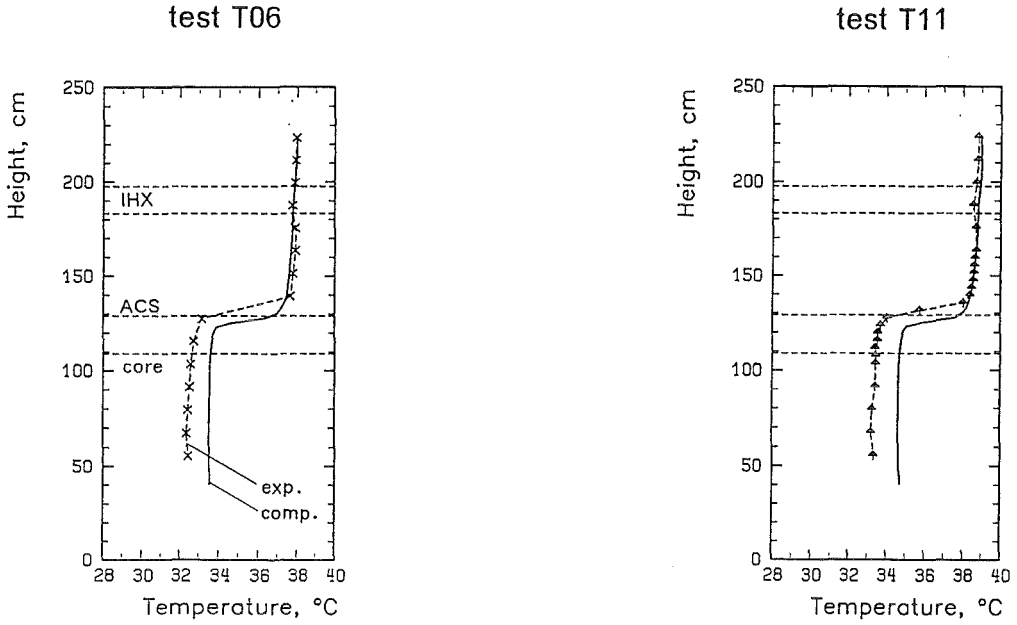

Fig. 89. Influence of the flow path blockages at the IHX primary sides on the measured and computed axial temperature profiles in the UP, tests T06 and T11.

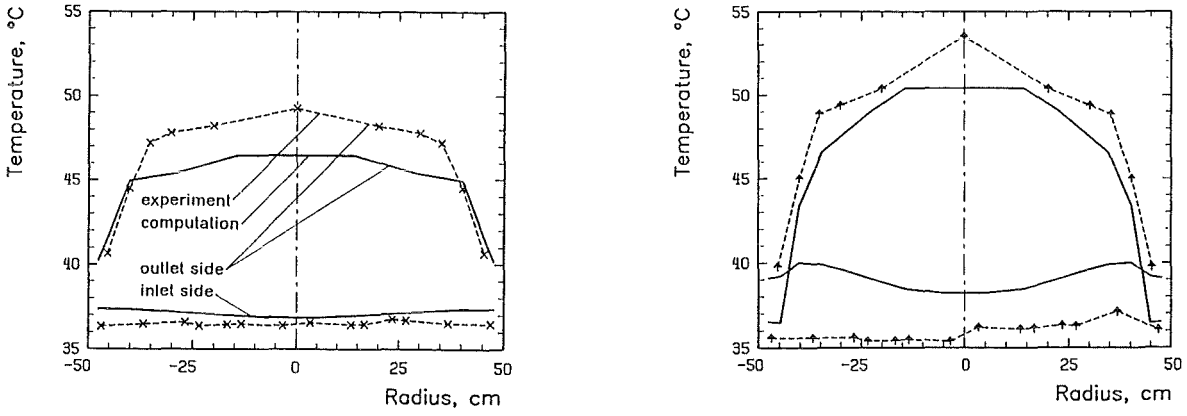

Fig. 90. Influence of the flow path blockages at the IHX primary sides on the measured and computed radial temperature profiles at the inlet and outlet side of heated SAs, tests T06 and T11.

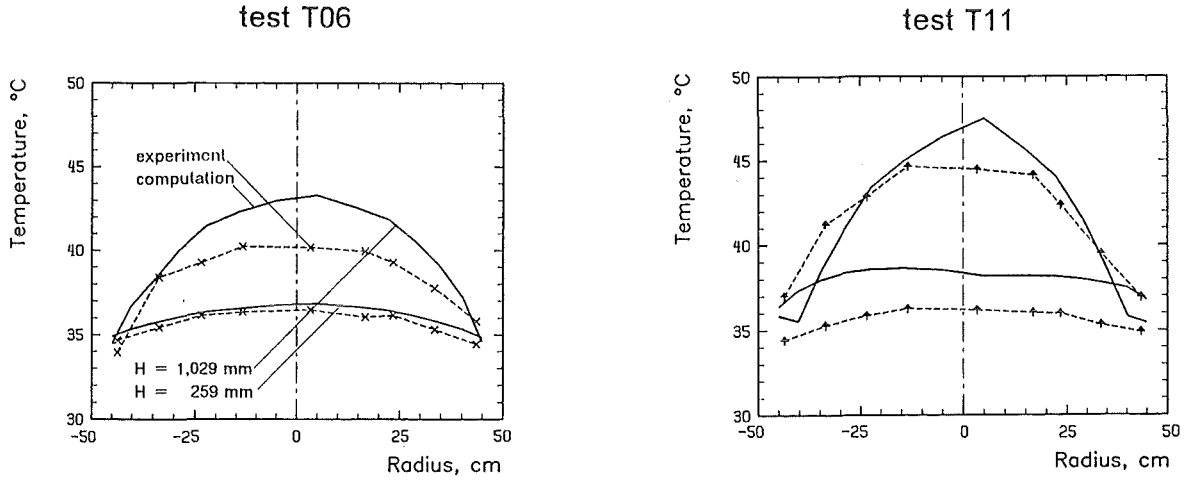

Fig. 91. Influence of the flow path blockages at the IHX primary sides on the measured and computed radial temperature profiles at the top and bottom end of the interwrapper space, tests T06 and T11.

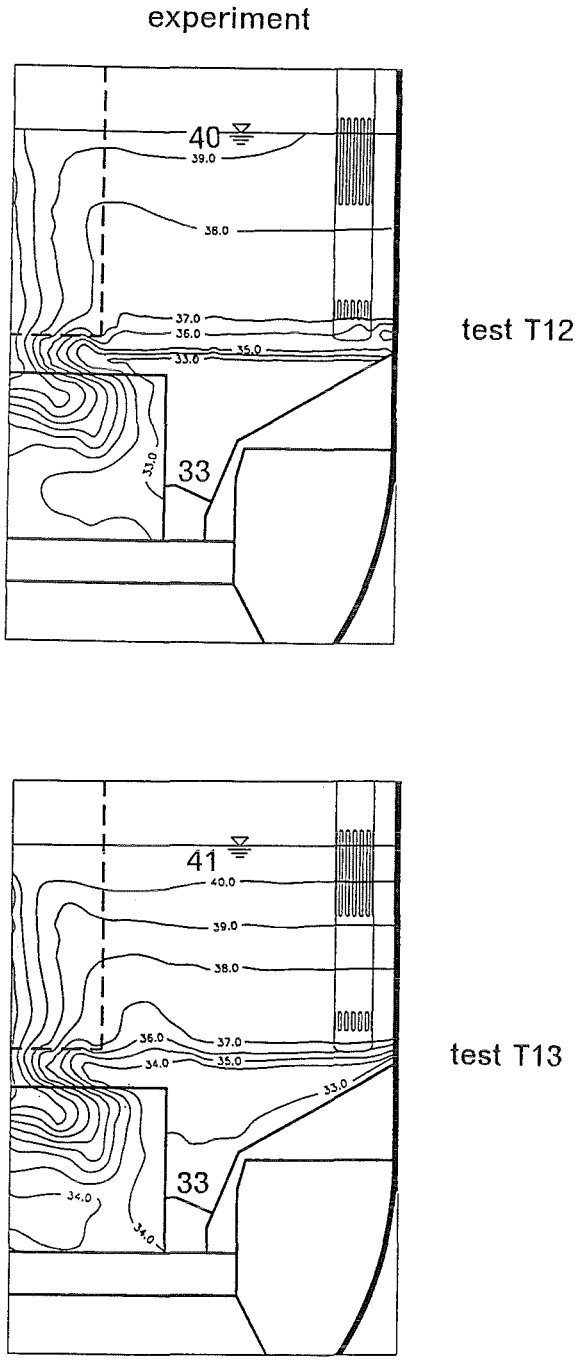

Fig. 92. Influence of the flow path blockages at the IHX primary sides on the measured isotherm fields, tests T12 and T13.

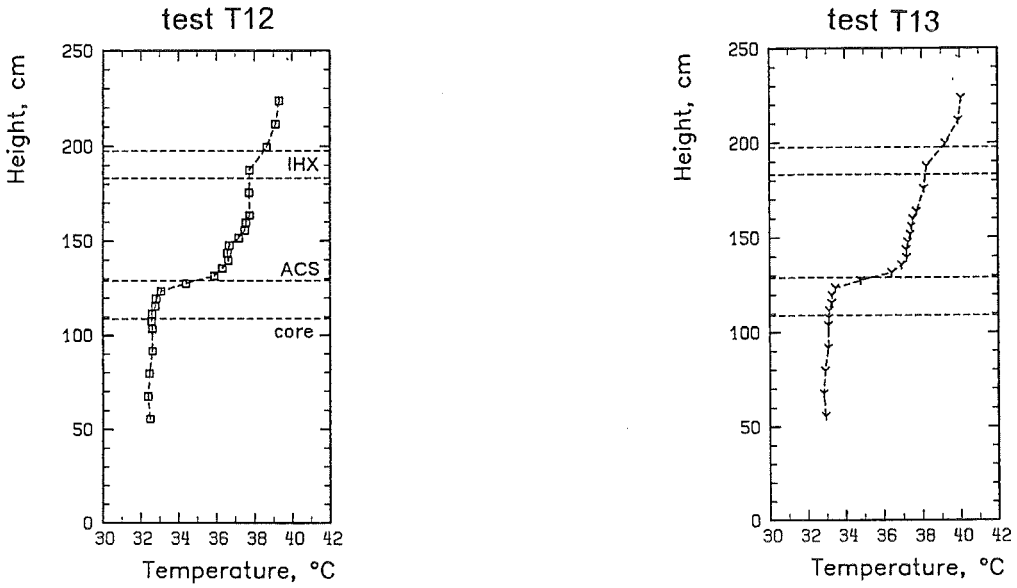

Fig. 93. Influence of the flow path blockages at the IHX primary sides on the measured axial temperature profiles in the UP, tests T12 and T13.

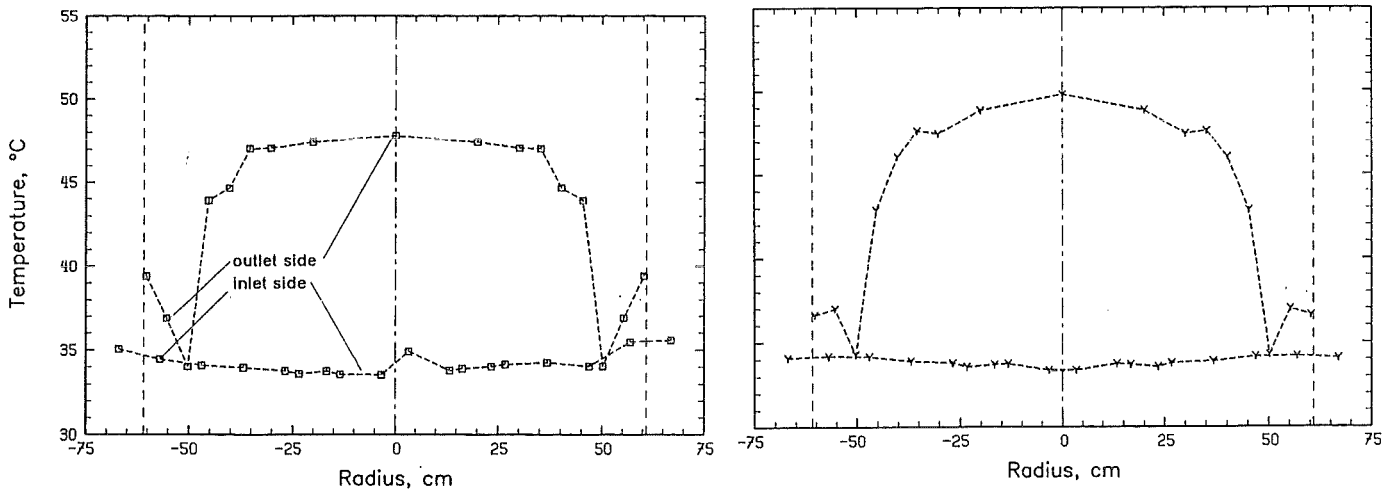

Fig. 94. Influence of the flow path blockages at the IHX primary sides on the radial temperature profiles measured at the inlet and outlet of heated SAs, tests T12 and T13.

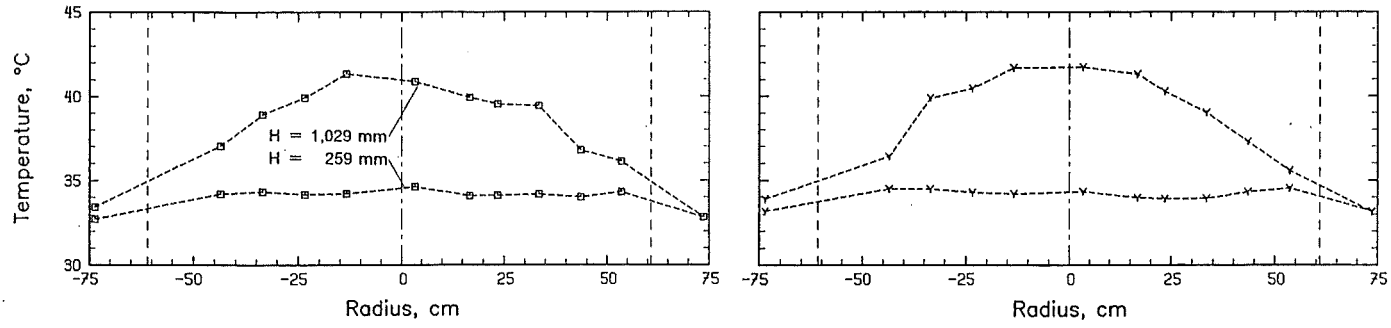

Fig. 95. Influence of the flow path blockages at the IHX primary sides on the radial temperature profiles measured at the top and bottom end of the interwrapper space, tests T12 and T13.

experiment

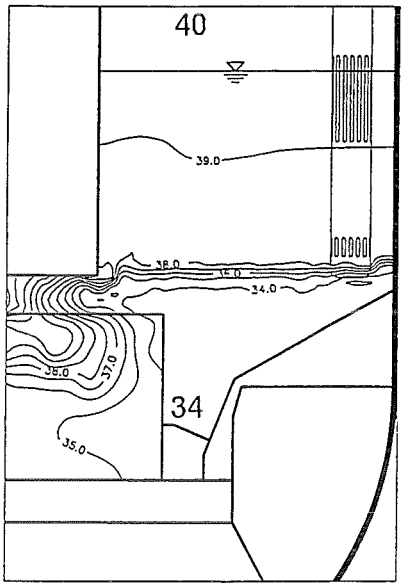

test T14

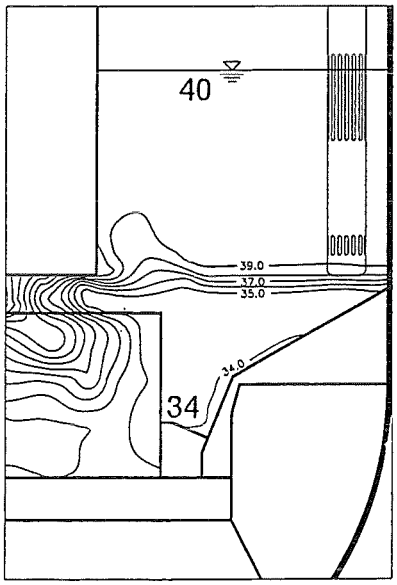

test T15

cross-section O-E-F-A

temperature, °C
isotherm interval of 1 K

Fig. 96. Influence of the flow path blockages at the IHX primary sides on the measured isotherm fields, tests T14 and T15.

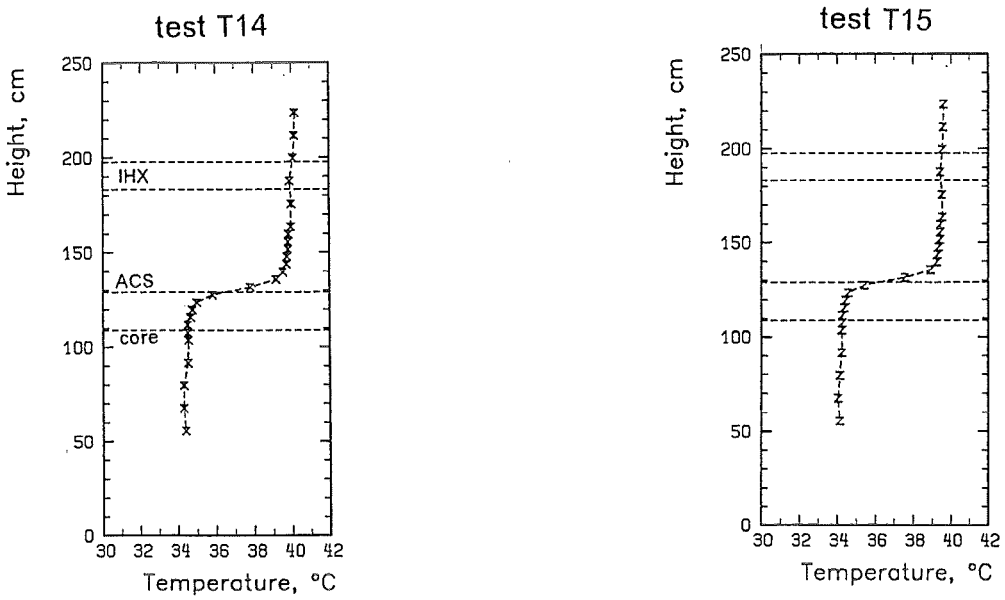

Fig. 97. Influence of the flow path blockages of the IHX primary sides on the measured axial temperature profiles in the UP, tests T14 and T15.

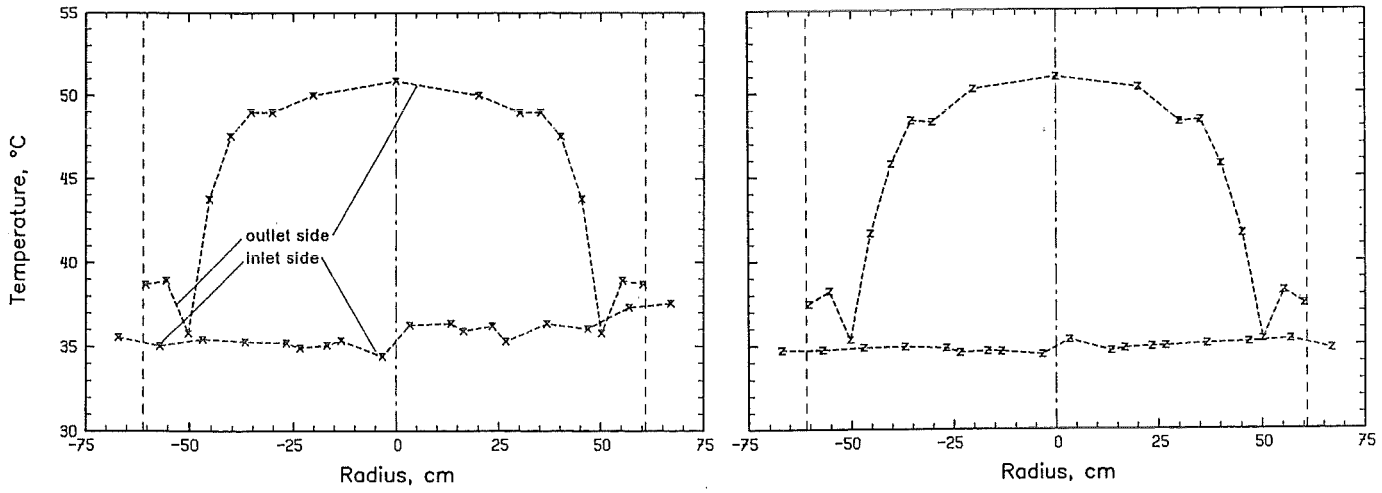

Fig. 98. Influence of the flow path blockages at the IHX primary sides on the measured and computed radial temperature profiles at the inlet and outlet side of heated SAs, tests T14 and T15.

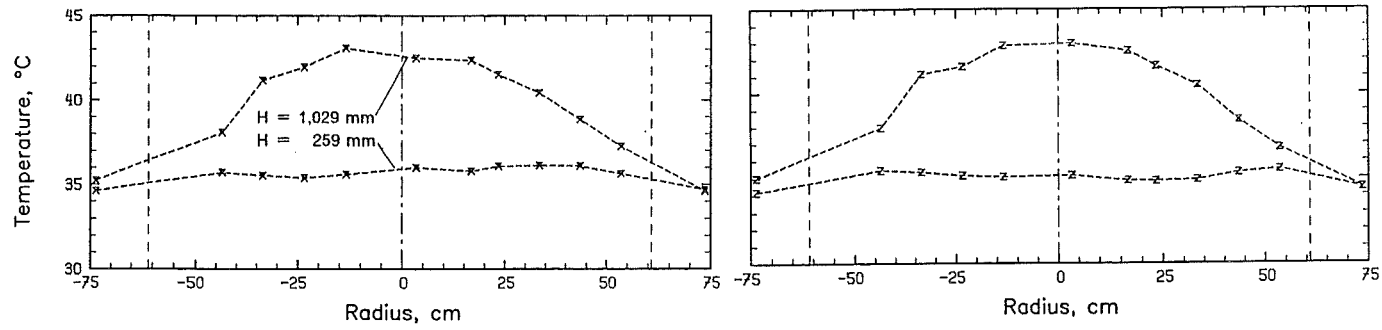

Fig. 99. Influence of the flow path blockages at the IHX primary sides on the measured and computed radial temperature profiles at the top and bottom end of the interwrapper space, tests T14 and T15.

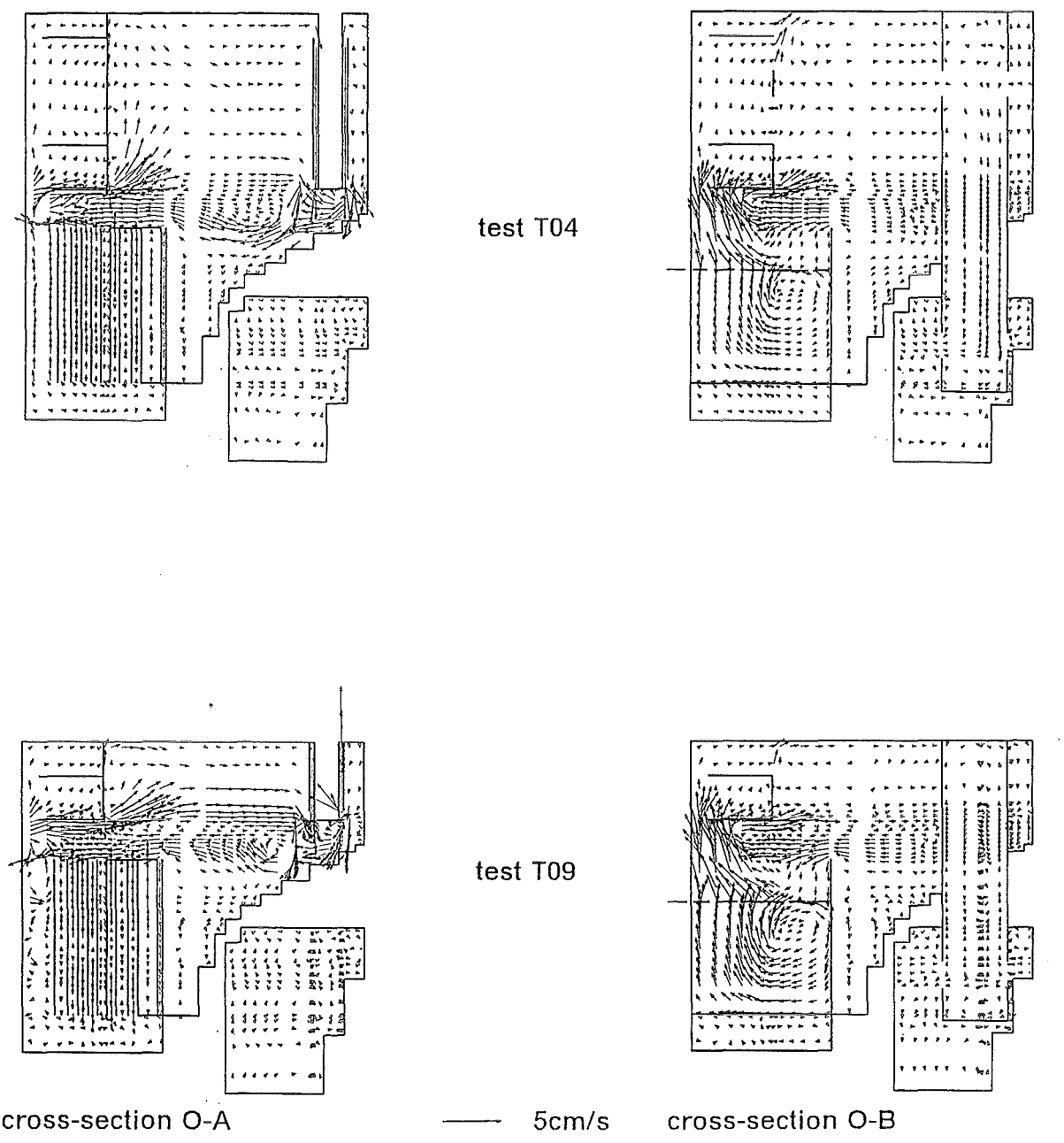

Fig. 100. Influence of the water level in the UP on the computed velocity fields, tests T04 and T09.

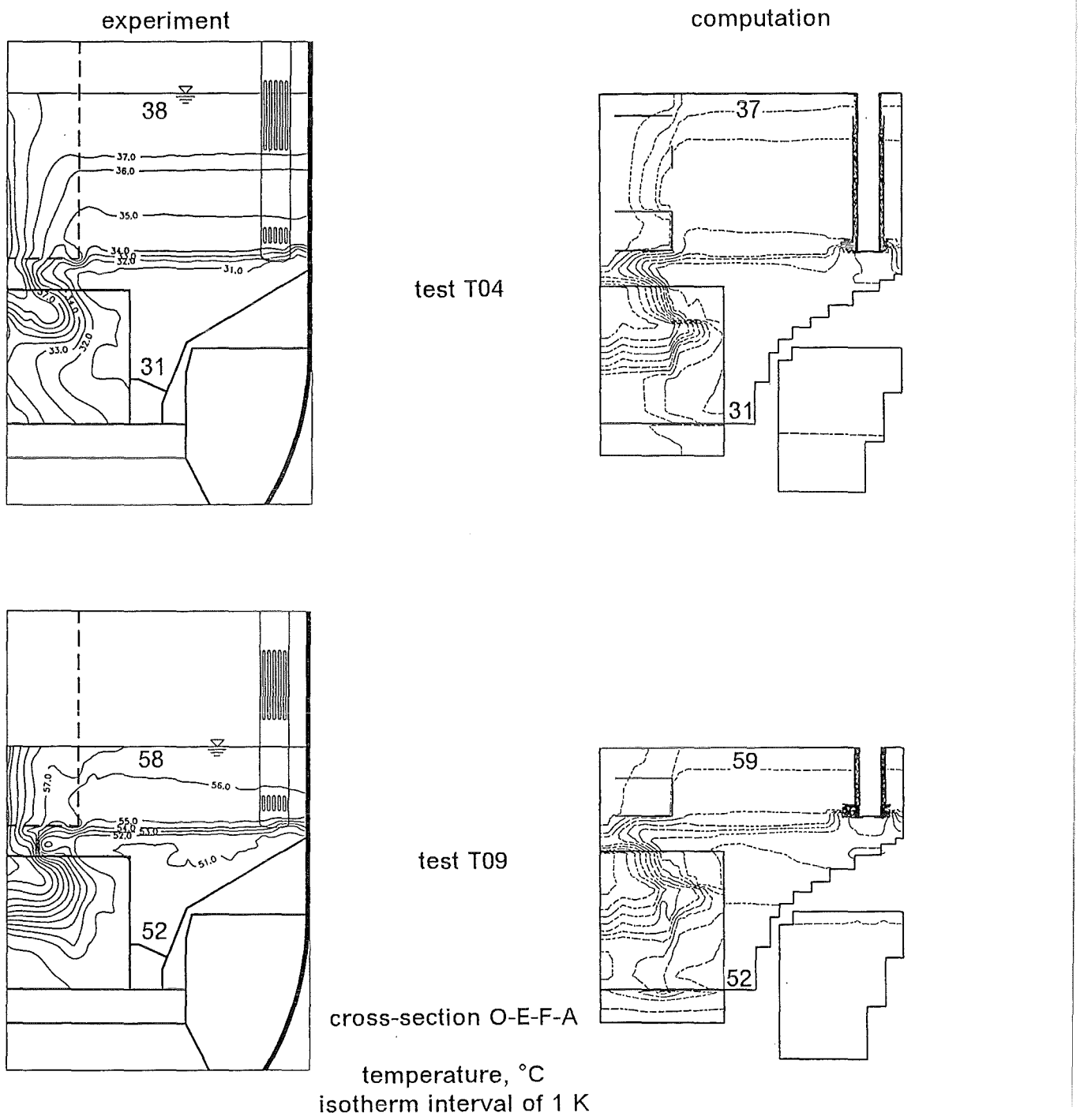

Fig. 101. Influence of the water level in the UP on the measured and computed isotherm fields, tests T04 and T09.

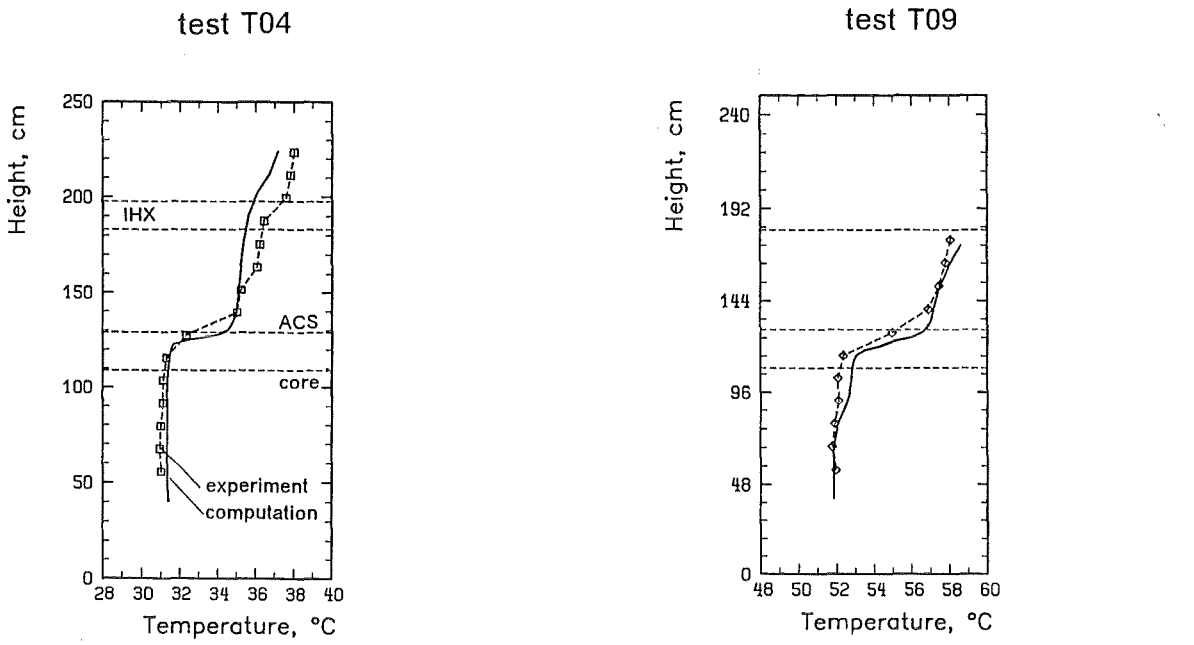

Fig. 102. Influence of the water level in the UP on the measured and computed axial temperature profiles in the UP, tests T04 and T09.

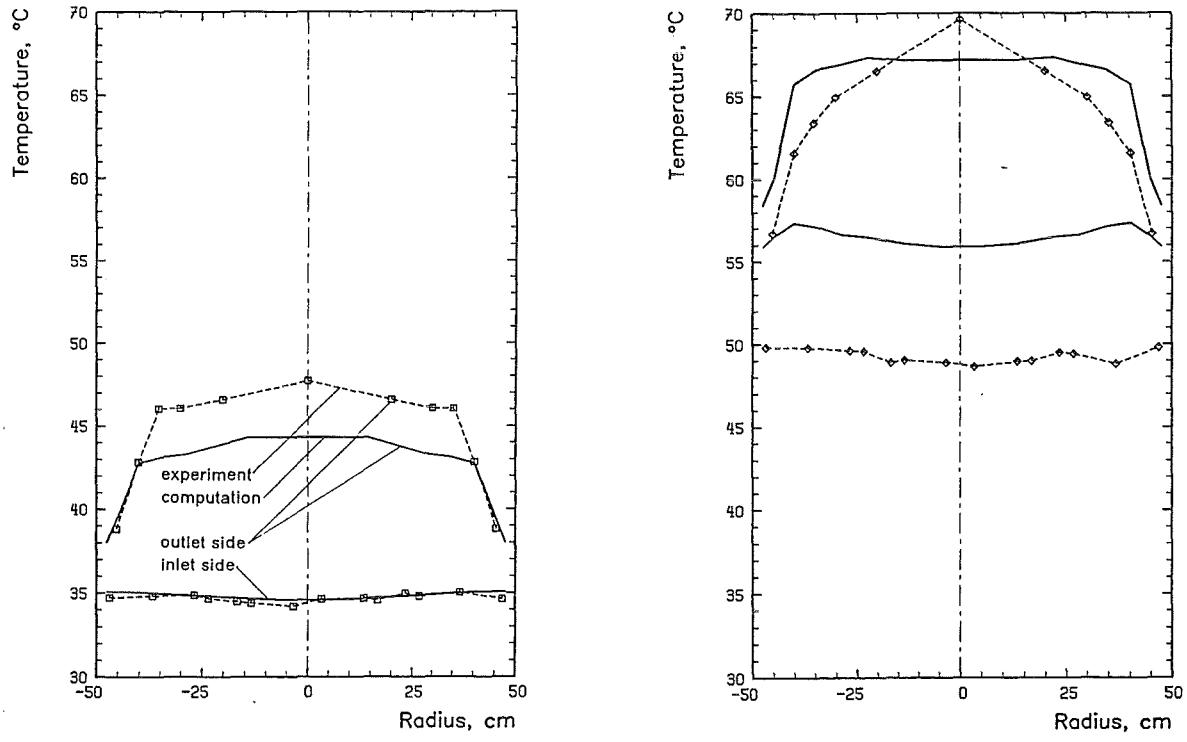

Fig. 103. Influence of the water level in the UP on the measured and computed radial temperature profiles at the inlet and outlet side of heated SAs, tests T04 and T09.

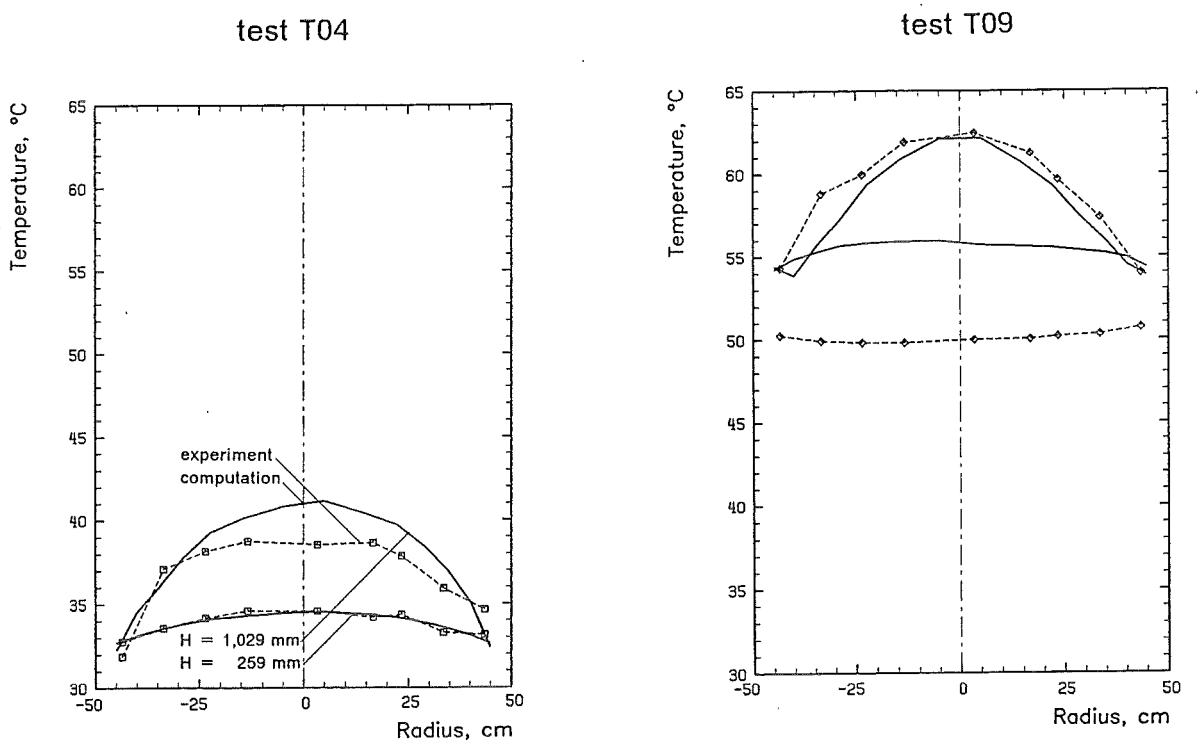

Fig. 104. Influence of the water level in the UP on the measured and computed radial temperature profiles at the top and bottom end of the interwrapper space, tests T04 and T09.

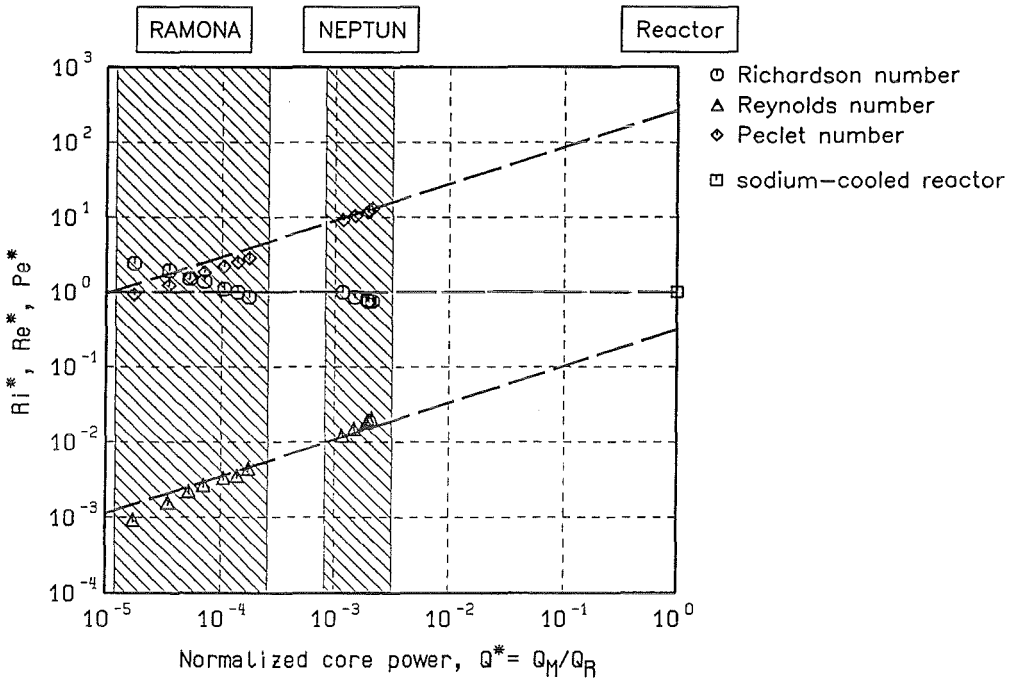

Fig. 105. Characteristic numbers as function of the normalized power.

16. APPENDIX

Table A.1. Data comparison.
Design of the ACS shell.

Test No. / Parameter	Design of ACS shell	Total core power, kW	Number of heated SA groups	Number of operated DHXs	Fluid level in the upper plenum	Flow path via reflector and storage elements	Flow path via IHX primary loops
T01	permeable without skirt	221	6	4	normal	blocked	unblocked
T02	impermeable without skirt	221	6	4	normal	blocked	unblocked
T03	impermeable with skirt	221	6	4	normal	blocked	unblocked

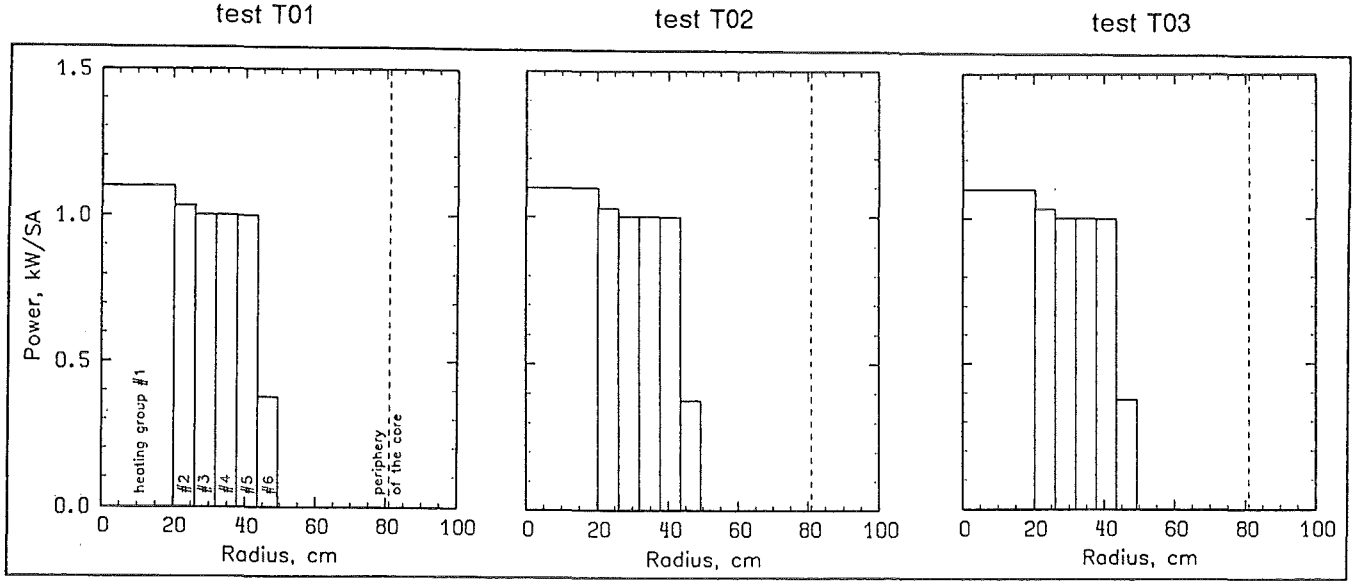

a) Radial power profile.

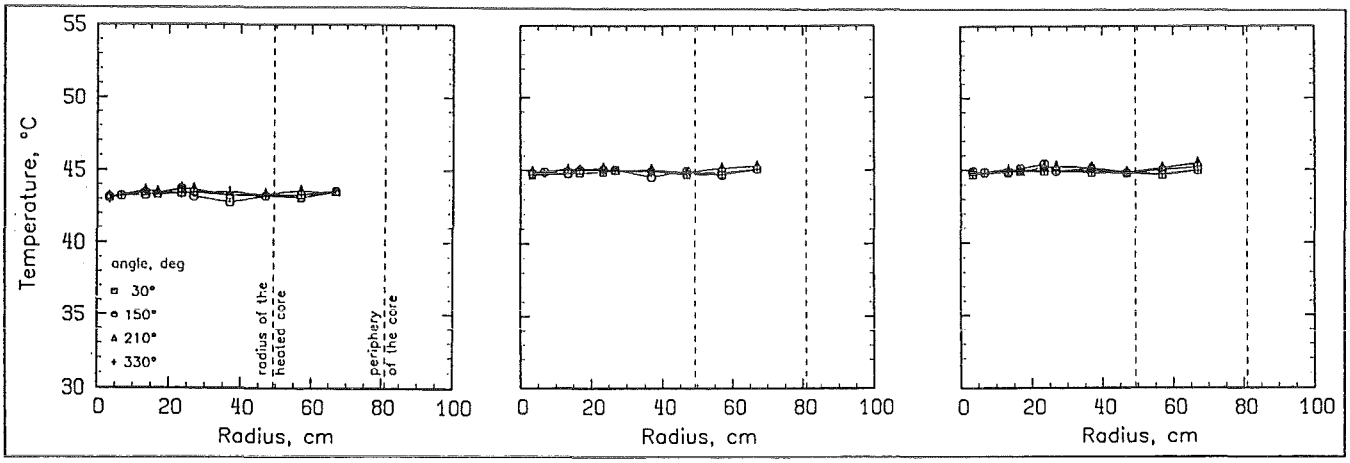

b) Radial temperature profiles of the coolant measured at the SA inlet sides.

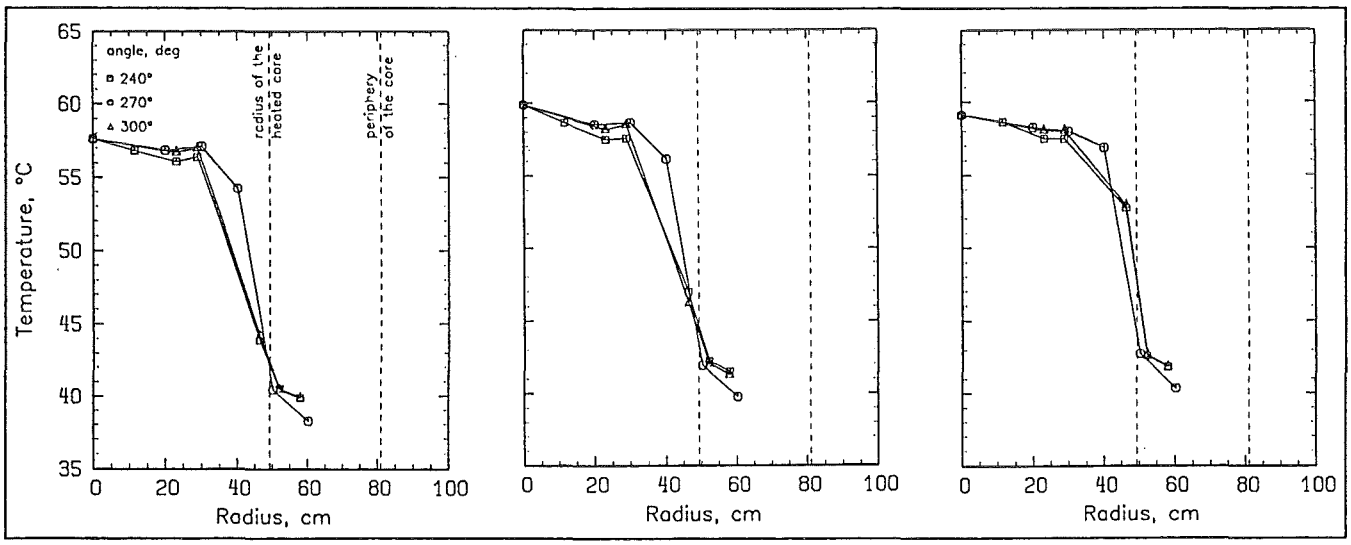

c) Radial temperature profiles of the coolant measured at the SA outlet sides.

Fig. A.1.1. Influence of the ACS design; tests T01, T02, T03.

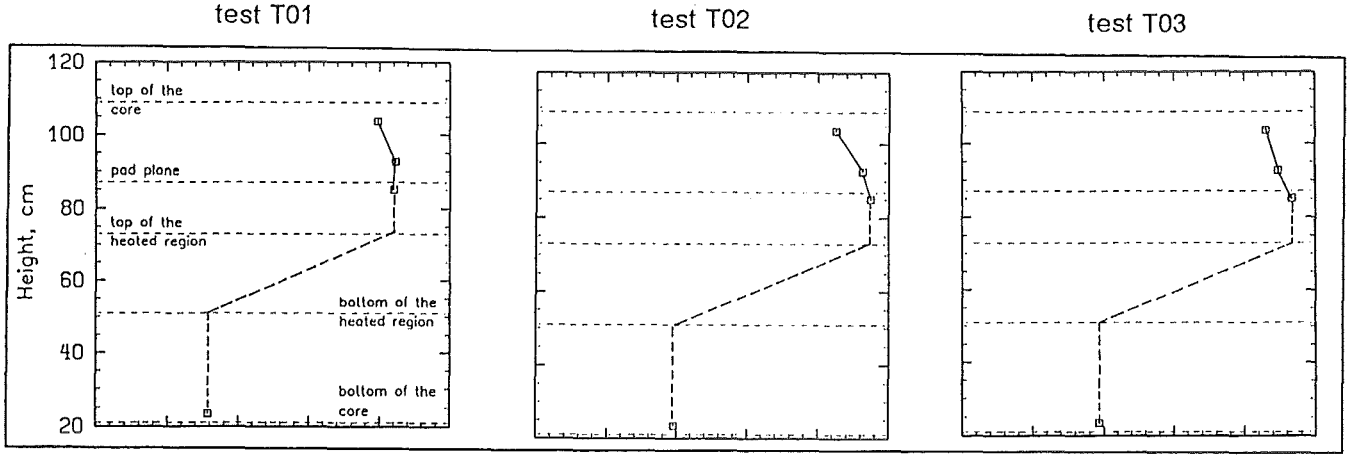

a) Axial temperature profile of the coolant measured inside SA 813 (heating group #4).

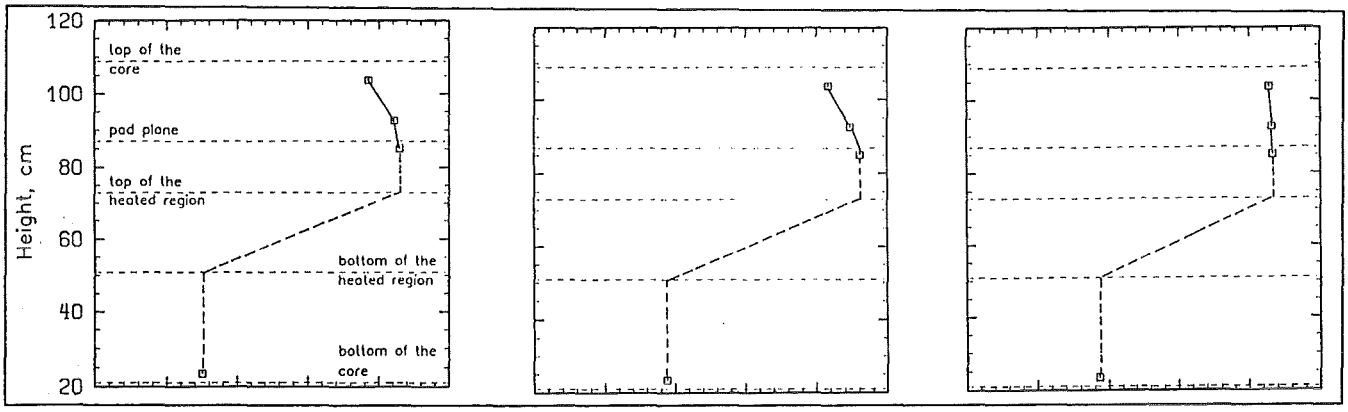

b) Axial temperature profile of the coolant measured inside SA 913 (heating group #5).

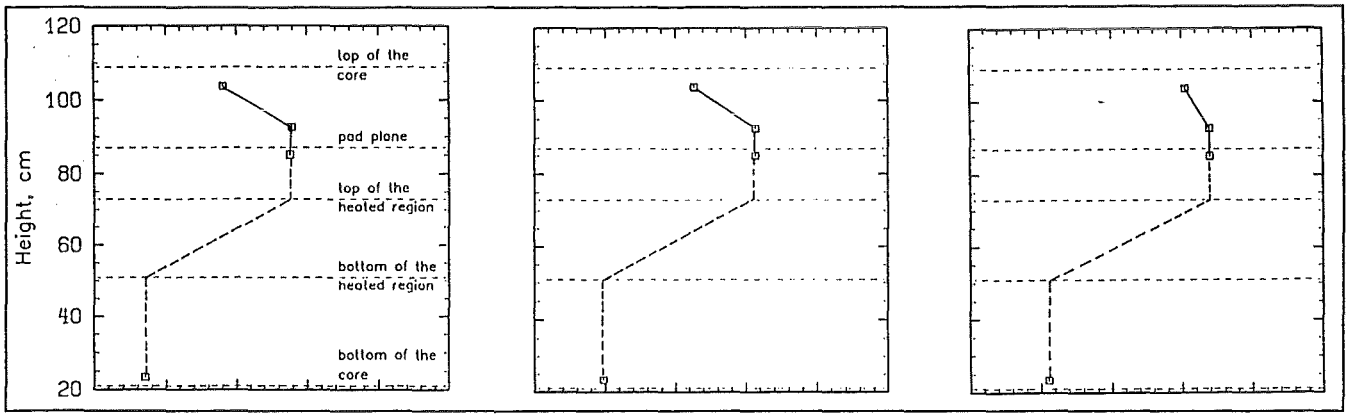

c) Axial temperature profile of the coolant measured inside SA 1017 (heating group #6).

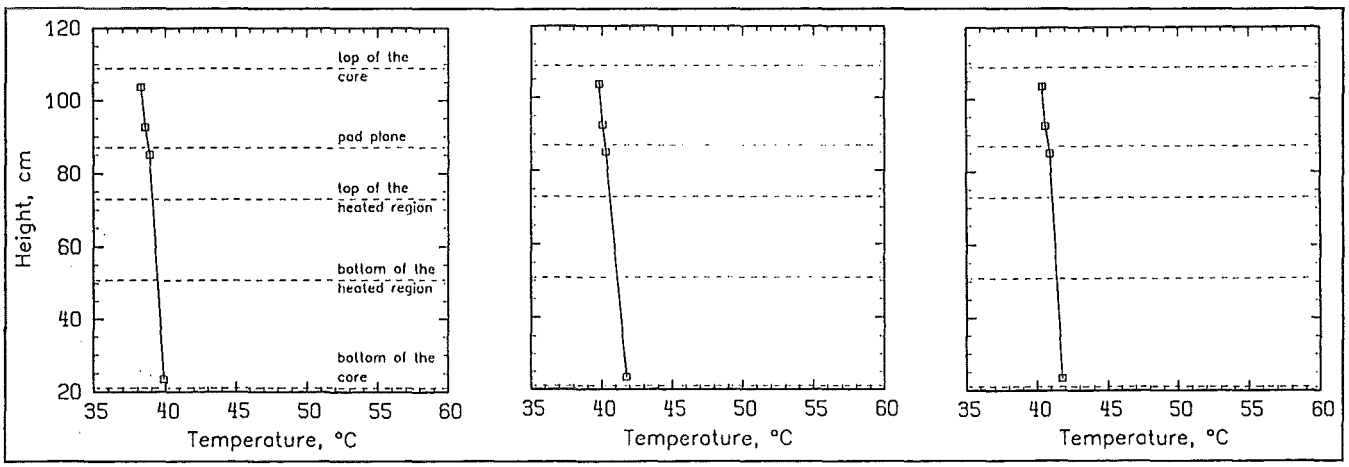

d) Axial temperature profile of the coolant measured inside SA 1319 (unheated group #7).

Fig. A.1.2. Influence of the ACS design; tests T01, T02, T03.

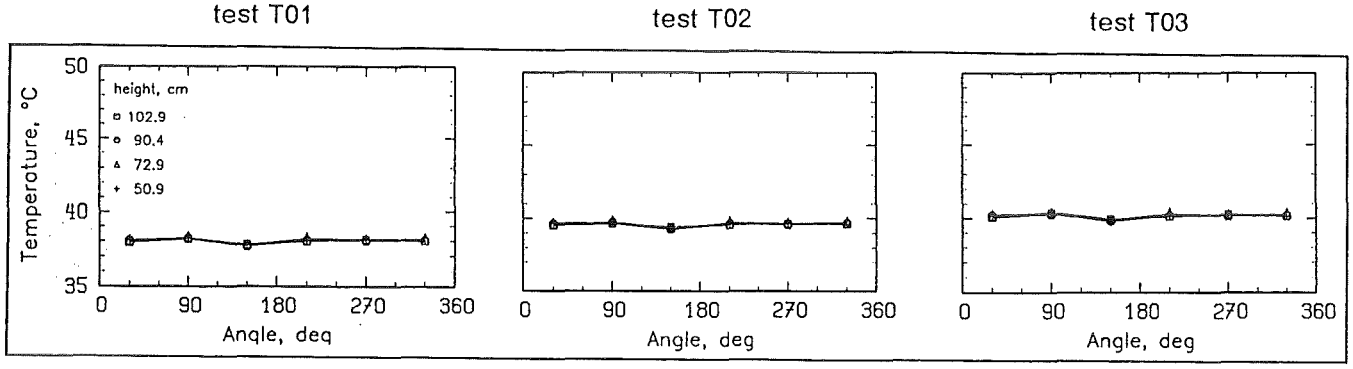

a) Azimuthal temperature profiles of the interstitial flow measured at the core periphery.

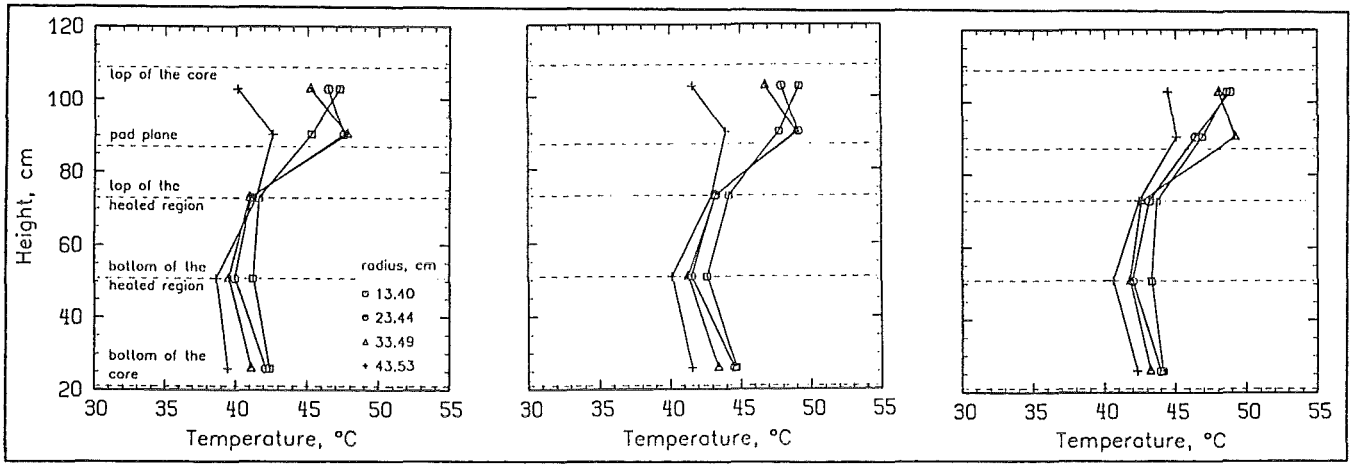

b) Axial temperature profiles of the interstitial flow measured at different radial positions (center → 90°).

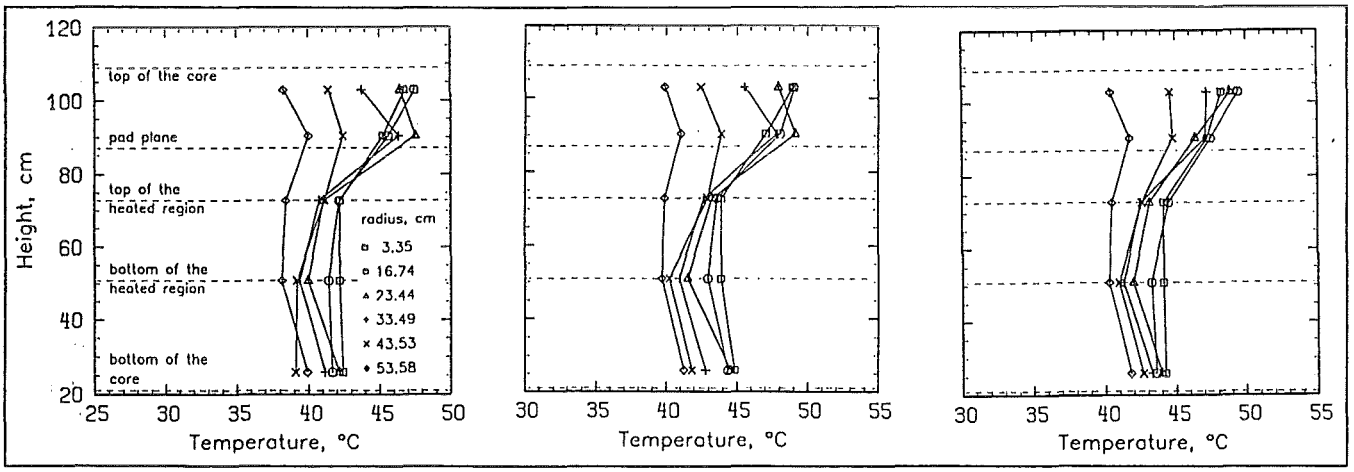

c) Axial temperature profiles of the interstitial flow measured at different radial positions (center → 270°).

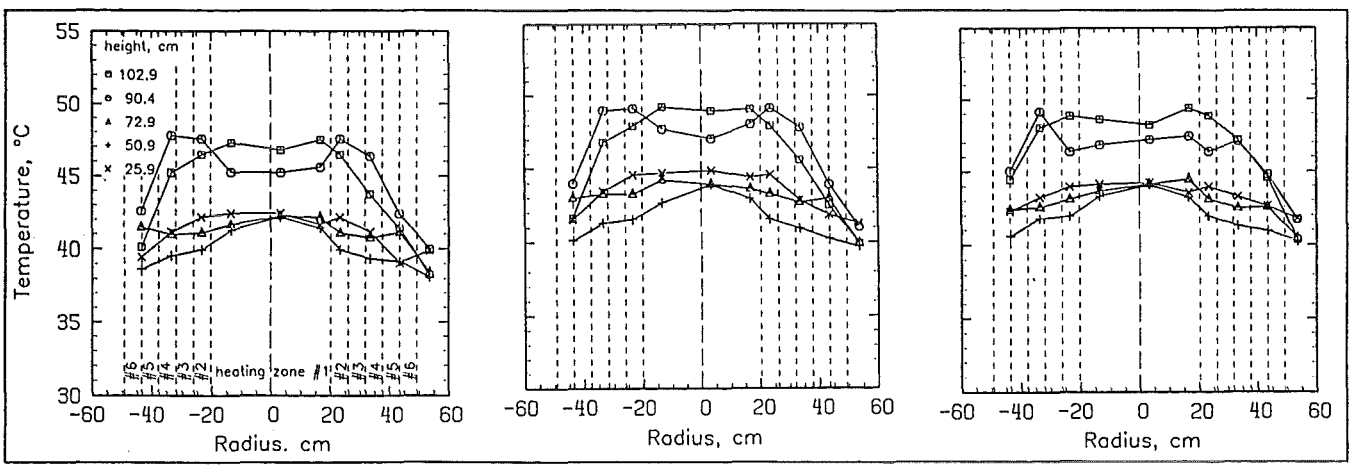

d) Horizontal temperature profiles of the interstitial flow measured across the core (90° → 270°).

Fig. A.1.3. Influence of the ACS design; tests T01, T02, T03.

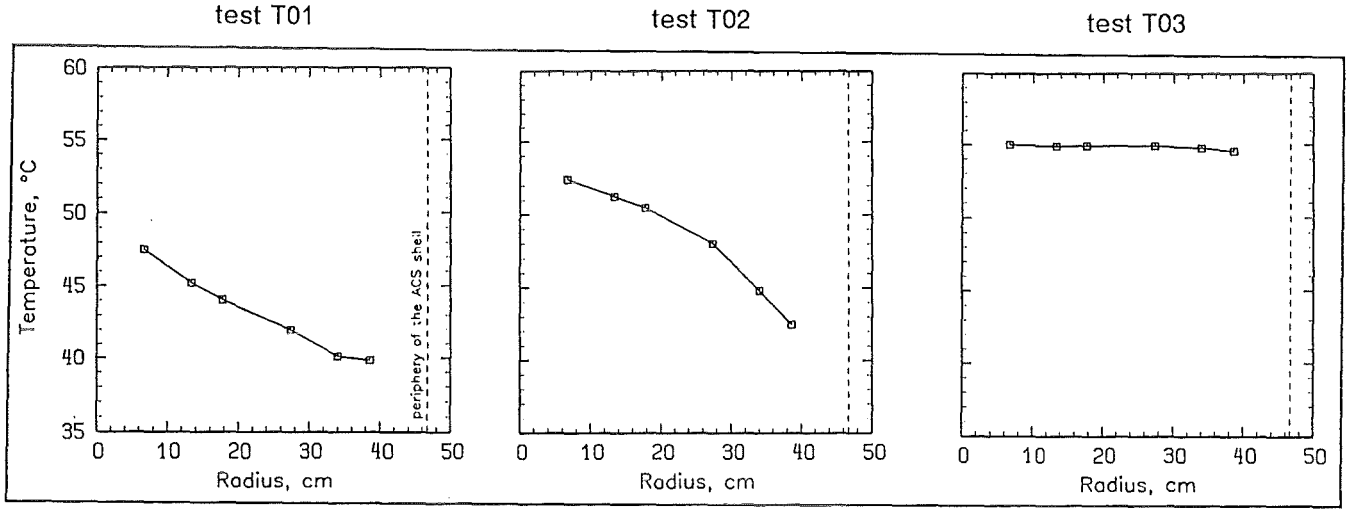

a) Radial temperature profile measured at the bottom end of the ACS (z = 1,248 mm).

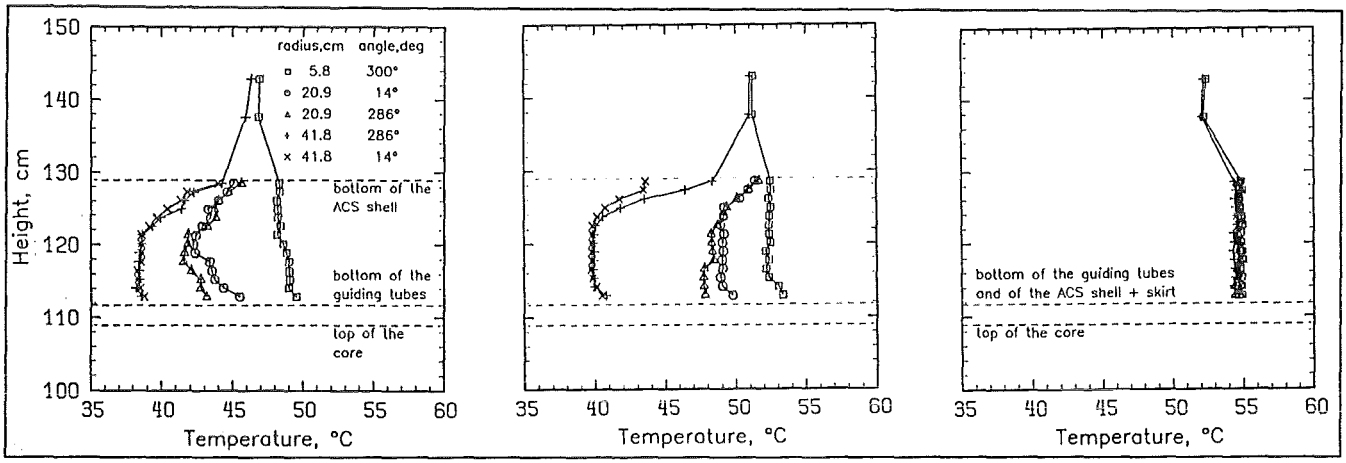

b) Axial temperature profiles measured at the bottom end and inside the lower part of the ACS.

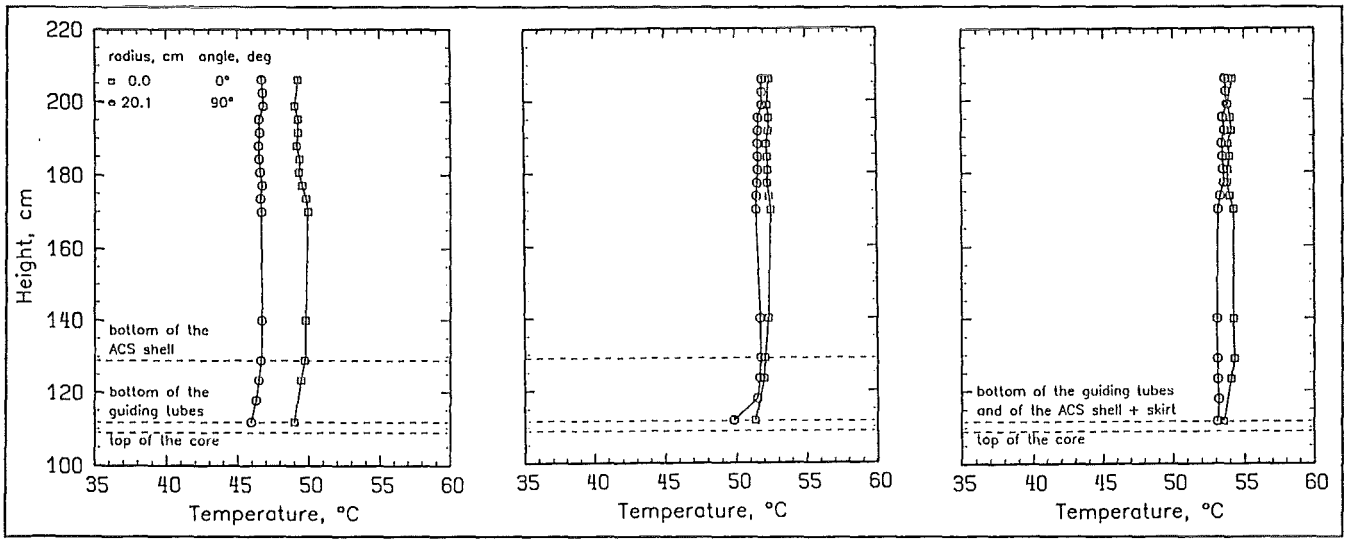

c) Axial temperature profiles measured inside the ACS.

Fig. A.1.4. Influence of the ACS design; tests T01, T02, T03.

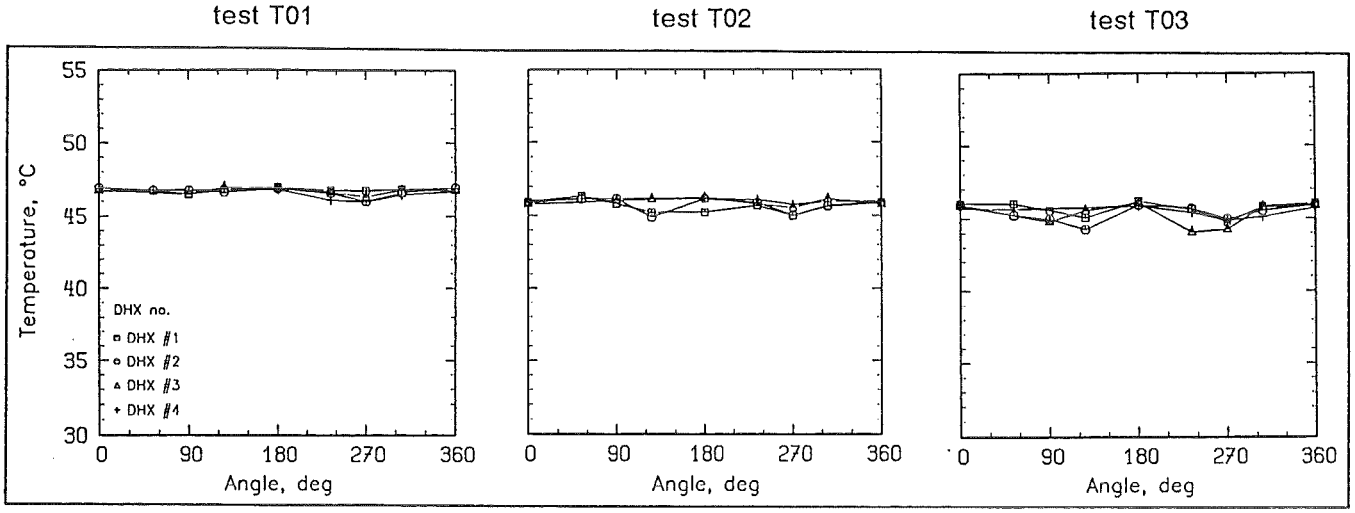

a) Azimuthal temperature profiles measured at the DHX inlet windows (z = 2,299 mm).

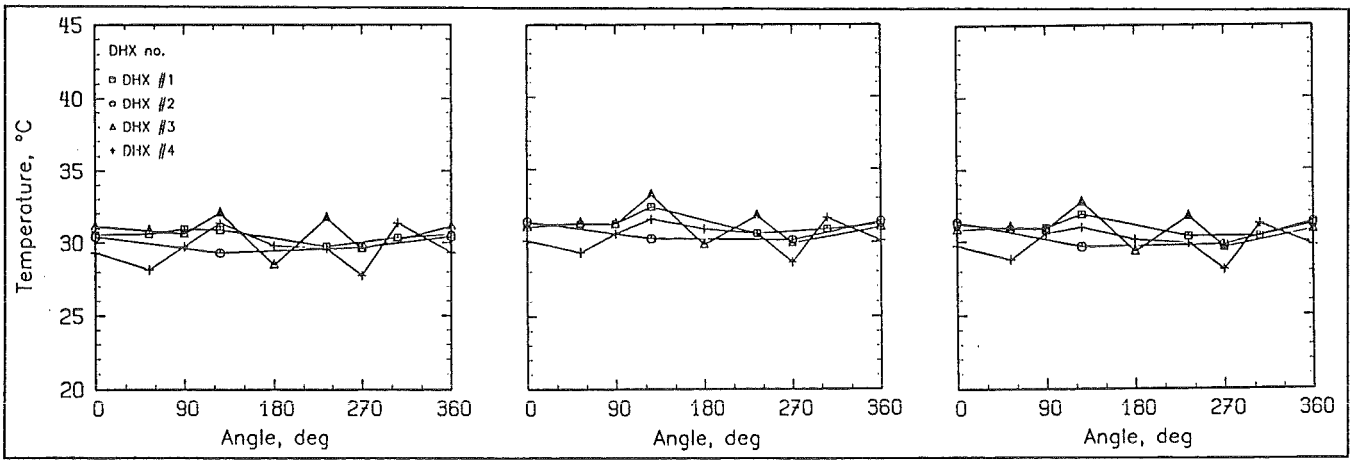

b) Azimuthal temperature profiles measured at the DHX outlet windows (z = 1,391 mm).

Fig. A.1.5. Influence of the ACS design; tests T01, T02, T03.

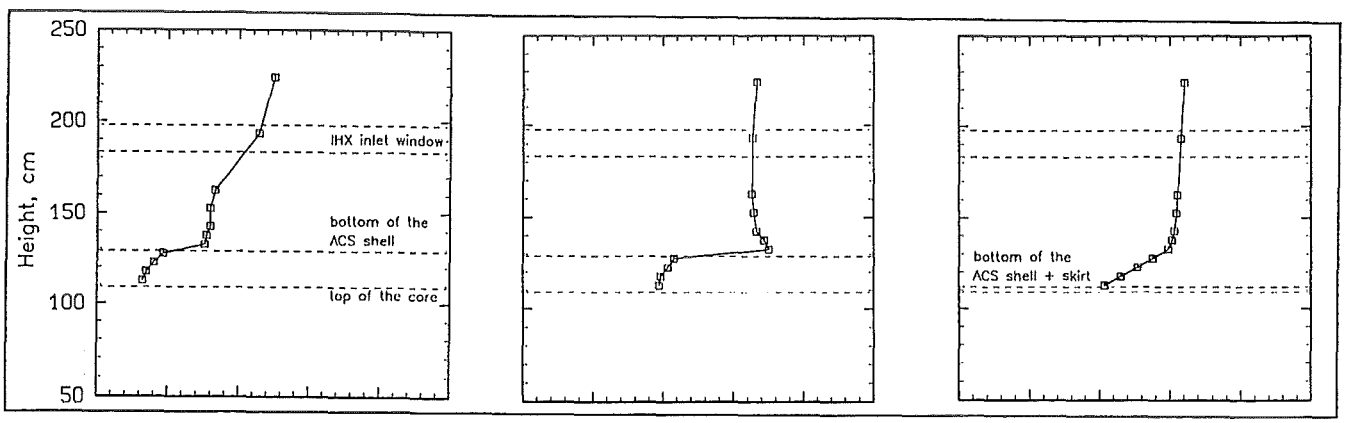

a) Axial temperature profile measured in the UP along the MER-1 device.

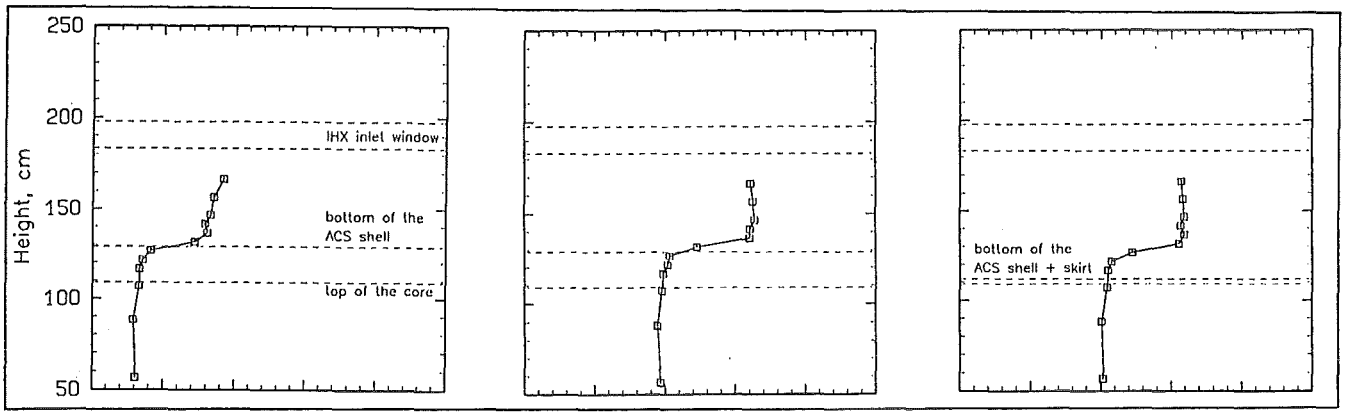

b) Axial temperature profile measured in the UP along the MER-2 device.

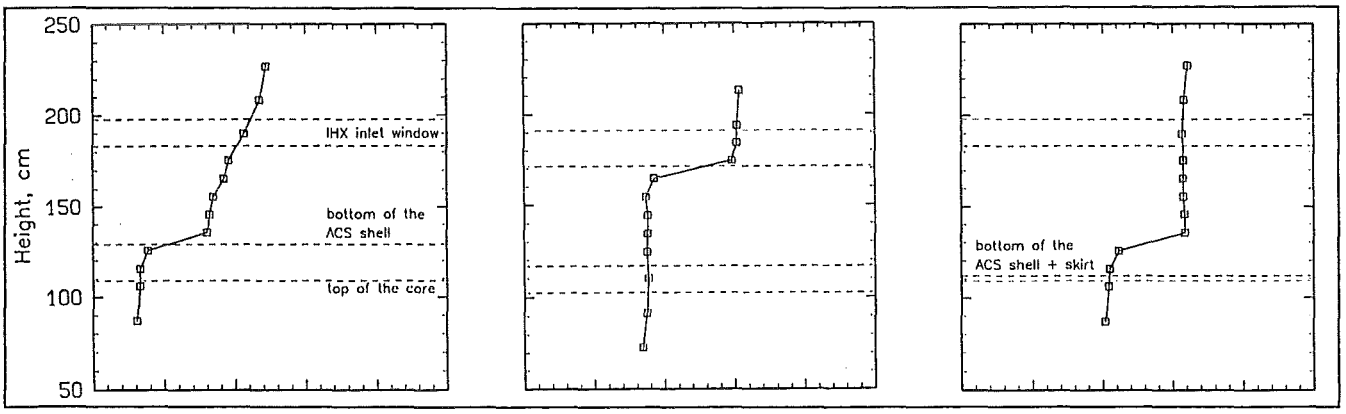

c) Axial temperature profile measured in the UP along the MER-3 device.

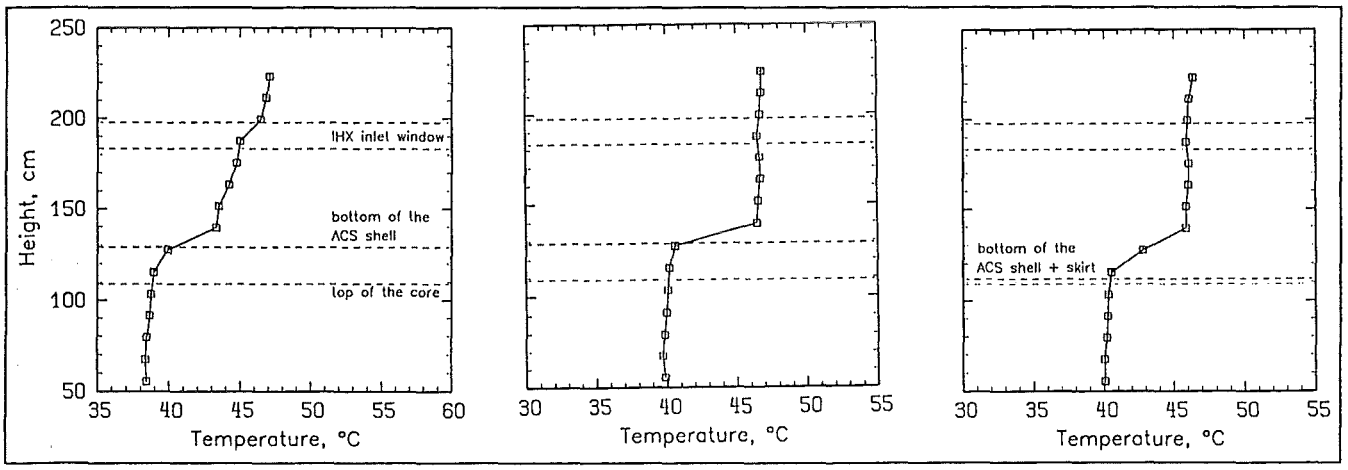

d) Axial temperature profile measured in the UP along the MEL device.

Fig. A.1.6. Influence of the ACS design; tests T01, T02, T03.

Table A.2. Data comparison (cont'd.).

Level of the core power.

a) permeable design of the ACS shell.

Test No. / Parameter	Design of ACS shell	Total core power, kW	Number of heated SA groups	Number of operated DHXs	Fluid level in the upper plenum	Flow path via reflector and storage elements	Flow path via IHX primary loops
T04	permeable without skirt	133	6	4	normal	blocked	unblocked
T05	permeable without skirt	170	6	4	normal	blocked	unblocked
T01	permeable without skirt	221	6	4	normal	blocked	unblocked

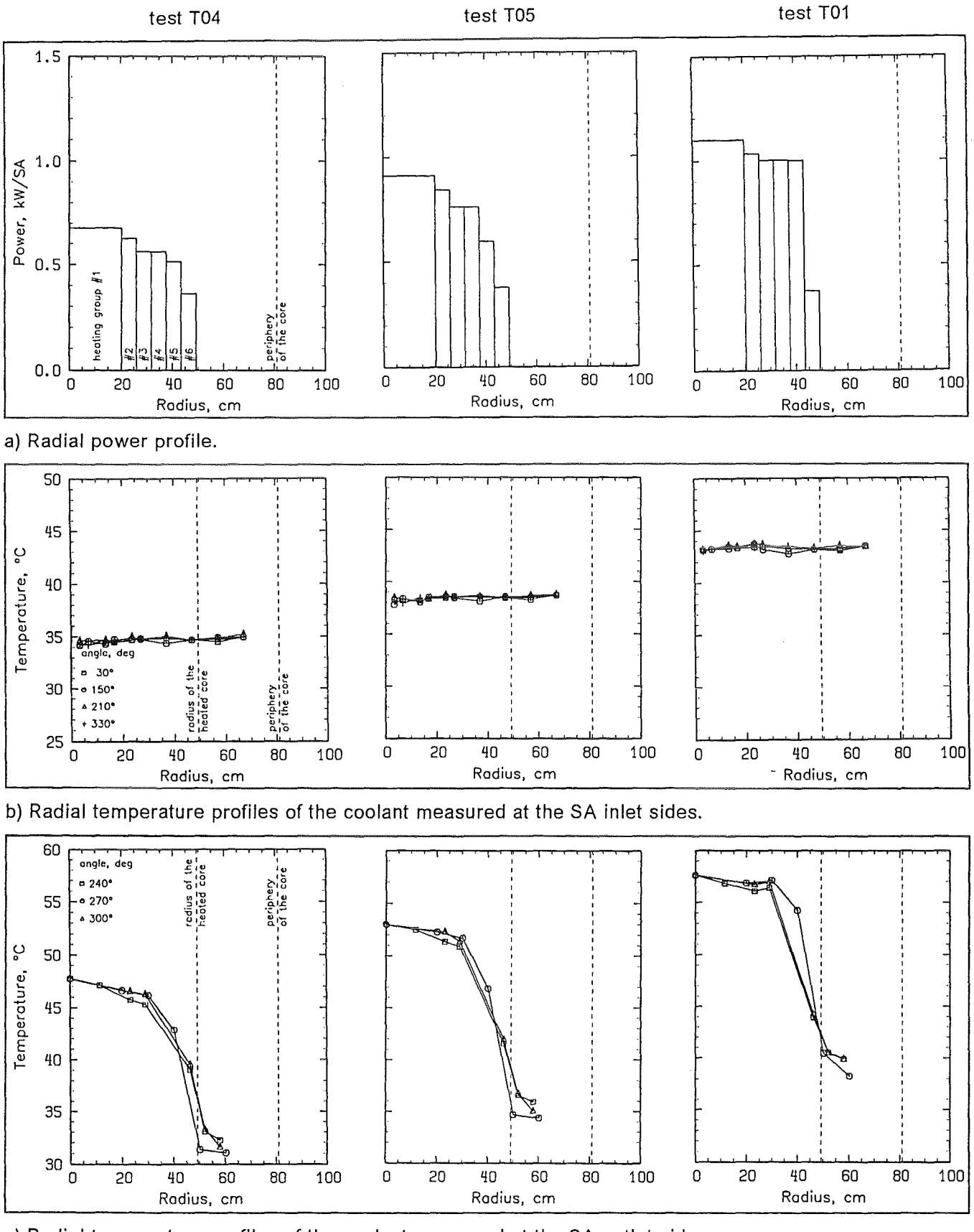

a) Radial power profile.

b) Radial temperature profiles of the coolant measured at the SA inlet sides.

c) Radial temperature profiles of the coolant measured at the SA outlet sides.

Fig. A.2.1. Influence of the core power; tests T04, T05, T01.

test T04 test T05 test T01

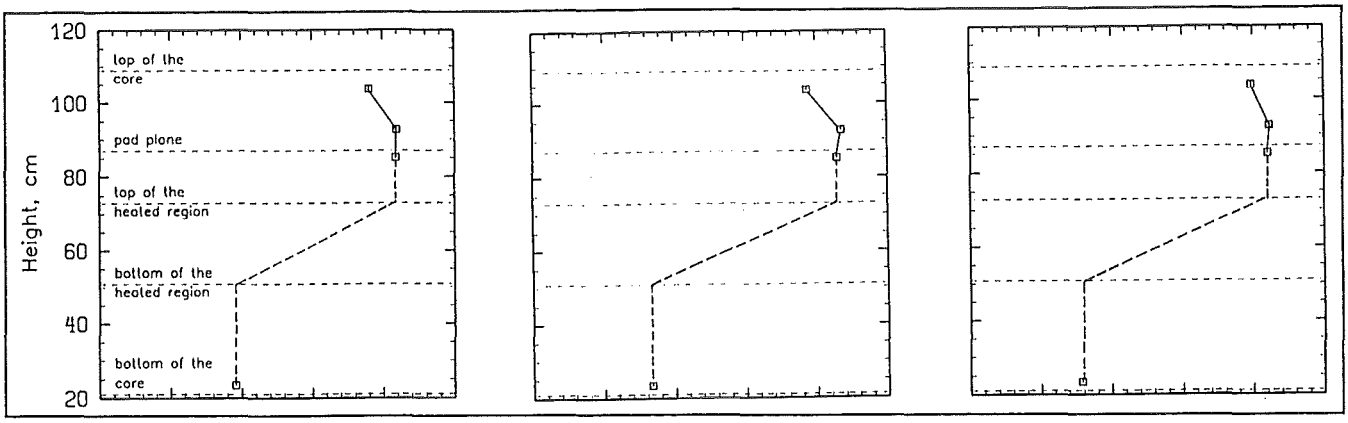

a) Axial temperature profile of the coolant measured inside SA 813 (heating group #4).

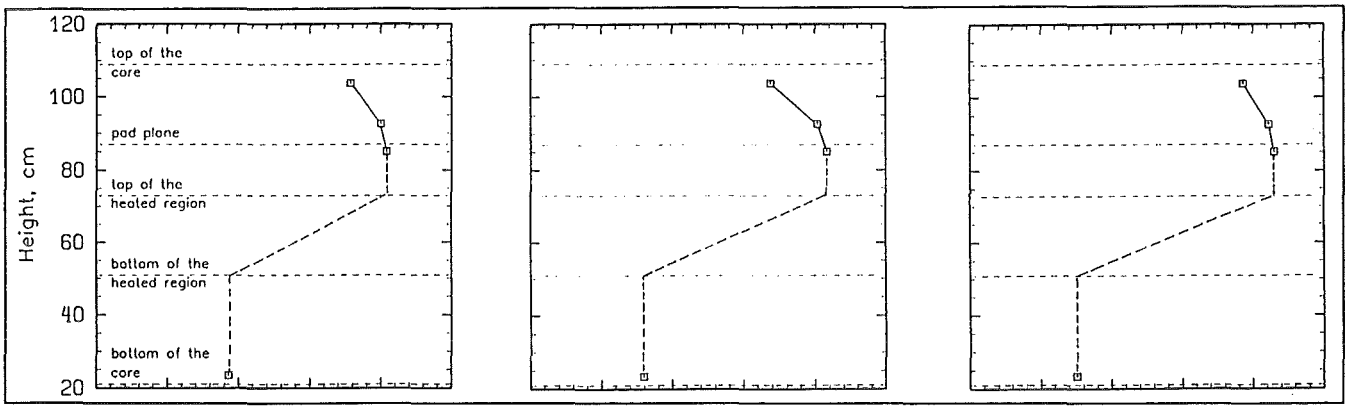

b) Axial temperature profile of the coolant measured inside SA 913 (heating group #5).

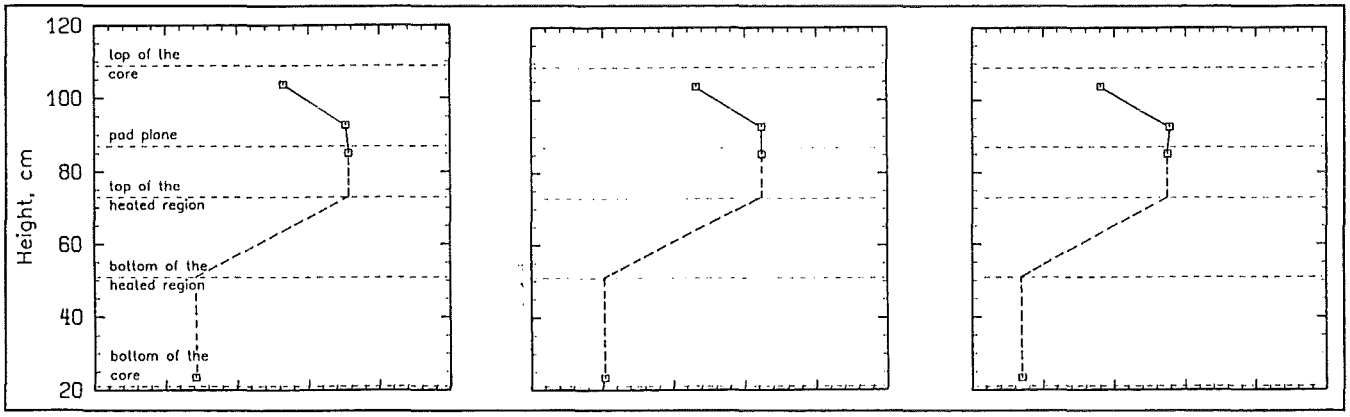

c) Axial temperature profile of the coolant measured inside SA 1017 (heating group #6).

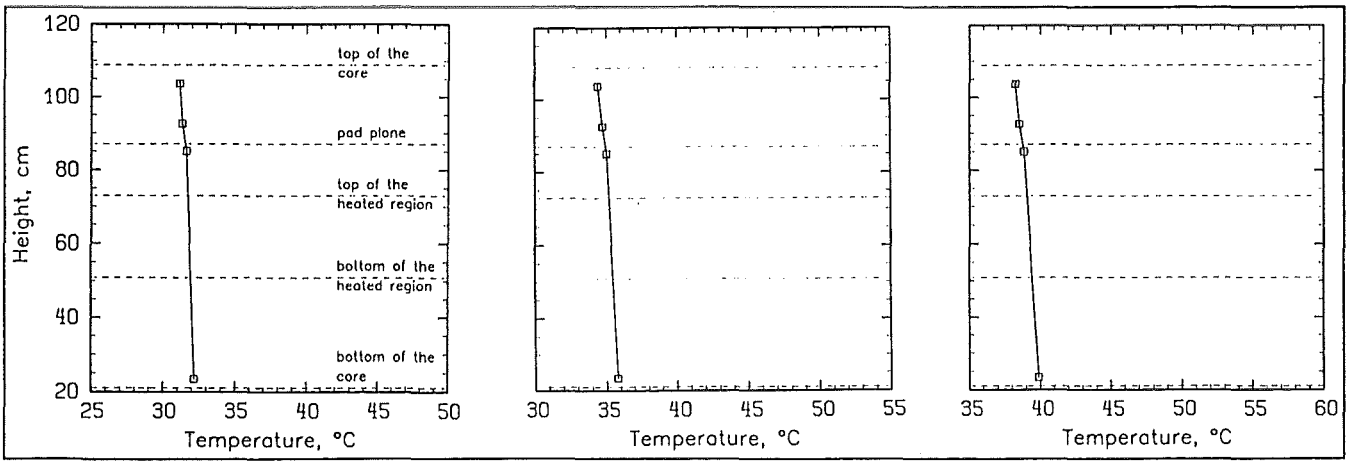

d) Axial temperature profile of the coolant measured inside SA 1319 (unheated group #7).

Fig. A.2.2. Influence of the core power; tests T04, T05, T01.

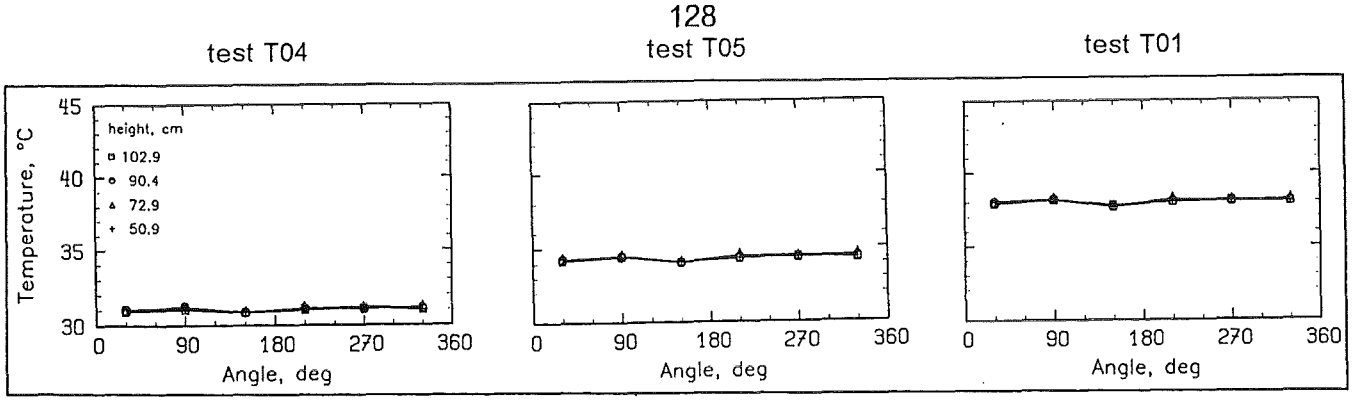

a) Azimuthal temperature profiles of the interstitial flow measured at the core periphery.

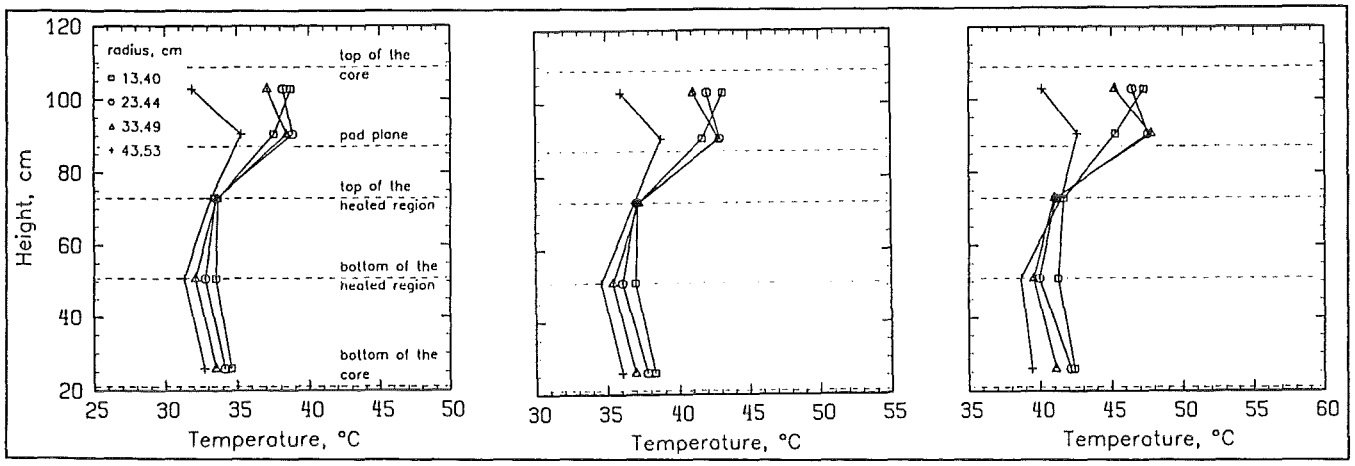

b) Axial temperature profiles of the interstitial flow measured at different radial positions (center → 90°).

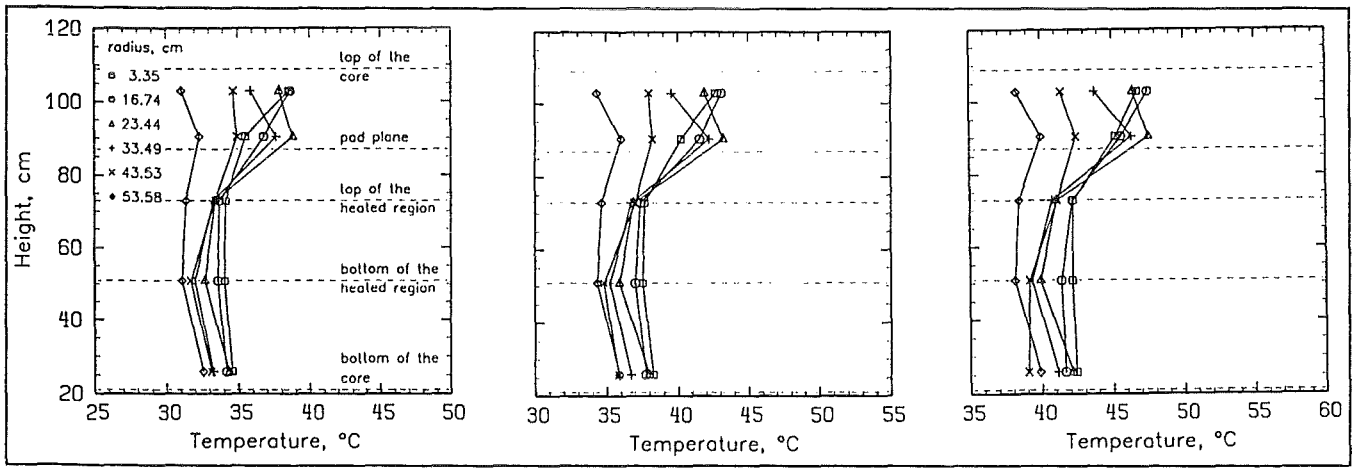

c) Axial temperature profiles of the interstitial flow measured at different radial positions (center → 270°).

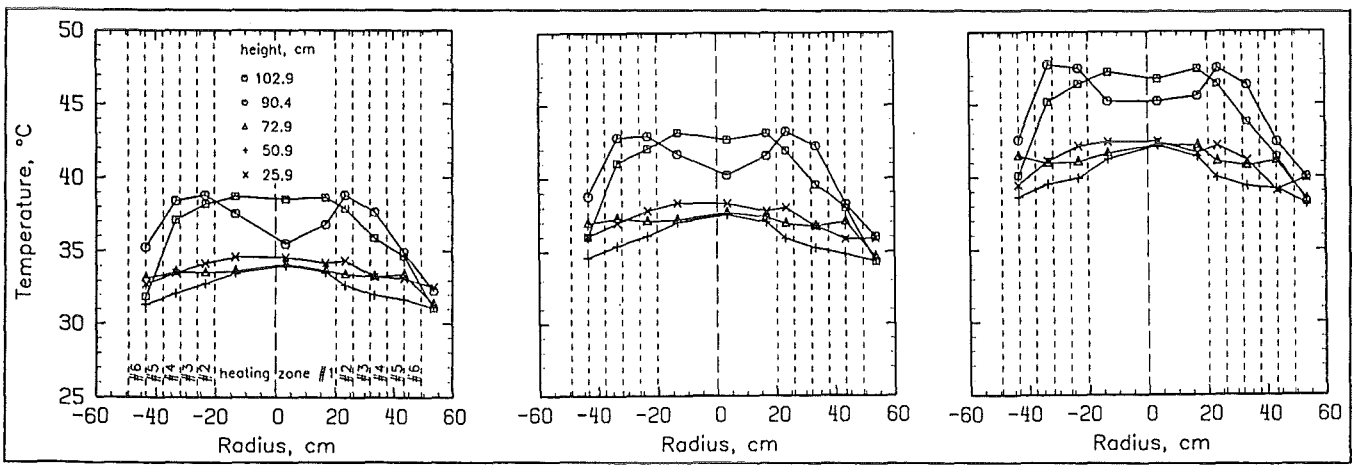

d) Horizontal temperature profiles of the interstitial flow measured across the core (90° → 270°).

Fig. A.2.3. Influence of the core power; tests T04, T05, T01.

test T04 test T05 test T01

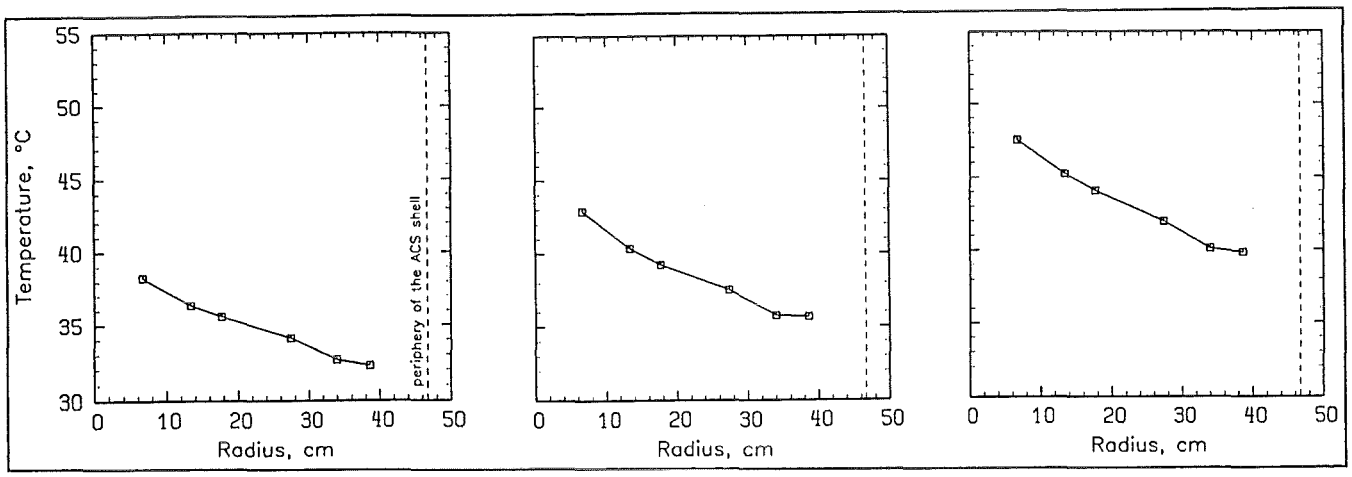

a) Radial temperature profile measured at the bottom end of the ACS (z = 1,248 mm).

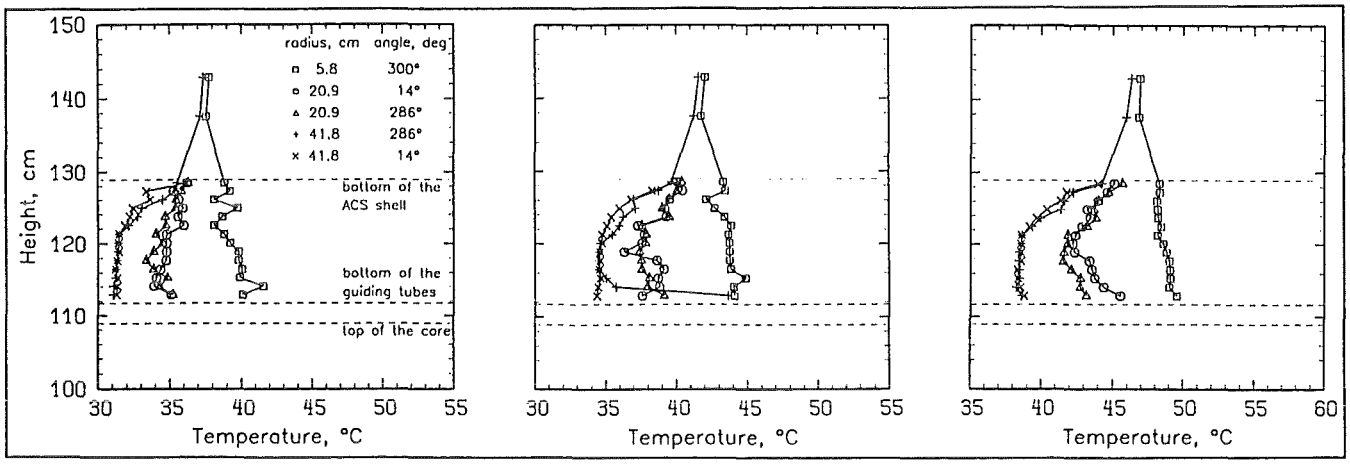

b) Axial temperature profiles measured at the bottom end and inside the lower part of the ACS.

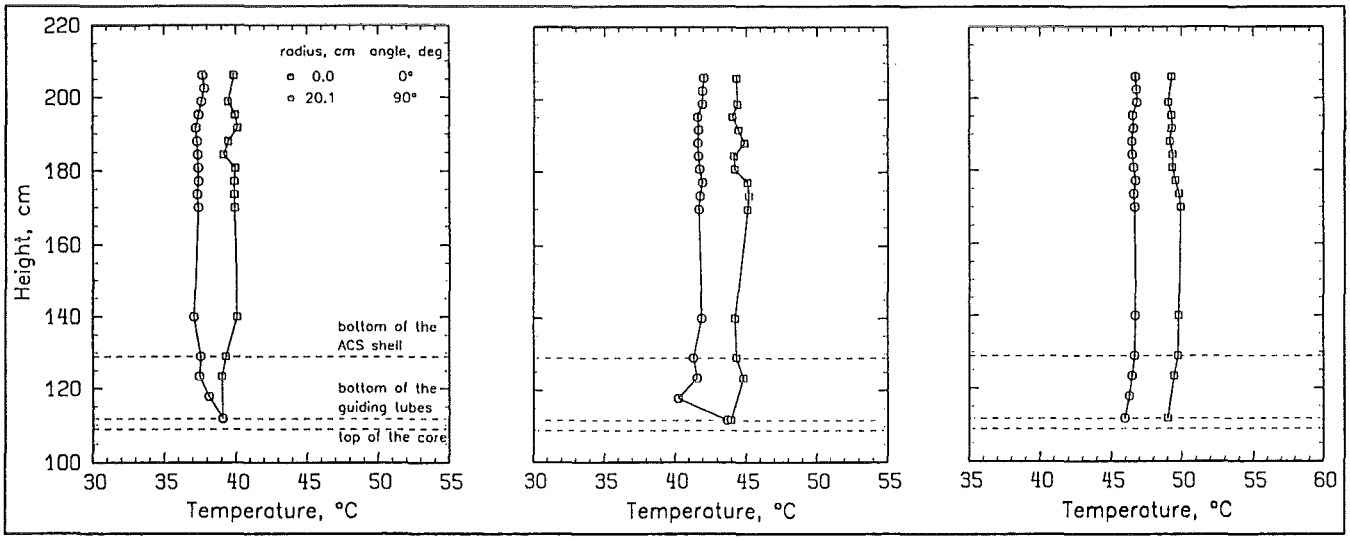

c) Axial temperature profiles measured inside the ACS.

Fig. A.2.4. Influence of the core power; tests T04, T05, T01.

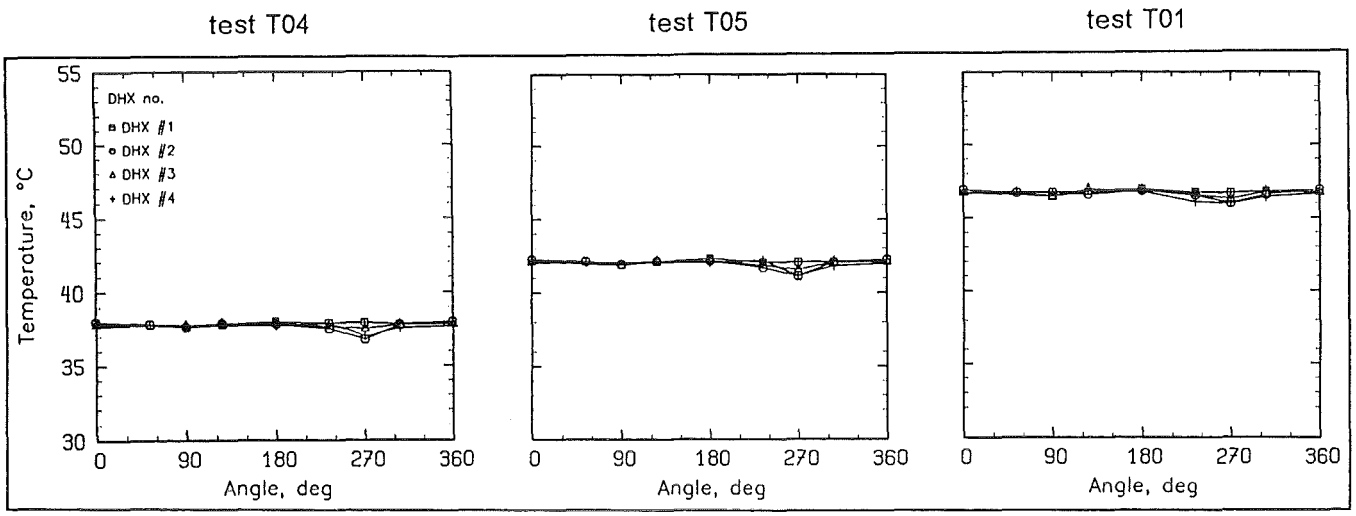

a) Azimuthal temperature profiles measured at the DHX inlet windows (z = 2,299 mm).

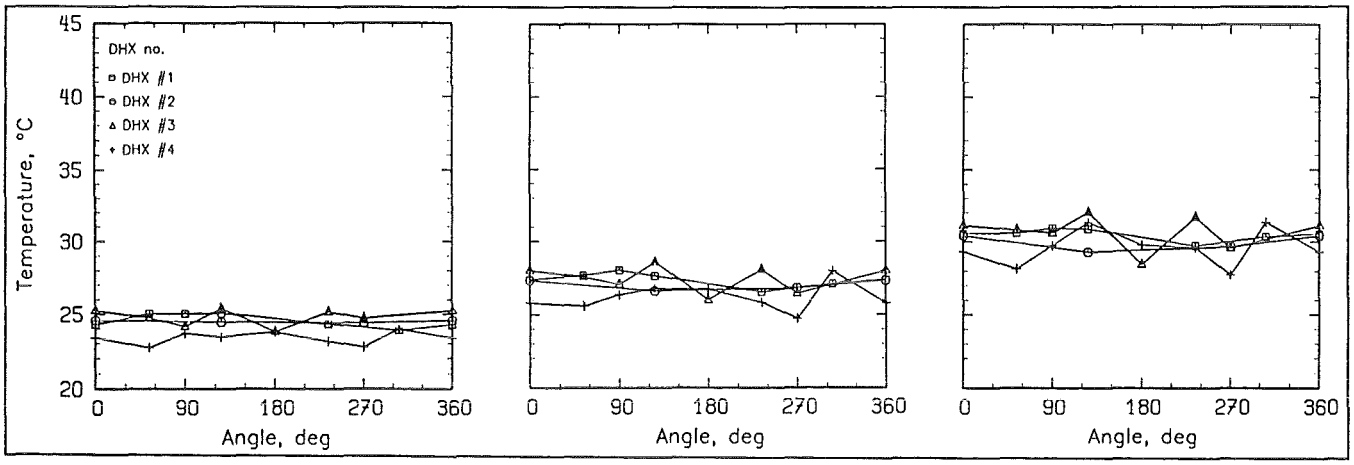

b) Azimuthal temperature profiles measured at the DHX outlet windows (z = 1,391 mm).

Fig. A.2.5. Influence of the core power; tests T04, T05, T01.

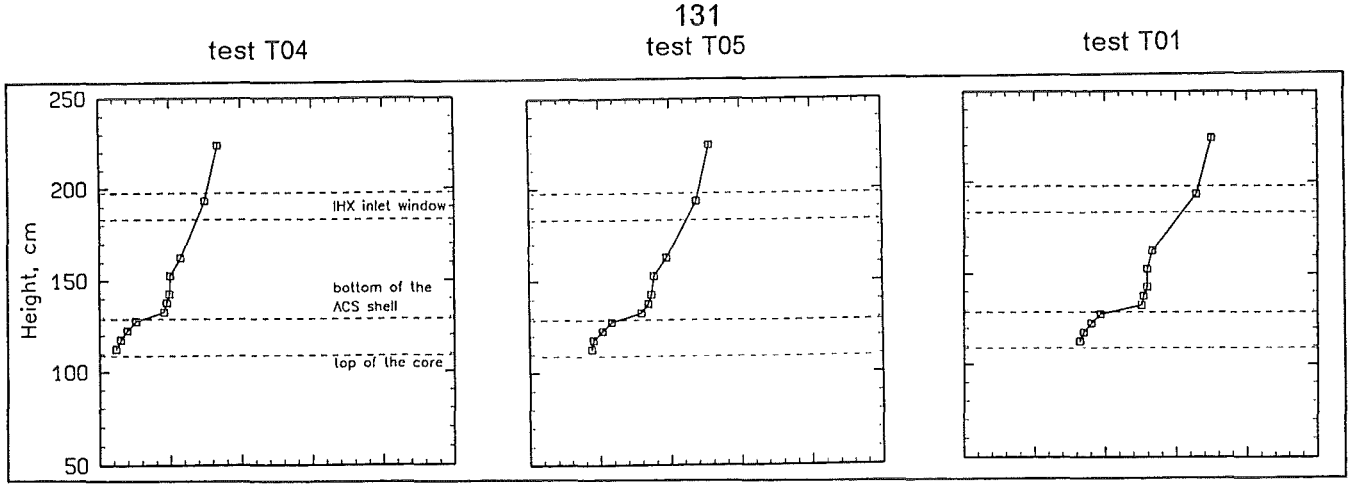

a) Axial temperature profile measured in the UP along the MER-1 device.

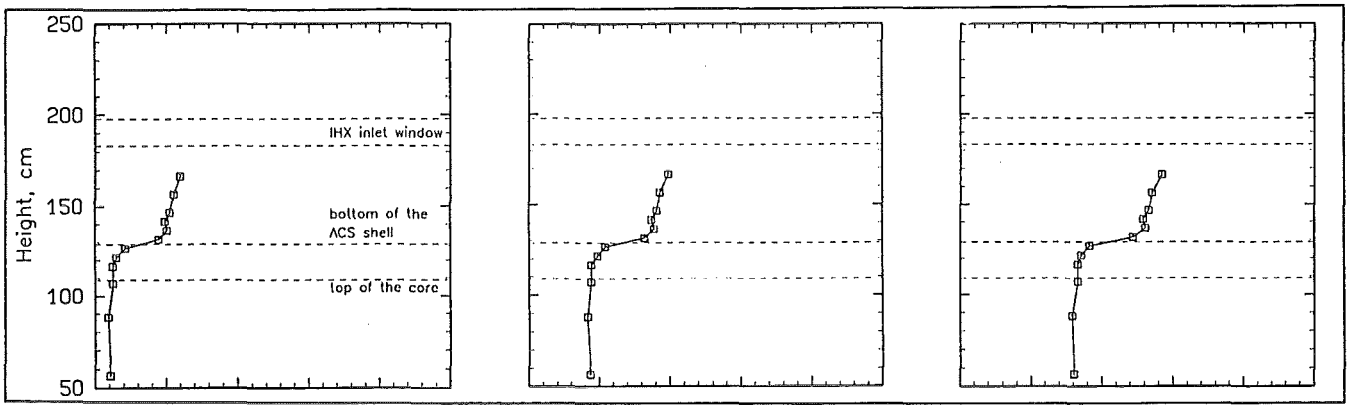

b) Axial temperature profile measured in the UP along the MER-2 device.

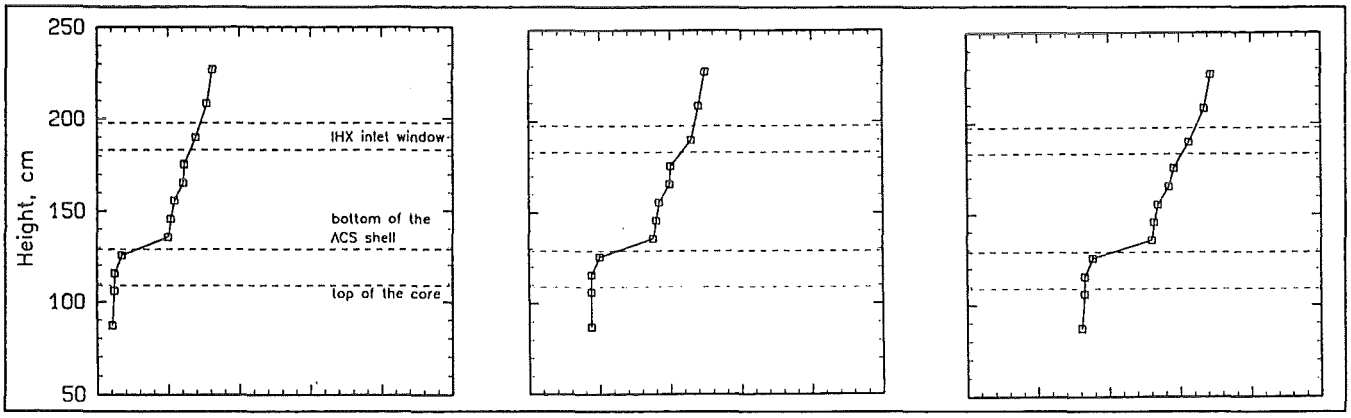

c) Axial temperature profile measured in the UP along the MER-3 device.

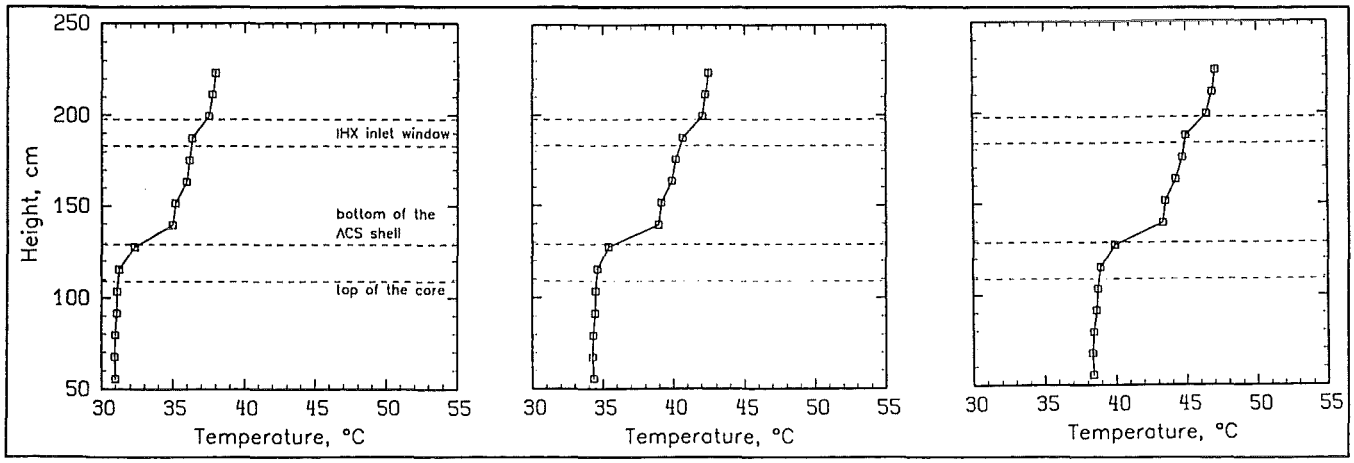

d) Axial temperature profile measured in the UP along the MEL device.

Fig. A.2.6. Influence of the core power; tests T04, T05, T01.

Table A.3. Data comparison (cont'd.).
Level of the core power.
b) impermeable design of the ACS shell.

Test No. / Parameter	Design of ACS shell	Total core power, kW	Number of heated SA groups	Number of operated DHXs	Fluid level in the upper plenum	Flow path via reflector and storage elements	Flow path via IHX primary loops
T06	impermeable without skirt	133	6	4	normal	blocked	unblocked
T07	impermeable without skirt	170	6	4	normal	blocked	unblocked
T02	impermeable without skirt	221	6	4	normal	blocked	unblocked

test T06 test T07 test T02

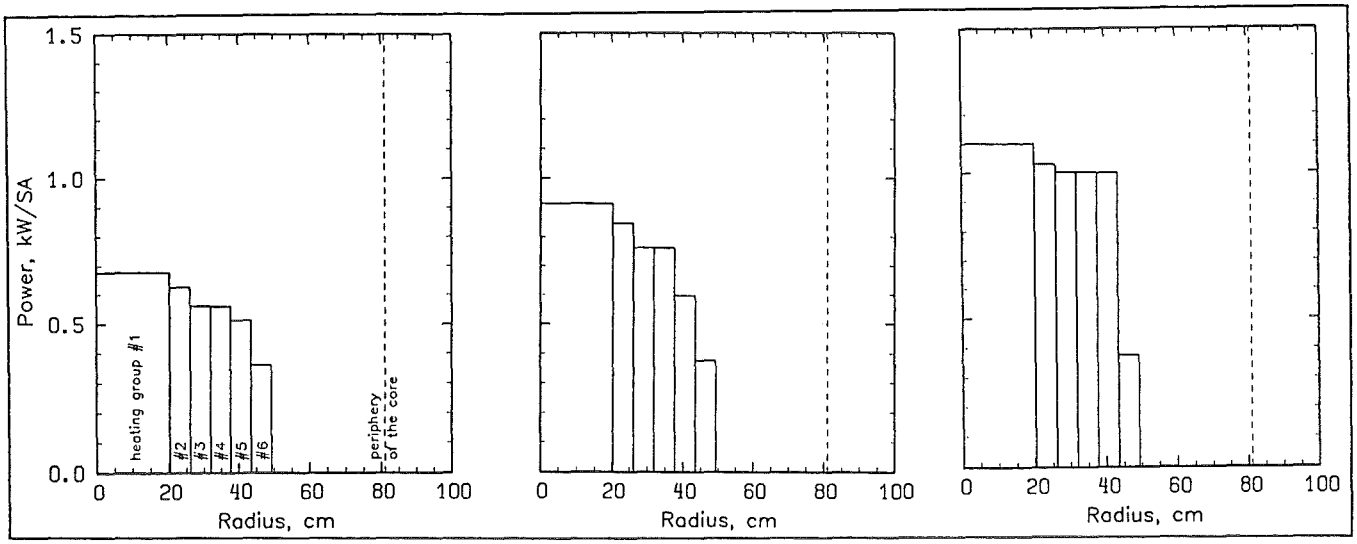

a) Radial power profile.

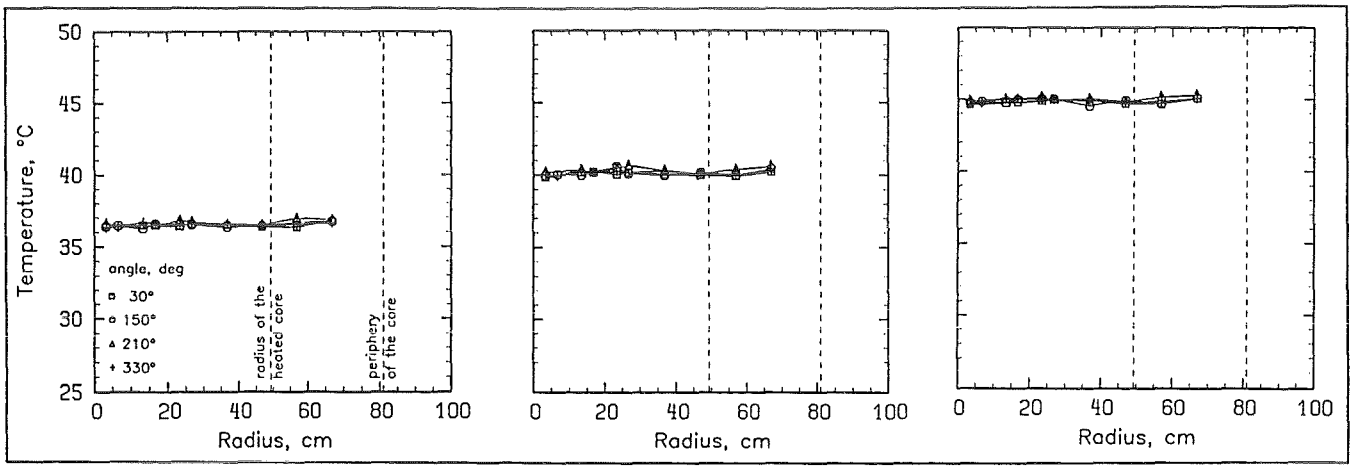

b) Radial temperature profiles of the coolant measured at the SA inlet sides.

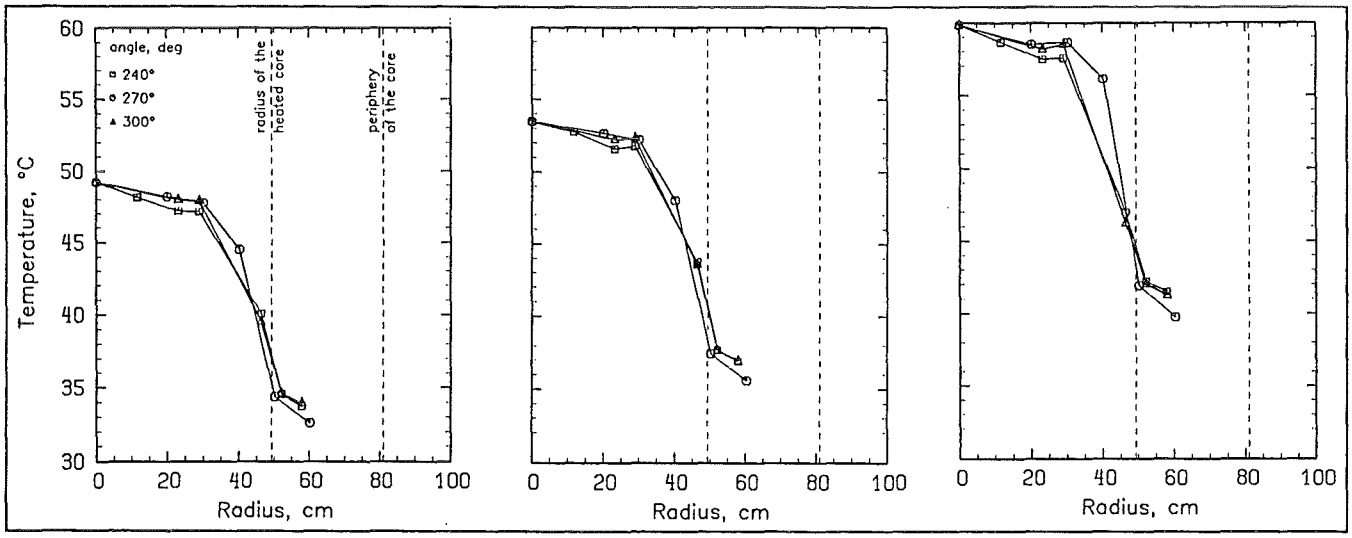

c) Radial temperature profiles of the coolant measured at the SA outlet sides.

Fig. A.3.1. Influence of the core power; tests T06, T07, T02.

test T06 test T07 test T02

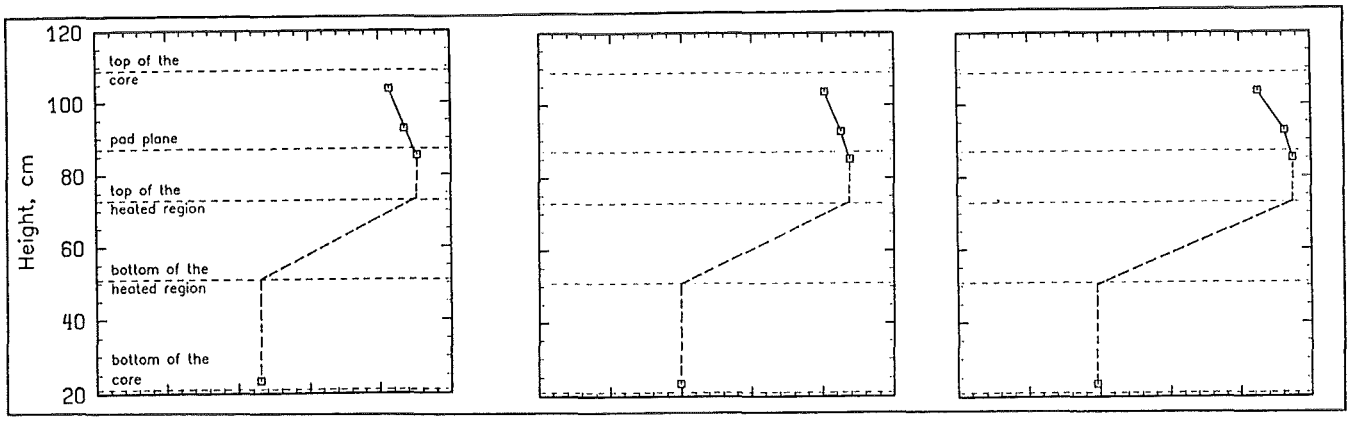

a) Axial temperature profile of the coolant measured inside SA 813 (heating group #4).

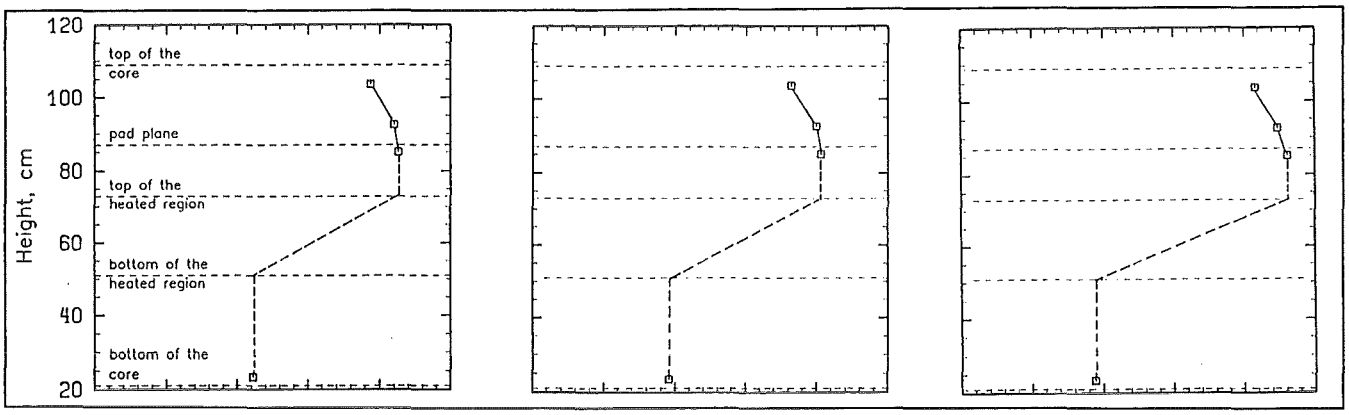

b) Axial temperature profile of the coolant measured inside SA 913 (heating group #5).

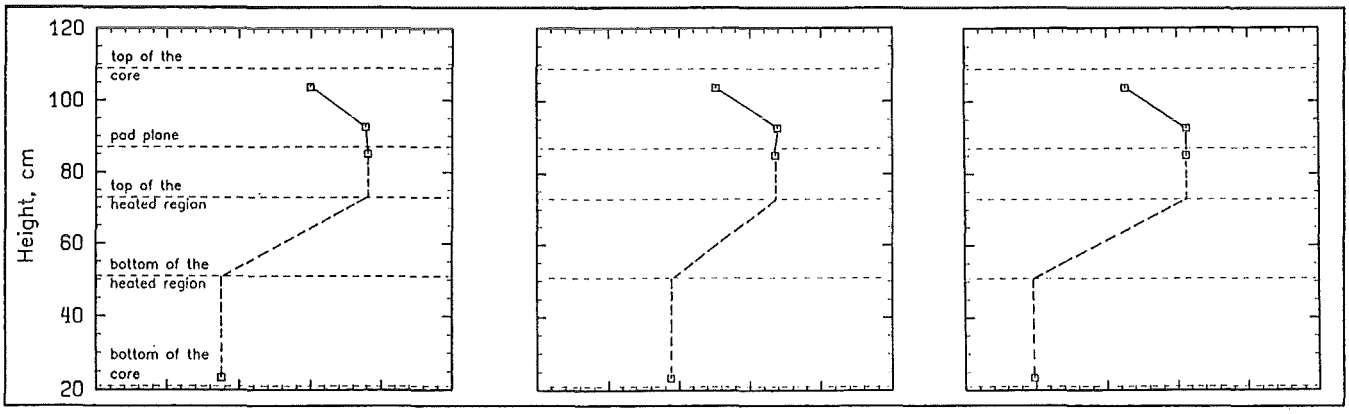

c) Axial temperature profile of the coolant measured inside SA 1017 (heating group #6).

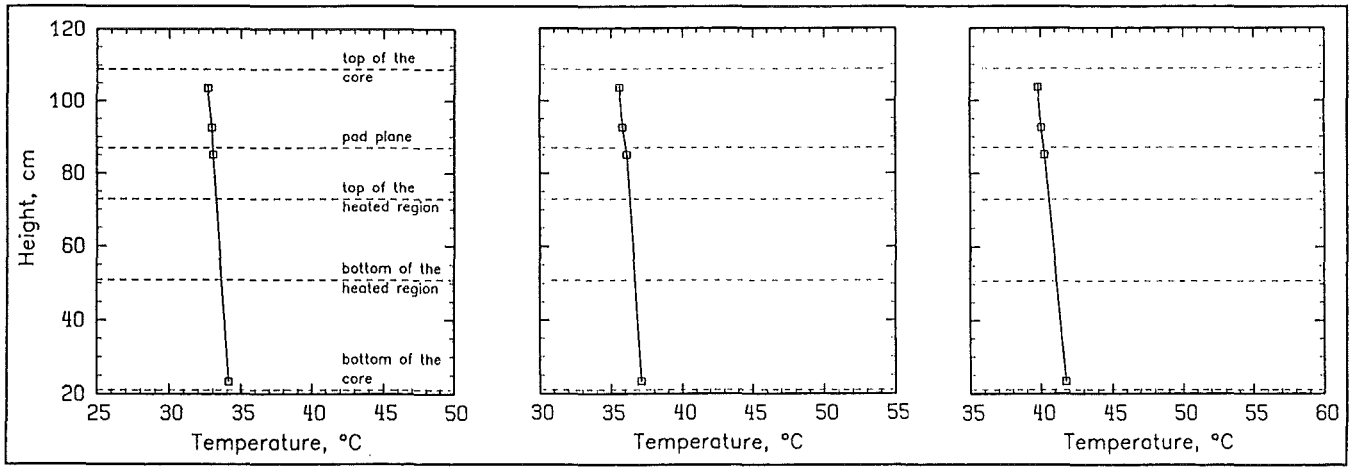

d) Axial temperature profile of the coolant measured inside SA 1319 (unheated group #7).

Fig. A.3.2. Influence of the core power; tests T06, T07, T02.

test T06 test T07 test T02

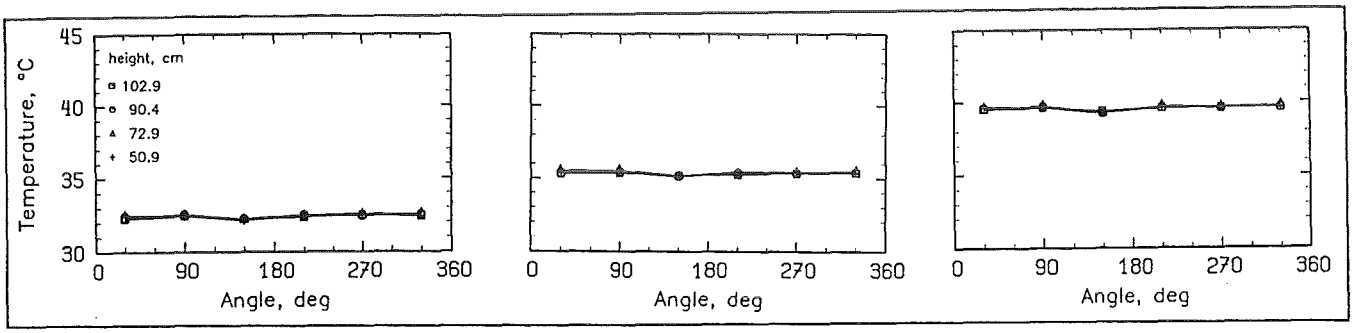

a) Azimuthal temperature profiles of the interstitial flow measured at the core periphery.

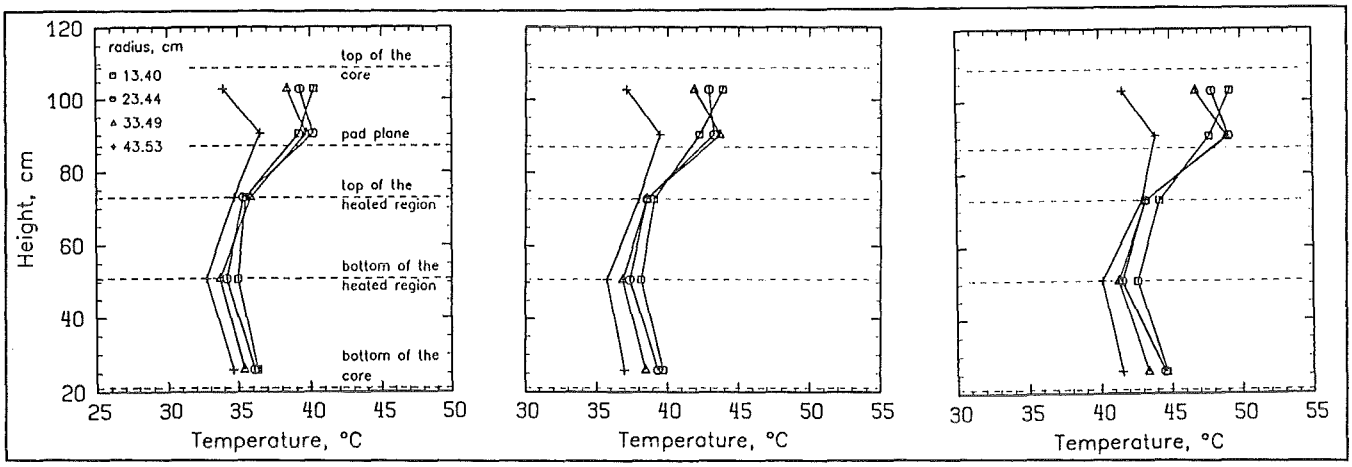

b) Axial temperature profiles of the interstitial flow measured at different radial positions (center → 90°).

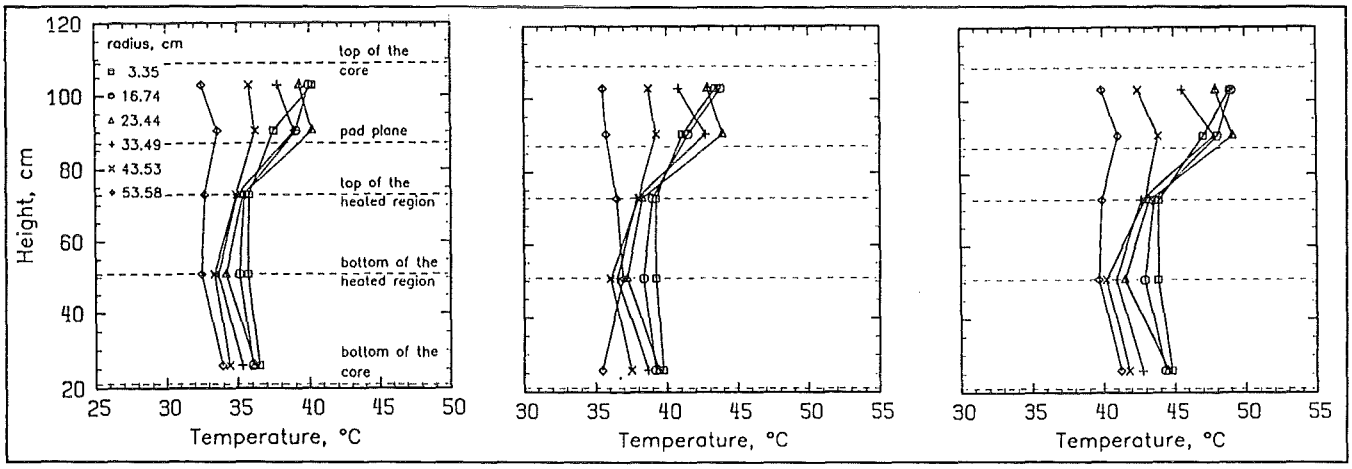

c) Axial temperature profiles of the interstitial flow measured at different radial positions (center → 270°).

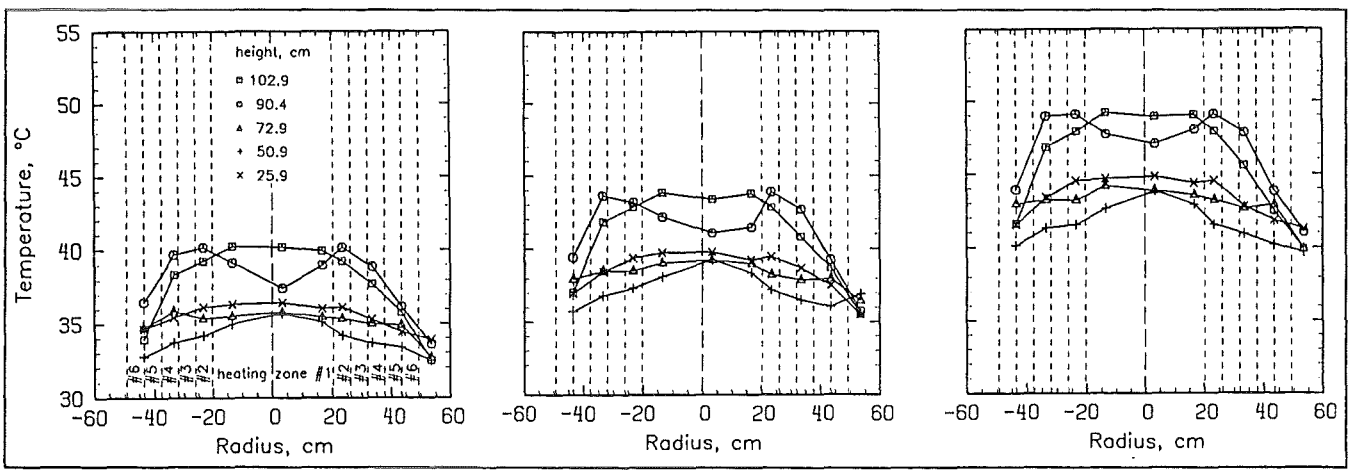

d) Horizontal temperature profiles of the interstitial flow measured across the core (90° → 270°).

Fig. A.3.3. Influence of the core power; tests T06, T07, T02.

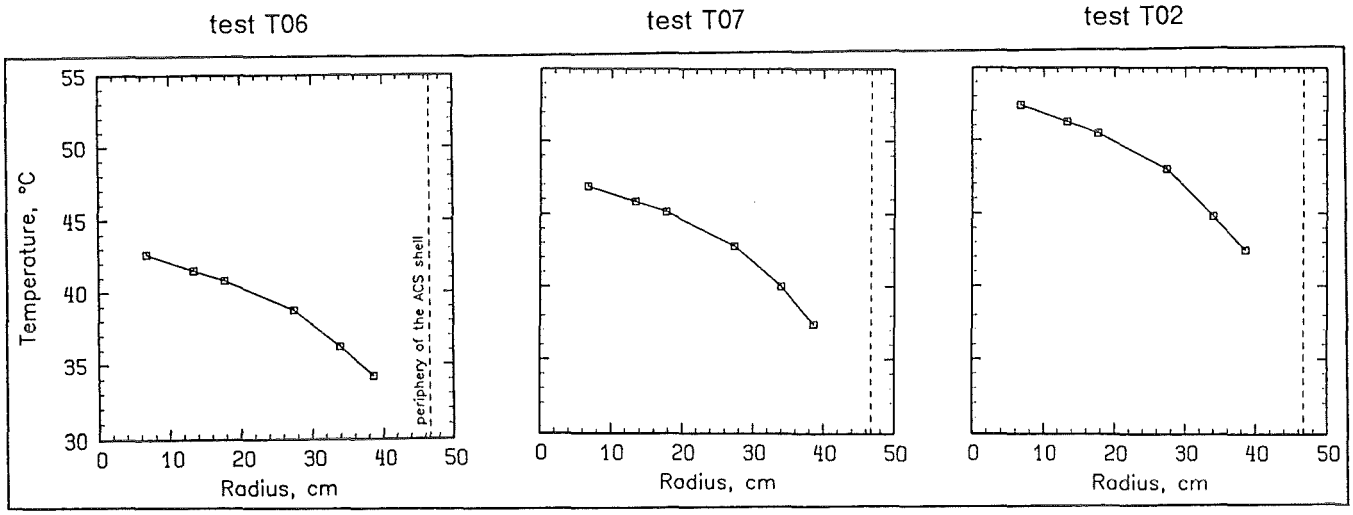

a) Radial temperature profile measured at the bottom end of the ACS (z = 1,248 mm).

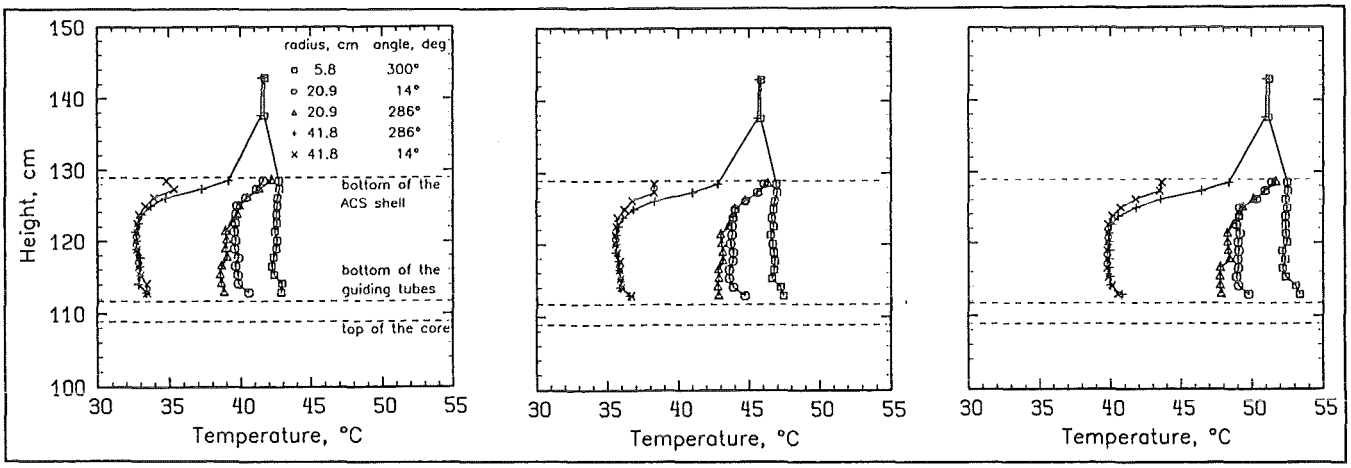

b) Axial temperature profiles measured at the bottom end and inside the lower part of the ACS.

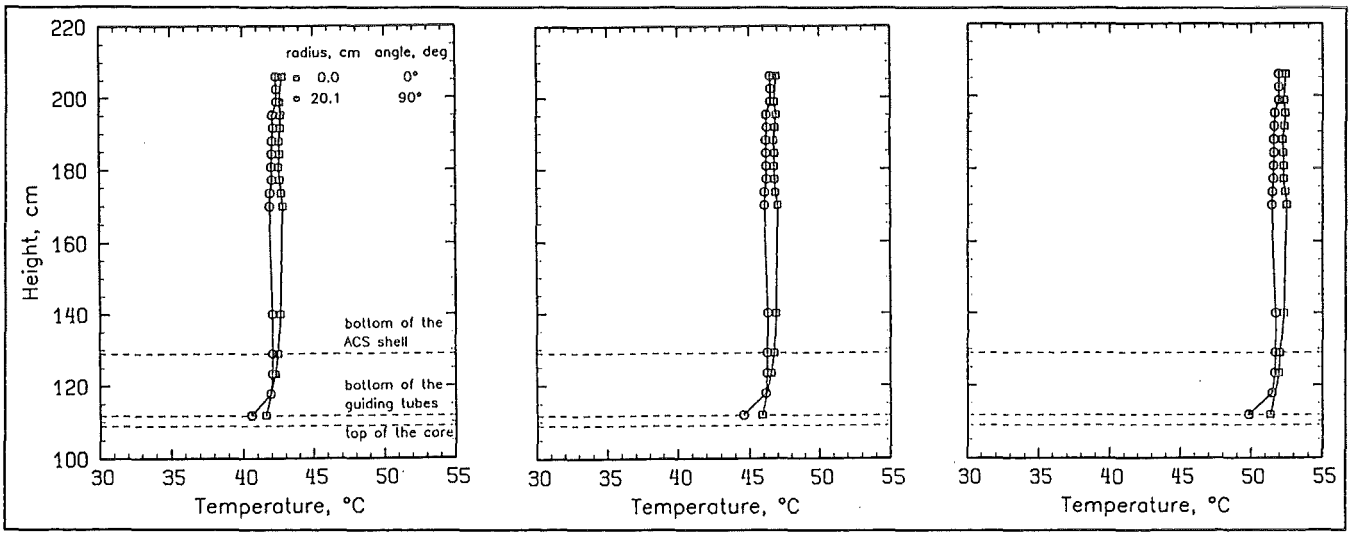

c) Axial temperature profiles measured inside the ACS.

Fig. A.3.4. Influence of the core power; tests T06, T07, T02.

test T06 test T07 test T02

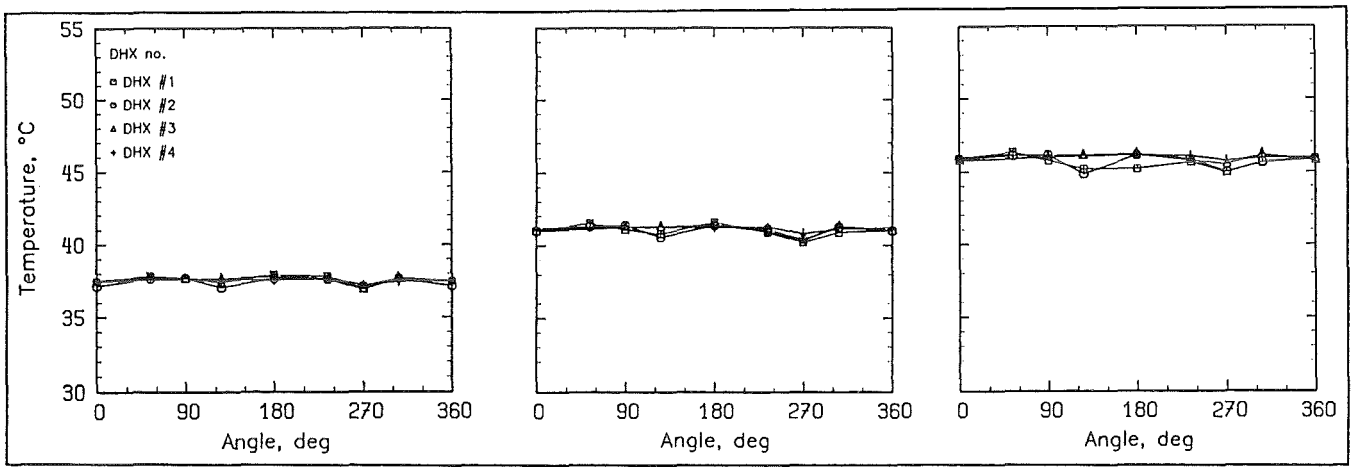

a) Azimuthal temperature profiles measured at the DHX inlet windows (z = 2,299 mm).

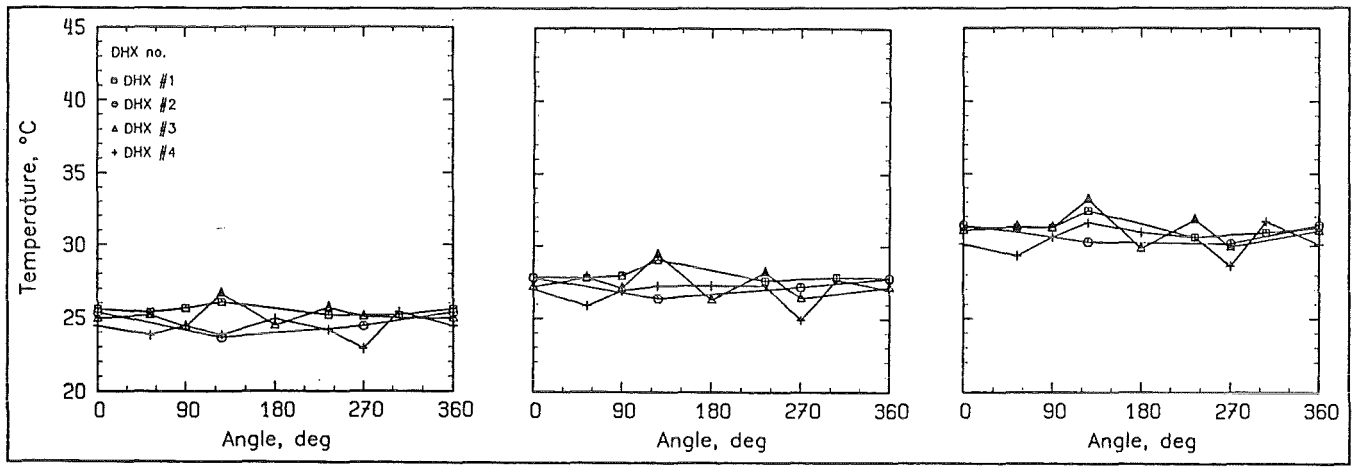

b) Azimuthal temperature profiles measured at the DHX outlet windows (z = 1,391 mm).

Fig. A.3.5. Influence of the core power; tests T06, T07, T02.

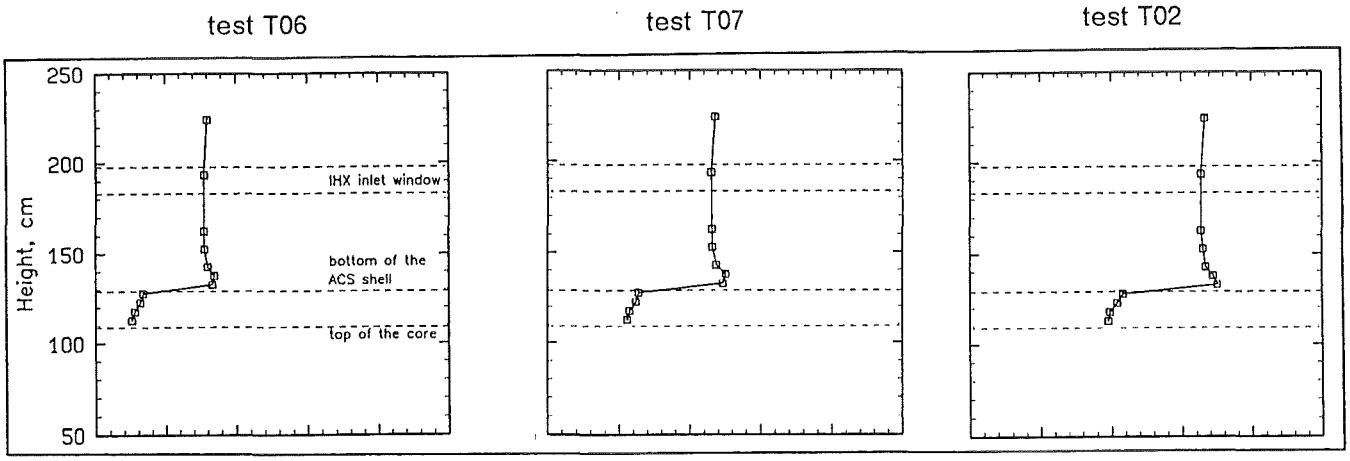

a) Axial temperature profile measured in the UP along the MER-1 device.

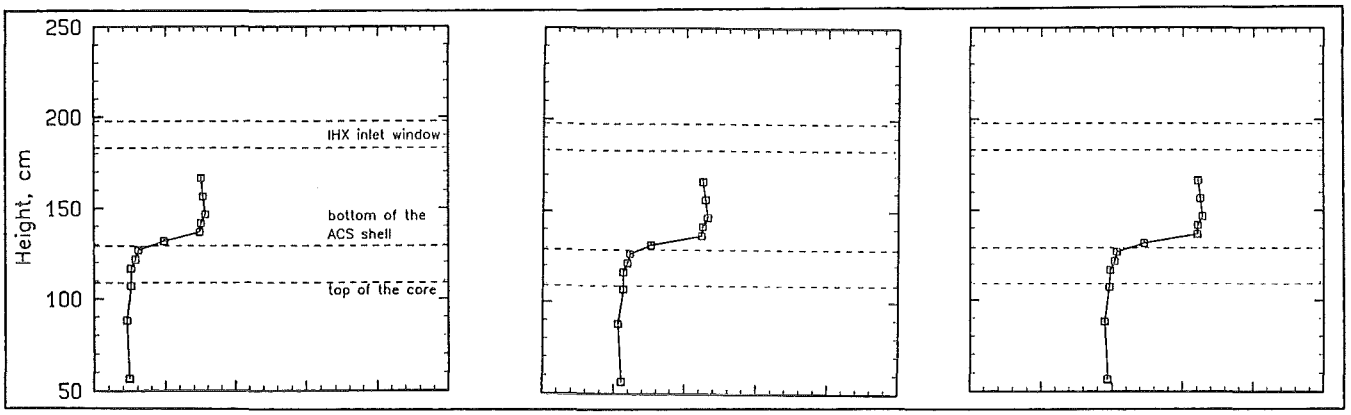

b) Axial temperature profile measured in the UP along the MER-2 device.

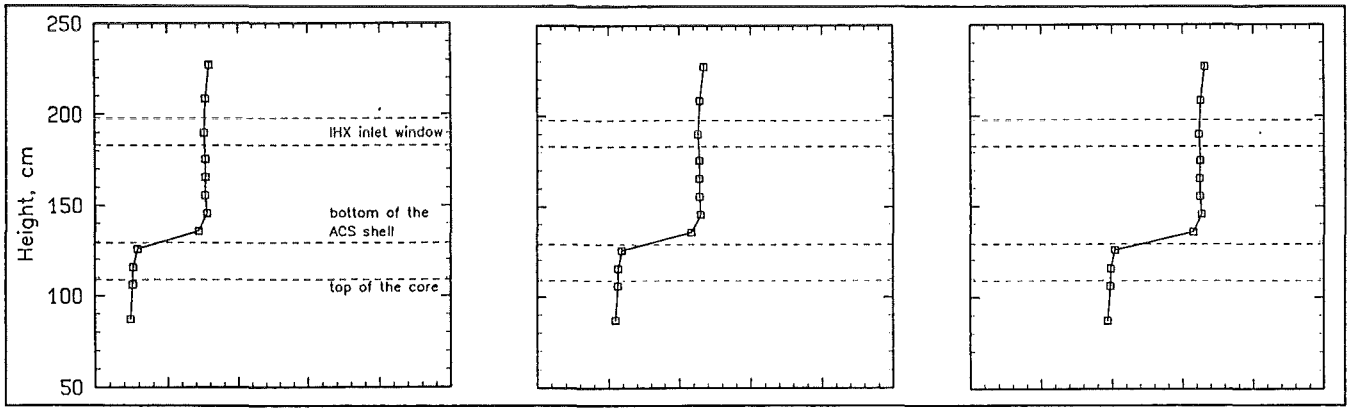

c) Axial temperature profile measured in the UP along the MER-3 device.

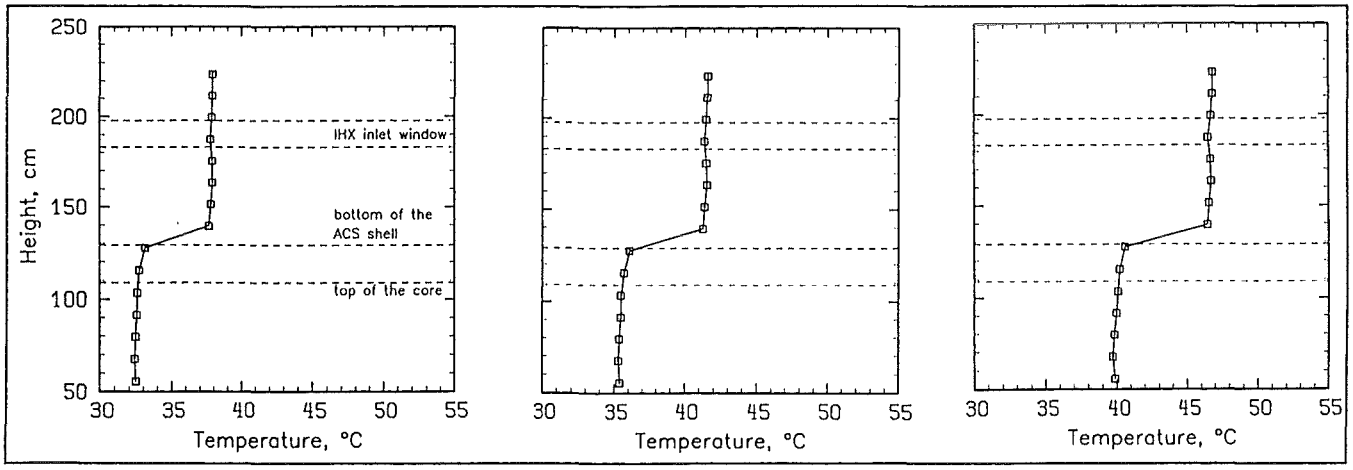

d) Axial temperature profile measured in the UP along the MEL device.

Fig. A.3.6. Influence of the core power; tests T06, T07, T02.

Table A.4. Data comparison (cont'd.).
Number of DHX circuits put in operation.

Test No. / Parameter	Design of ACS shell	Total core power, kW	Number of heated SA groups	Number of operated DHXs	Fluid level in the upper plenum	Flow path via reflector and storage elements	Flow path via IHX primary loops
T06	impermeable without skirt	133	6	4	normal	blocked	unblocked
T08	impermeable without skirt	133	6	2	normal	blocked	unblocked

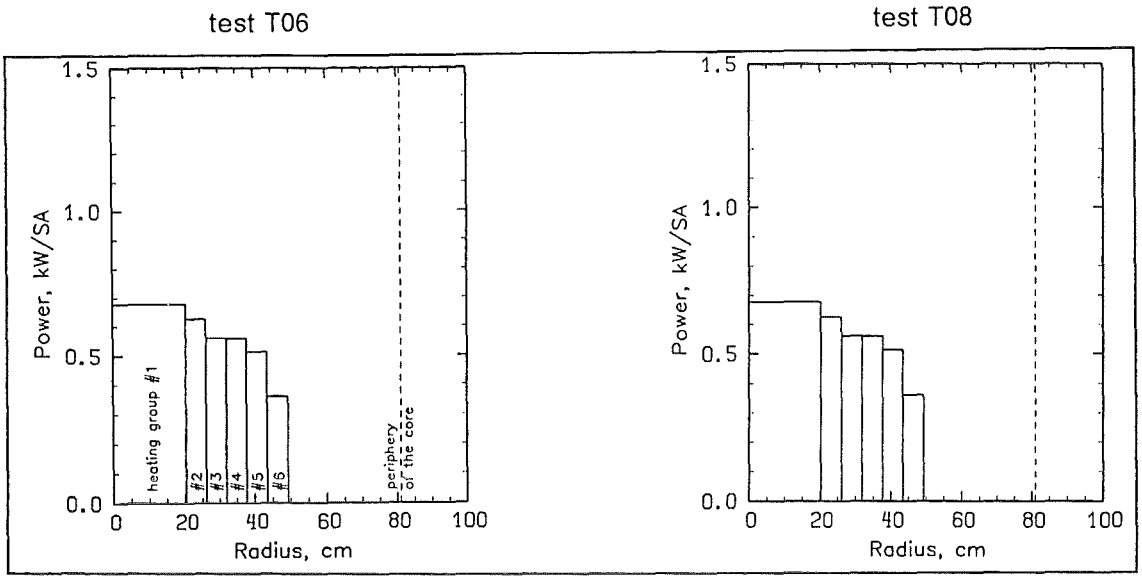

a) Radial power profile.

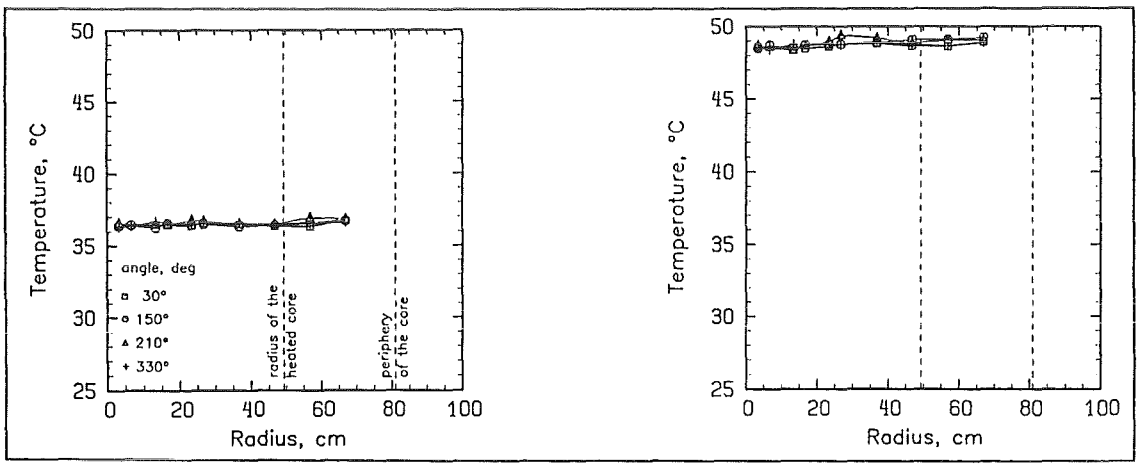

b) Radial temperature profiles of the coolant measured at the SA inlet sides.

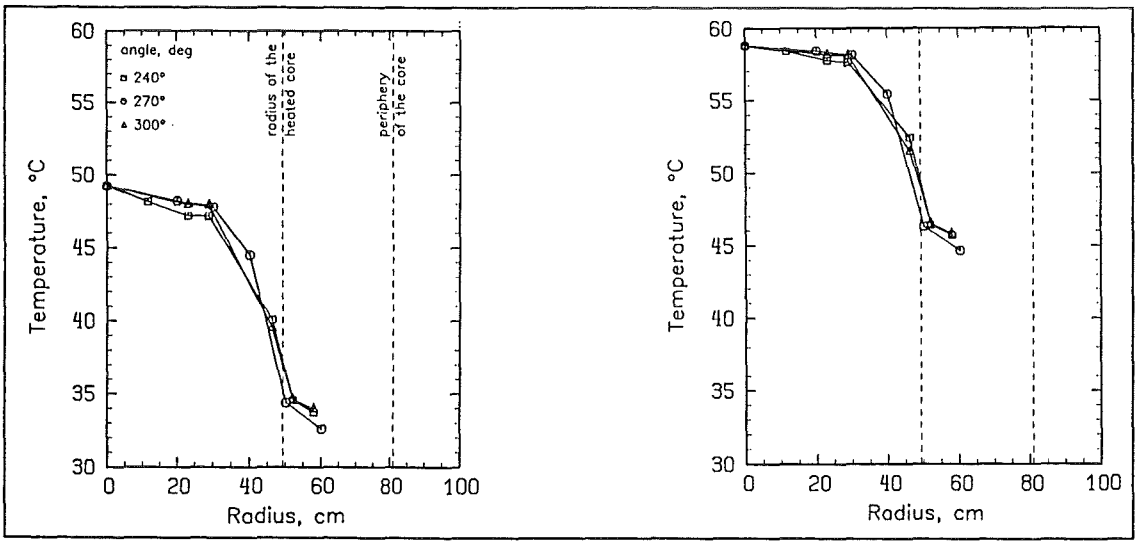

c) Radial temperature profiles of the coolant measured at the SA outlet sides.

Fig. A.4.1. Influence of the number of DHX circuits put in operation; tests T06, T08.

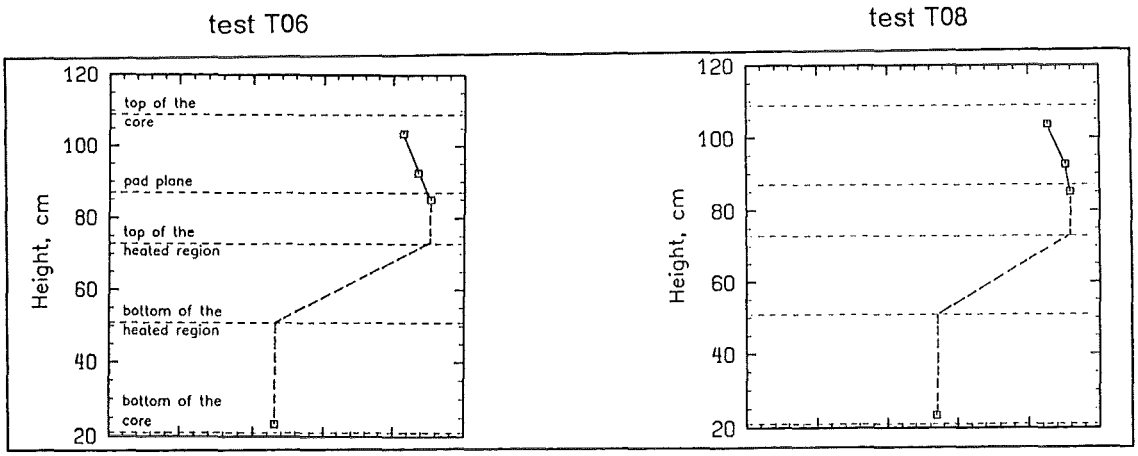

a) Axial temperature profile of the coolant measured inside SA 813 (heating group #4).

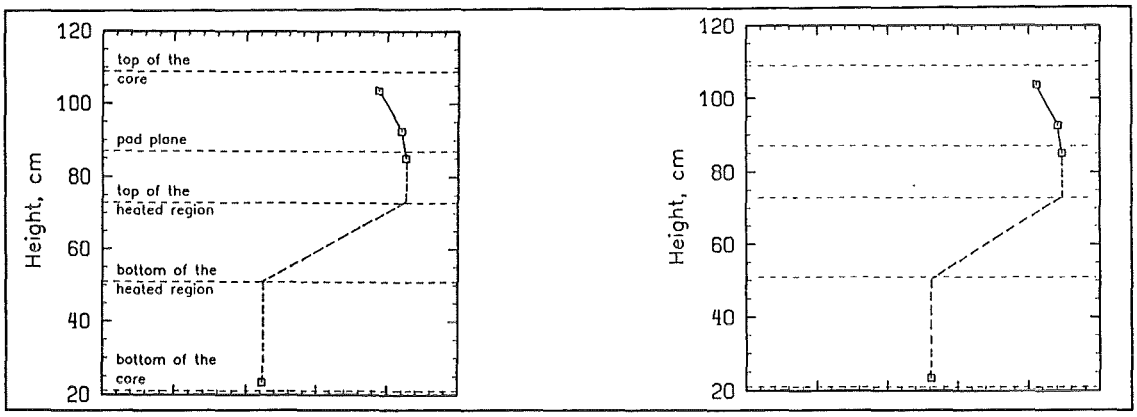

b) Axial temperature profile of the coolant measured inside SA 913 (heating group #5).

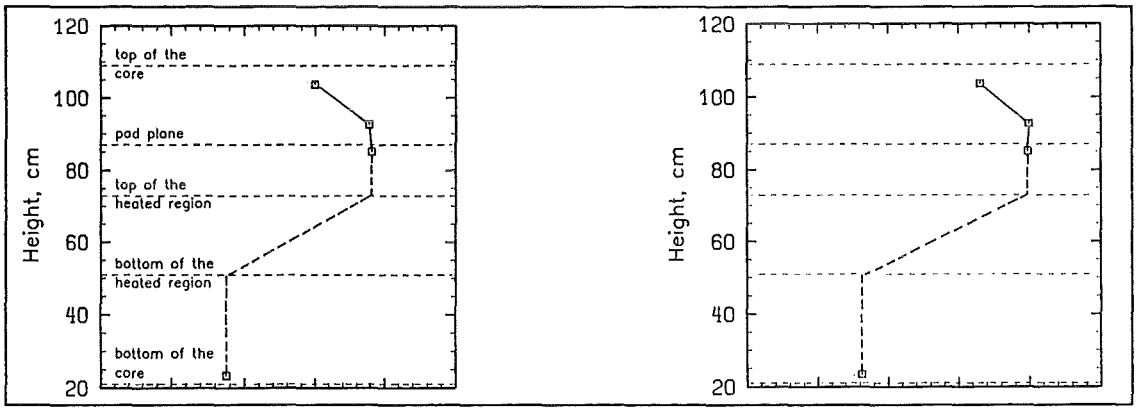

c) Axial temperature profile of the coolant measured inside SA 1017 (heating group #6).

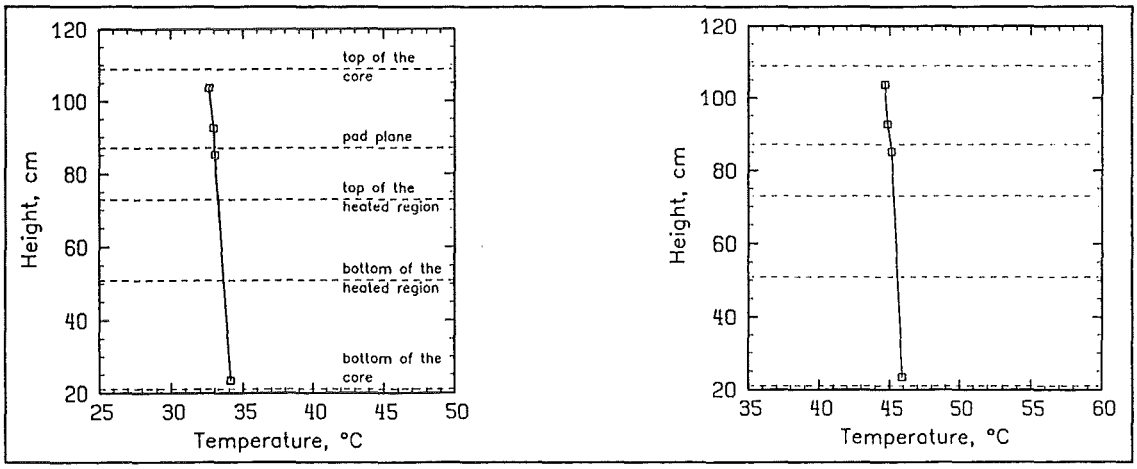

d) Axial temperature profile of the coolant measured inside SA 1319 (unheated group #7).

Fig. A.4.2. Influence of the number of DHX circuits put in operation; tests T06, T08.

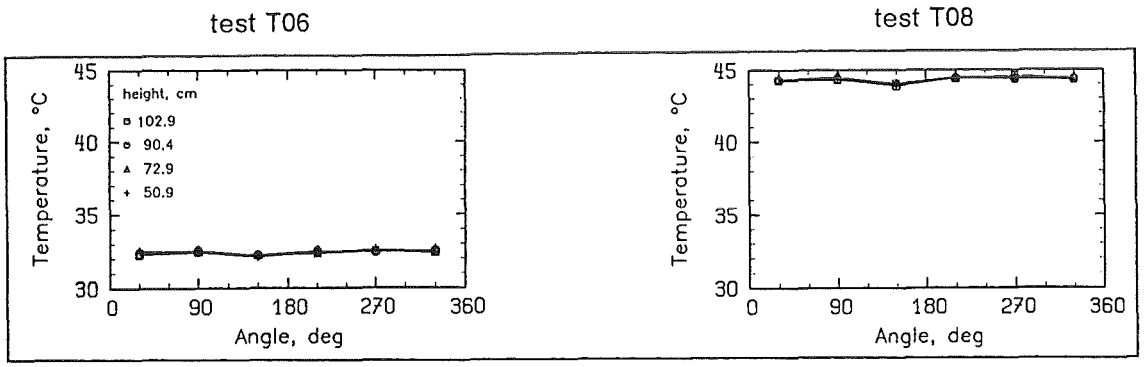

a) Azimuthal temperature profiles of the interstitial flow measured at the core periphery.

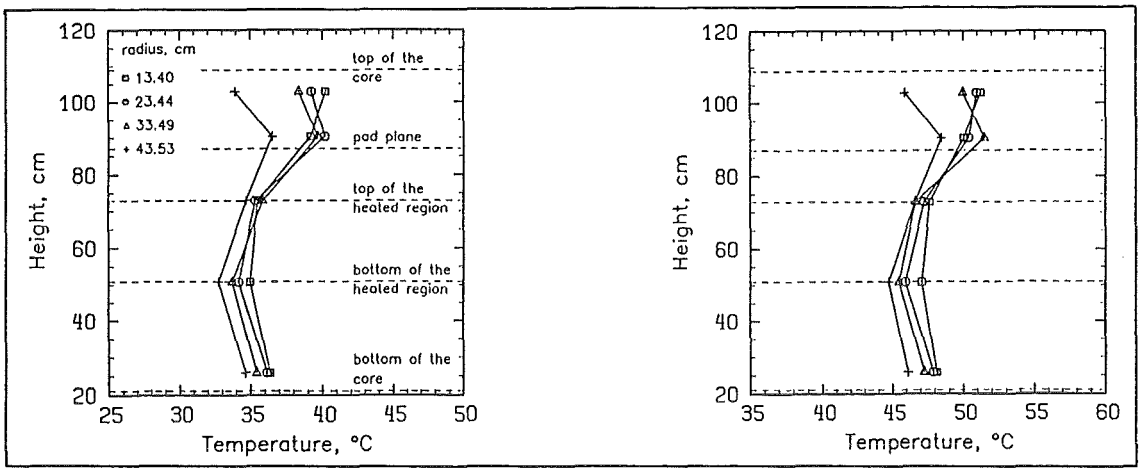

b) Axial temperatures of the interstitial flow at different radial positions (center → 90°).

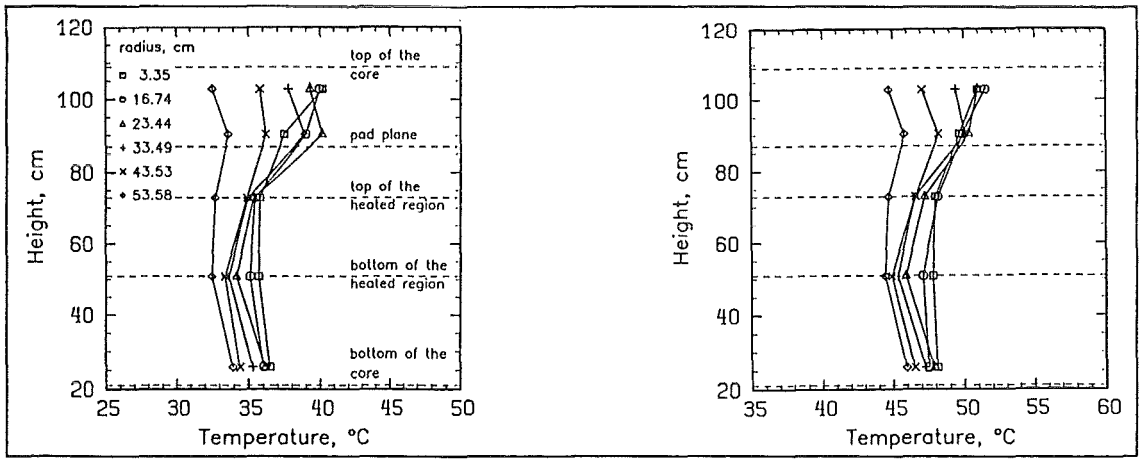

c) Axial temperatures of the interstitial flow at different radial positions (center → 270°).

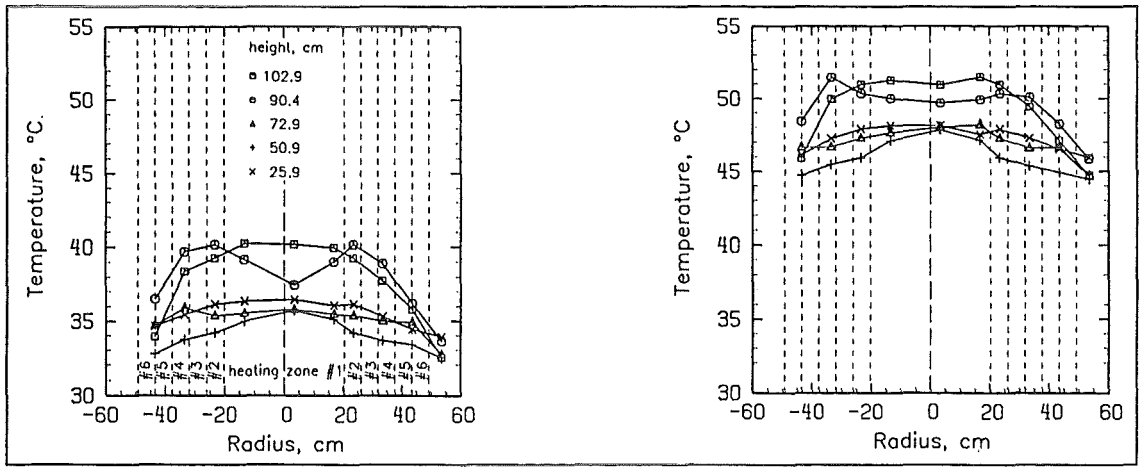

d) Horizontal temperatures of the interstitial flow across the core (90° → 270°).

Fig. A.4.3. Influence of the number of DHX circuits put in operation; tests T06, T08.

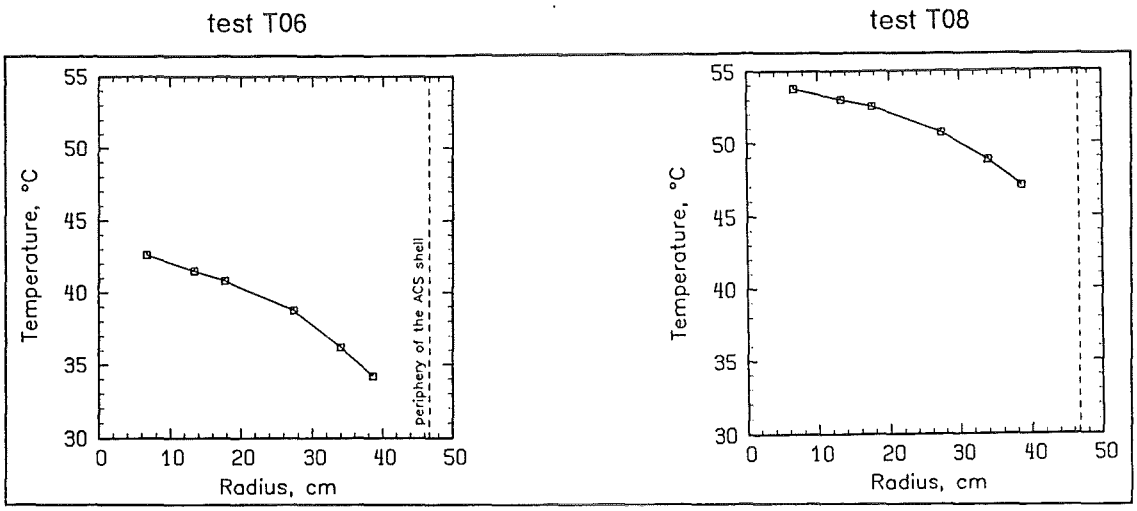

a) Radial temperature profile measured at the bottom end of the ACS (z = 1,248 mm).

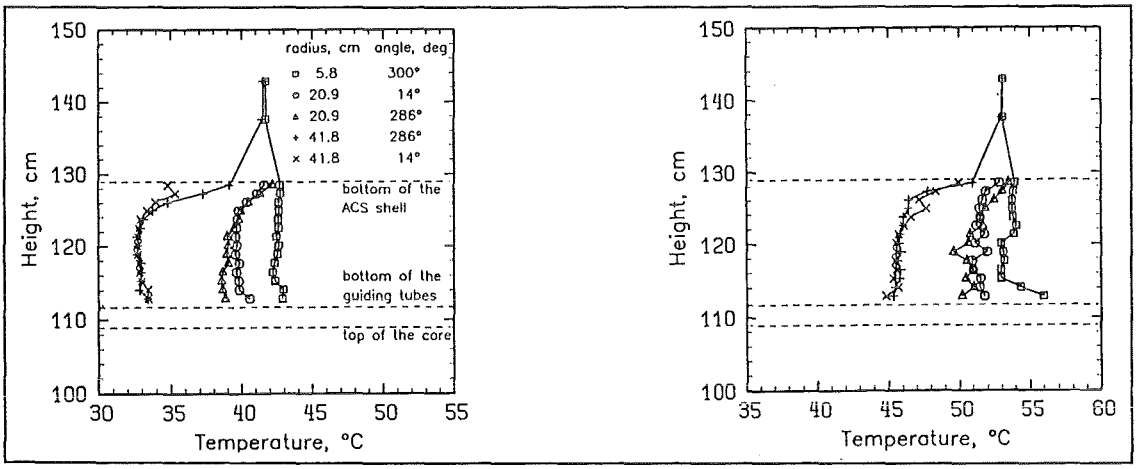

b) Axial temperature profiles at the bottom end and inside the lower part of the ACS.

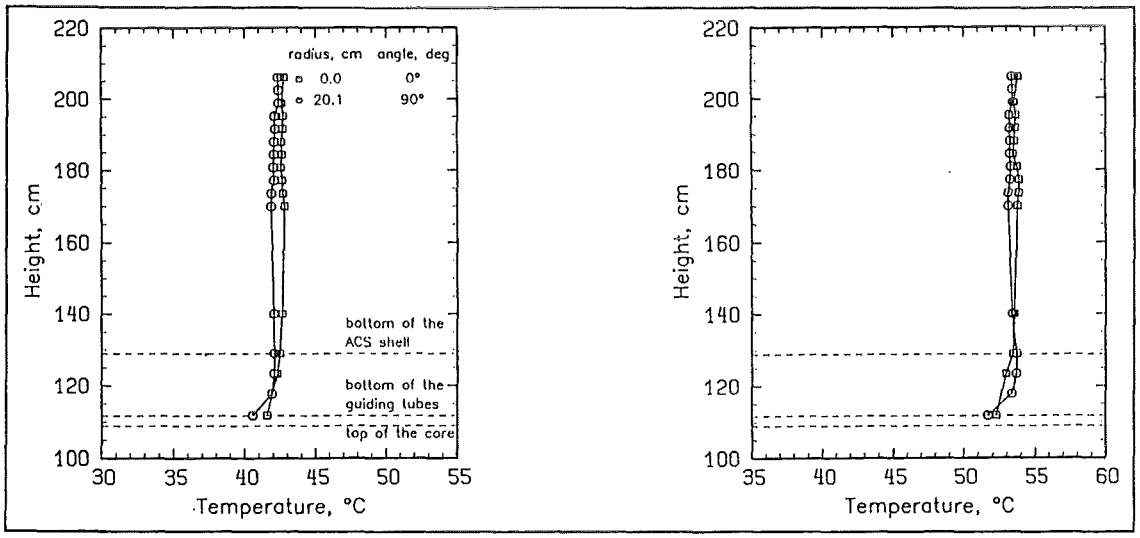

c) Axial temperature profiles measured inside the ACS.

Fig. A.4.4. Influence of the number of DHX circuits put in operation; tests T06, T08.

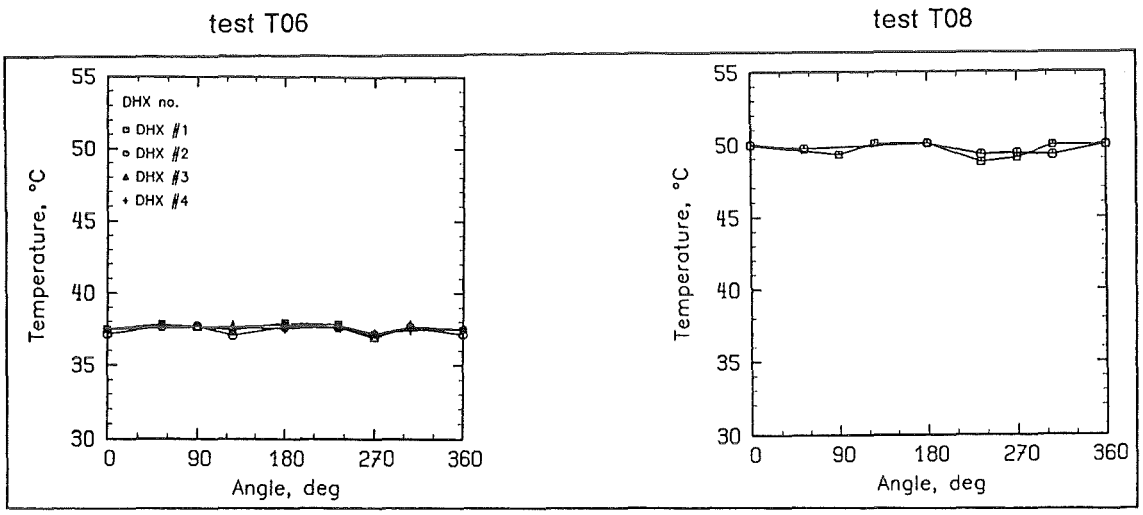

a) Azimuthal temperature profiles measured at the DHX inlet windows (z = 2,299 mm).

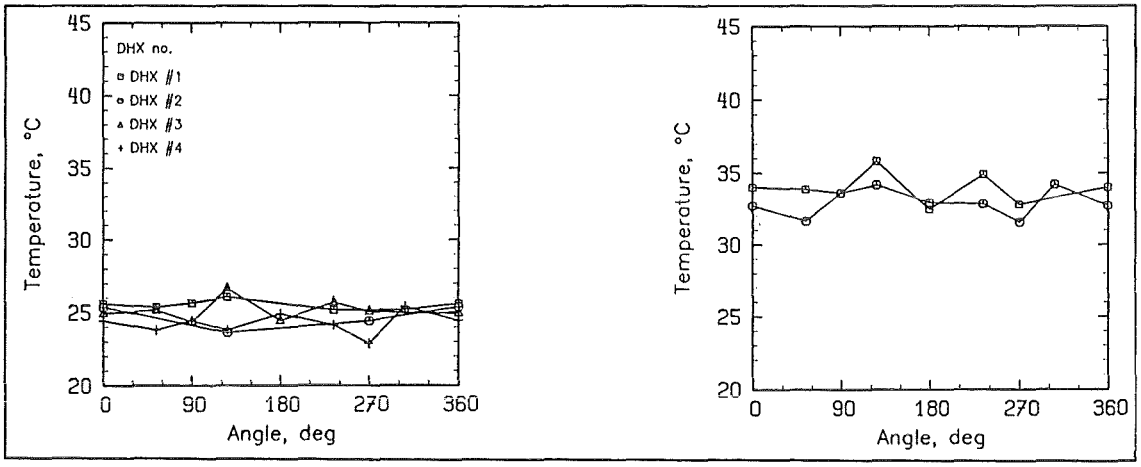

b) Azimuthal temperature profiles measured at the DHX outlet windows (z = 1,391 mm).

Fig. A.4.5. Influence of the number of DHX circuits put in operation; tests T06, T08.

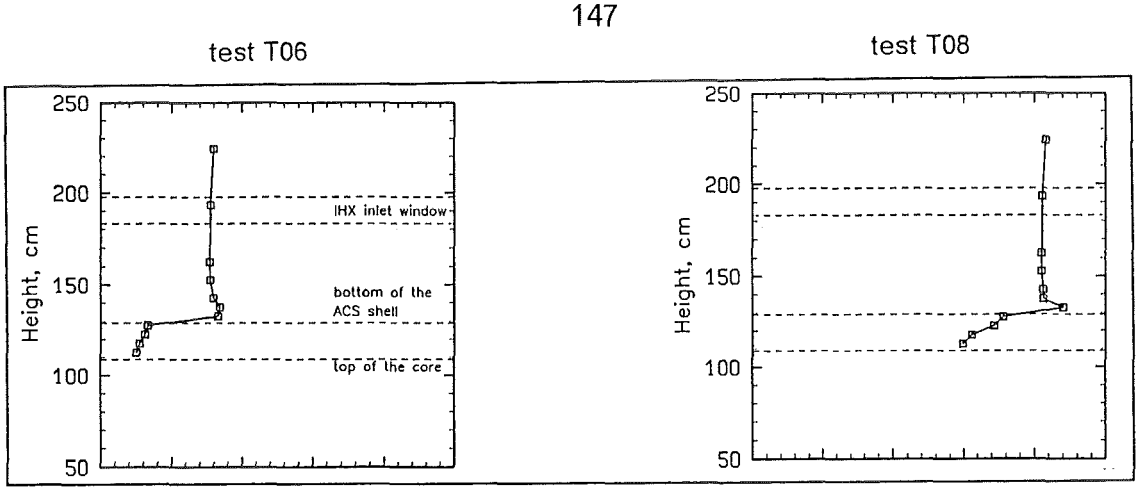

a) Axial temperature profile measured in the UP along the MER-1 device.

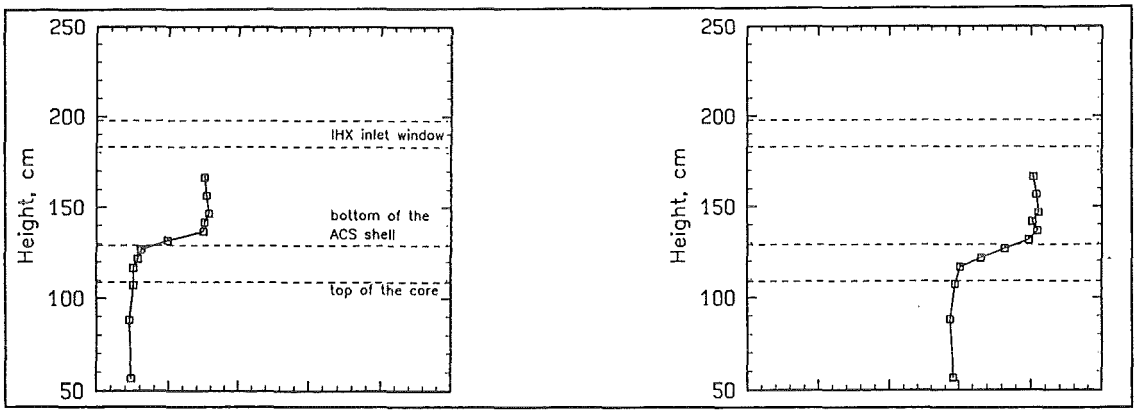

b) Axial temperature profile measured in the UP along the MER-2 device.

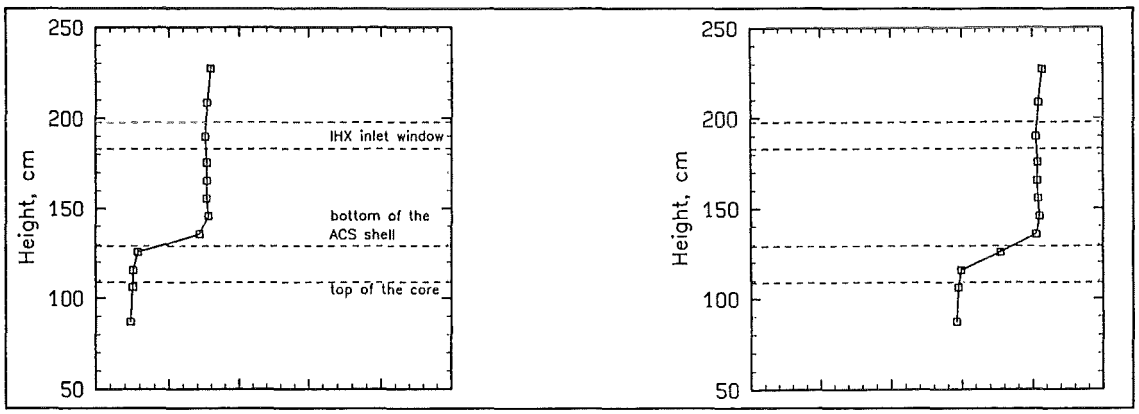

c) Axial temperature profile measured in the UP along the MER-3 device.

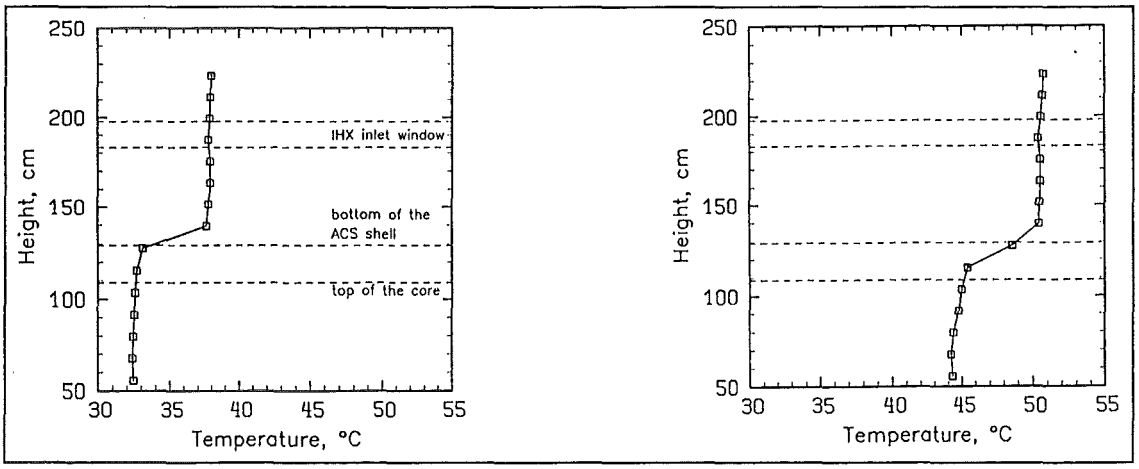

d) Axial temperature profile measured in the UP along the MEL device.

Fig. A.4.6. Influence of the number of DHX circuits put in operation; tests T06, T08.

Table A.5. Data comparison (cont'd.).

Flow path blockage of the IHX primary sides.

a) permeable design of the ACS shell,
core power of 133 kW,
6 heated SA groups,
blocked flow paths via reflector and storage elements.

Test No. / Parameter	Design of ACS shell	Total core power, kW	Number of heated SA groups	Number of operated DHXs	Fluid level in the upper plenum	Flow path via reflector and storage elements	Flow path via IHX primary loops
T04	permeable without skirt	133	6	4	normal	blocked	unblocked
T10	permeable without skirt	133	6	4	normal	blocked	blocked

test T04 test T10

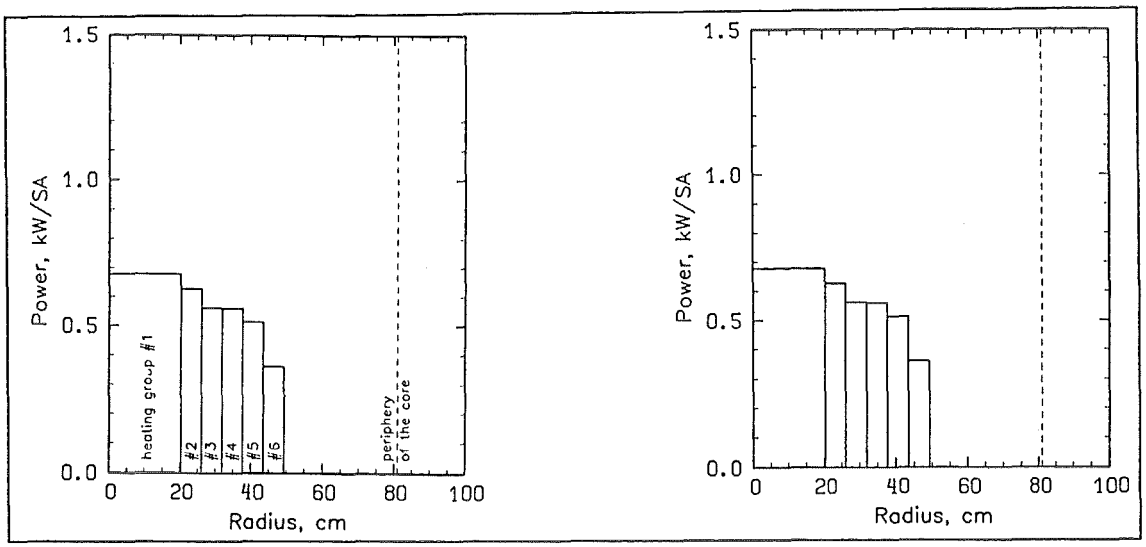

a) Radial power profile.

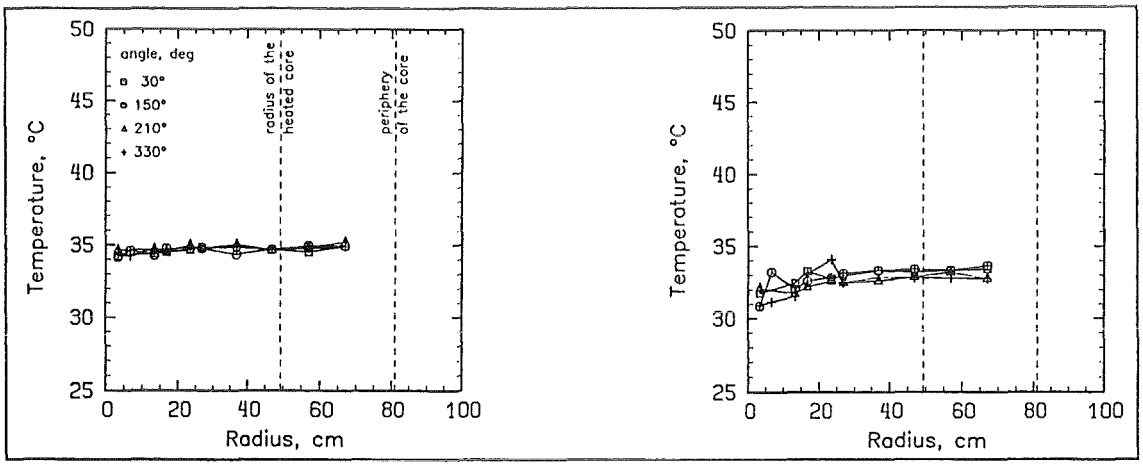

b) Radial temperature profiles of the coolant measured at the SA inlet sides.

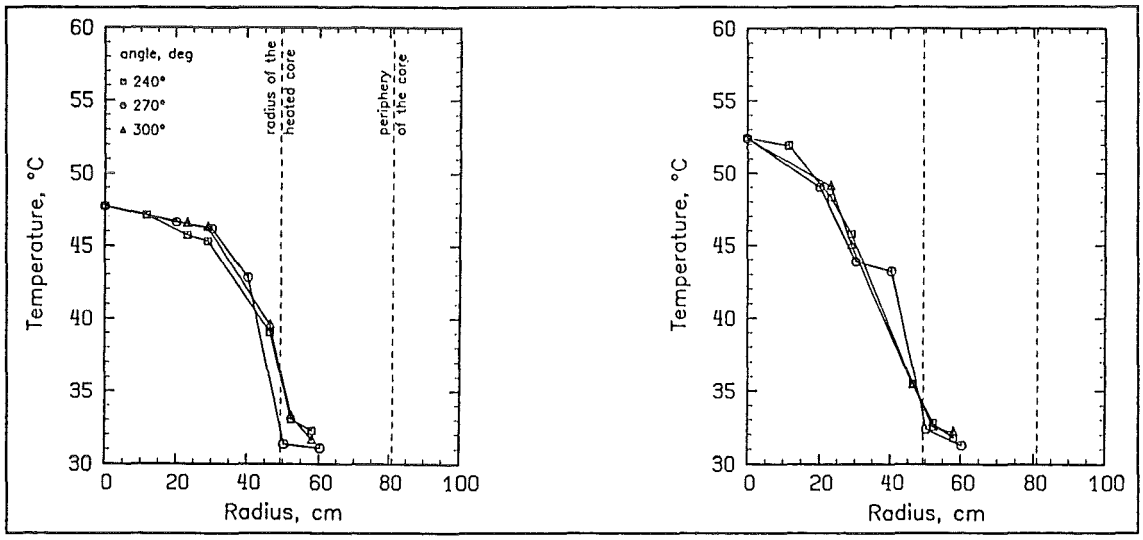

c) Radial temperature profiles of the coolant measured at the SA outlet sides.

Fig. A.5.1. Influence of blocked flow paths via IHX primary loops; tests T04, T10.

test T04 test T10

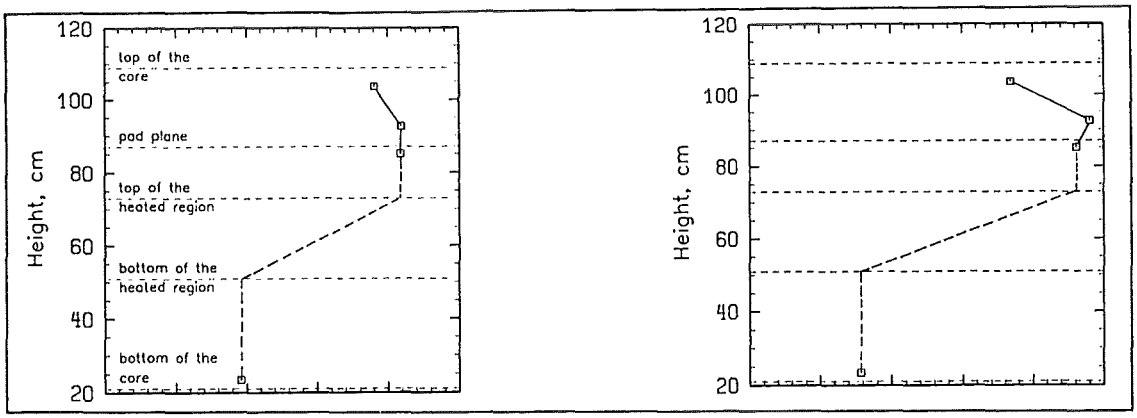

a) Axial temperature profile of the coolant measured inside SA 813 (heating group #4).

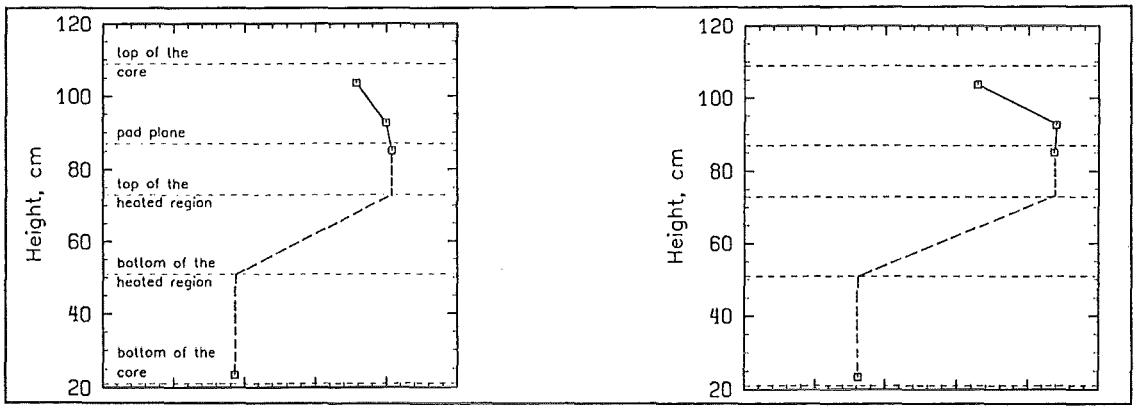

b) Axial temperature profile of the coolant measured inside SA 913 (heating group #5).

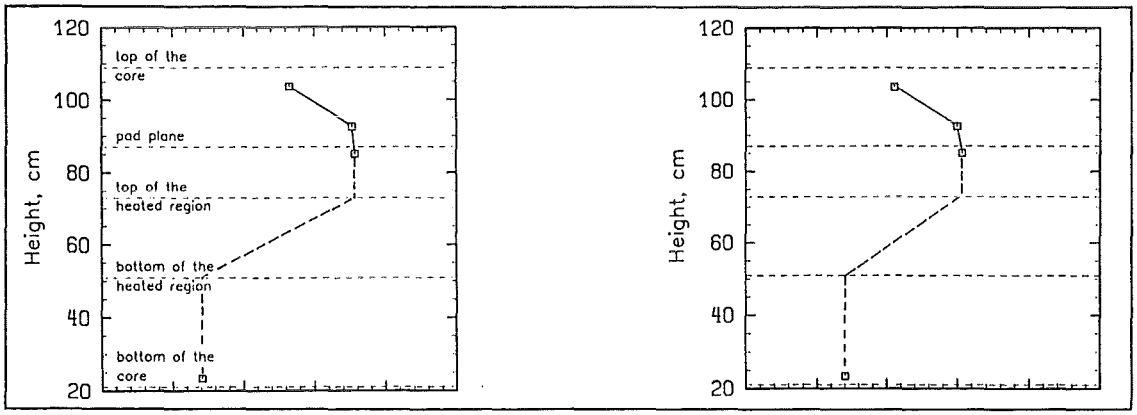

c) Axial temperature profile of the coolant measured inside SA 1017 (heating group #6).

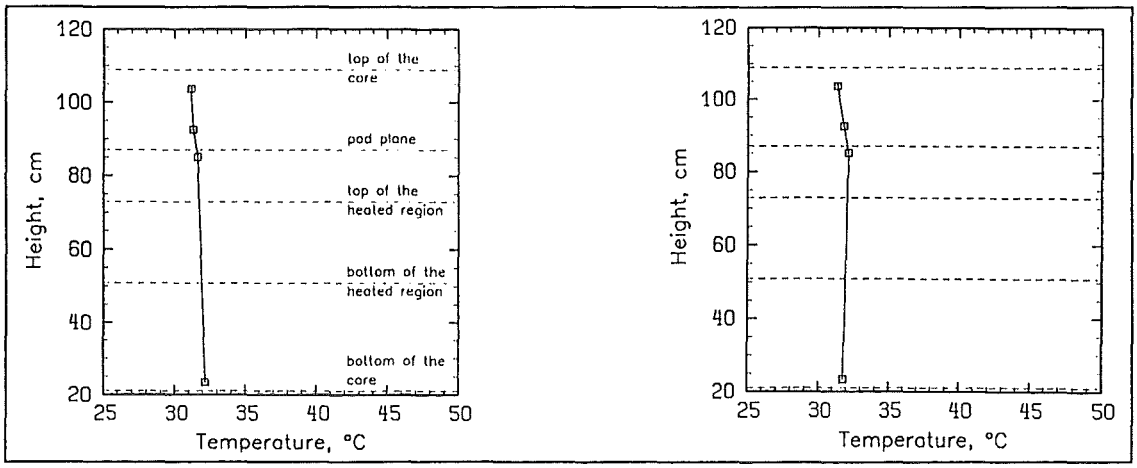

d) Axial temperature profile of the coolant measured inside SA 1319 (unheated group #7).

Fig. A.5.2. Influence of blocked flow paths via IHX primary loops; tests T04, T10.

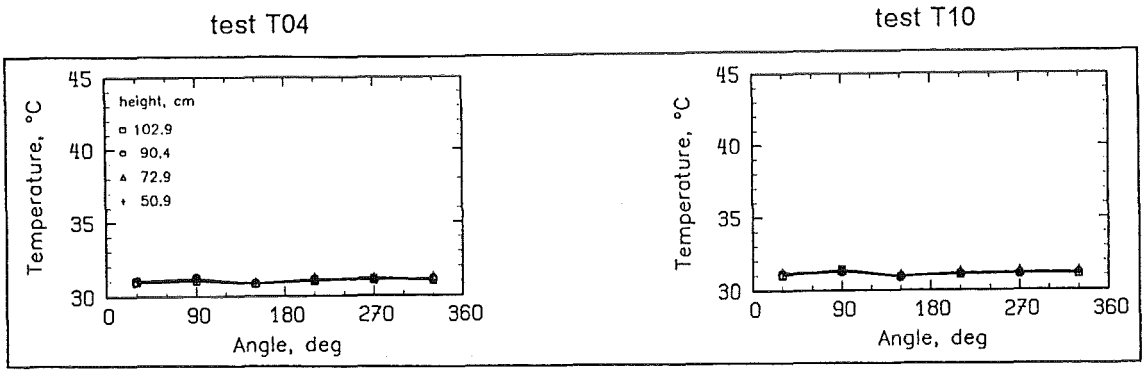

a) Azimuthal temperature profiles of the interstitial flow measured at the core periphery.

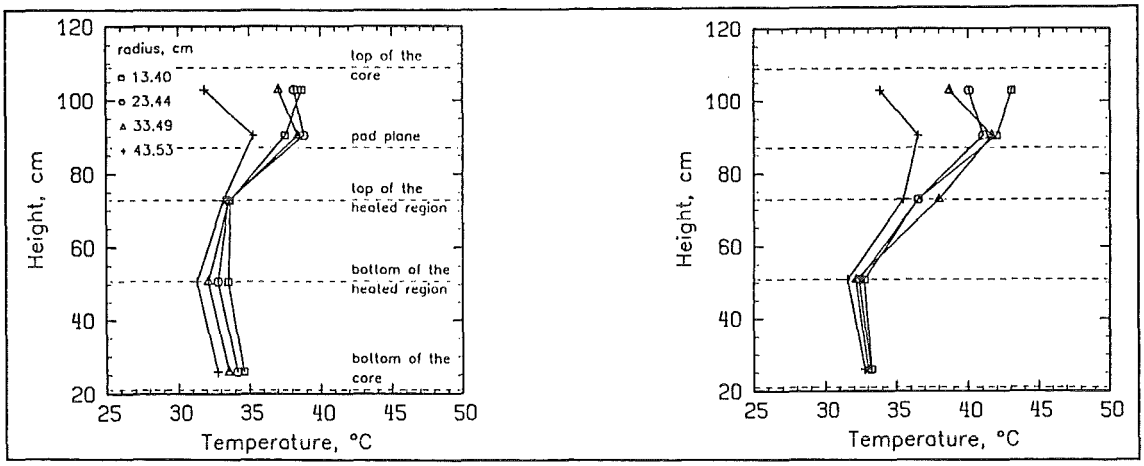

b) Axial temperatures of the interstitial flow at different radial positions (center → 90°).

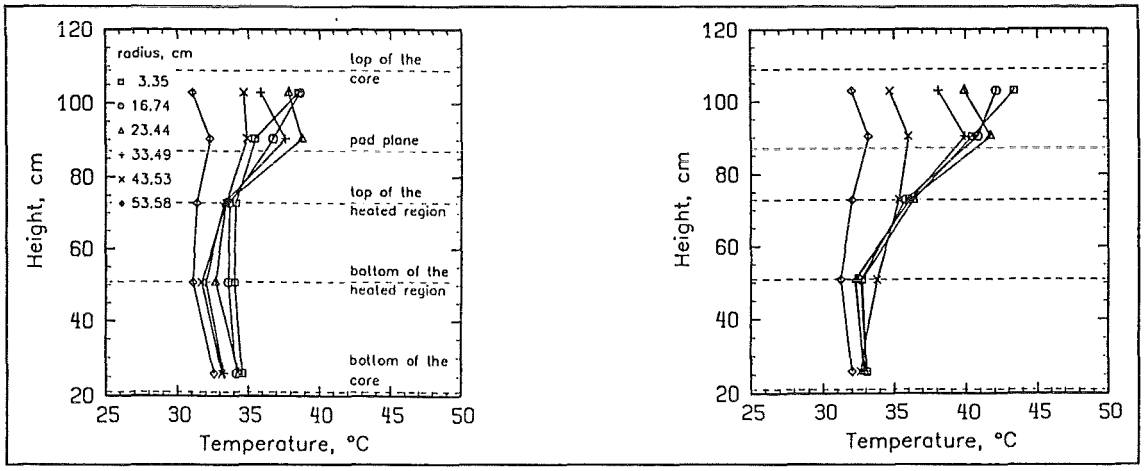

c) Axial temperatures of the interstitial flow at different radial positions (center → 270°).

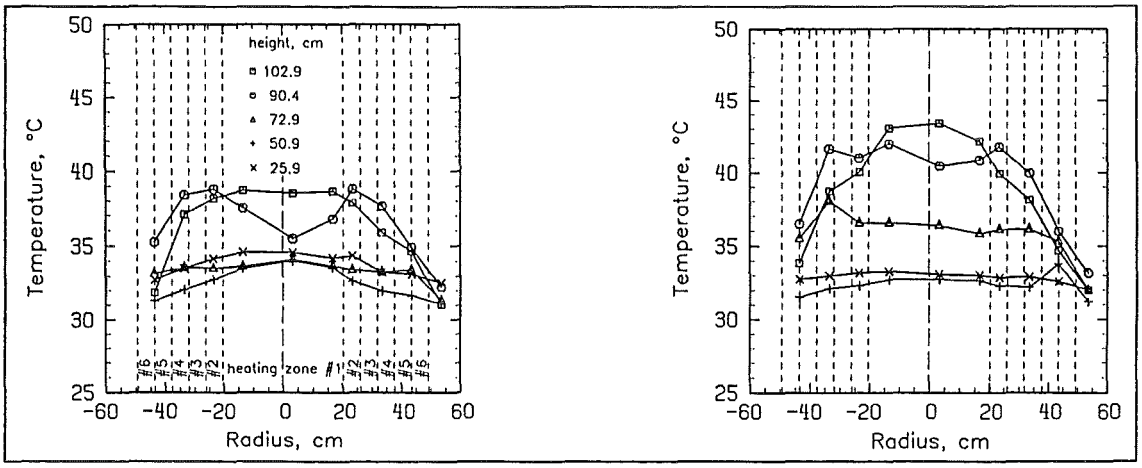

d) Horizontal temperatures of the interstitial flow across the core (90° → 270°).

Fig. A.5.3. Influence of blocked flow paths via IHX primary loops; tests T04, T10.

test T04 test T10

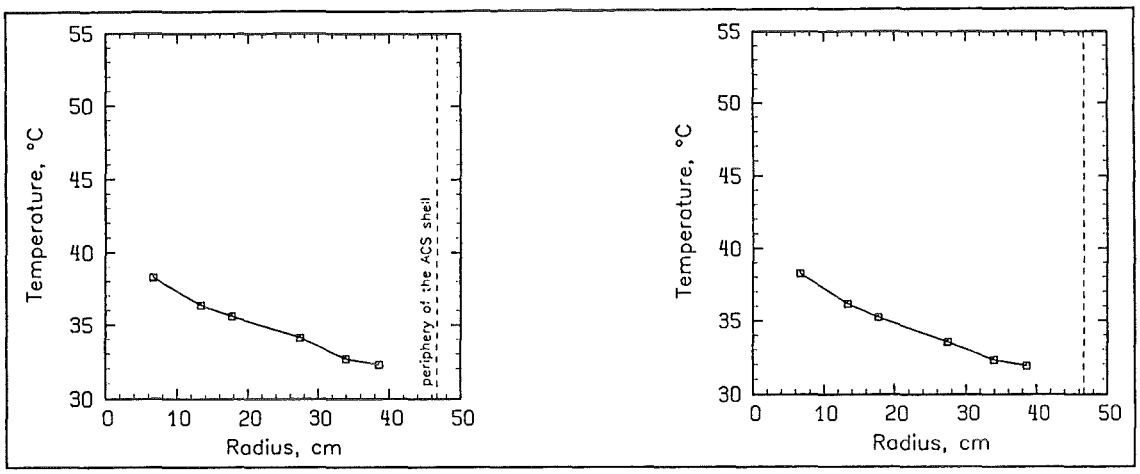

a) Radial temperature profile measured at the bottom end of the ACS (z = 1,248 mm).

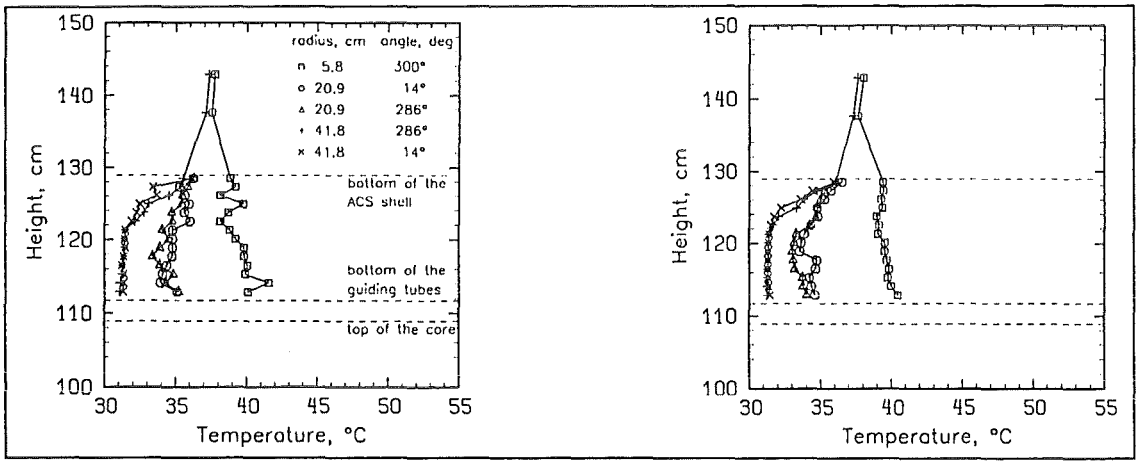

b) Axial temperature profiles at the bottom end and inside the lower part of the ACS.

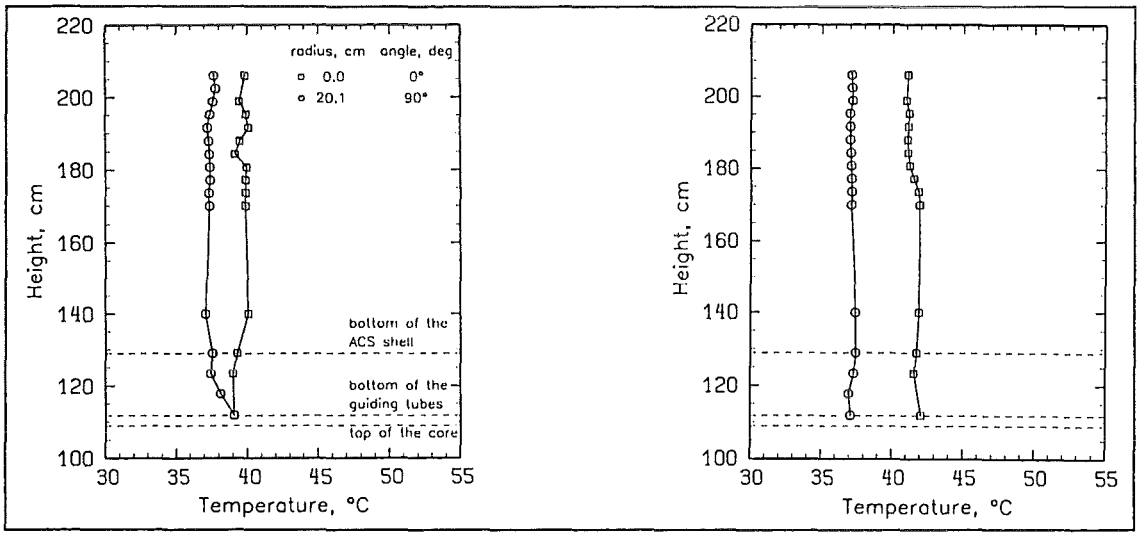

c) Axial temperature profiles measured inside the ACS.

Fig. A.5.4. Influence of blocked flow paths via IHX primary loops; tests T04, T10.

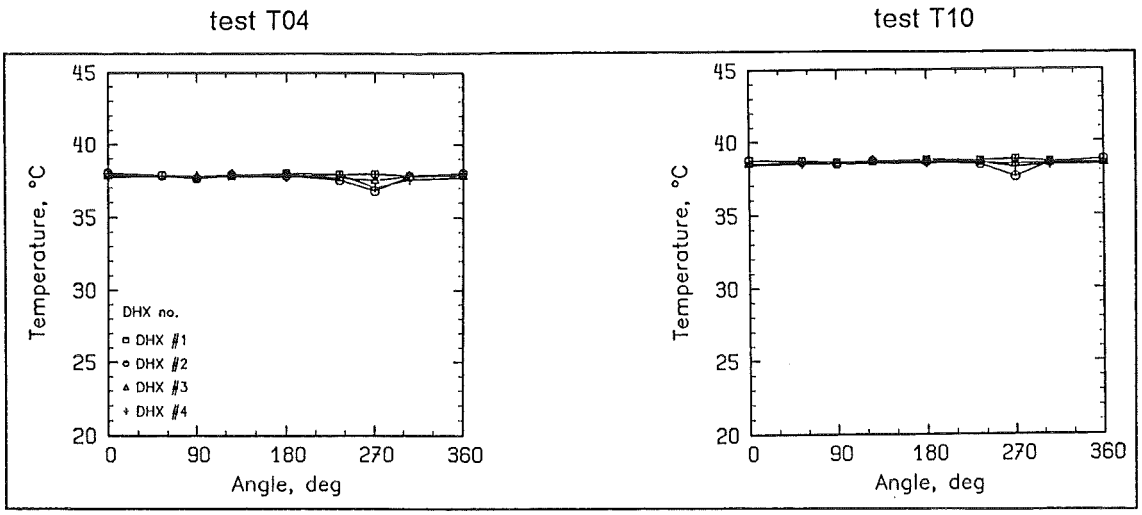

a) Azimuthal temperature profiles measured at the DHX inlet windows (z = 2,299 mm).

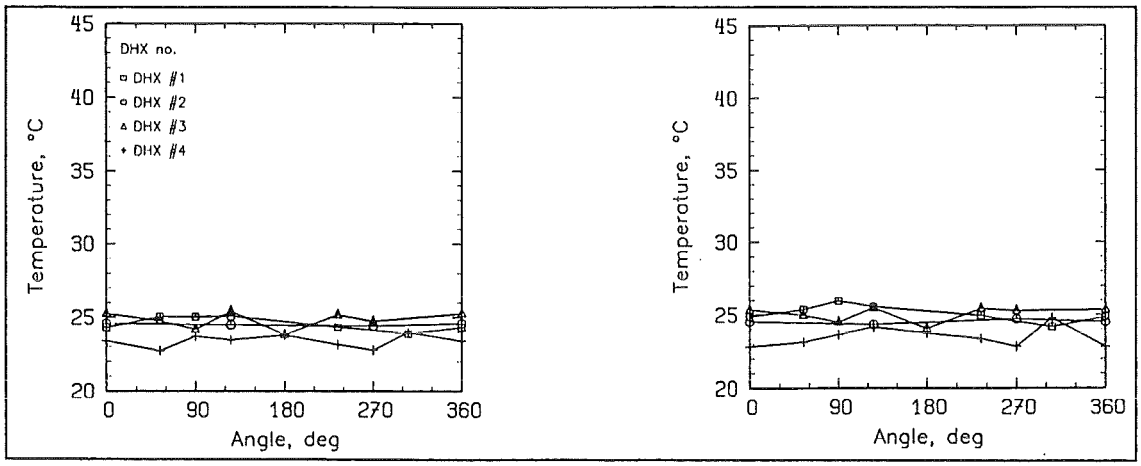

b) Azimuthal temperature profiles measured at the DHX outlet windows (z = 1,391 mm).

Fig. A.5.5. Influence of blocked flow paths via IHX primary loops; tests T04, T10.

test T04 test T10

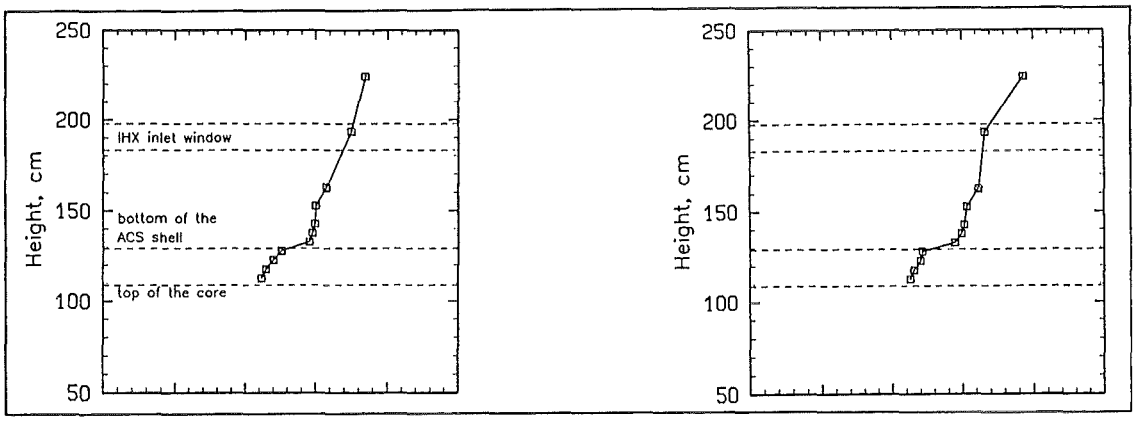

a) Axial temperature profile measured in the UP along the MER-1 device.

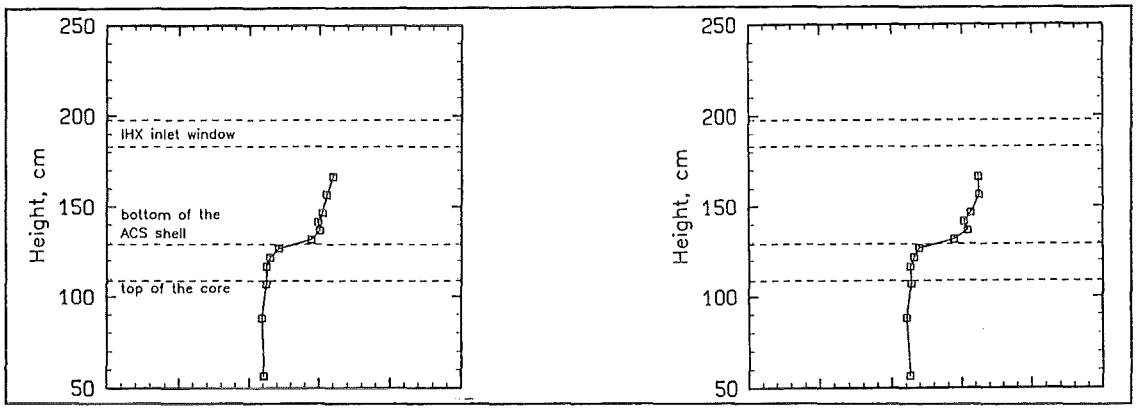

b) Axial temperature profile measured in the UP along the MER-2 device.

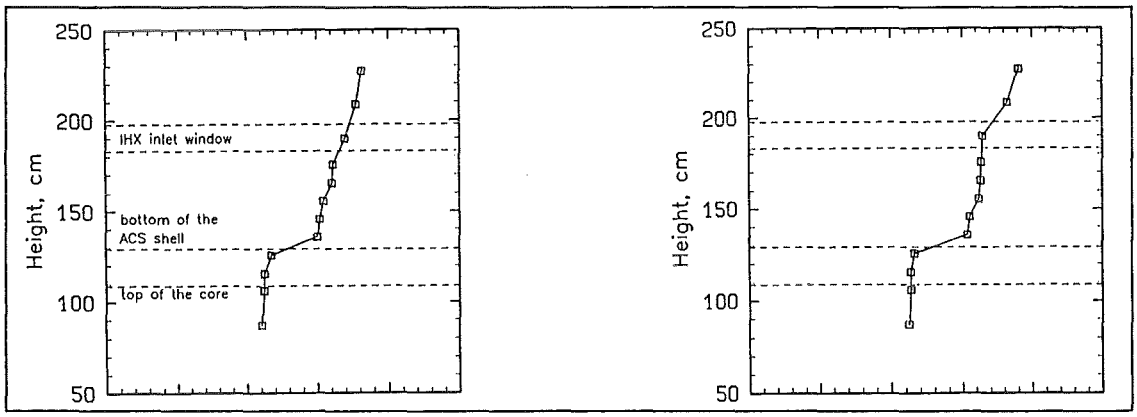

c) Axial temperature profile measured in the UP along the MER-3 device.

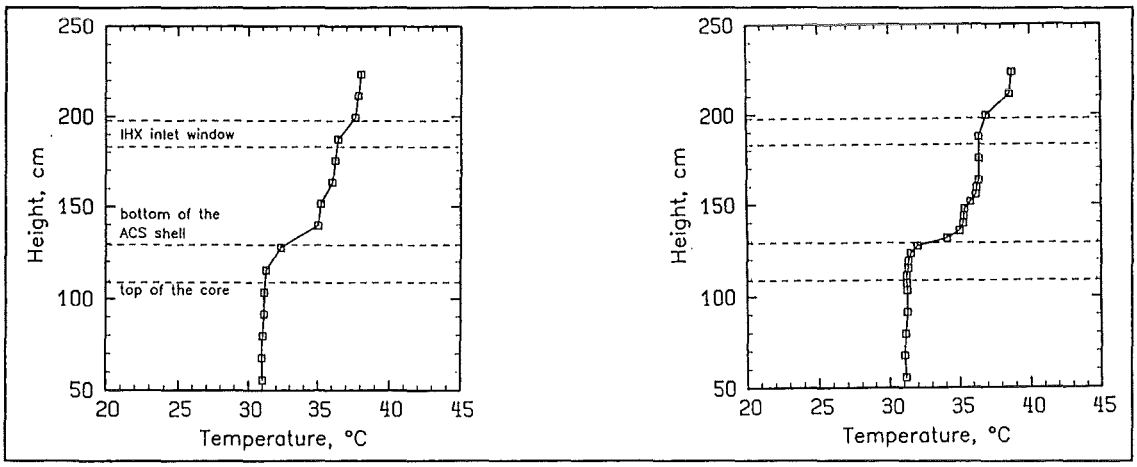

d) Axial temperature profile measured in the UP along the MEL device.

Fig. A.5.6. Influence of blocked flow paths via IHX primary loops; tests T04, T10.

Table A.6. Data comparison (cont'd.).

Flow path blockage of the IHX primary sides.

b) impermeable design of the ACS shell,
core power of 133 kW,
6 heated SA groups,
blocked flow paths via reflector and storage elements.

Test No. / Parameter	Design of ACS shell	Total core power, kW	Number of heated SA groups	Number of operated DHXs	Fluid level in the upper plenum	Flow path via reflector and storage elements	Flow path via IHX primary loops
T06	impermeable without skirt	133	6	4	normal	blocked	unblocked
T11 [1)]	impermeable without skirt	133	6	4	normal	blocked	blocked

[1)] Data of transient tests after reaching steady state conditions of natural convection.

test T06 test T11

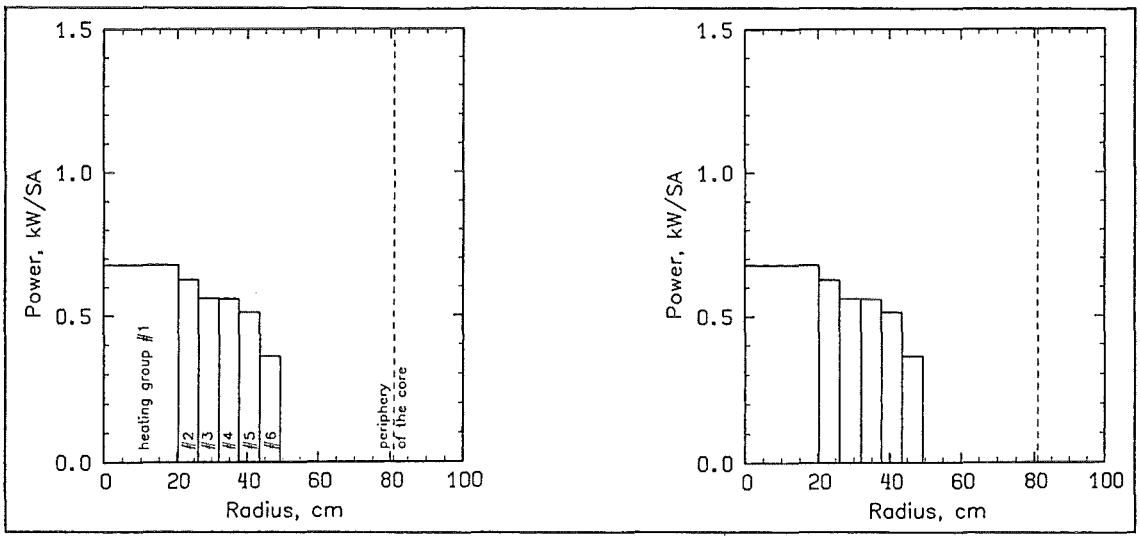

a) Radial power profile.

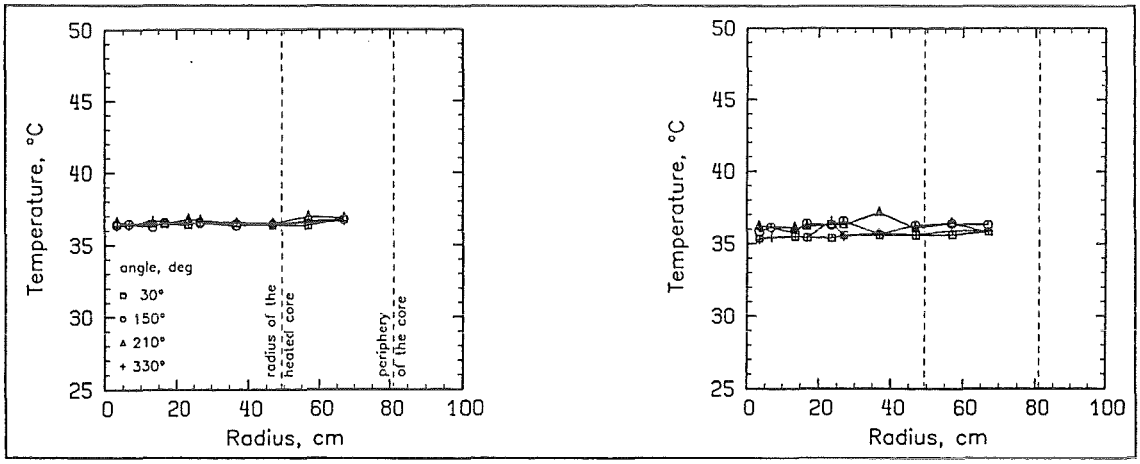

b) Radial temperature profiles of the coolant measured at the SA inlet sides.

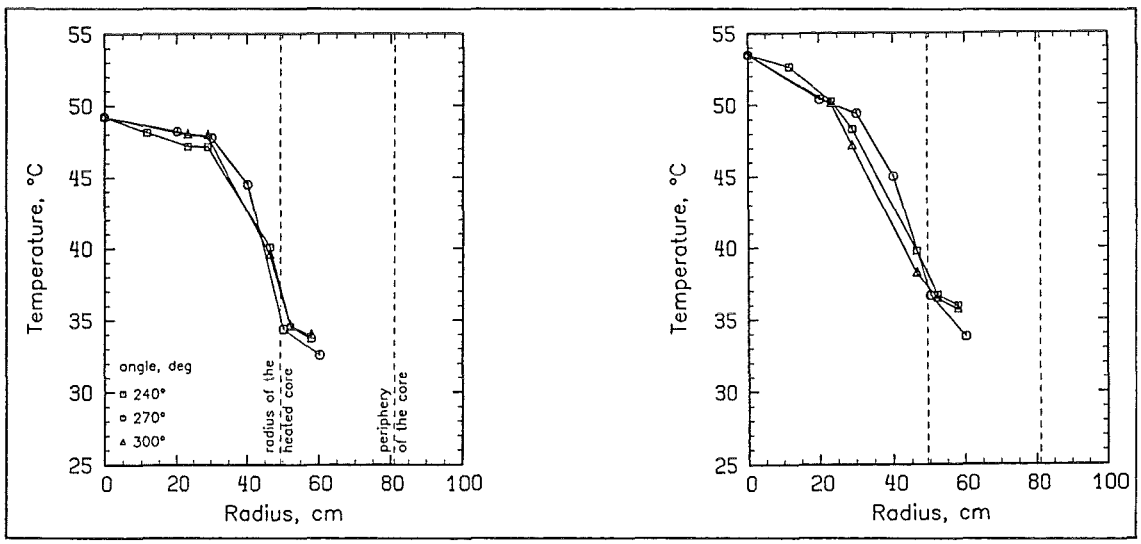

c) Radial temperature profiles of the coolant measured at the SA outlet sides.

Fig. A.6.1. Influence of blocked flow paths via IHX primary loops; tests T06, T11.

test T06 test T11

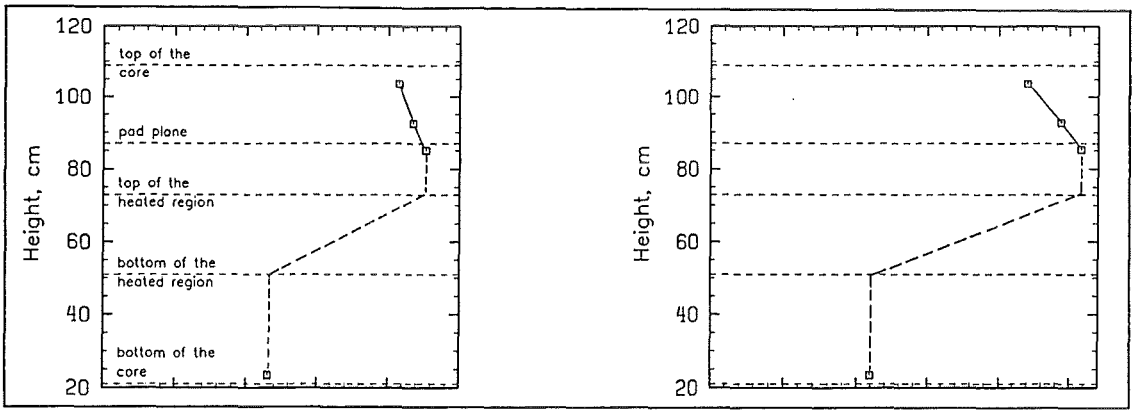

a) Axial temperature profile of the coolant measured inside SA 813 (heating group #4).

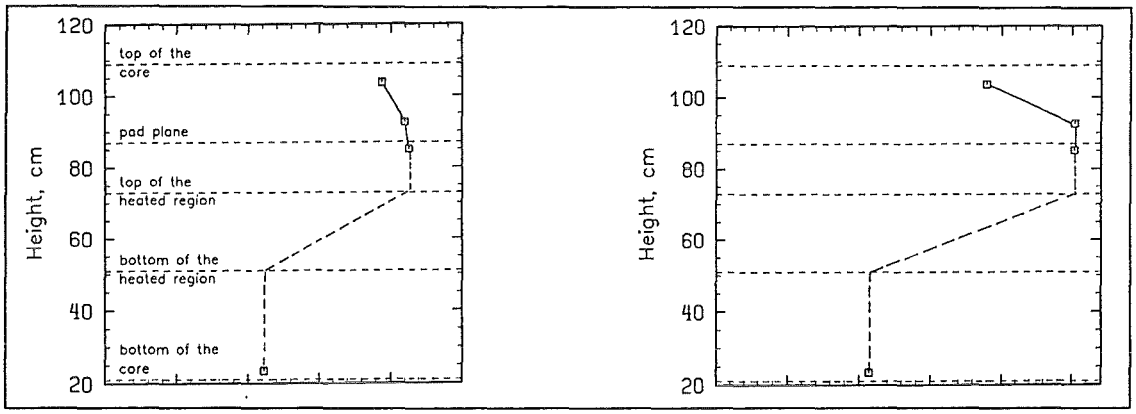

b) Axial temperature profile of the coolant measured inside SA 913 (heating group #5).

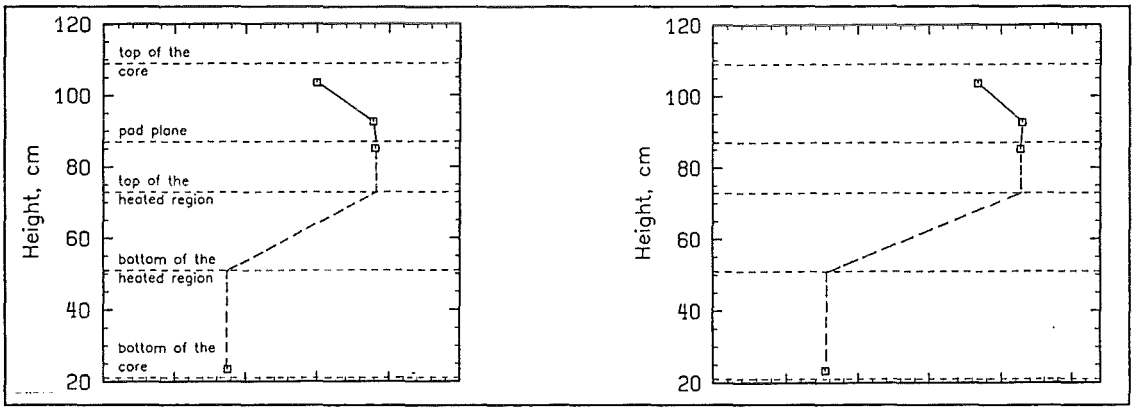

c) Axial temperature profile of the coolant measured inside SA 1017 (heating group #6).

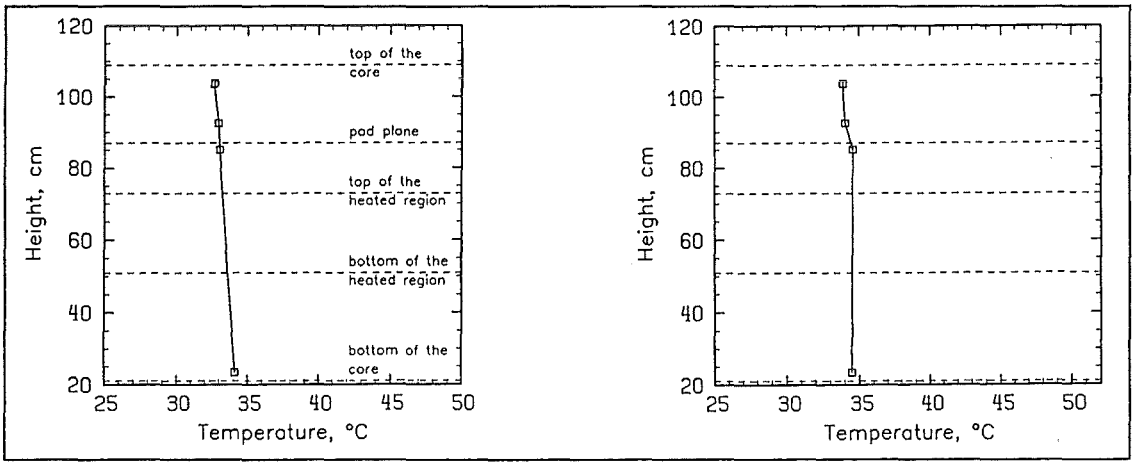

d) Axial temperature profile of the coolant measured inside SA 1319 (unheated group #7).

Fig. A.6.2. Influence of blocked flow paths via IHX primary loops; tests T06, T11.

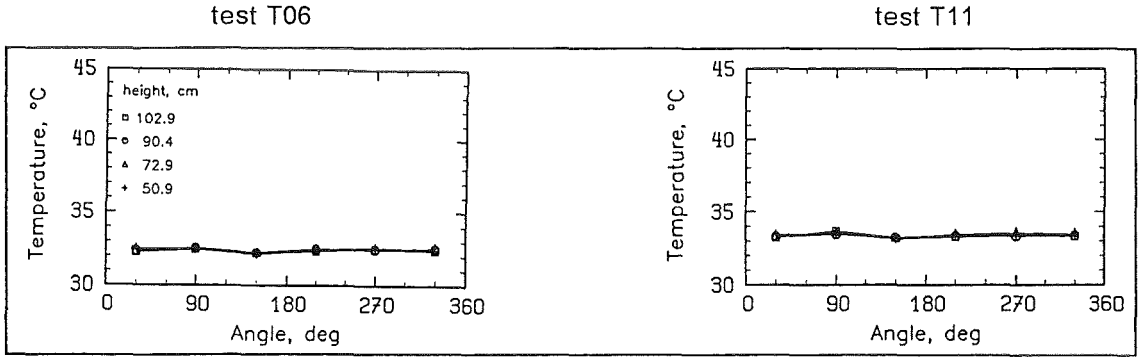

a) Azimuthal temperature profiles of the interstitial flow measured at the core periphery.

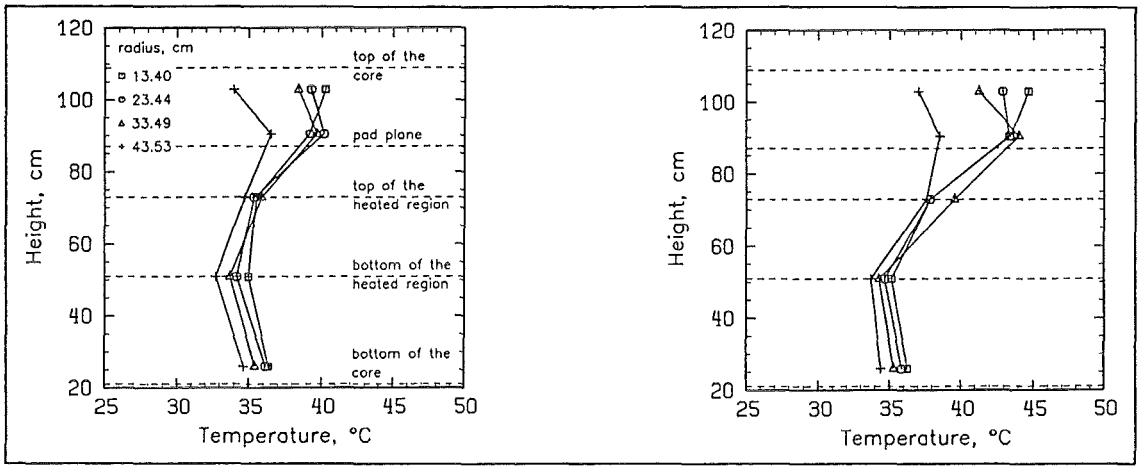

b) Axial temperatures of the interstitial flow at different radial positions (center → 90°).

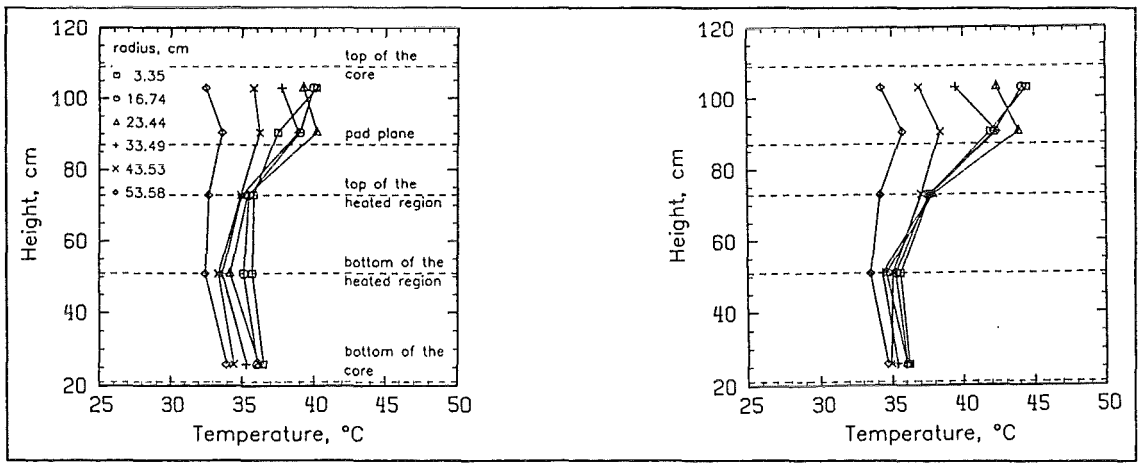

c) Axial temperatures of the interstitial flow at different radial positions (center → 270°).

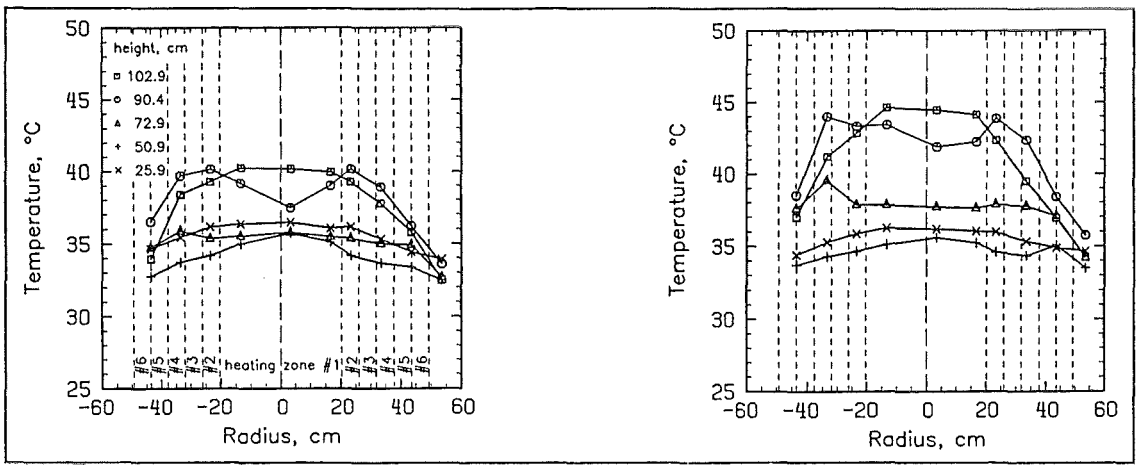

d) Horizontal temperatures of the interstitial flow across the core (90° → 270°).

Fig. A.6.3. Influence of blocked flow paths via IHX primary loops; tests T06, T11.

test T06 test T11

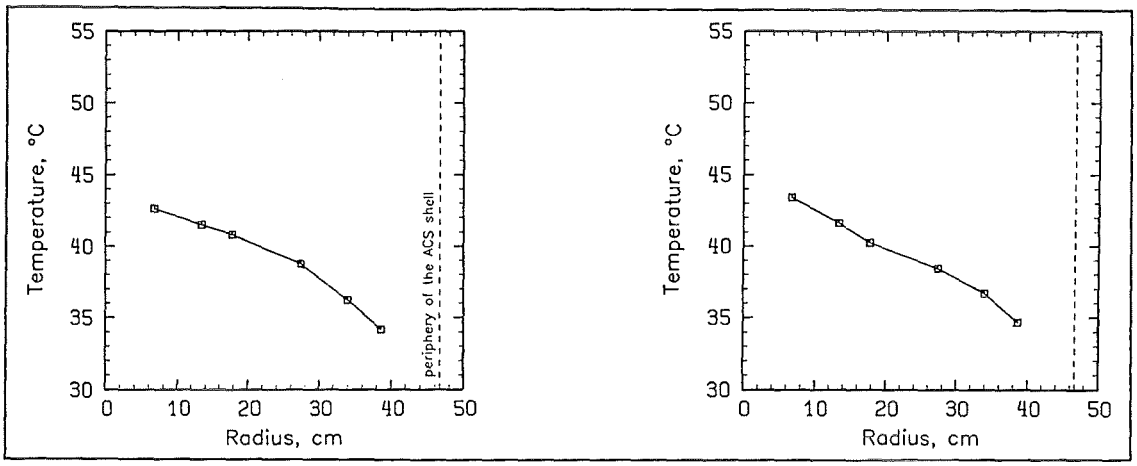

a) Radial temperature profile measured at the bottom end of the ACS (z = 1,248 mm).

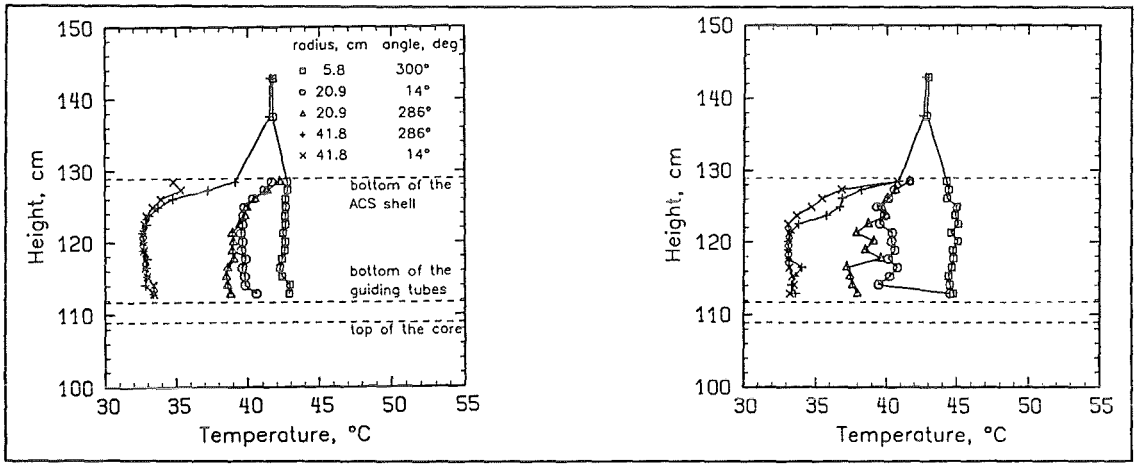

b) Axial temperature profiles at the bottom end and inside the lower part of the ACS.

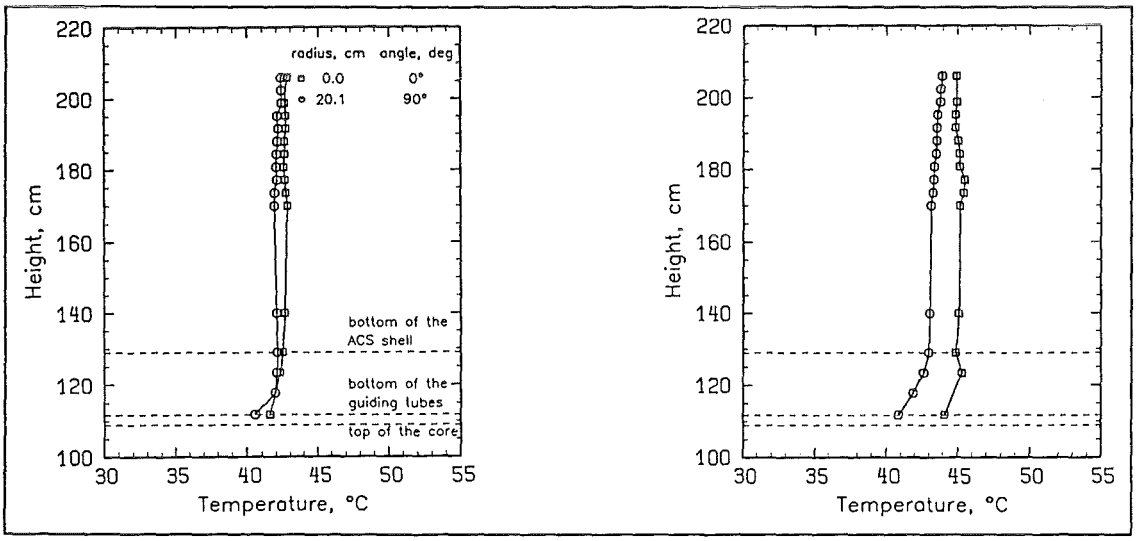

c) Axial temperature profiles measured inside the ACS.

Fig. A.6.4. Influence of blocked flow paths via IHX primary loops; tests T06, T11.

test T06 test T11

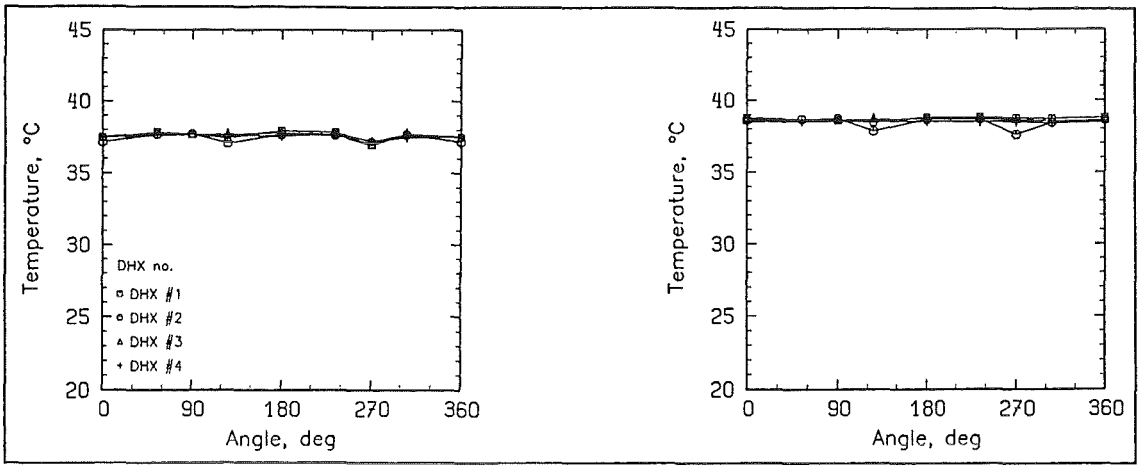

a) Azimuthal temperature profiles measured at the DHX inlet windows (z = 2,299 mm).

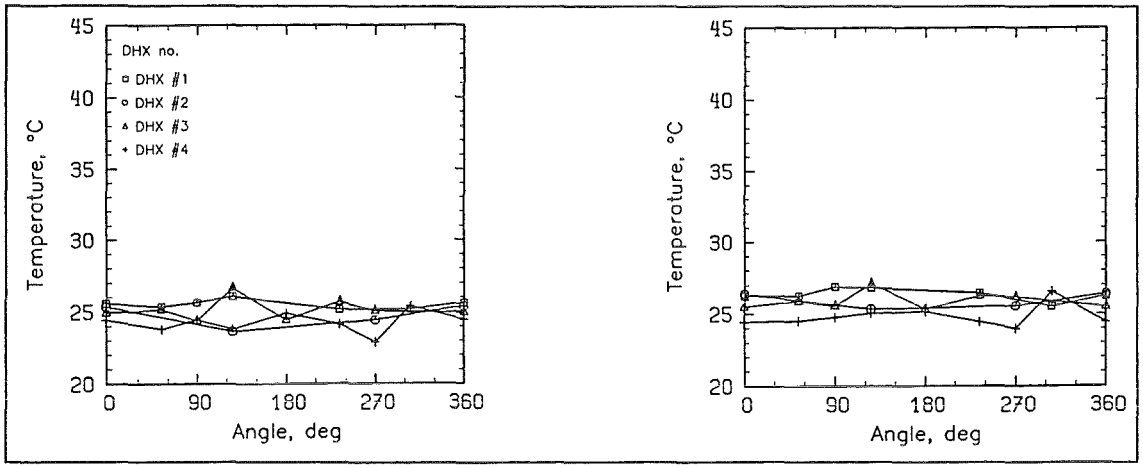

b) Azimuthal temperature profiles measured at the DHX outlet windows (z = 1,391 mm).

Fig. A.6.5. Influence of blocked flow paths via IHX primary loops; tests T06, T11.

test T06 test T11

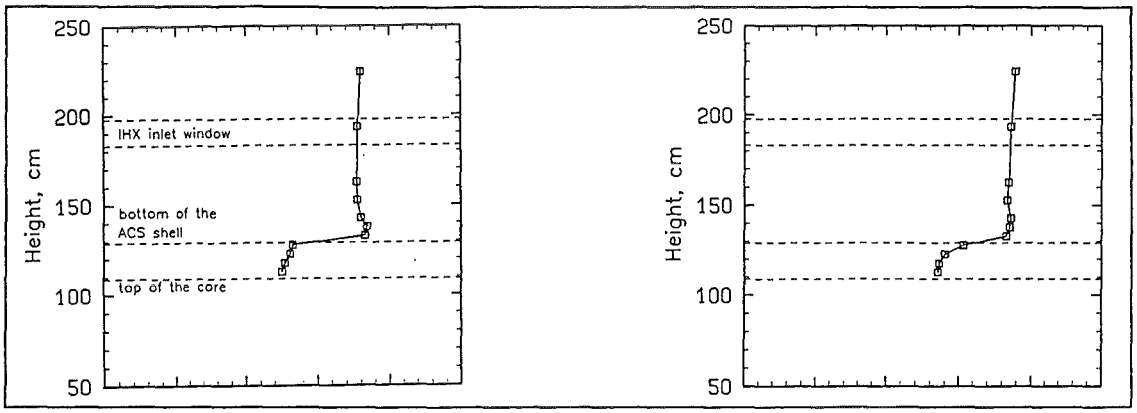

a) Axial temperature profile measured in the UP along the MER-1 device.

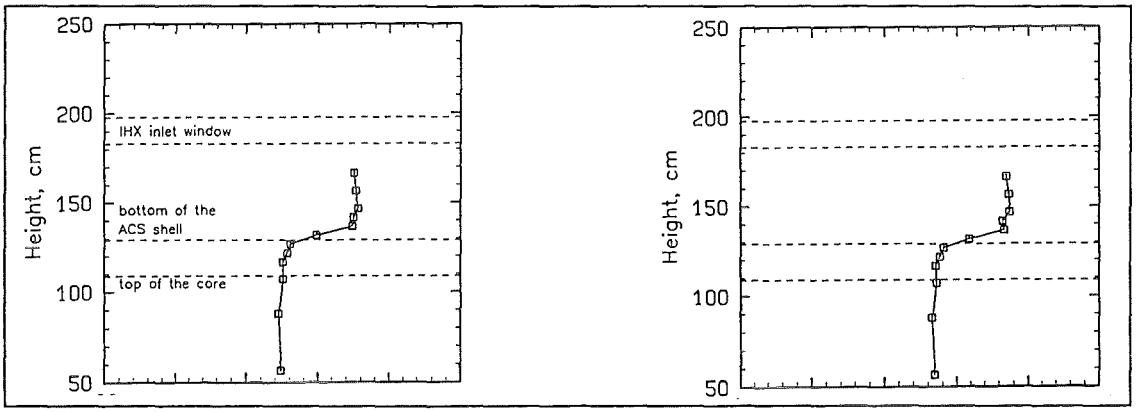

b) Axial temperature profile measured in the UP along the MER-2 device.

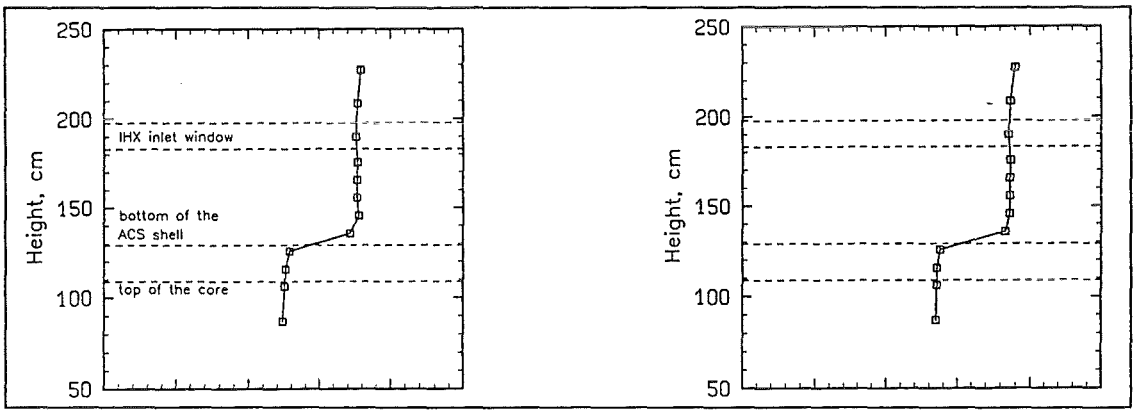

c) Axial temperature profile measured in the UP along the MER-3 device.

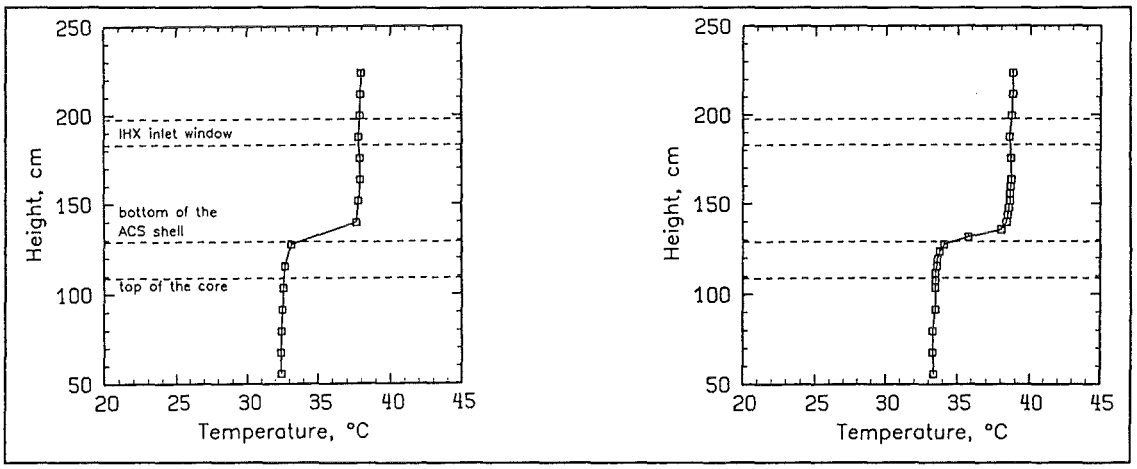

d) Axial temperature profile measured in the UP along the MEL device.

Fig. A.6.6. Influence of blocked flow paths via IHX primary loops; tests T06, T11.

Table A.7. Data comparison (cont'd.).

Flow path blockage of the IHX primary sides.

c) permeable design of the ACS shell,
core power of 150 kW,
7 heated SA groups,
unblocked flow paths via reflector and storage elements.

Test No. / Parameter	Design of ACS shell	Total core power, kW	Number of heated SA groups	Number of operated DHXs	Fluid level in the upper plenum	Flow path via reflector and storage elements	Flow path via IHX primary loops
T12	permeable without skirt	150	7	4	normal	unblocked	unblocked
T13 [1)]	permeable without skirt	150	7	4	normal	unblocked	blocked

[1)] Data of transient tests after reaching steady state conditions of natural convection.

test T12 test T13

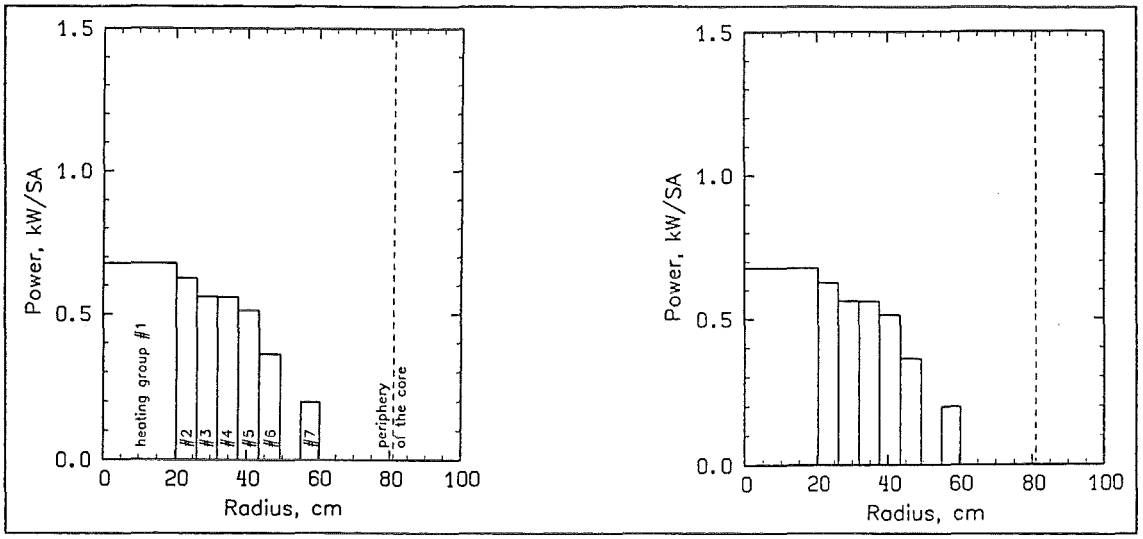

a) Radial power profile.

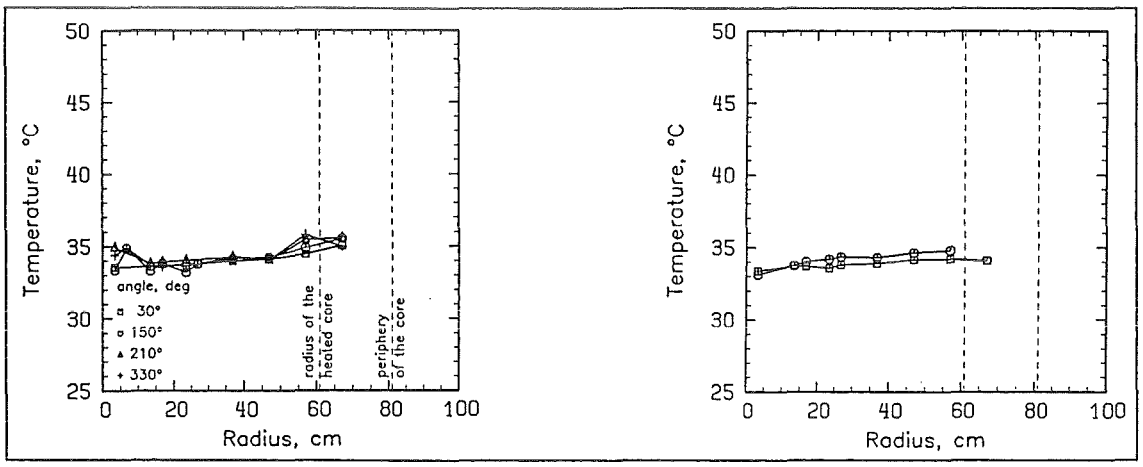

b) Radial temperature profiles of the coolant measured at the SA inlet sides.

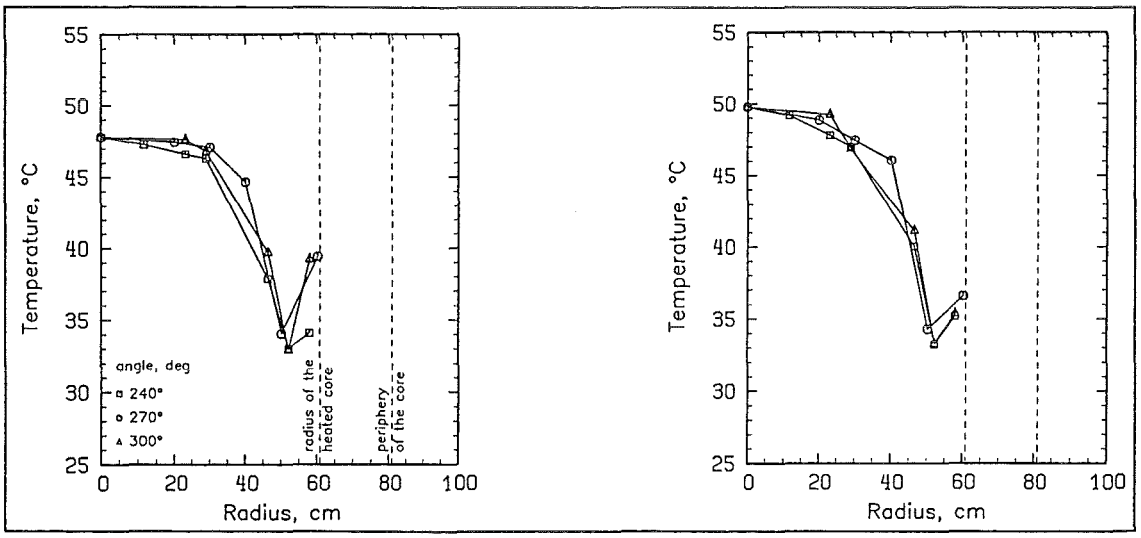

c) Radial temperature profiles of the coolant measured at the SA outlet sides.

Fig. A.7.1. Influence of blocked flow paths via IHX primary loops; tests T12, T13.

test T12 test T13

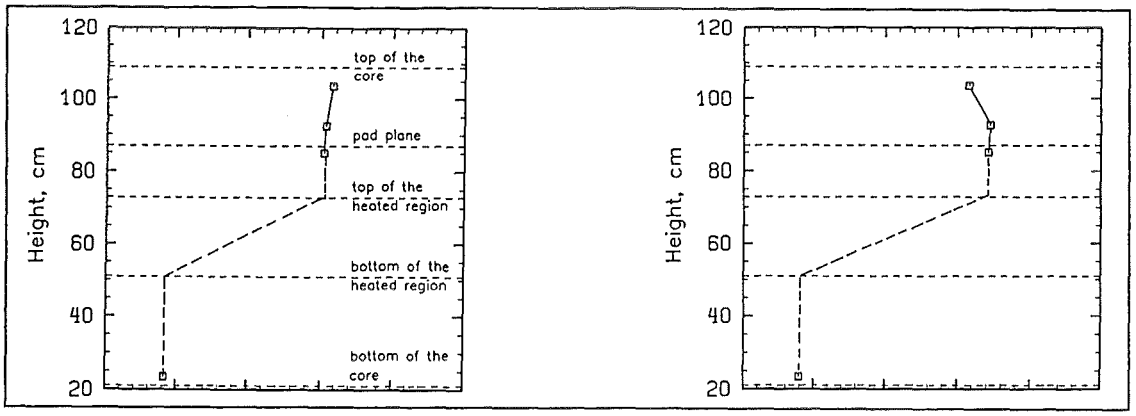

a) Axial temperature profile of the coolant measured inside SA 813 (heating group #4).

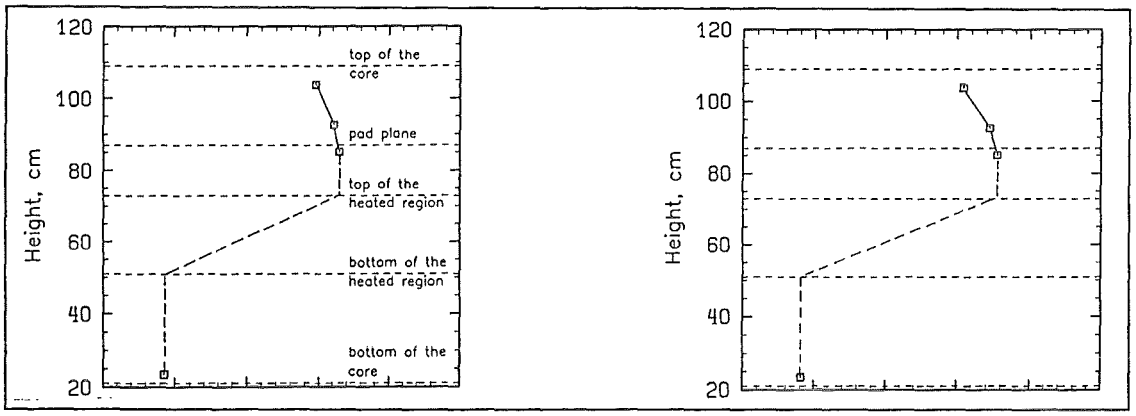

b) Axial temperature profile of the coolant measured inside SA 913 (heating group #5).

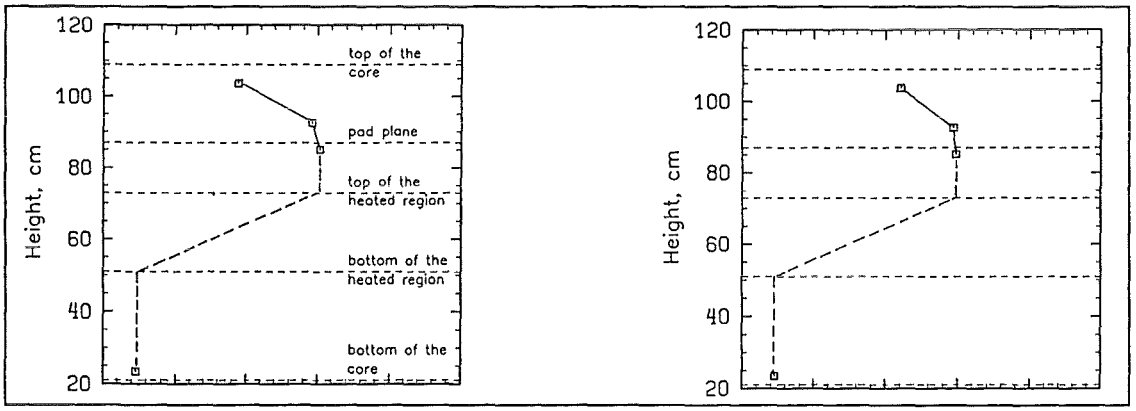

c) Axial temperature profile of the coolant measured inside SA 1017 (heating group #6).

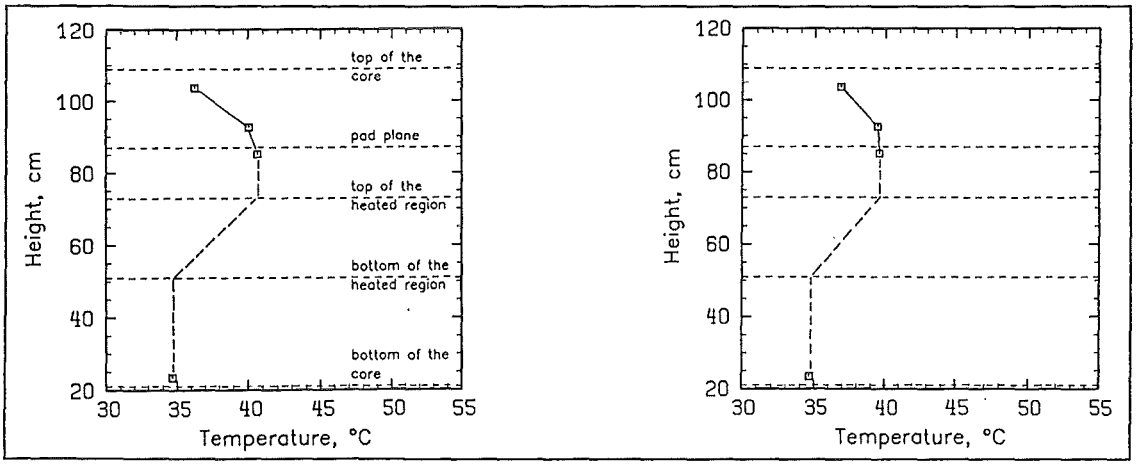

d) Axial temperature profile of the coolant measured inside SA 1319 (heating group #7).

Fig. A.7.2. Influence of blocked flow paths via IHX primary loops; tests T12, T13.

test T12 test T13

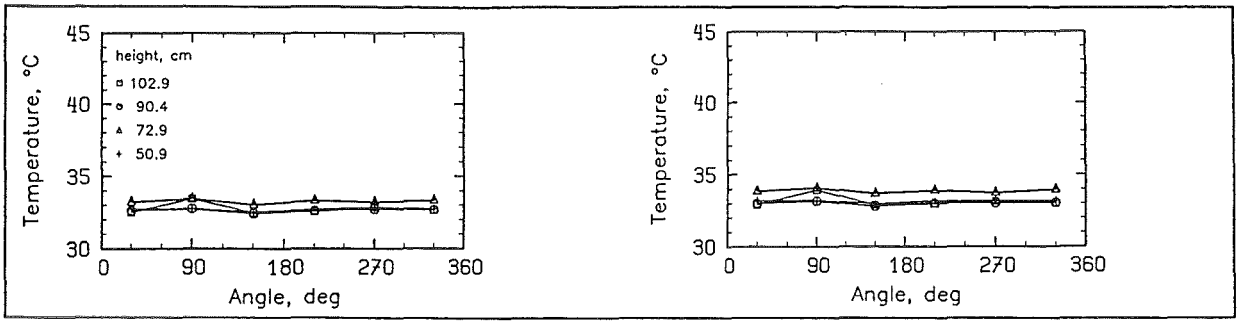

a) Azimuthal temperature profiles of the interstitial flow measured at the core periphery.

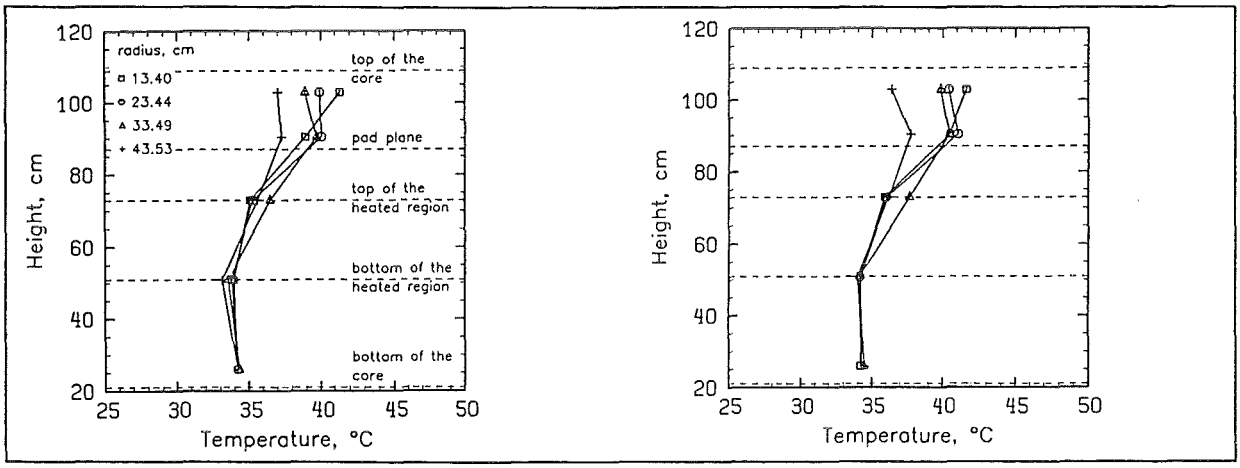

b) Axial temperatures of the interstitial flow at different radial positions (center → 90°).

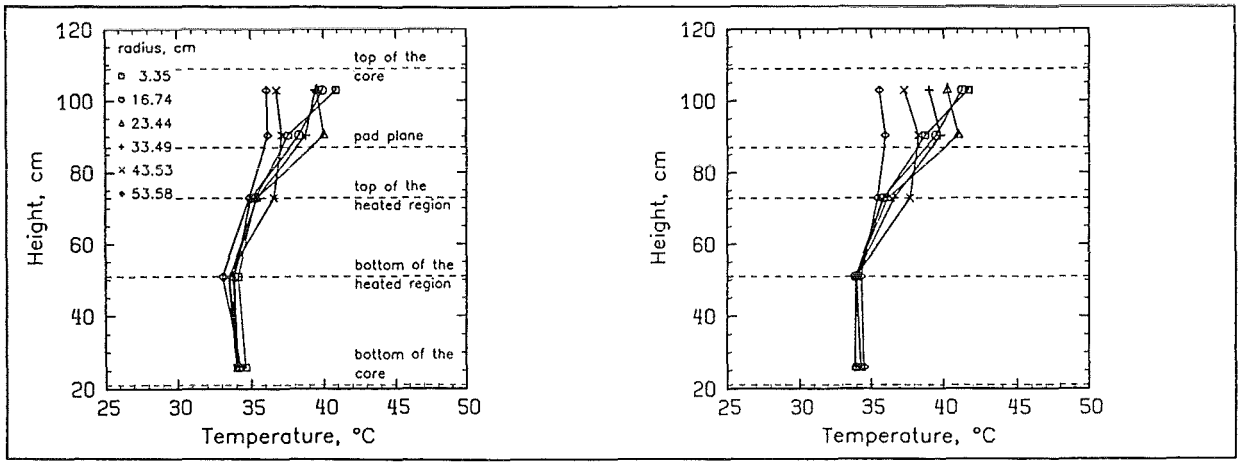

c) Axial temperatures of the interstitial flow at different radial positions (center → 270°).

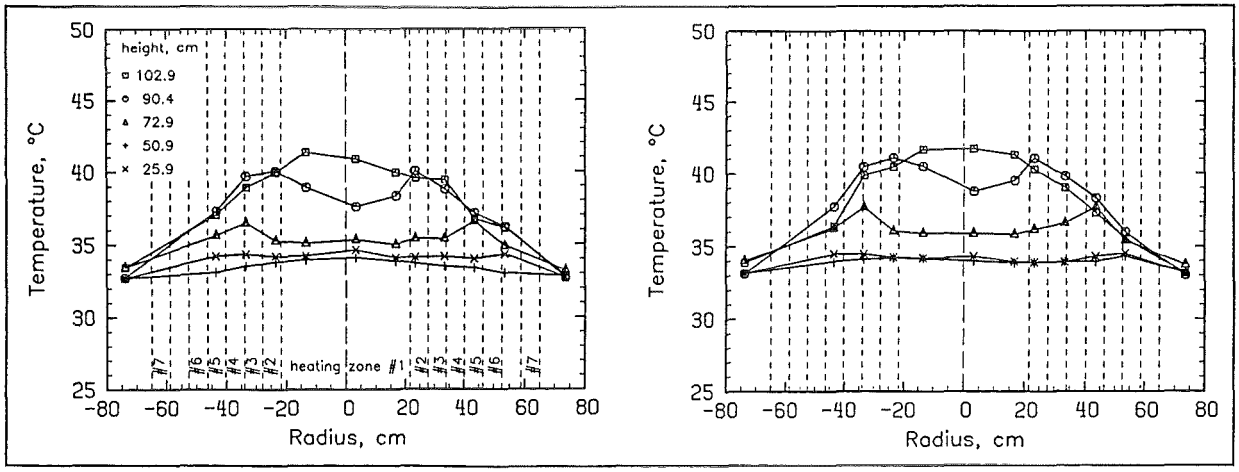

d) Horizontal temperatures of the interstitial flow across the core (90° → 270°).

Fig. A.7.3. Influence of blocked flow paths via IHX primary loops; tests T12, T13.

test T12 test T13

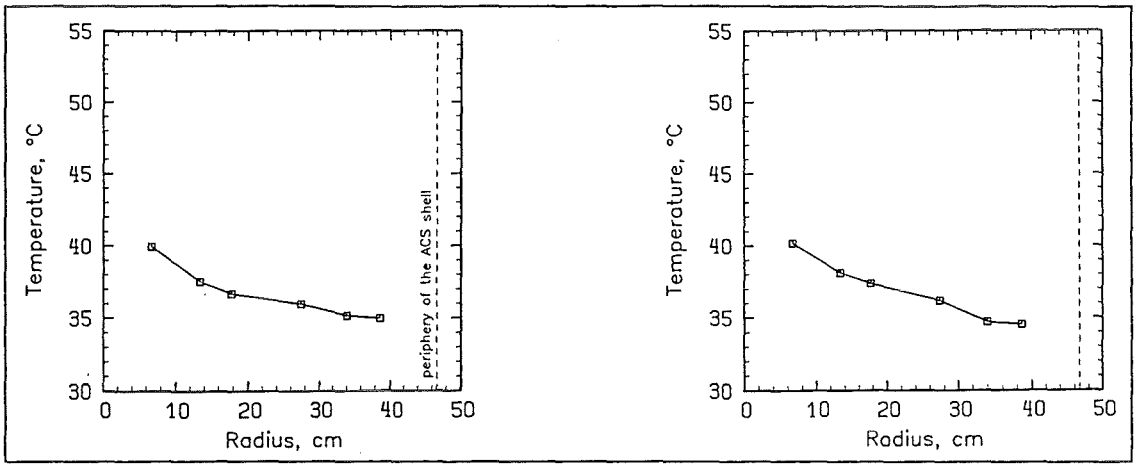

a) Radial temperature profile measured at the bottom end of the ACS (z = 1,248 mm).

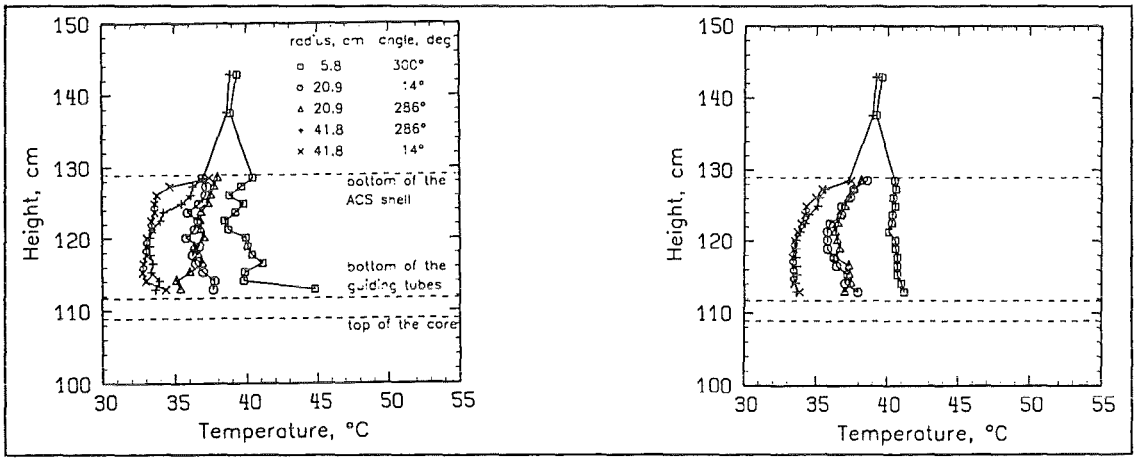

b) Axial temperature profiles at the bottom end and inside the lower part of the ACS.

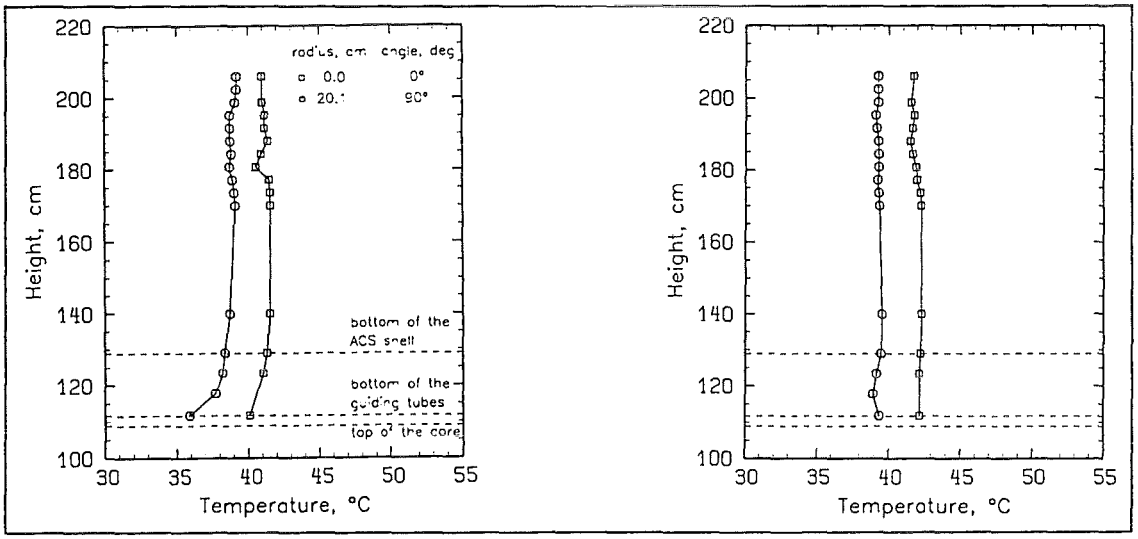

c) Axial temperature profiles measured inside the ACS.

Fig. A.7.4. Influence of blocked flow paths via IHX primary loops; tests T12, T13.

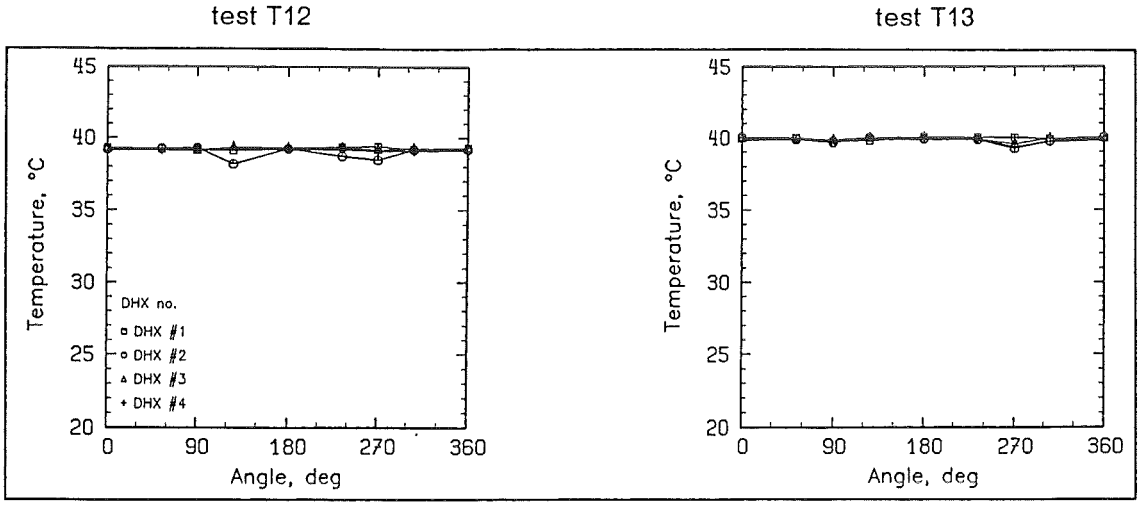

a) Azimuthal temperature profiles measured at the DHX inlet windows (z = 2,299 mm).

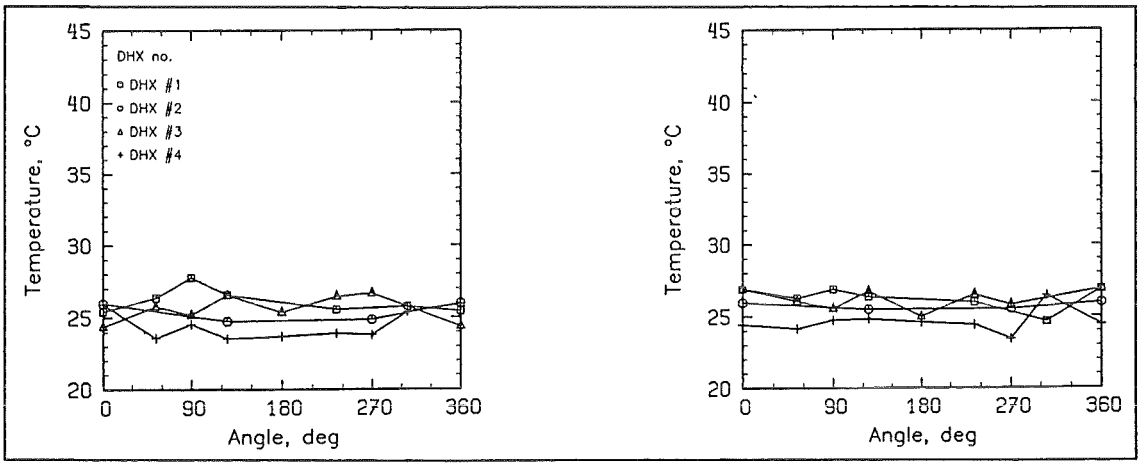

b) Azimuthal temperature profiles measured at the DHX outlet windows (z = 1,391 mm).

Fig. A.7.5. Influence of blocked flow paths via IHX primary loops; tests T12, T13.

test T12 test T13

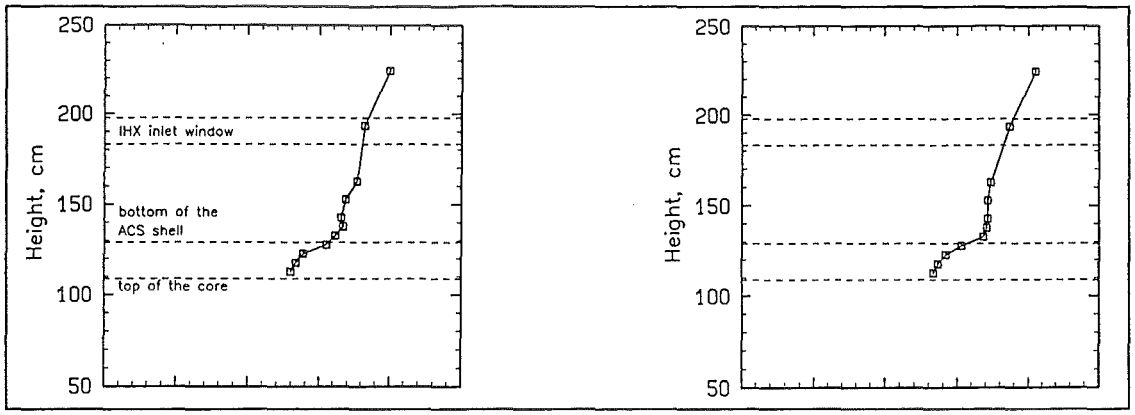

a) Axial temperature profile measured in the UP along the MER-1 device.

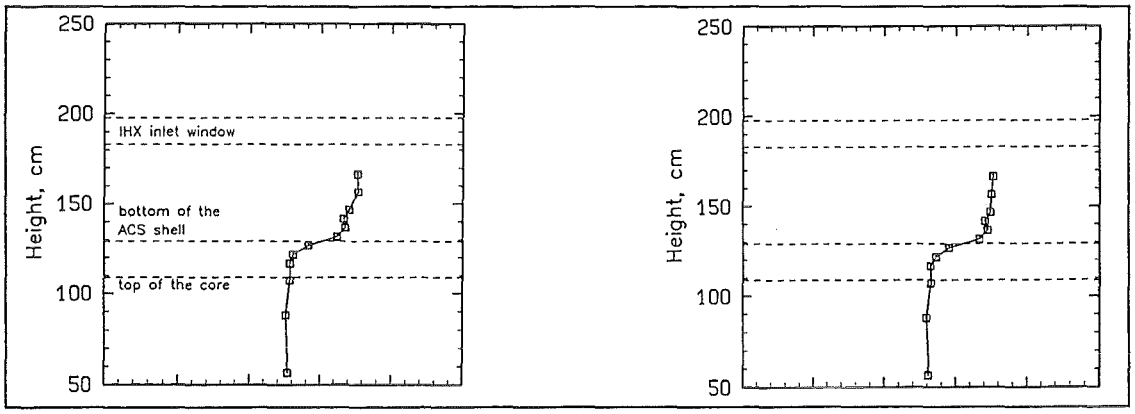

b) Axial temperature profile measured in the UP along the MER-2 device.

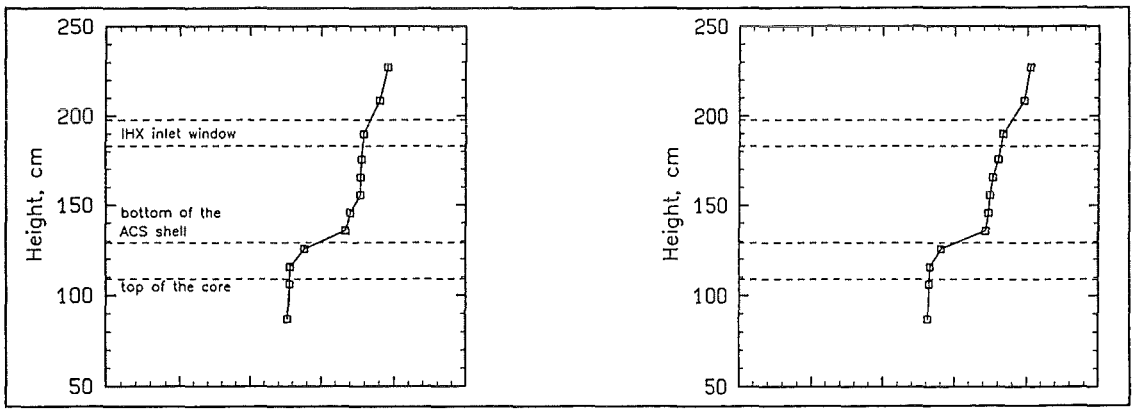

c) Axial temperature profile measured in the UP along the MER-3 device.

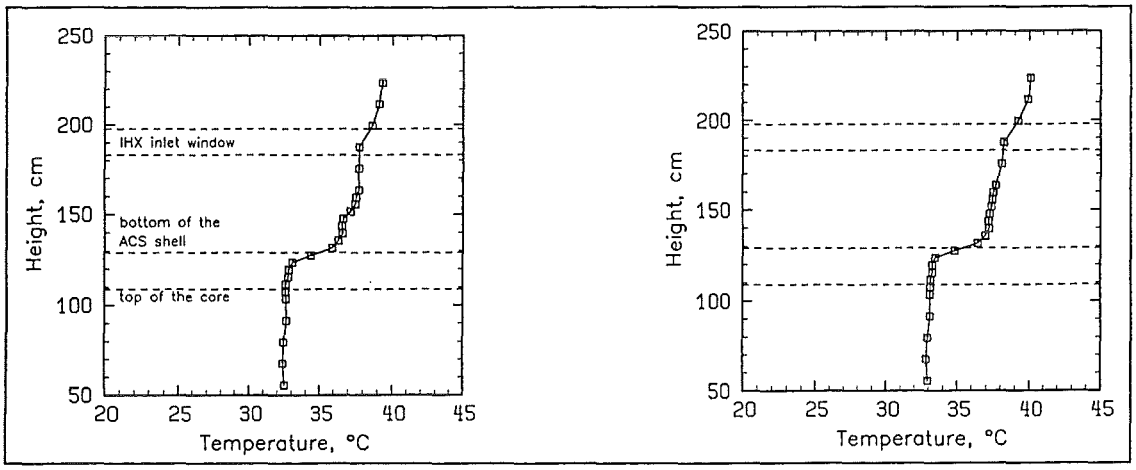

d) Axial temperature profile measured in the UP along the MEL device.

Fig. A.7.6. Influence of blocked flow paths via IHX primary loops; tests T12, T13.

Table A.8. Data comparison (cont'd.).

Flow path blockage of the IHX primary sides.

d) impermeable design of the ACS shell,
core power of 150 kW,
7 heated SA groups,
unblocked flow paths via reflector and storage elements.

Test No. / Parameter	Design of ACS shell	Total core power, kW	Number of heated SA groups	Number of operated DHXs	Fluid level in the upper plenum	Flow path via reflector and storage elements	Flow path via IHX primary loops
T14 [1)]	impermeable without skirt	150	7	4	normal	unblocked	unblocked
T15 [1)]	impermeable without skirt	150	7	4	normal	unblocked	blocked

[1)] Data of transient tests after reaching steady state conditions of natural convection.

test T14 test T15

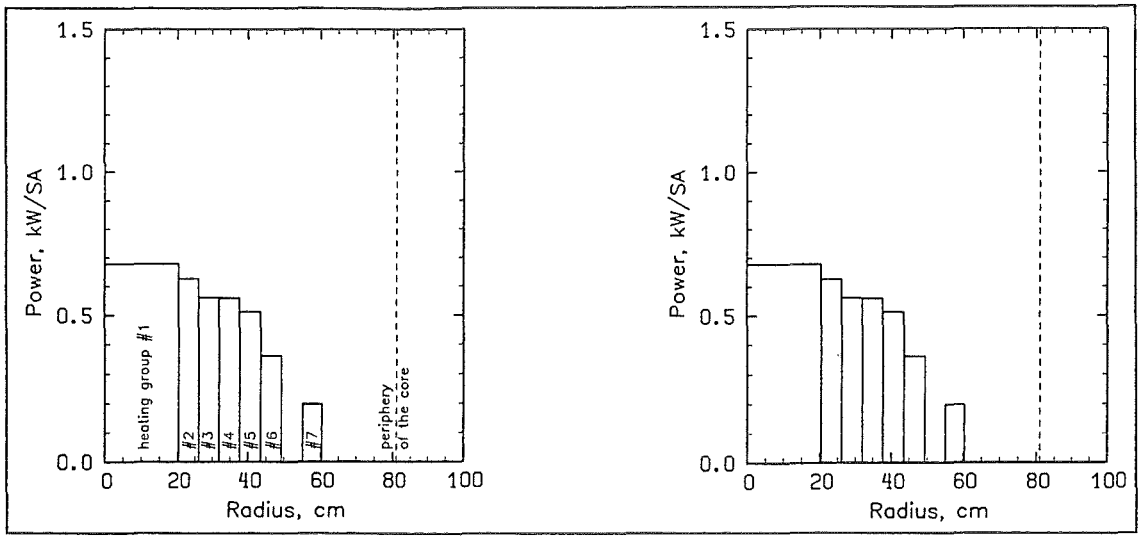

a) Radial power profile.

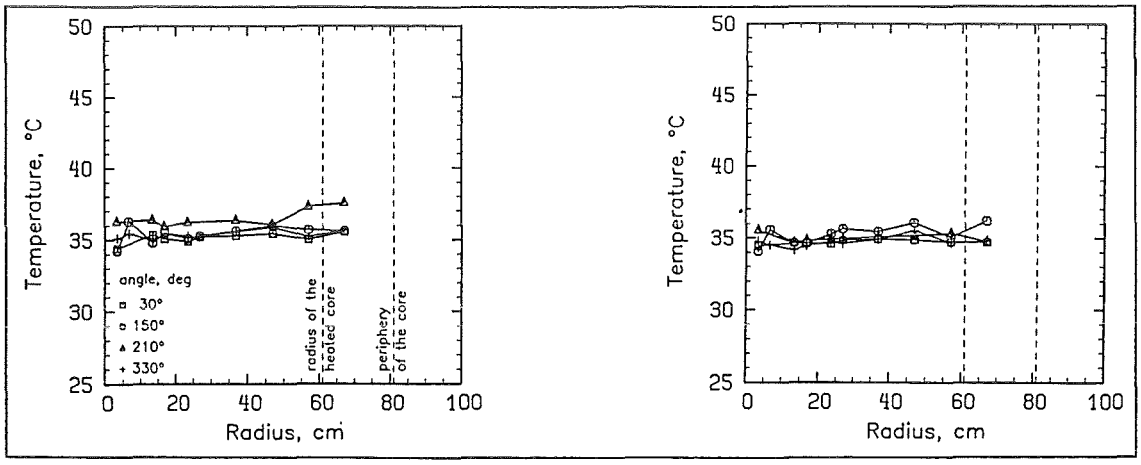

b) Radial temperature profiles of the coolant measured at the SA inlet sides.

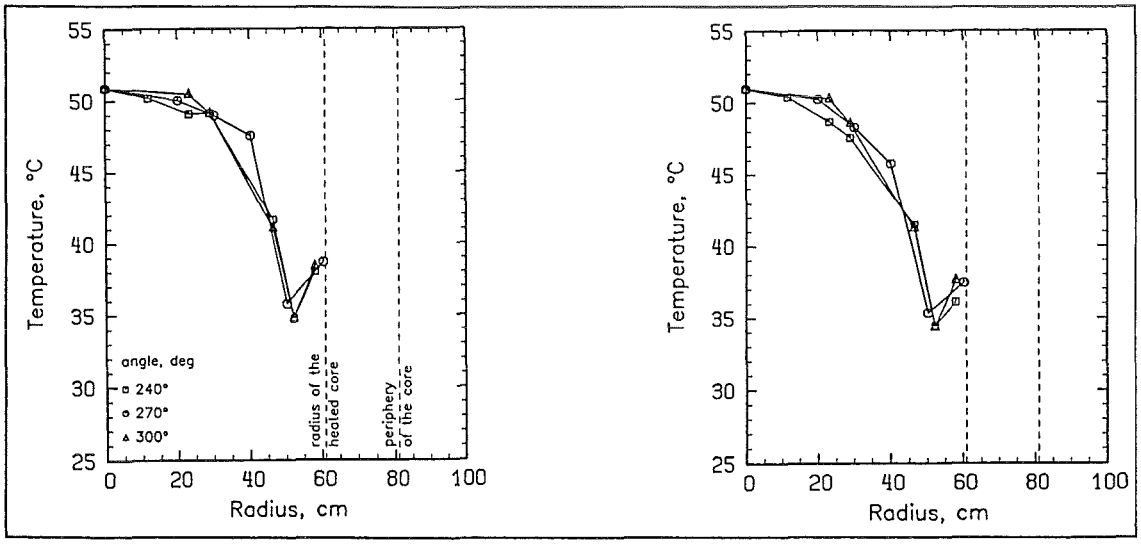

c) Radial temperature profiles of the coolant measured at the SA outlet sides.

Fig. A.8.1. Influence of blocked flow paths via IHX primary loops; tests T14, T15.

test T14 test T15

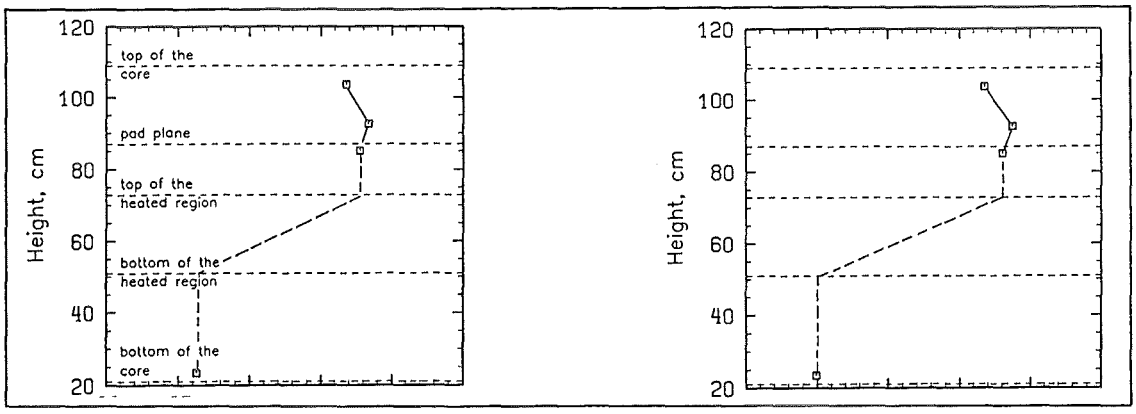

a) Axial temperature profile of the coolant measured inside SA 813 (heating group #4).

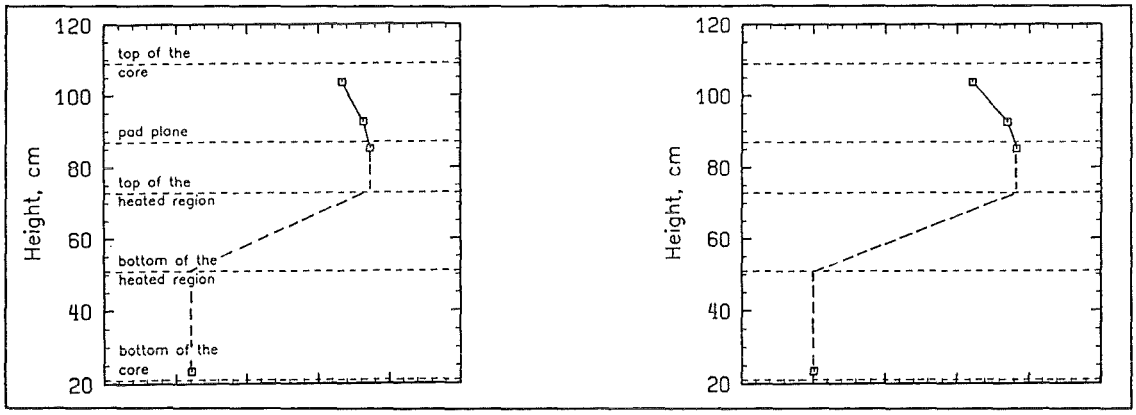

b) Axial temperature profile of the coolant measured inside SA 913 (heating group #5).

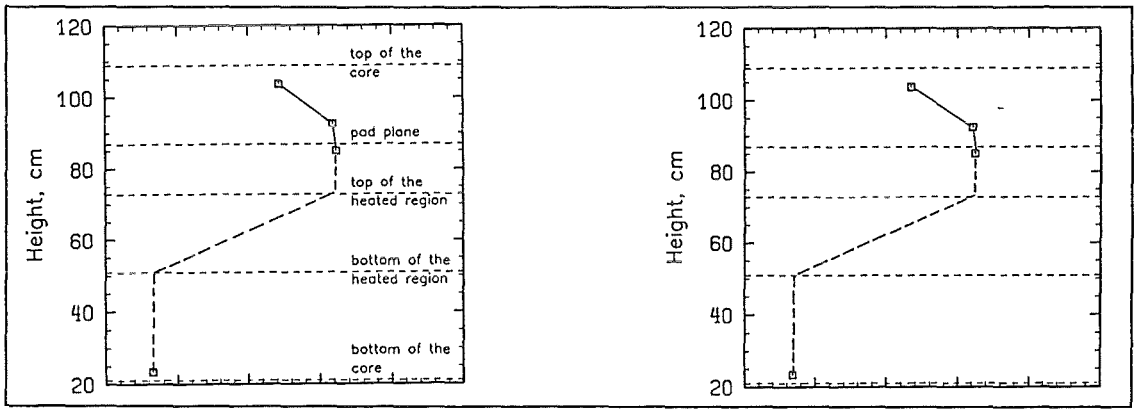

c) Axial temperature profile of the coolant measured inside SA 1017 (heating group #6).

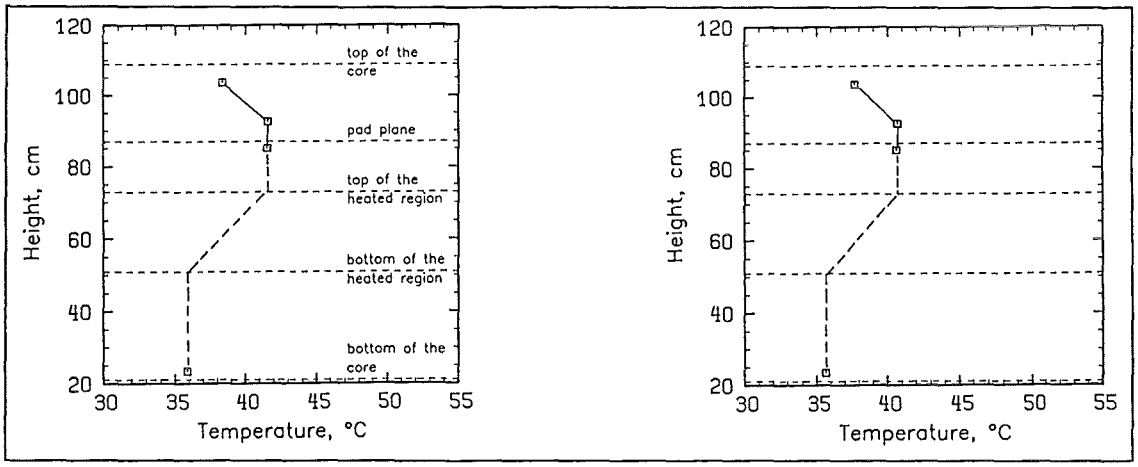

d) Axial temperature profile of the coolant measured inside SA 1319 (heating group #7).

Fig. A.8.2. Influence of blocked flow paths via IHX primary loops; tests T14, T15.

test T14 test T15

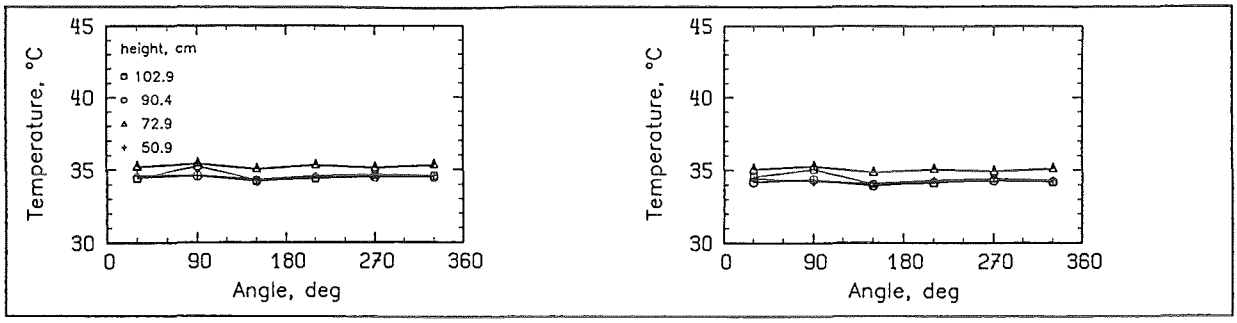

a) Azimuthal temperature profiles of the interstitial flow measured at the core periphery.

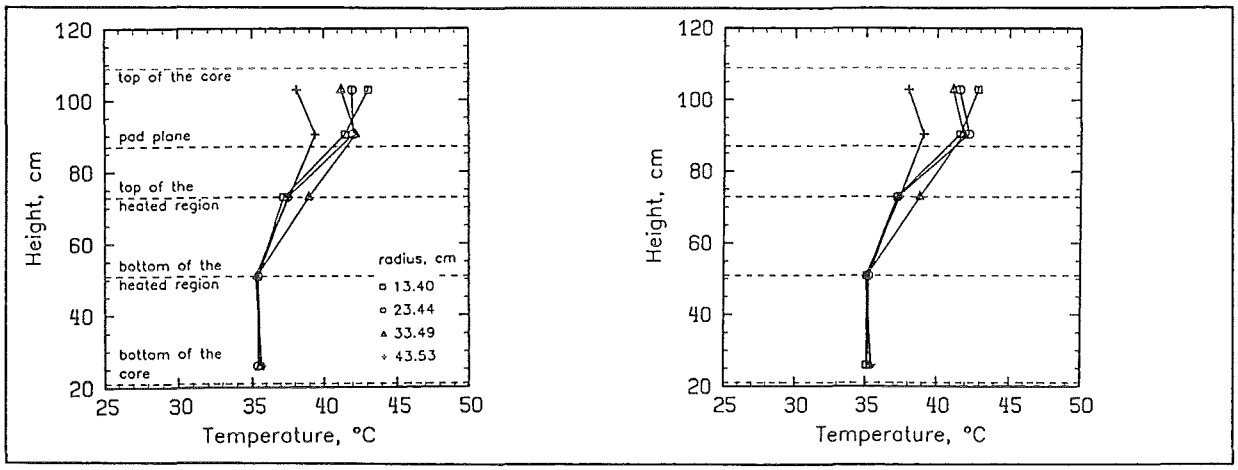

b) Axial temperatures of the interstitial flow at different radial positions (center → 90°).

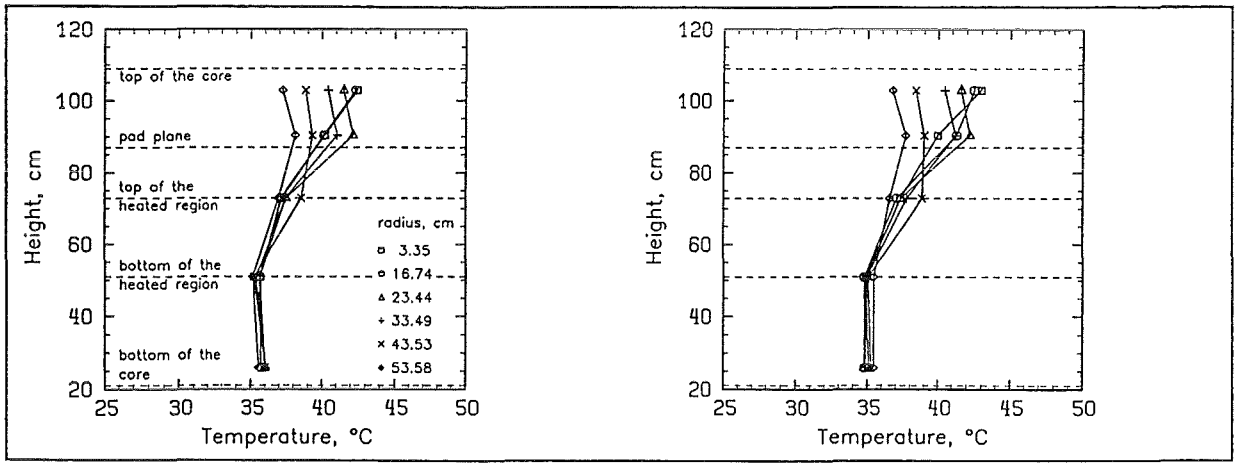

c) Axial temperatures of the interstitial flow at different radial positions (center → 270°).

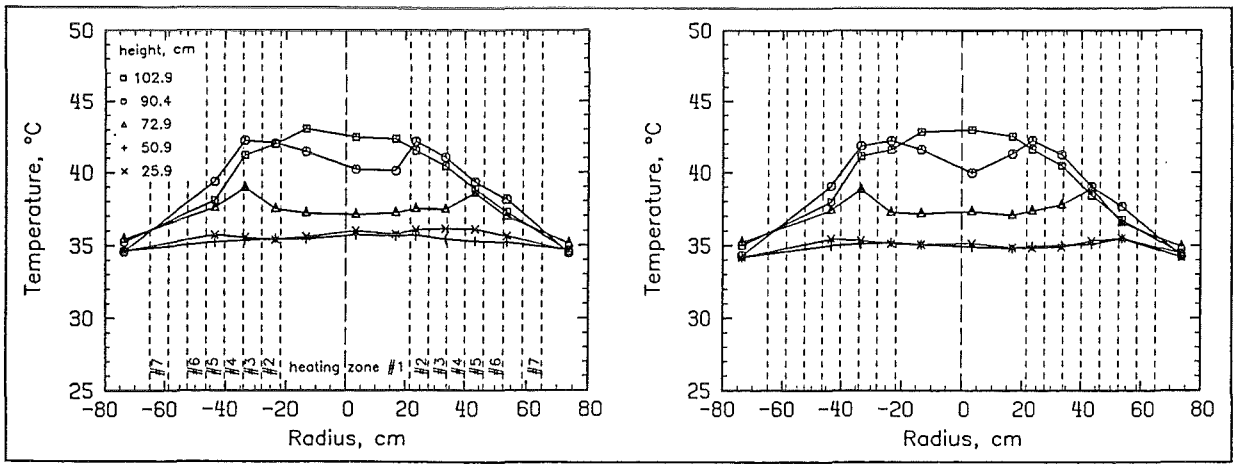

d) Horizontal temperatures of the interstitial flow across the core (90° → 270°).

Fig. A.8.3. Influence of blocked flow paths via IHX primary loops; tests T14, T15.

test T14 test T15

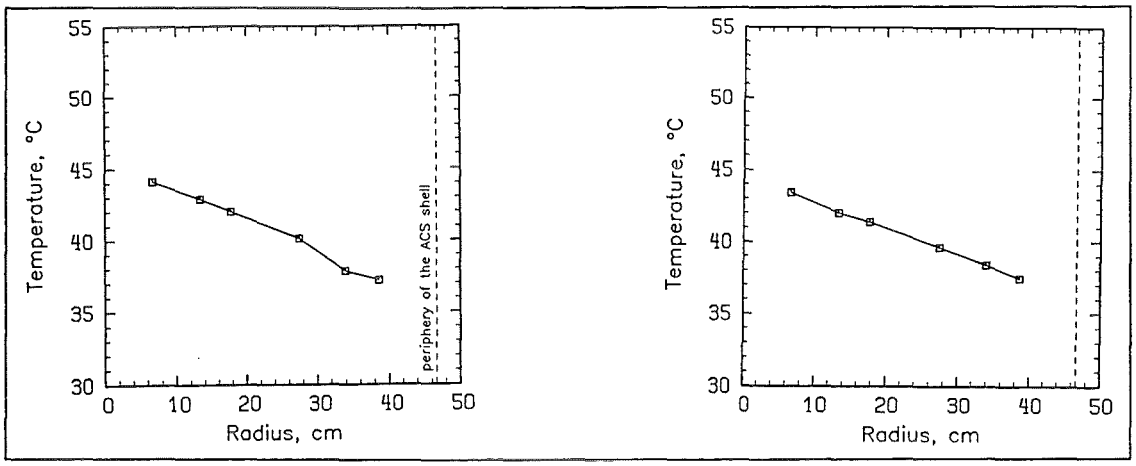

a) Radial temperature profile measured at the bottom end of the ACS (z = 1,248 mm).

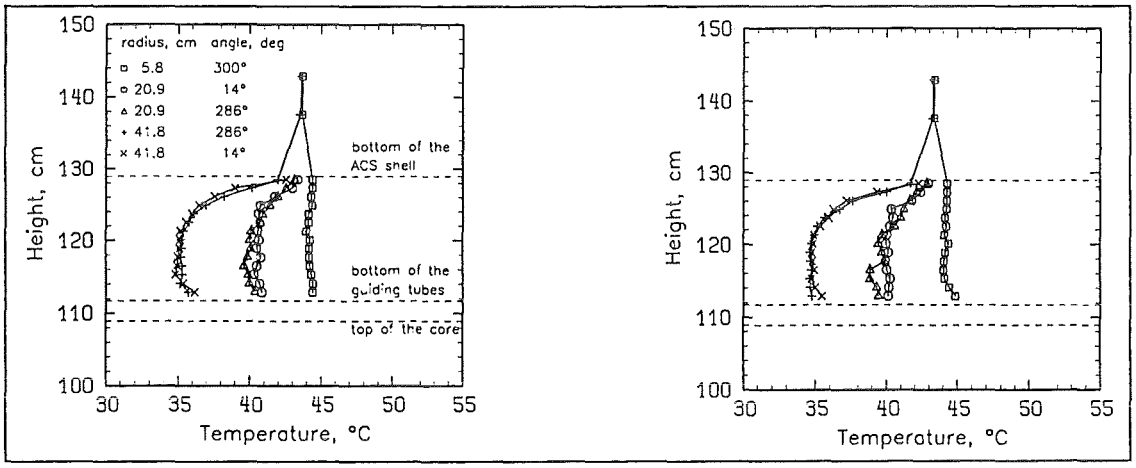

b) Axial temperature profiles at the bottom end and inside the lower part of the ACS.

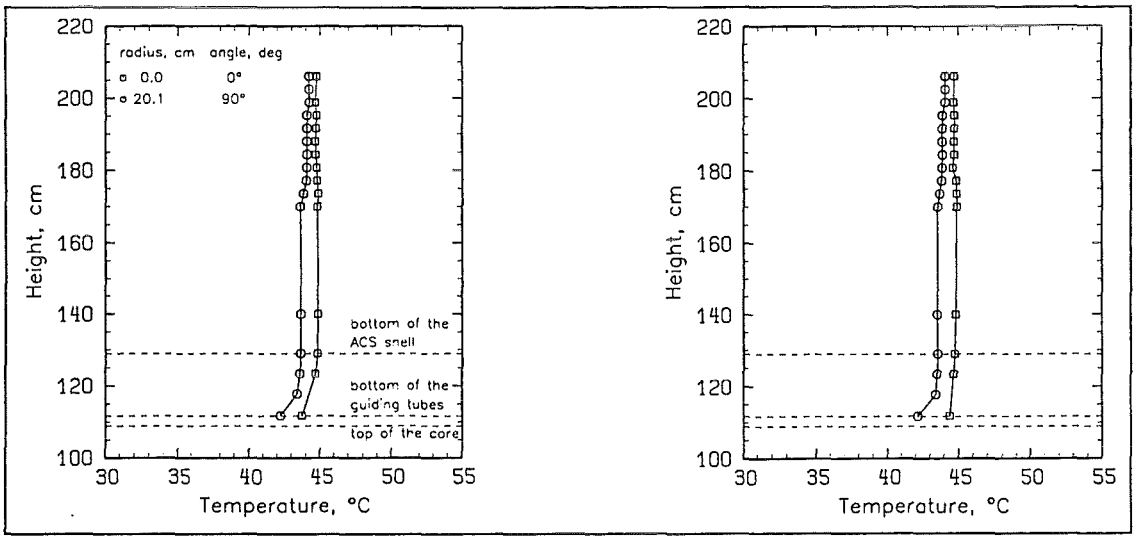

c) Axial temperature profiles measured inside the ACS.

Fig. A.8.4. Influence of blocked flow paths via IHX primary loops; tests T14, T15.

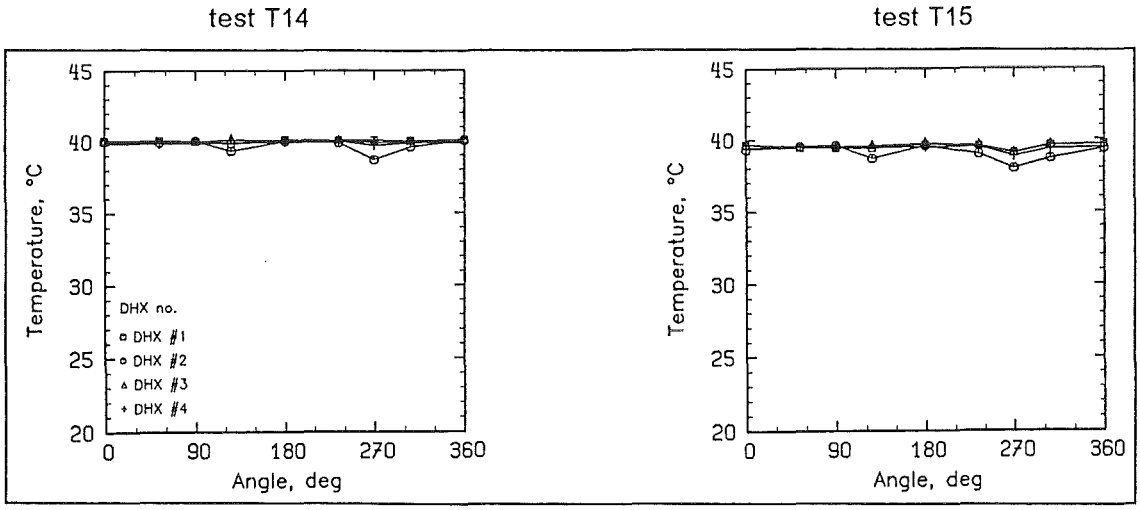

a) Azimuthal temperature profiles measured at the DHX inlet windows (z = 2,299 mm).

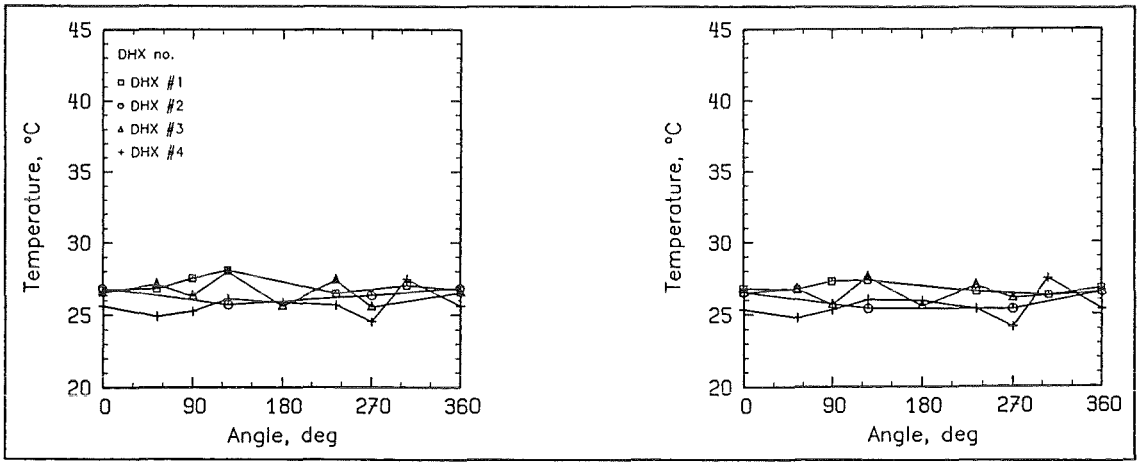

b) Azimuthal temperature profiles measured at the DHX outlet windows (z = 1,391 mm).

Fig. A.8.5. Influence of blocked flow paths via IHX primary loops; tests T14, T15.

test T14 test T15

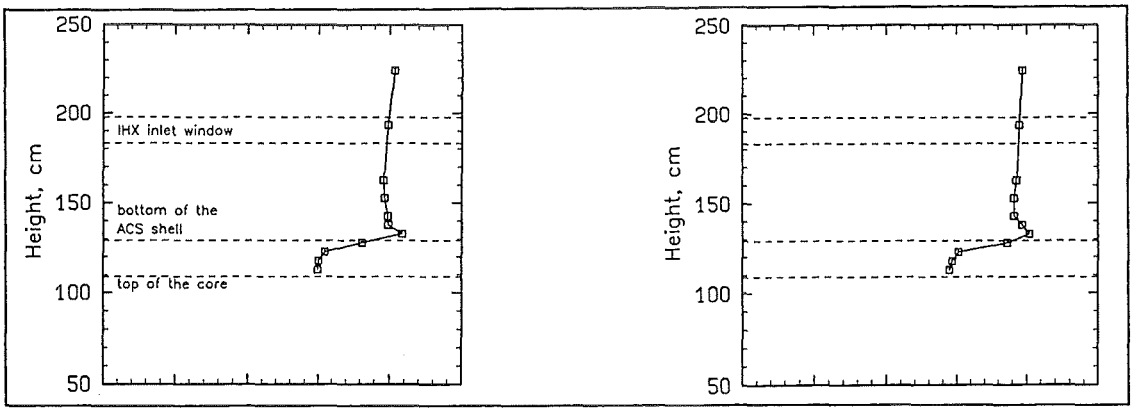

a) Axial temperature profile measured in the UP along the MER-1 device.

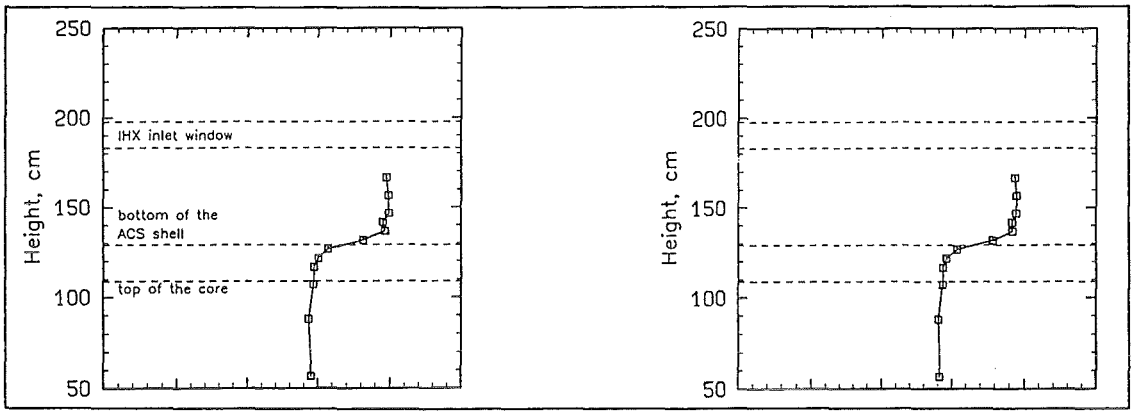

b) Axial temperature profile measured in the UP along the MER-2 device.

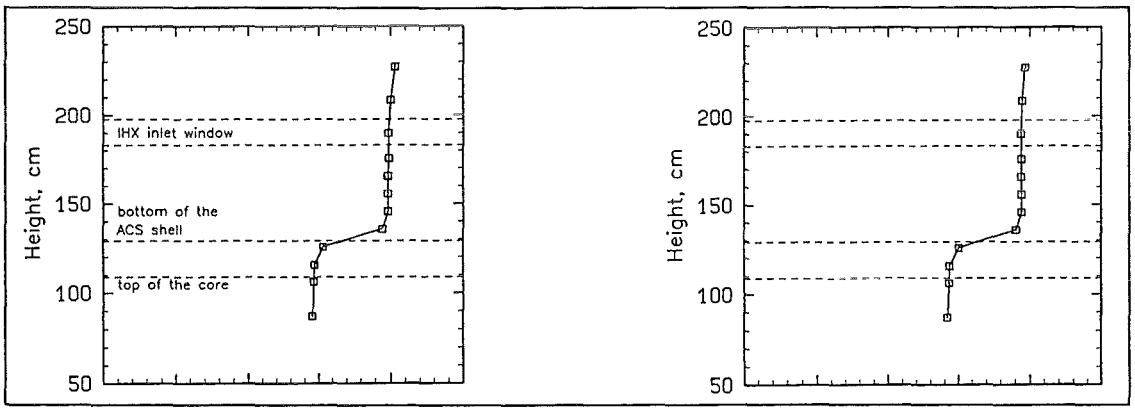

c) Axial temperature profile measured in the UP along the MER-3 device.

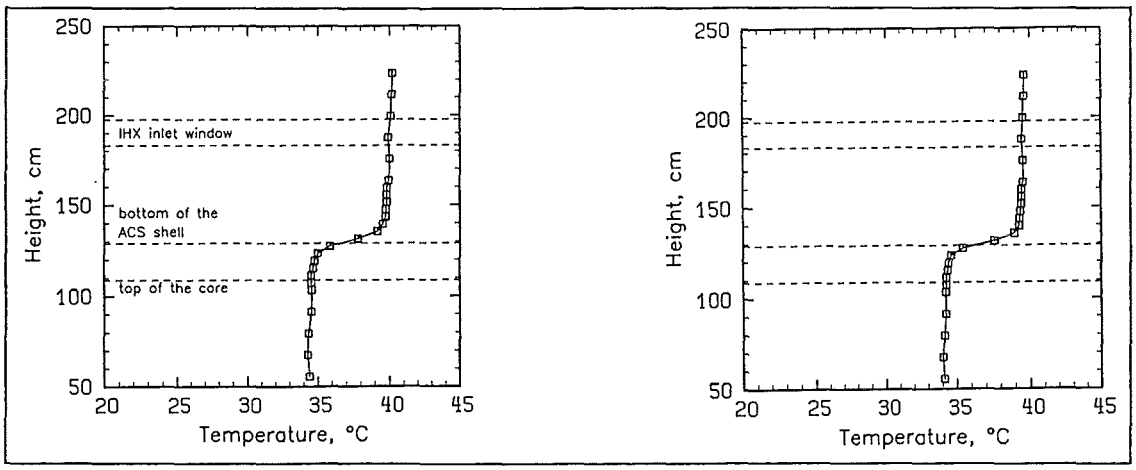

d) Axial temperature profile measured in the UP along the MEL device.

Fig. A.8.6. Influence of blocked flow paths via IHX primary loops; tests T14, T15.

Table A.9. Data comparison (cont'd.).
Fluid level in the upper plenum.

Test No. / Parameter	Design of ACS shell	Total core power, kW	Number of heated SA groups	Number of operated DHXs	Fluid level in the upper plenum	Flow path via reflector and storage elements	Flow path via IHX primary loops
T04	permeable without skirt	133	6	4	normal	blocked	unblocked
T09	permeable without skirt	133	6	4	lowered	blocked	unblocked

test T04 test T09

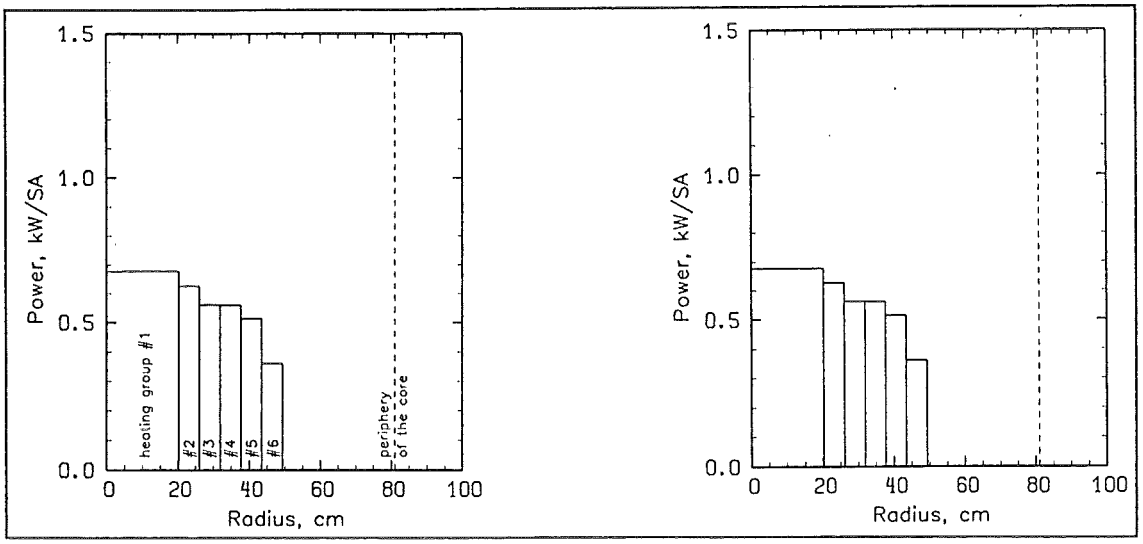

a) Radial power profile.

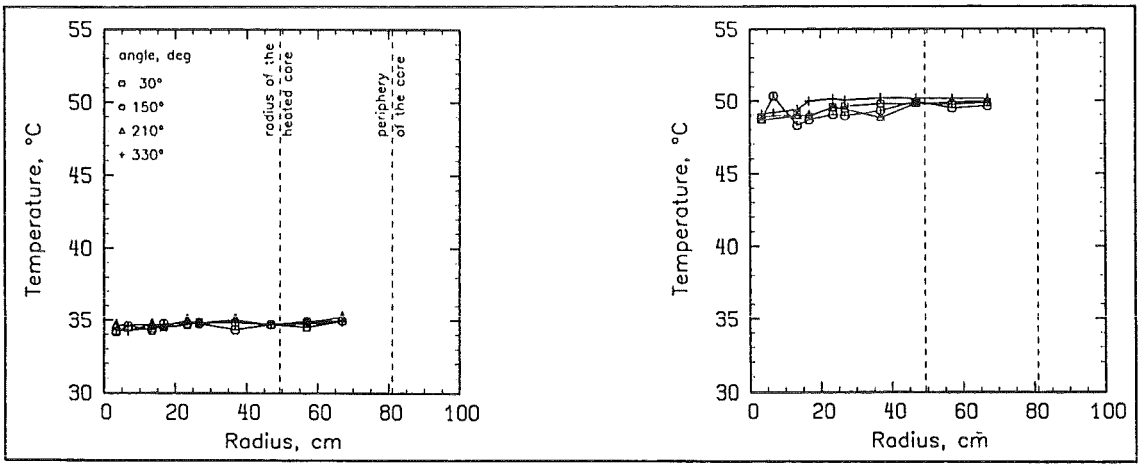

b) Radial temperature profiles of the coolant measured at the SA inlet sides.

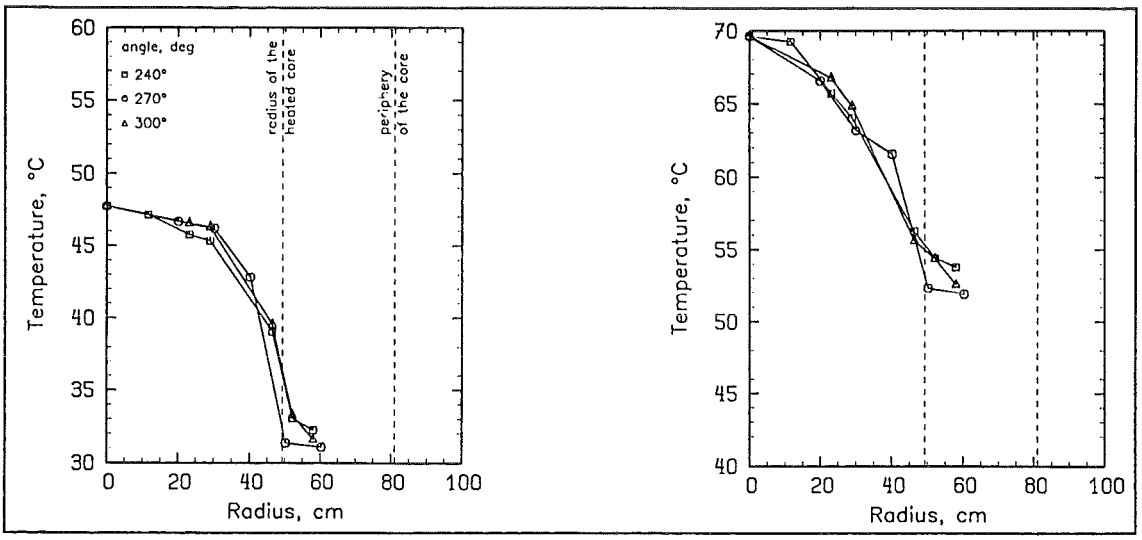

c) Radial temperature profiles of the coolant measured at the SA outlet sides.

Fig. A.9.1. Influence of the fluid level in the UP; tests T04, T09.

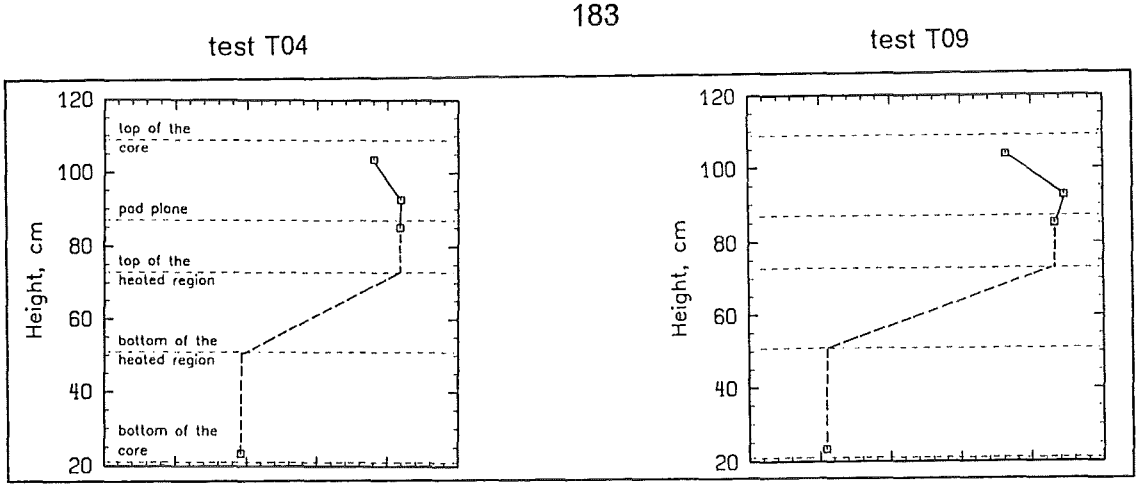

a) Axial temperature profile of the coolant measured inside SA 813 (heating group #4).

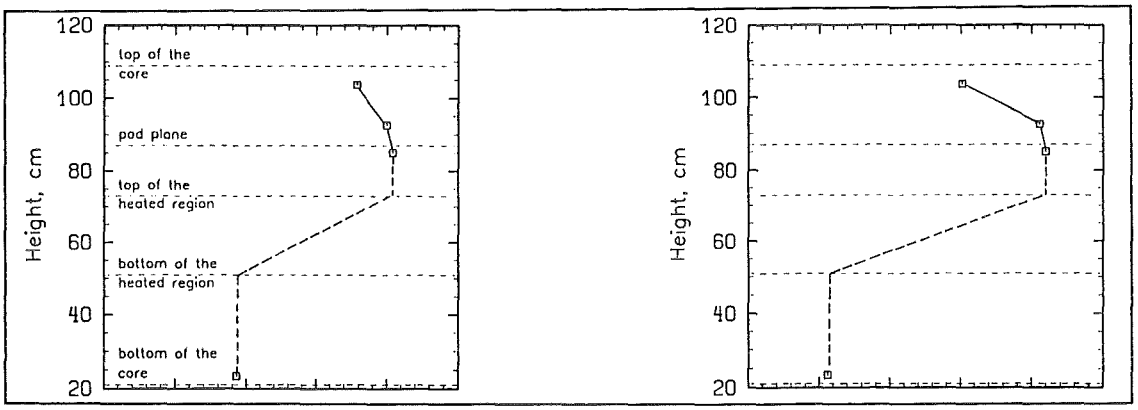

b) Axial temperature profile of the coolant measured inside SA 913 (heating group #5).

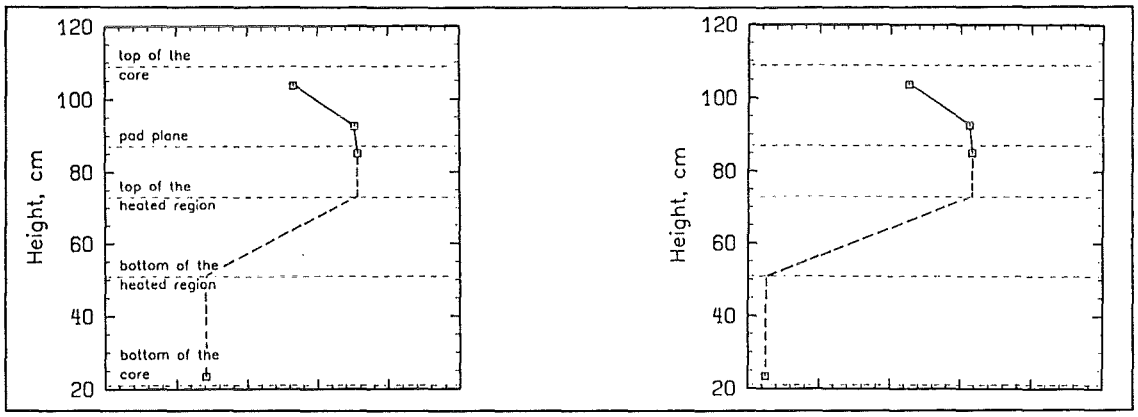

c) Axial temperature profile of the coolant measured inside SA 1017 (heating group #6).

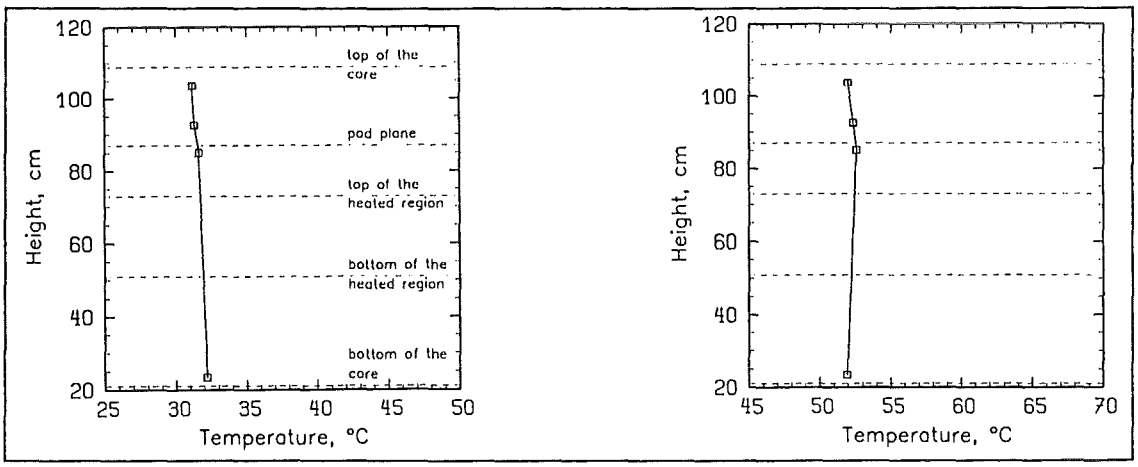

d) Axial temperature profile of the coolant measured inside SA 1319 (unheated group #7).

Fig. A.9.2. Influence of the fluid level in the UP; tests T04, T09.

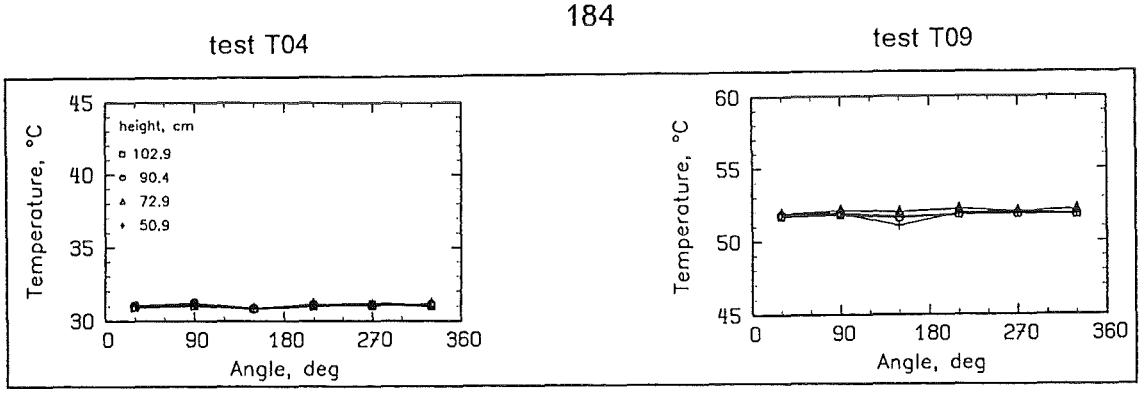

a) Azimuthal temperature profiles of the interstitial flow measured at the core periphery.

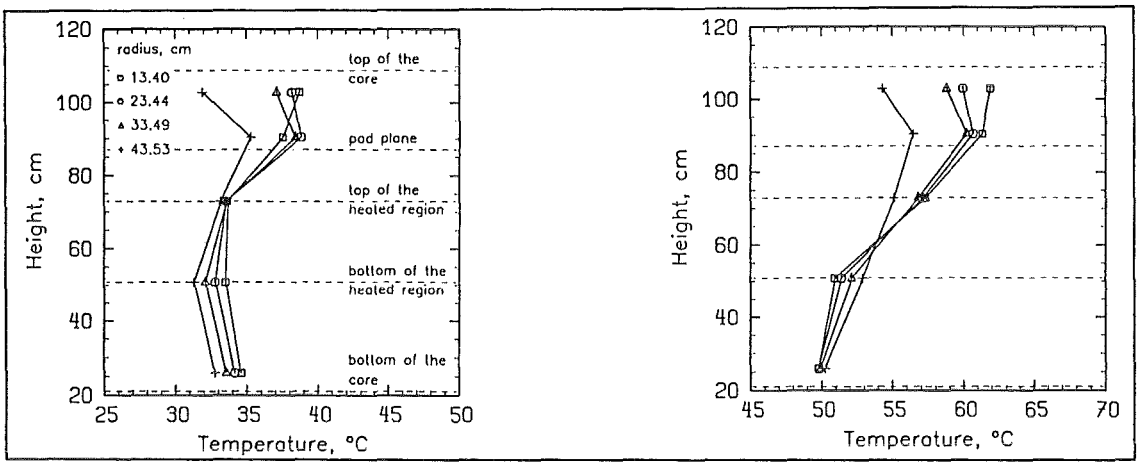

b) Axial temperatures of the interstitial flow at different radial positions (center → 90°).

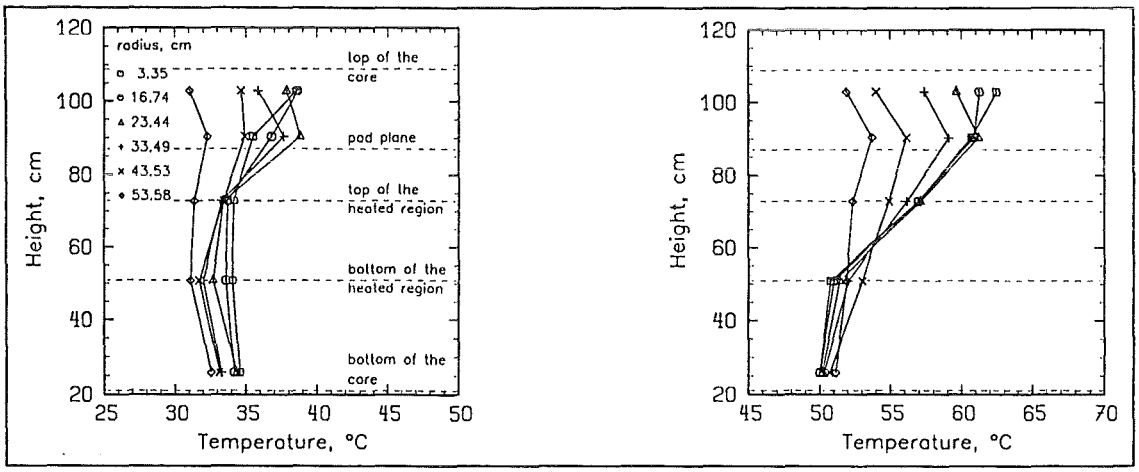

c) Axial temperatures of the interstitial flow at different radial positions (center → 270°).

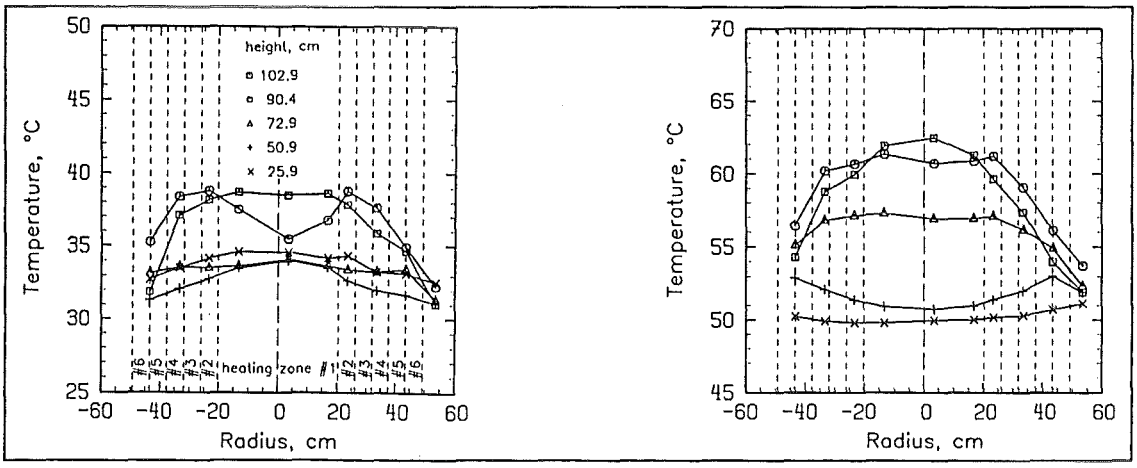

d) Horizontal temperatures of the interstitial flow across the core (90° → 270°).

Fig. A.9.3. Influence of the fluid level in the UP; tests T04, T09.

test T04 test T09

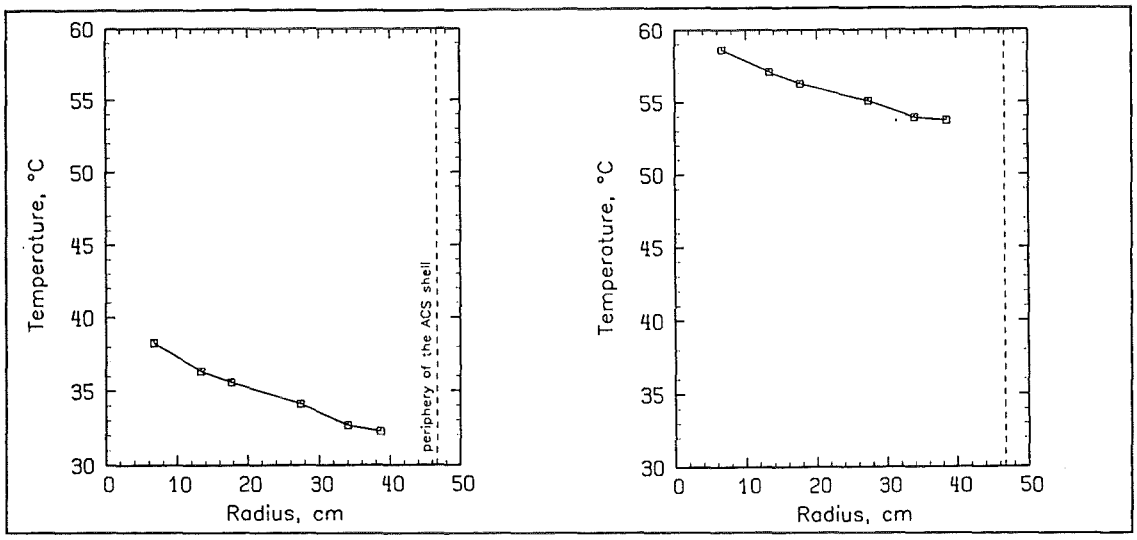

a) Radial temperature profile measured at the bottom end of the ACS (z = 1,248 mm).

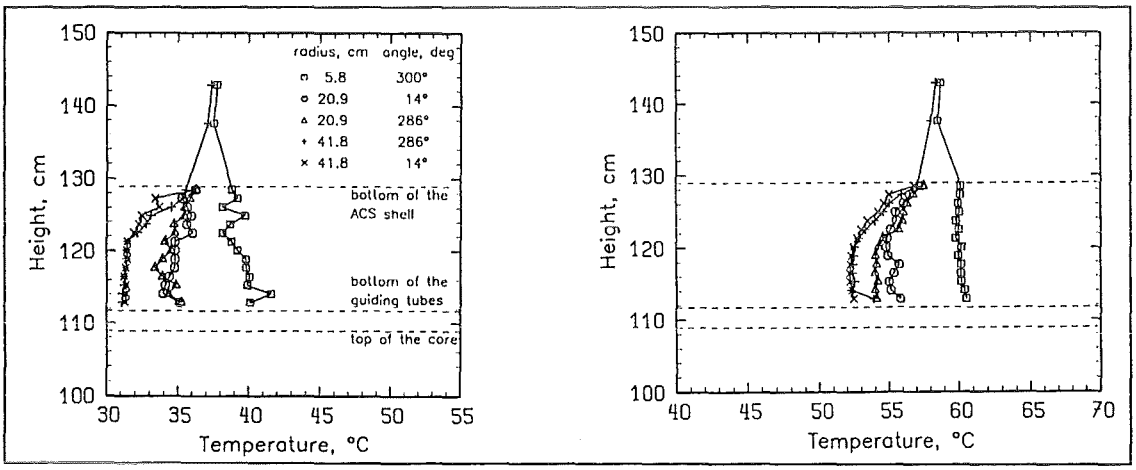

b) Axial temperature profiles at the bottom end and inside the lower part of the ACS.

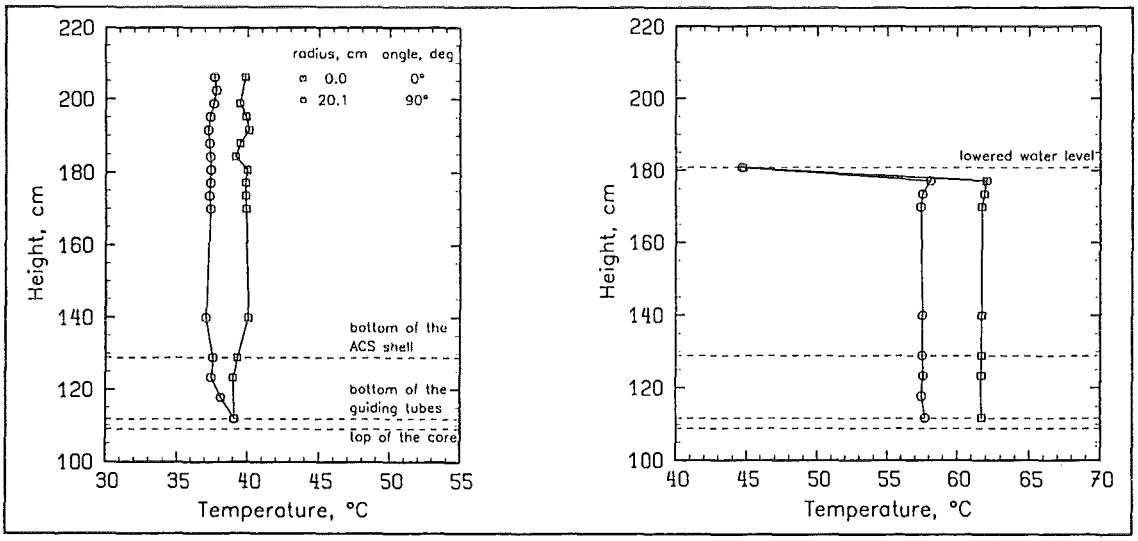

c) Axial temperature profiles measured inside the ACS.

Fig. A.9.4. Influence of the fluid level in the UP; tests T04, T09.

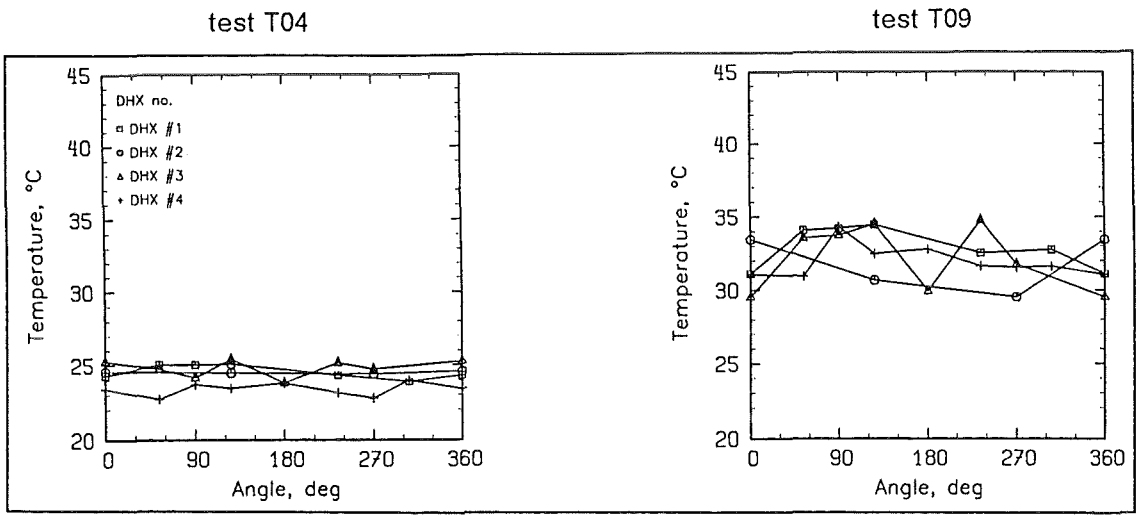

Azimuthal temperature profiles measured at the DHX outlet windows (z = 1,391 mm).

Fig. A.9.5. Influence of the fluid level in the UP; tests T04, T09.

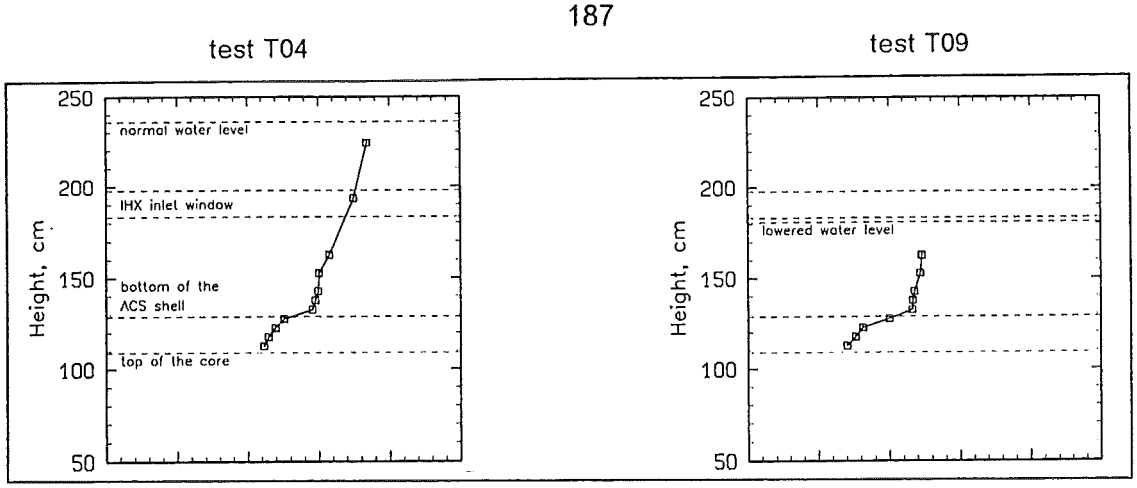

a) Axial temperature profile measured in the UP along the MER-1 device.

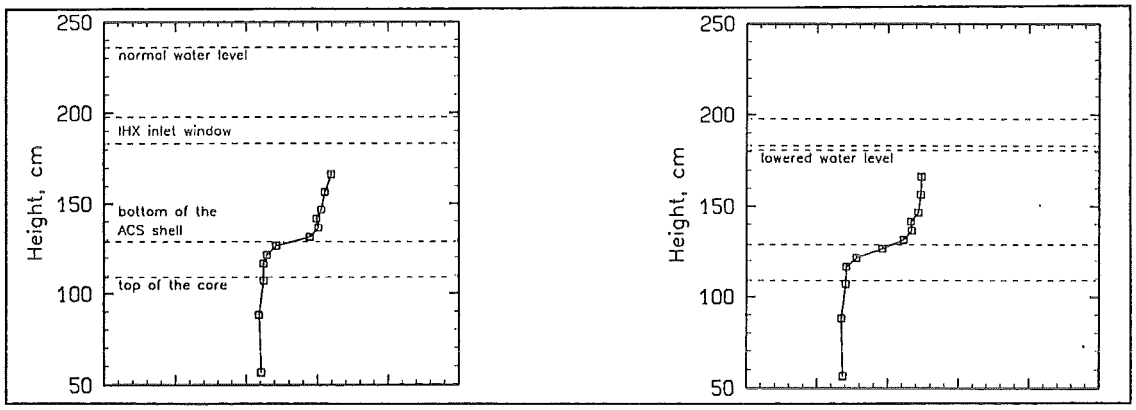

b) Axial temperature profile measured in the UP along the MER-2 device.

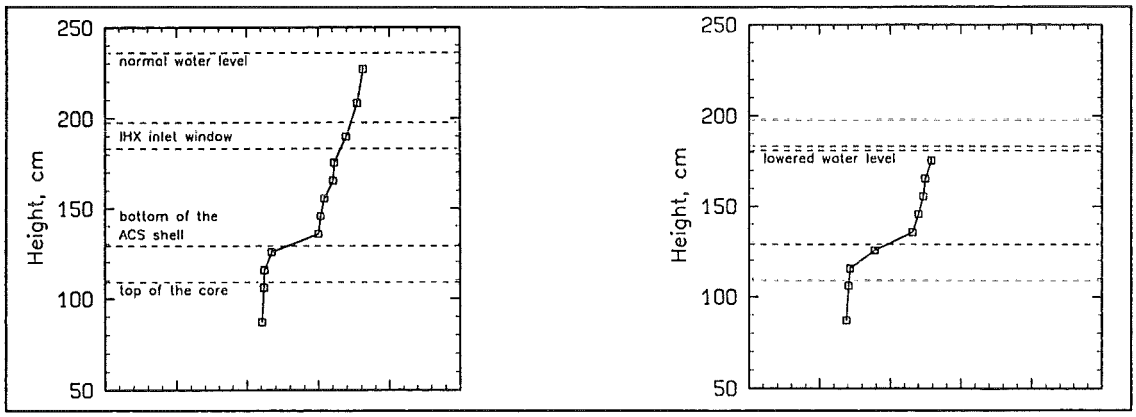

c) Axial temperature profile measured in the UP along the MER-3 device.

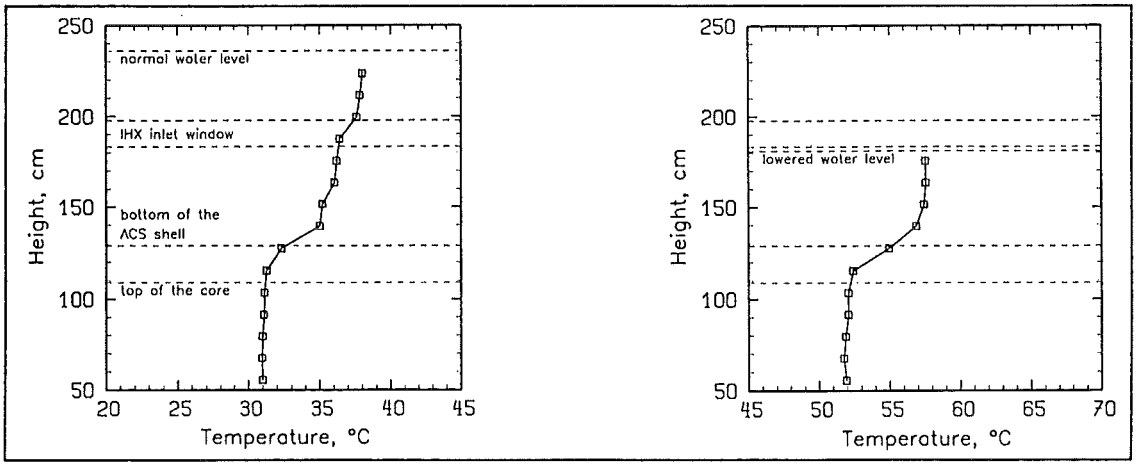

d) Axial temperature profile measured in the UP along the MEL device.

Fig. A.9.6. Influence of the fluid level in the UP; tests T04, T09.